Laser Conduction Welding of Aluminium Alloys

A thesis submitted in accordance with the requirements of the University of Liverpool for the degree of Doctor of Philosophy

by

Panton Okon

September, 2003

Declaration

This dissertation is submitted for the degree of Doctor of Philosophy in the University of Liverpool. The research described in this work was carried out by me under the supervision of Dr. G. Dearden in the Department of Engineering at the University of Liverpool.

The research was funded by the Engineering and Physical Sciences Research Council.

The contents of this dissertation are to the best of my knowledge, original except where due reference has been made to the work of others and nothing is included which is the outcome of work done in collaboration. No part of the dissertation has been, or is currently being, submitted for any degree, diploma or other qualification at any university. It is less than 60000 words in length.

Panton Okon

September, 2003

Panton Okon

Abstract

As the move towards global industrial cost-effectiveness and competitiveness becomes even more pronounced, manufacturing companies are looking for cheaper, lighter and yet stronger materials. One of such materials is aluminium and its alloys. Interest in these materials naturally gravitates to the point where questions are asked about the joining properties of these materials. Laser welding has an advantage over more conventional methods of joining due to its flexibility, automation, and controllability. However laser keyhole welding is not without its technical drawbacks, e.g. solidification cracking, porosity, spattering, blow-out, etc.

In this work, an alternative way of laser welding was investigated, namely laser conduction welding using a defocused high-power laser beam. This was opposed to conventional laser conduction welding that involved the use of low-power focused laser beams. The conventional type of conduction welding is only ideal for wafer thin materials. In this work 2mm and 3mm gauge aluminium alloys were welded.

The aim of this work was to investigate the alternative laser conduction welding process that would eliminate or drastically reduce the deficiencies of keyhole welding. It was envisaged that this new process would eradicate the need for very high power densities (that give rise to the evaporation of constituent elements) during welding of aluminium alloys, and that the consequent decrease in welding speed would reduce the solidification rate (that usually results in porosity) of the molten pool, thereby producing a stronger weld.

Results obtained from tensile strength tests showed that laser conduction butt-welds are stronger that laser keyhole butt-welds. Furthermore it was observed that the penetration depth of laser conduction welds increased with spot radius up to a maximum and then decreased.

Acknowledgements

I am grateful to my supervisor, Dr. Geoff Dearden for the privilege that I was given to pursue the PhD programme and also for his valuable input during the course of this research work. I also want to thank my Thesis Advisor Prof. K. G. Watkins for his assistance and useful suggestions.

I am indebted to my wife, Christine for her unflinching support and my pastor and spiritual mentor, Rev. (Dr.) Ebi Edward-Inatimi for his fatherly advice, support and prayers. He has truly been an inspiration to me, challenging as well as encouraging me to be all I can be for God. Many thanks go to Pastors Gloria Edward-Inatimi, Daniel Awotwi, and Tony Obaigbona for their brotherly and sisterly love and encouragement.

Thanks to John and Andy and Dave of the Laser Group for going out of their way to help me during the period of my research. I am grateful to Dr. Paul French, and Dr. Martin Sharp for their cooperation during my work at the Laser Engineering Centre, Lairdside.

Last but not the least, I am grateful for the financial support given by EPSRC.

List of Symbols:

$\underset{\sim}{q}$	Heat flux vector	
$\underset{\sim}{n}$	Unit outward normal to the surface	
$\underset{\sim}{x}$	Displacement vector	
ρ	Density	kgm^{-3}
ε	Emmissivity	
λ	Laser beam wavelength	mm
σ	Stefan-Boltzmann constant	$Wm^{-2}K^{-4}$
α, a	Thermal diffusivity	m^2s^{-1}
A	Absorptivity	
C_p	Specific heat capacity	$Jkg^{-1}K^{-1}$
D	Unfocused laser beam diameter	mm
F	Lens focal length	mm
I, H	Intensity/Power density	Wm^{-2}
K	Thermal conductivity	$Wm^{-1}K^{-1}$
m	mass	kg
M^2	Laser beam quality factor	
P, Q, q	Laser beam power	W
R, r	Spot radius	mm
r_0	Focused laser beam radius	mm
R_s	Surface reflectance	
S	Heat source term	
T	Temperature	K
t	Time	s

T_b	Boiling temperature	K
T_m	Melting temperature	K
u, v	Welding speed	ms^{-1}
w_0	Focused beam radius	mm
x	Distance in x direction	mm
y	Distance in y direction	mm
z	Distance in z direction	mm
z_m	Penetration depth	mm

Contents

1. Introduction

1.1 Aim of Research

Aluminium alloys are one of the most widely used materials in the manufacturing industry due to their relatively low weight-strength ratio. The use of aluminium alloys in various manufacturing industries, as sheets, extrusions or castings is increasing (Jones, 1992), thereby necessitating a closer examination of joining methods for aluminium alloys. Various joining techniques have been used for aluminium alloy structures in manufacturing industry and the decision to use one or a combination of more than one process is driven by economic factors, process efficiency, properties of joints, and safety of process. Examples of some joining methods used are arc welding, resistance-spot welding, friction stir welding and laser welding. Each of the afore-mentioned methods has its own relative advantages and disadvantages but there has been renewed interest in the laser welding process. "Laser welding offers a rapid, flexible, low distortion, automated manufacturing route for many components" (Jones, 1996). With regard to laser welding, keyhole welding has been the preferred mode of welding due to the fact that it produces very small heat-affected zones (HAZ), high processing speeds are possible (Dausinger et al, 1996, Barnes et al, 2000), and welds have a high aspect ratio (depth to width ratio).

Laser welding of aluminium requires high power densities because of the material properties of aluminium, e.g. high thermal conductivity, high specific heat capacity, tenacious thin layer of aluminium oxide that gives aluminium its anti-corrosive properties, and its reflectivity. The two main types of lasers used for sheet metals namely CO_2 and Nd:YAG lasers, are capable of producing continuous and pulsed power outputs and in recent years laser welding has been utilised in the aerospace, marine and automobile industries. For example, Volvo has now incorporated CO_2 and

Nd:YAG laser systems for work on the body line of the 850 series. Opel of Germany have utilised laser welding for the Astra model and Audi is undertaking a lot of research to determine the suitability of laser welding for production of space frame vehicles (Barnes et al, 2000); airframe structures are now produced by means of laser welding. Laser keyhole welding of aluminium, however, is not without its disadvantages namely, porosity, solidification cracking, blowholes, and undercutting (Forsman, 2000).

The aims and objectives of this project were to investigate an alternative laser conduction welding method that would reduce some of the deficiencies of laser keyhole welding, especially for 2mm – 3mm gauge aluminium alloy materials. It was envisaged that this new process would eradicate the need for very high power densities (that gave rise to the evaporation of constituent elements such as magnesium) during the welding of aluminium alloys; that the consequent decrease in welding speed would reduce the solidification rate that would eventually contribute to a reduction in porosity in the welds. Conventional laser conduction welding entails the use of low-power focused laser beams that are used to weld wafer-thin electronic components and is therefore not suited to the material gauges mentioned above. In this work, high-power defocused laser beams were employed and the experiments were performed using the following aluminium alloys, AA5083-O, AA2024-T4 and AA6061-O. The uses and chemical composition of these alloys are described below.

1.2 Composition and uses of Aluminium Alloys

Pure aluminium is alloyed with metals and in some cases non-metals to produce high-strength alloys with a range of physical and mechanical properties. Some of these alloys are heat-treatable (dependent on alloy composition and heat treatment for

strength) while others are non-heat-treatable (dependent on the effect of work hardening and solid solution hardening for strength). There is an internationally adopted system of temper designation which is applied both to wrought and cast alloys. A process of shaping such as rolling, extruding and forging produces wrought alloys. Alloys that have compositions that are suitable for fabrication by pouring or injecting into a mould, so that the molten metal takes the shape of the mould are known as cast alloys (The Aluminium Association, 1998).

1.2.1. Aluminium Alloy Designation System

For wrought aluminium alloys, the first digit represents the principal alloying constituent(s), the second digit represents variations of initial alloy while the third and fourth digits represent individual alloy variations – numbers that are unique but have no significance (The Aluminium Association, 1998).

The alloy designations are

1xxx	Pure Al (99% or greater)
2xxx	Al-Cu alloys
3xxx	Al-Mn alloys
4xxx	Al-Si alloys
5xxx	Al-Mg alloys
6xxx	Al-mg-si alloys
7xxx	Al-Zn alloys
8xxx	Al + other elements

All alloys used in this research work are wrought alloys and their composition and uses are as described below:

1.2.2. AA5083-O

The chemical composition of this alloy is shown in table 1.

Element	% by weight
Aluminium (Al)	94.8
Zinc (Zn)	Max. 0.25
Chromium (Cr)	0.05 – 0.25
Copper (Cu)	Max. 0.1
Manganese (Mn)	0.4 – 1
Silicon (Si)	Max. 0.4
Iron (Fe)	Max. 0.4
Titanium (Ti)	Max. 0.15
Magnesium (Mg)	4 – 4.9

Table 1 – Chemical composition of Aluminium Alloy 5083-O

AA5083 is an annealed non heat-treatable alloy. The designation 'O' represents an annealed state. The alloy has been heated to produce the lowest strength condition and to improve ductility and dimensional stability. It is used for in the construction of hulls, hull stiffeners, and decks for high-speed ships (Mandal, 2002). This alloy is also used for tanks for liquefied natural gas.

1.2.3. AA2024-T3

The chemical composition of this alloy is shown in table 2.

Element	% by weight
Aluminium (Al)	93.5
Zinc (Zn)	Max. 0.25

Chromium (Cr)	0.1
Copper (Cu)	3.8 – 4.9
Manganese (Mn)	0.3 – 0.9
Silicon (Si)	Max. 0.5
Iron (Fe)	Max. 0.5
Titanium (Ti)	Max. 0.15
Magnesium (Mg)	1.2 – 1.8

Table 2 – Chemical composition of Aluminium Alloy 2024-T3

AA2024-T3 belongs to the aluminium alloy series that is heat-treatable. The designation 'T3'represents the fact that the alloy has been solution treated and naturally aged. AA2024 plates are used for the construction of aircraft internal structures (Mandal, 2002). AA2024-T3 is used for aircraft fittings, gears and shafts, bolts, clock parts, computer parts, couplings, fuse parts, hydraulic valve bodies, missile parts, munitions, nuts, pistons, rectifier parts, worm gears, fastening devices, veterinary and orthopaedic equipment.

1.2.4. AA6061-O

The chemical composition of this alloy is shown in table 3.

Element	**% by weight**
Aluminium	98
Zinc (Zn)	Max. 0.25
Chromium (Cr)	0.04 – 0.35
Copper (Cu)	0.15 – 0.40
Manganese (Mn)	Max. 0.15

Silicon (Si)	0.4 –0.8
Iron (Fe)	Max. 0.7
Titanium (Ti)	Max. 0.15
Magnesium (Mg)	0.8 – 1.2

Table 3 – Chemical composition of Aluminium Alloy 6061-T6

AA6061-O has high corrosion resistance, is heat-treatable and of moderate strength; it is used for roof structures of arenas and gymnasiums. Structural members of trains in Europe and Japan are made partly with AA6061 (Mandal, 2002). AA6061-O is used for aircraft fittings, camera lens mounts, marine fittings and hardware, electrical fittings and connectors, hinge pins, couplings, magneto parts, brake pistons, hydraulic pistons, appliance fittings, valve and valve parts and bike frames.

1.3 Advantages of welding Aluminium Alloys

As already highlighted above, aluminium alloys are widely used in the manufacturing industry. Plates and sheets of these alloys are required for the marine, aerospace and automotive industries, giving rise to the need for joining. Some conventional methods employed in joining aluminium alloys are fusion welding methods such as tungsten inert gas (TIG) welding and gas metal arc welding (GMAW); solid state welding, e.g. friction welding and mechanical bonding methods such as riveting. However, welding has certain advantages over riveting which has been used considerably in the aerospace industry. These advantages are as follows:

(i) Welding is generally cheaper than riveting.

(ii) Since lesser material is used in welding, the finished product is much lighter and therefore less expensive.

(iii) Unlike riveting, caulking is unnecessary in welding. The joints are usually pressure tight

(iv) Welding can be used for the construction of certain designs that are impracticable to achieve by riveting.

(v) Welding is not as noisy as riveting.

(vi) Welding reduces labour required by riveting by about 60%.

1.3.1. Overview of welding processes for aluminium alloys

The main processes in use today for the welding of aluminium alloys include TIG (tungsten inert gas), MIG (metal inert gas), friction stir, resistance and laser beam welding. Polmear, (1995) gives the requirements for welding aluminium as follows:

1. An intense and localized heat source to counter the high thermal conductivity, specific heat and latent heat of the metal.
2. The ability to remove the surface oxide film which has a melting point (about 2000^0C). This tenacious oxide layer may become entrapped in the weld to form inclusions.
3. A high weld speed in order to minimize distortion arising from the relatively high coefficient of thermal expansion
4. Low hydrogen content because of the high affinity aluminium has for it. Porosity occurs in the weld due to entrapment during solidification.

The TIG welding method is better for thin light-gauge materials, when there is a need for good surface finish and when welding from one side, e.g. when welding pipes and/or when repairing castings. TIG welding is generally done with alternating current, which is struck between a tungsten electrode and the aluminium alloy. A filler rod may be used if required. Fluxes are not required because the arc cleans the electrode and aluminium; a shield of inert gas prevents re-oxidation. Other features of this process are (Norrish, 1992)

- Arc energy density is relatively high
- The process is very controllable
- Joint quality is usually high
- Deposition rates and joint completion rates are low.

This process has been applied in the aerospace, nuclear and power generation industries as well as for chemical processing plants and food processing/brewing equipment.

The MIG method is used primarily in the case of thicker or heavy-gauge materials when high welding speed is a priority and also for long, continuous welds. In this process, a direct current of arc of reverse polarity (with the electrode positive) is struck between the aluminium and a continuously fed aluminium wire electrode, which also acts as filler. As with the TIG process fluxes are not required because the arc cleans the aluminium and inert gas shielding prevents re-oxidation. Penetration during the MIG welding process cannot be controlled as closely as the TIG process so butt joints have to be backed or welded from both sides. Other features of this process are (Norrish, 1992)

- Low heat input compared to other arc welding processes

- Continuous operation
- High deposition rate
- No heavy slag leading to reduced post-weld cleaning
- Low hydrogen reducing risk of cold cracking.

This process has been employed for the fabrication of aluminium alloy cryogenic vessels and military vessels.

Resistance welding is a process in which two surfaces are joined by the heat generated by resistance to the flow of electric current through workpieces that are held together under force by electrodes. The contacting surfaces are heated by short-time pulse of low voltage, high amperage current to form a fused nugget of weld metal. When the current ceases, the electrode force is maintained while the weld rapidly cools and solidifies. The electrodes are retracted after each weld, which usually is a fraction of a second.

In **Friction welding,** heat is generated by rotating one part against another while they are held together under pressure. Parts must be of a shape and size so that the adjoining surfaces include a common circular area. Surface melting and a slight upset at the joint area accompany formation of the weld. Friction welding is a form of solid state welding and the melting points of the components are not exceeded (Brandon et al, 1997). At the interface, extensive plastic flow occurs to relieve compressive stress. A new variation of friction welding, **friction stir welding,** has been developed by The Welding Institute (TWI). In this process, a tool or tip is rapidly rotated while being squeezed between two abutting workpieces (Messler, 1999). First a hole is pierced at

the start of a joint with the rotating tip or pin, which then moves forward in the direction of the welding. Friction produced by the rotating pin generates a plasticized zone around the tip. Pressure provided by the pin forces the plasticized material to the rear of the tip where it cools to form a bond. No melting occurs in the process.

The advantages of friction stir welding are

- No filler needed
- Fatigue resistance
- Easy to automate
- Low tooling cost

However, a backing bar and welding fixtures are needed. Friction stir welding can only be used on straight flat work pieces and it leaves an end hole when the tool is pulled out.

In **laser beam welding** a liquid melt pool created by the absorption of incident radiation. This melt pool is allowed to grow to a desired size and is the propagated through the solid interface (Dulcy, 1999). Melted material cools and solidifies behind the laser beam to form a weld. The two fundamental modes of laser welding are keyhole or penetration welding and conduction welding. The major difference between theses two modes of laser welding is that the weld pool remains unbroken during conduction welding and opens up in the case of keyhole welding to allow the laser beam to enter the melt pool (Duley, 1999).

Unlike keyhole welding there is less perturbation during conduction welding and because the weld pool does not open up, porosity due to gas entrapment is virtually non-existent. Laser conduction welding (LCW) therefore is a potential way forward for welding thin-gauge (2mm to 3mm) aluminium alloys.

Laser welding offers some unique advantages over arc welding methods that include

- Low distortion
- Reduced heat affected zones
- Automation and flexibility
- Non-contact process giving cleaner welds
- Faster welding speeds than conventional welding processes
- Single pass welding

The above advantages are reasons why laser welding is becoming more widely used in the manufacturing industry. The advantages of laser welding, over other conventional methods have been summarized by Duley (1999) as follows:

Parameter	**Process**			
	Laser Beam	**Gas Tungsten (TIG)**	**Gas Metal Arc (GMA)**	**Resistance Welding (RW)**
Joining efficiency	0	-	-	+
High Aspect Ratio	+	-	-	-
Small heat-affected zone	+	-	-	0
High Processing speed	+	-	+	-
Bead profile	+	0	0	0
Weld at atmospheric pressure	+	+	+	+
Weld reflective metals	-	+	+	+

Combine with filler	0	+	+	-
Automate process	+	+	0	+
Capital cost	-	+	+	+
Operating cost	0	+	+	+
Reliability	+	+	+	+
Fixturing	+	-	-	-

Table 2.1 – Table showing comparison of welding processes

Legend: +, advantageous; -, disadvantageous; 0, neutral

1.3.2. Laser Welding

There are mainly two types of laser welding namely, laser keyhole welding and laser conduction welding. In the case of keyhole welding, the power density required is about 10^6 W/cm^2 or more and the material or metal that is welded melts and vaporises. The vaporisation pressure of the molten metal creates a vapour channel that is held in place by heat transfer phenomena known as inverse Bremmsthralung which is the process of photons absorbed by electrons (Steen, 1998) and Fresnel absorptions (absorptions due to multiple reflections on the keyhole walls). This vapour channel is called the keyhole and it follows the path of traverse of the laser beam on the work piece, with molten metal swirling round it and closing it behind the laser beam. The aspect ratio (ratio of penetration depth to weld width) of keyhole welds is over 4:1. On the other hand the conduction weld has an aspect ratio of less than 4:1 (LIA Handbook, 2002). This type of weld occurs when the power density of the laser beam incident

on a work piece is insufficient to cause boiling (Steen, 1998), resulting in a shallow but relatively wide weld. The shape of a keyhole weld is such that the sides are very nearly parallel to each other with the top of the weld widening. Schematic diagrams of both welds are shown in figure 1.

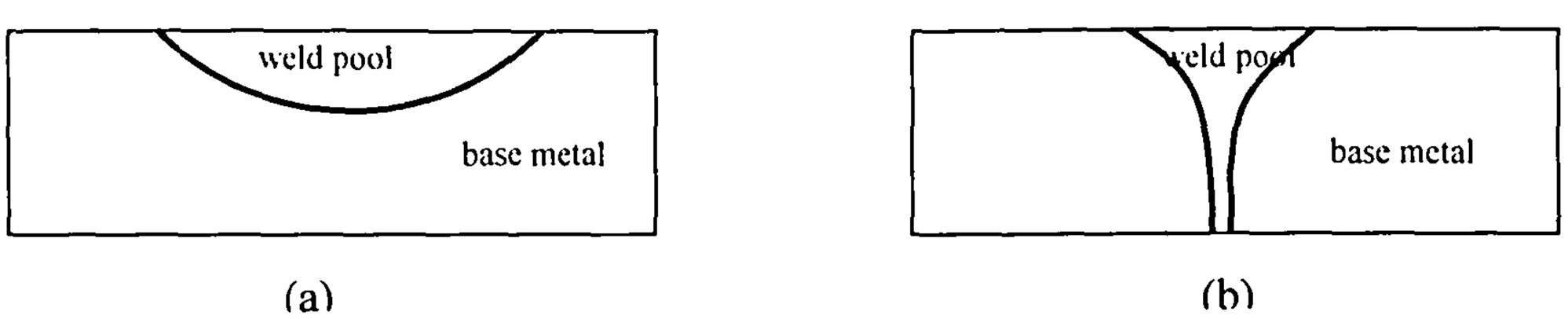

Figure 1 – Schematic showing (a) shape of a conduction weld and (b) shape of a keyhole weld

In this project aluminium alloys of up to 3mm in thickness have been welded in both bead-on-plate and butt-weld configurations. How that has been achieved and the advantages of LCW compared to LKH, both theoretically and experimentally are what is discussed in this work. Uniaxial tensile strength tests carried out on laser conduction and laser keyhole butt-welds indicate that laser conduction welds (LCW) are stronger than laser keyhole welds (LKH).

1.3.3. Properties influencing/ affecting laser welding of aluminium alloys

Properties that affect laser welding of aluminium alloys are (i) Oxide layer, (ii) Thermal conductivity, (iii) Viscosity of melt (Forsmann, 2000), and (iv) Hydrogen solubility

- **Oxide Layer** Aluminium has a high affinity for oxygen and this results in a thin oxide layer that continues to grow at a decreasing rate to reach a thickness of tens

of nanometres (Polmear, 1995). Aluminium oxide melts at 2050^{0}C whereas the base metal has a melting point of approximately 650^{0}C. If metal sheet is not thoroughly cleaned, tiny pieces of the oxide become lodged in the weld pool producing an adverse effect on the weld-metal flow and solidification (Mandal, 2000). The result is usually incomplete fusion

- **Thermal Conductivity** Aluminium alloys have thermal conductivities 4 to 15 times higher than that of iron based materials depending on the type of steel they are made of, mild steel or stainless steel (Dausinger et al, 1996). This means that about 5 to 25 times greater intensity is required to produce deep penetration welds in aluminium alloys than in steels. This high thermal conductivity makes aluminium sensitive to fluctuations in heat input by the welding process.
- **Melt Viscosity** Melt viscosity of pure aluminium is relatively lower than that of other metals. This may increase when it is alloyed with other metals or elements. The low melt viscosity gives rise to melt sagging and less damping of irregular keyhole movements.
- **Hydrogen Solubility** Hydrogen dissolves very rapidly in molten aluminium although it has almost no solubility in solid aluminium. The high temperatures of the weld pool allow a large amount of hydrogen to be absorbed, and as the pool solidifies, the solubility of hydrogen is greatly reduced. Hydrogen that exceeds the effective solubility limit forms gas porosity, if it does not escape from the solidifying weld.

This thesis is organized as follows:

Chapter 1 – Introduction

Chapter 2 – Literature Review

Chapter 3 – Theoretical aspects

Chapter 4 – Experimental

Chapter 5 – Results

Chapter 6 – Discussion

Chapter 7 - Conclusions

References:

- Barnes et al, *'Joining Techniques for Aluminium Spaceframes used in Automobiles, Part 1 – Solid and Liquid Phase Welding'*, Journal of Materials Processing Technology, vol. 99, pp. 62-71, 2000
- Brandon, D. and Kaplan, W., Joining Processes: An Introduction, John Wiley & Sons, 1997
- Dausinger et al, '*Welding of Aluminium: A Challenging Opportunity for Laser Technology*', Journal of Laser Applications, Vol. 8, pp. 285-290, 1996
- Duley, W.W., Laser Welding, John Wiley & Sons, Inc., 1999
- Forsman, T, *"Laser Welding of Aluminium Alloys"*, PhD Thesis, University of Lulea, Sweden, 2000
- Jones, I.A. et al, *"CO_2 Laser Welding of Aluminium Alloys"*, Proceedings of LAMP'92, Nagaoka, Japan, pp.523-528, June 1992
- Jones, I.A. " *Laser Welding of Aluminium*", International Conference on Advances in Welding Technology (ICAWT), Ohio, USA, November,1996
- LIA Handbook of Laser Materials Processing, Ready, J (Editor In Chief), 2001
- Mandal, N.R. Aluminium Welding, Alpha Science International Ltd., 2002
- Messler, R., Principles of Welding, John Wiley & Sons, Inc., 1999
- Norrish, J. Advanced Welding Processes, IOP Publishing Ltd., 1992
- Polmear, I.J., Light Alloys- Metallurgy of Light Metals, Arnold, 1995
- Steen, W, Laser Material Processing, Springer-Verlag London Ltd., 1998
- The Aluminium Association Inc., Aluminium Alloy Selection and Application, The Aluminium Association Inc., 1998

2. Literature review

2.1. Laser Fundamentals

The word laser is an acronym for **L**ight **A**mplification by **S**timulated **E**mission of **R**adiation. A focused high-power coherent (all parts in phase) and monochromatic (single wavelength) light beam is utilised for laser welding (Welding Handbook). A laser beam is produced when an active medium, within a laser cavity, is excited by means of a flash lamp or electric discharge (Dawes, 1992). For a CO_2 laser, this medium consists of a combination of carbon dioxide, helium and nitrogen whereas for a Nd:YAG laser the active medium is a crystal rod. A schematic diagram is shown in figure 2.1.

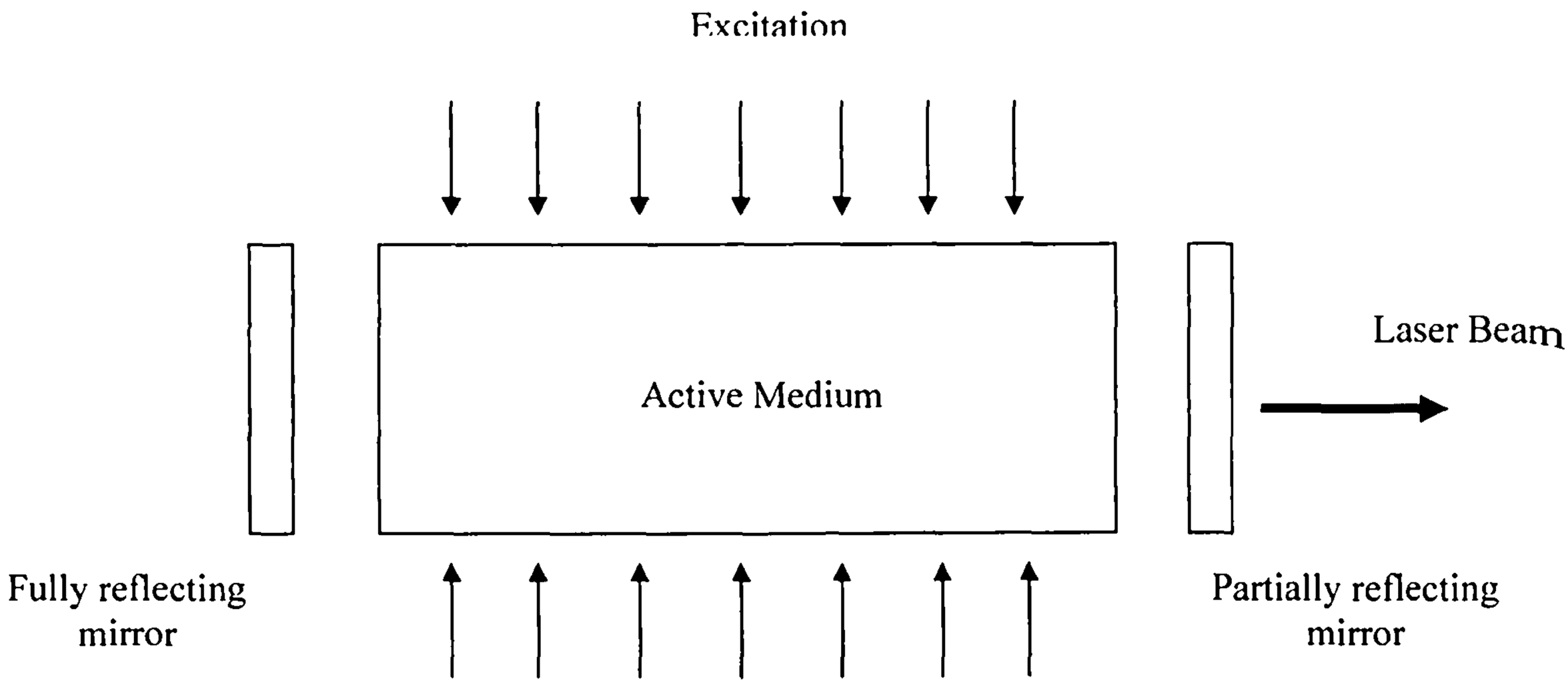

Figure 2.1 – Schematic of laser cavity

The cavity has mirrors at each end, one partially reflecting and the other fully reflecting and the whole arrangement constitutes an optical oscillator (Steen, 1998). The active medium consists of atoms, molecules or ions that absorb energy when

excited. They emit photons in their excited state and then return to their former state. This form of emission of photons is called spontaneous emission. When a photon collides with an excited atom, a photon is released from the atom and the resulting two photons will collide with other atoms to release more photons. This build-up of photons is termed stimulated emission. The optical oscillator makes it possible for light (photons) to travel back and forth between mirrors till the resulting amplified light escapes via the partially reflecting mirror, in the form of laser radiation. The laser beam is then focused by means of optics (lens and mirrors) to a spot on the material to be processed.

Illustrations of spontaneous and stimulated emissions are shown below:

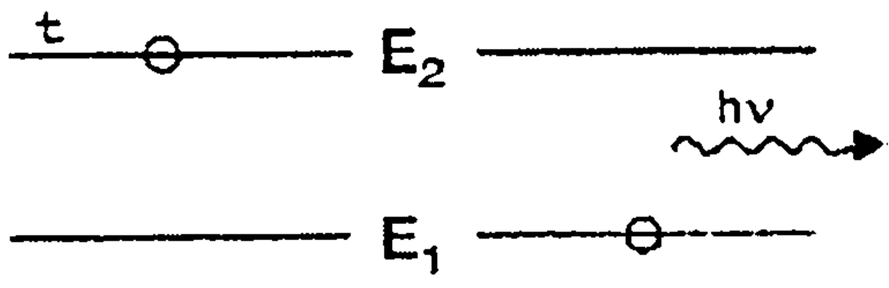

Spontaneous Emission (from TRUMPF GmBH, 1994)

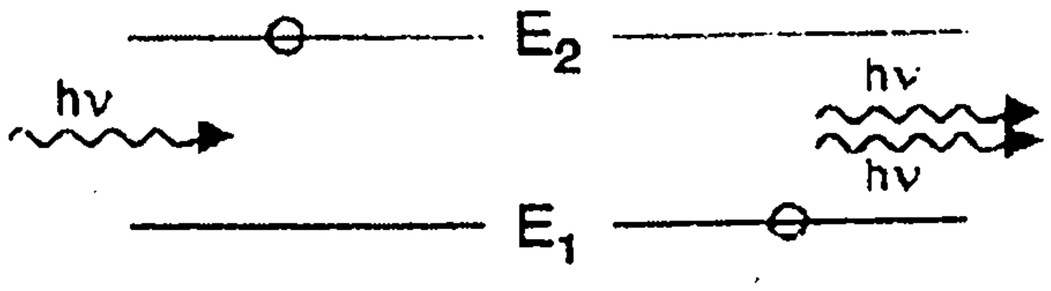

Stimulated Emission (from TRUMPF GmBH, 1994)

Atoms exist only in distinct energy levels. Normally they are in their lowest energy-level state, the ground state (Trumpf, 1994). They absorb the radiation emanating

from an electromagnetic field at the very moment when the energy quanta, hν, equals the energy difference ($E_2 - E_1$) between two atomic states.

In the case of spontaneous emission, an atom having absorbed a photon rises to a higher state of energy excitation (E_2). Since this is not a permanent state, it reverts to its original state (E_1) during which a photon is released.

For stimulated emission, photons collide with excited atoms which release more photons as they fall to a lower energy state. More and more photons are generated from other excited atoms. The energy change between the excited state of the photons and a lower state releases radiation which is essentially the laser beam.

Important properties of the laser beam are:

Coherence

Monochromaticity

Divergence

Polarization

Mode structure

Wavelength

Coherence

Coherence describes the property that different parts of the laser beam, which is essentially an electromagnetic radiation, remain in phase. Laser radiation is coherent both in time and space (LIA Handbook, 2002).

Monochromaticity

This is the property that describes the fact that most lasers are designed to produce a single wavelength (LIA Handbook, 2002). For example, CO_2 lasers produce laser beams of wavelength 10.6 microns while Nd:YAG lasers produce laser beams with a wavelength of 1.06microns.

Divergence

Laser light emerging from the laser cavity is very closely parallel to the optical axis. Divergence describes the angle of spread from the optical axis as the laser radiation travels along. This is governed by the inherent diffraction of the beam itself. The divergence of a laser beam is given by

$$\Theta = \frac{\lambda}{2w_0} \text{ where}$$

λ = wavelength and w_0 = beam radius.

The variation of the beam radius with distance is given by

$$w = w_0\sqrt{1+(\frac{z}{z_R})^2} \qquad (2.1)$$

where $z_R = \frac{{w_0}^2\pi}{\lambda}$; z_R is called the Rayleigh length over which the beam radius does not vary by more that a factor of $\sqrt{2}w_0$. w_0 is the smallest beam radius and its location $z = 0$ is called the beam waist(Schuocker, 1999).

Polarization

The orientation of the electric vectors of a laser beam is what characterises the polarization of the beam. Laser beams consist of two components namely, electric vector field and a magnetic vector field. The laser beam is said to be polarised if the

electric vectors are aligned in a given direction in space (LIA Handbook, 2002). The direction of the electric field determines the polarisation of the laser beam.

Mode Structure

This describes the configuration of the electromagnetic field within the confines of the laser cavity that is defined by the cavity geometry (Steen, 1998). Laser beams have both longitudinal and transverse modes, the former resulting from the axial modes and the latter from the reflections from the sides of the cavity. In the laser cavity, standing waves are set up and a number of such off-axis waves interfere with each other to produce transverse waves that are characterised by the mode structure of the cavity (Steen, 1998). These modes are called transverse electromagnetic modes and are represented by $TEM_{mn,}$ where m denotes the number of antinodes in the x or r directions and n denotes the number of antinodes in the y or θ directions, for rectangular or cylindrical co-ordinate systems respectively. The fundamental mode is TEM_{00} corresponds to a near-perfect Gaussian beam. Gaussian-Laguerre (cylindrical) and Gaussian-Hermite (rectangular) functions describe the transverse field distributions mathematically. The rectangular function is given below:

$$E(x,y) = E_0 H_m(\sqrt{2}\frac{x}{w}) H_n(\sqrt{2}\frac{y}{w}) \exp(-\frac{x^2+y^2}{w^2}) \qquad (2.2)$$

where E_0 is a constant amplitude factor. $H_n(x)$ is the Hermite polynomial of n^{th} order defined by

$$H_n(x) = (-1)^n e^{x^2} \frac{d^n}{dx^n} e^{-x^2} = n! \sum_{v=0}^{[n,2]} \frac{(-1)^v (2x)^{n-2v}}{v!(n-2v)!} \qquad (2.3)$$

$[n,2] = \frac{n}{2}$ *or* $\frac{(n-1)}{2}$ depending on whether n is even or odd. Some Hermite polynomials of low order are

$H_0(x) = 1$

$H_1(x) = 2x$

$H_2(x) = 4x^2 - 2$

$H_4(x) = 8x^3 - 12x$

w is the beam radius or spot size

The laser mode is important because each transverse resonator mode features a typical characteristic distribution of energy in the cross section of the laser beam. Below are some examples of TEM modes.

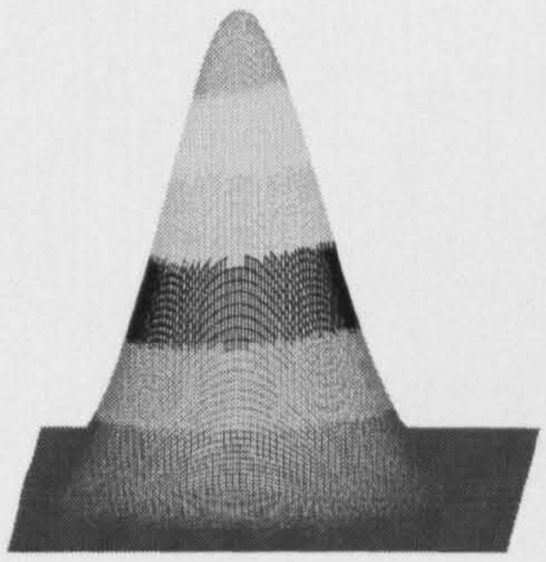

TEM_{00}

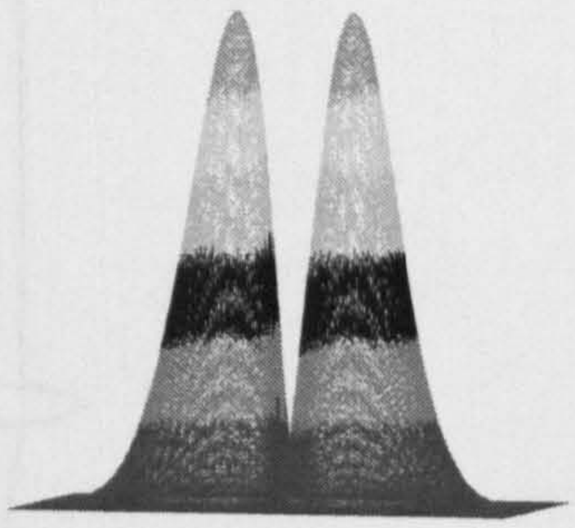

TEM_{01}

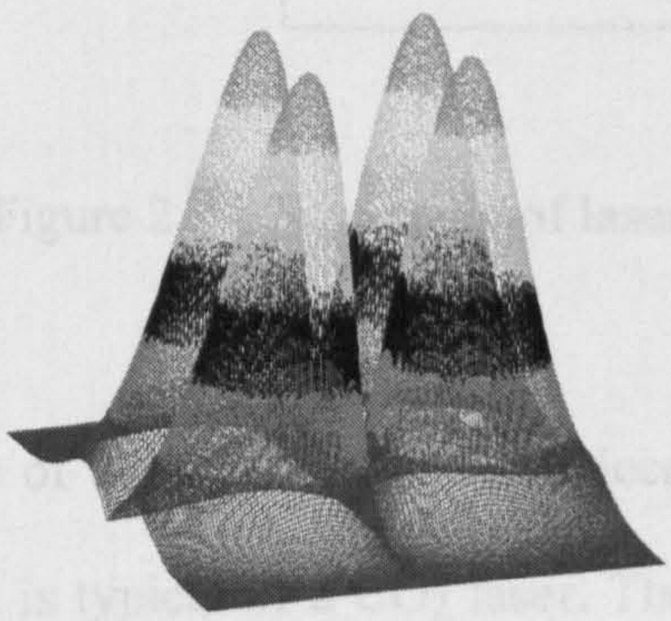

TEM_{11}

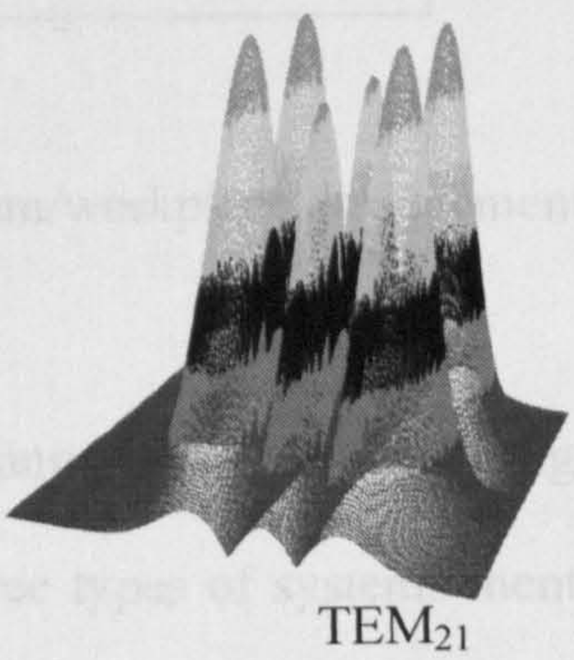

TEM_{21}

2.2 Principle of laser welding

The laser radiation created by the laser is directed by optics (mirrors and lenses) to a focus on the workpiece. Beam delivery to the workpiece may be accomplished using three systems (Crafer and Oakley, 1993) namely:

- Moving laser
- Moving workpiece
- Moving optics

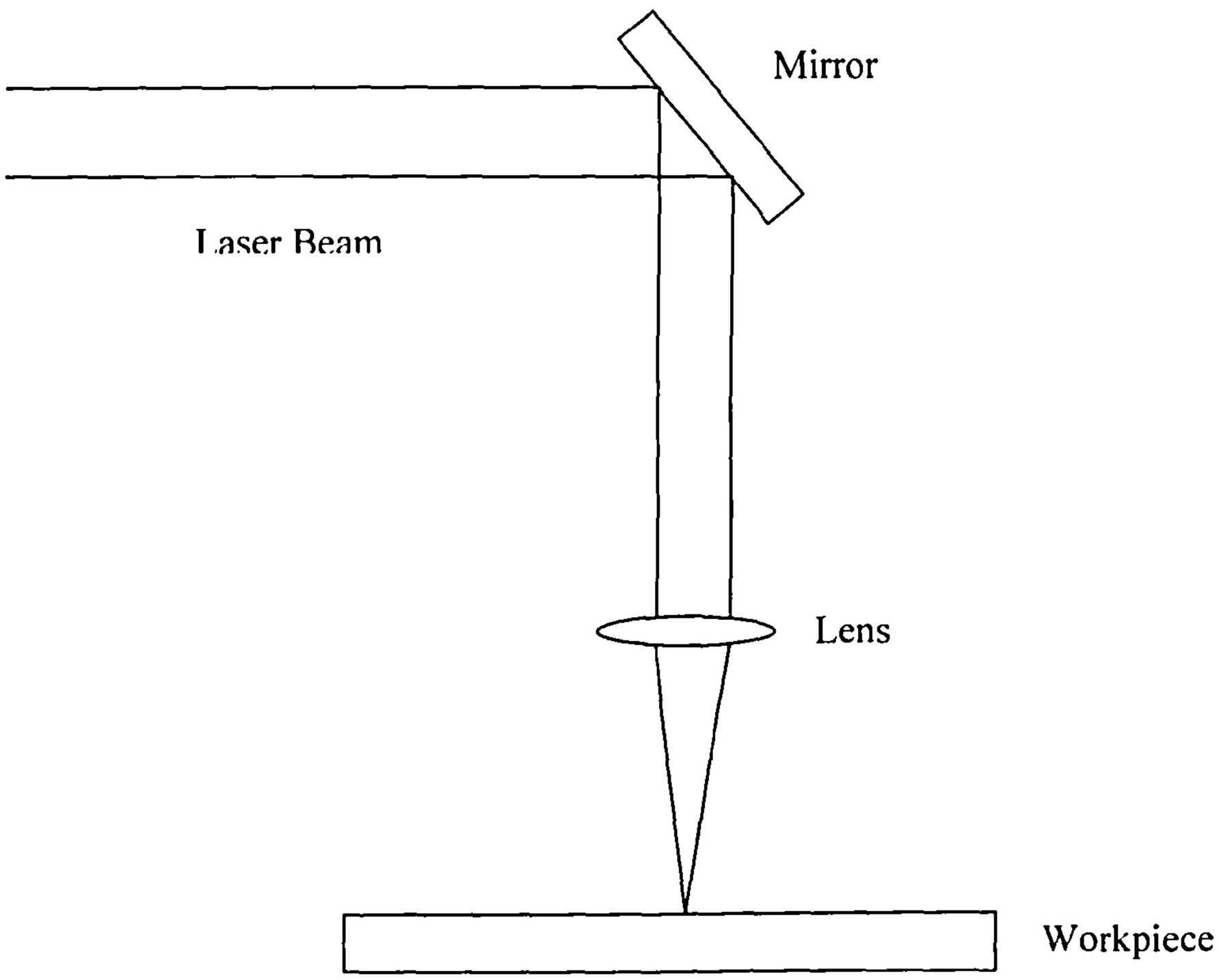

Figure 2.2 – Schematic of laser beam/workpiece arrangement

A schematic of the laser beam/ workpiece arrangement is shown in figure 2.2. The arrangement is typical of a CO_2 laser. The three types of systems mentioned above are illustrated in figure 2.3. In order to minimise oxidation of the material and also to prevent damage to the focussing lens, inert gases such as argon and helium are used

during the welding process. The white arrows show the direction of movement in all three cases.

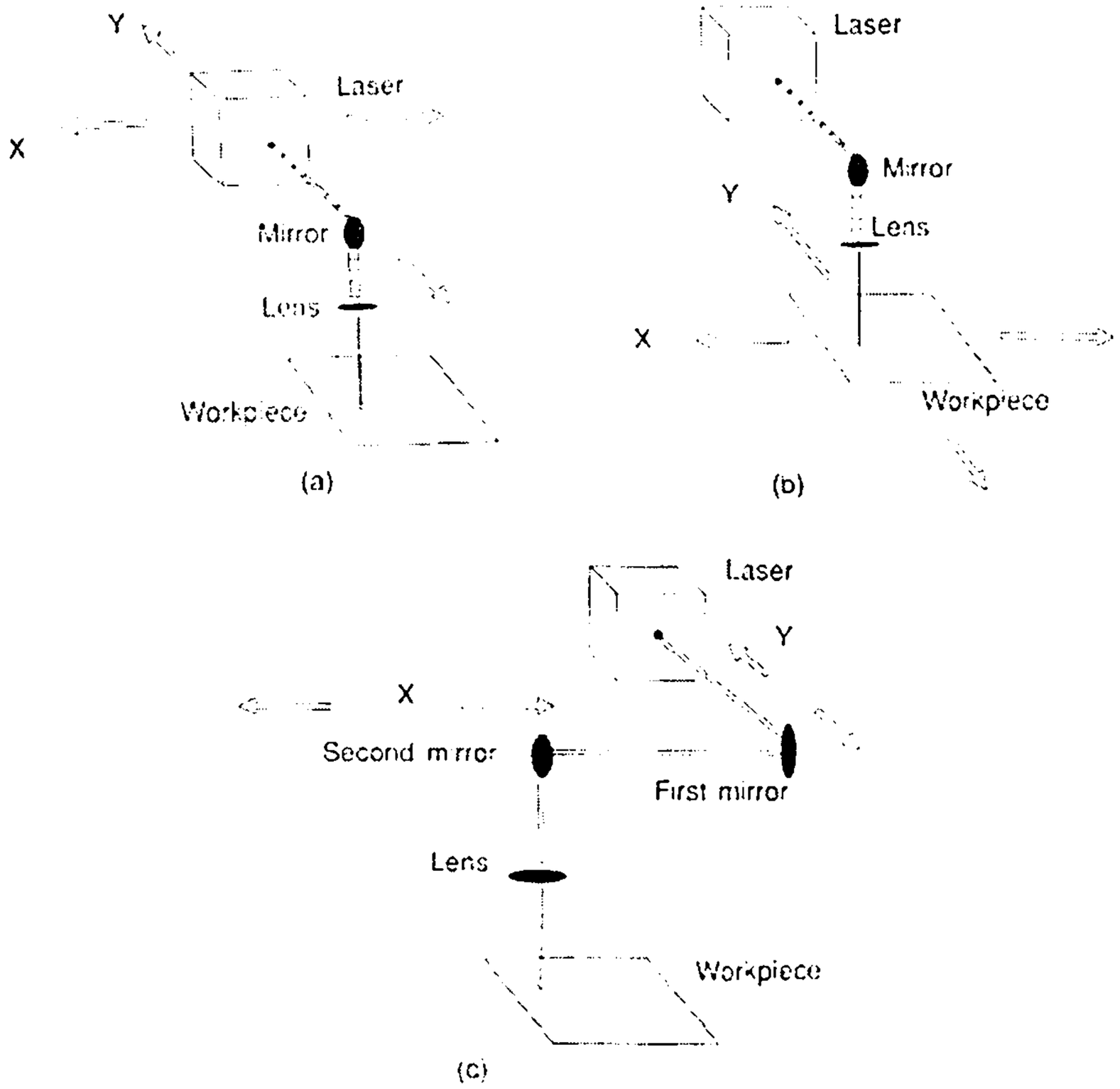

Figure 2.3 CO_2 laser system types (a) Moving laser (b) Moving workpiece (c) Moving optics (from Crafer and Oakley, 1993)

With the moving laser system, the disadvantages are that it is fairly slow and very often restricted to flat sheets. For moving workpiece systems, the weight of the material may exceed the capacity of the table when large sheets are processed. Where moving optics systems are utilized, only certain sizes of sheets can be accommodated and there is the problem of beam expansion down the optical path. The inert gas is directed towards the weld seam either coaxially or through a side jet. In the case of a Nd:YAG, fibre optics are used for laser beam delivery to the workpiece. This obviously gives the Nd:YAG more flexibility than the CO_2 laser and

makes robotic programming a tenable option. Unlike the 10.6μm wavelength CO_2 laser beam, the 1.06μm Nd:YAG laser beam can pass through fibre optics without producing any damage.

2.3. Parameters of Laser Welding

Parameters of laser welding can be divided into three groups namely (Schuocker, 1999):

(i) Design parameters – these describe the geometry of the workpieces to be joined.

(ii) Technological parameters – these deal with all the properties of the laser beam, of gas supply and the motion unit

(iii) Material parameters – these have to do with material properties such as thermal conductivity, specific heat capacity, density, etc.

2.3.1. Design Parameters

- ***Joint geometry*** – Examples of these are butt welds, bead-on-plate and lap welds. In butt-welding, the edges of two plates to be joined are brought together in close fit-up. Bead-on-plate welds are welds that are produced on a single plate without a joint. In the case of lap welds, the joints are produced when two plates placed one on top of the other are welded through. The diagrams below illustrate this.

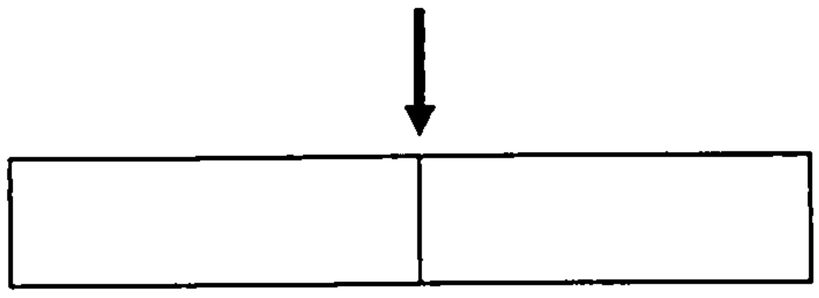

Butt joint

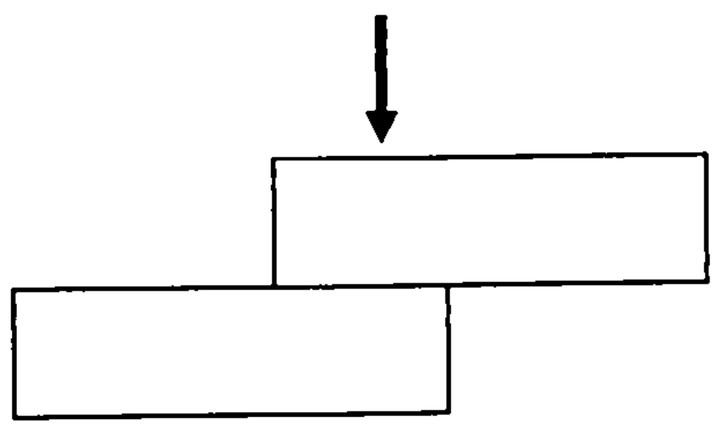

Lap joint

Other joints are T-joints and flange joints. In this work only bead-on-plate and butt joints were produced.

- ***Weld gap width*** – If the gap is too large, the laser beam passes straight through without interacting with the edges of the workpiece. For keyhole welding, it is crucial that very close fit-up should be achieved if good quality weld s are to be produced. There is a little more flexibility in this regard for conduction mode welding especially when using dcfocuscd beams.
- ***Material thickness*** – This parameter will determine the welding speed and laser power to be used if efficient coupling is to be achieved. Obviously thicker workpieces would require greater laser power and/or lower welding speeds

2.3.2. Technological Parameters

- ***Average Intensity*** – This is determined both by the laser power and beam spot radius. Basically it is given by

$$I = \frac{P}{A}$$

where I = Intensity, P = Laser Power and A = Spot area (πr^2, if a circular spot is assumed)

- ***Beam Power*** – Obtained by an integration of the intensity distribution across the beam cross section. The intensity distribution is not constant across the beam cross section.
- ***Polarization*** – A weld seam produced by a polarized laser beam shows a dependence on the direction of the welding process. As explained earlier, the direction of the electric vectors determines the polarization of a laser beam. In order to avoid this effect, most laser beams are circularly polarized.

- ***Focal Position*** – This is closely related to the focal length of a lens. This is usually situated close to the surface of the workpiece and sometimes may be placed a few millimetres below the surface of the workpiece depending on the material. The appropriate focal position is one that enhances coupling efficiency.
- ***Welding Speed*** – In keyhole welding, the welding speed is chosen to be as high as possible since the higher the speed for a given power, the lower the risk of distortion and crack initiation. However, too large a welding speed will produce insufficient heat supply to the workpiece causing reduced penetration depths. In this research low welding speeds have been used for conduction mode welding but the workpieces have been placed on specially designed jigs with copper base plates so as to reduce overheating.

2.3.3. Material Parameters

These are namely; thermal conductivity, heat capacity, thermal expansion, melting point, boiling point, elastic modulus, etc. It goes without saying that the quality of welds produced for any material will depend very much on its material properties. Thermal conductivity is a measure of rate of flow of heat in a body while the heat capacity is a measure of the quantity of heat required to raise the temperature of a given mass of material by 1^0C.

2.4. Physics of Laser Keyhole Welding

Laser keyhole or penetration welding is usually the preferred mode of laser welding. During this process, a power density exceeding 10^6 W/cm^2 is required. The laser beam that is incident on the work piece initially heats and melts through the metal. As the liquid metal vaporizes a column of metal vapour, surrounded by narrow

cylinder of liquid metal is produced (LIA Handbook, 2001). This column of metal vapour is what is referred to as the keyhole. As the laser beam traverses through the length of the workpiece, liquid metal flows around and along the base of the keyhole. This liquid metal re-solidifies at the trailing edge of the keyhole, forming the weld. For the keyhole to be formed and maintained there has to be a balance between the irradiance and weld speed. The flow structure of the molten metal affects the final frozen weld bead geometry (Steen, 1998).

2.4.1. Studies on Laser Keyhole Welding

A number of complex phenomena take place inside and outside the keyhole during laser keyhole welding. Studies on laser keyhole welding have incorporated some of these phenomena in an attempt to understand the dynamic nature of the keyhole and, theoretical predictions are usually compared to experimental results. Andrews and Atthey (1976) postulated two distinct physical regimes that govern the depth of penetration. It was found that the power density limited the depth of shallow holes whereas the depth of the deep holes was dependent on the power per unit radius when gravity is the only restoring force. The above case was applicable only to a stationary laser beam. Mazumder and Steen (1979) formulated a 3D heat transfer model for laser materials processing that assumed the laser beam to be incident at right angles at the centre of the workpiece that was infinite in length but finite in width and depth. The reflectivity of the laser beam was assumed to be zero if the temperature exceeded boiling point with some of the absorbed energy lost by radiation and convection from the surface while the rest of the energy was conducted into the workpiece. There was a close comparison between experimental and predicted fusion zones for mild steel and titanium welds produced by laser welding.

Dowden et al (1987) found that the pressure in the keyhole was determined principally by surface tension and that the energy balance between the solid and vapour states determined the radius of the keyhole. However, their model did not provide a good description for the weld-pool at the upper end of the keyhole. Akhter et al (1989) represented characteristics of thermal absorption during keyhole welding using a point and line model. This model showed that there was substantial absorption near the surface of the workpiece in many cases but also a fall in absorption with depth before an increase, in other cases. DebRoy et al (1991) used principles of gas dynamics and weld pool transport phenomena to predict laser induced vaporization rates that were in good agreement with experimental values. Ducharme et al (1994) formulated a model that took into account the inverse Bremsstrahlung absorption in the plasma and Fresnel absorption at the keyhole walls, of laser energy. It was discovered that the weld pool changed shape from teardrop to a more parallel-sided oval as the degree of penetration reduced. Model calculations agreed well with experimental results. Dumord et al (1995) studied the keyhole during cw Nd:YaG laser welding, taking into account the balance pressures acting upon the keyhole. The pressures considered in this model were (i) the hydrostatic pressure due to gravity, (ii) the pressure due to surface tensions, (iii) the hydrodynamic pressure due to melting metal flow around the keyhole and (iv) the recoil pressure due to evaporation. That these pressures contribute considerably to the dynamics of the keyhole was verified judging from the fact that the shapes of the keyhole as observed on X-rays corresponded to those obtained from the solution of the equations. Sudnik et al (1996) formulated a self-consistent model that took the following into consideration, (i) laser-induced channel formation, (ii) multiple reflection of the laser beam in the channel or keyhole and (iii) plasma generation.

The geometry of the keyhole was determined on the basis of the pressure equilibrium at the keyhole surface taking the enthalpy of the molten mass into consideration. The model was verified with welding experiments on steel and aluminium. Metzbower (1997) took into account the inverse Bremsstralung absorption, and power loss resulting from evaporation of an element of the workpiece material. The nail-head geometry of the keyhole was explained through the analysis and theoretical calculations gave a close approximation to experimental results for temperature distribution across the surface of the molten metal and keyhole. Fabbro et al (2000) studied the keyhole geometry with a model that took into account welding speed, laser incident intensity and sample material and such phenomena as weld displacement. It was concluded that the front keyhole wall was inclined while the rear keyhole wall fluctuated around an apparent equilibrium. It was found that the complete keyhole geometry could be determined taking into account the multiple reflections in it.

The above studies indicate that phenomena such as inverse Bremsstralung absorption, Fresnel absorption, phase transition from solid to liquid and from liquid to vapour, plasma generation and absorption, weld shape and location, and the corresponding forces/pressures play an important role in the formation, maintenance and even closure of the keyhole. Most models endeavour to account for some of the phenomena incorporating just enough to give a reasonable result. Ki et al (2002) carried out a comprehensive study of laser keyhole welding which incorporated such phenomena as free surface evolution, evaporation, multiple reflections, homogenous boiling and thermo-capillary force and recoil pressure. Some of the conclusions arrived at were:

1. Evaporation-generated recoil pressure is the major contributing factor that differentiates keyhole-type welding from conduction-type welding. It is the key to many characteristic behaviours of the keyhole (Ohji et al, 1994).
2. Effective laser absorptivity keeps fluctuating as the keyhole deepens. Keyhole fluctuation is a phenomenon that occurs at all times, no matter what process parameters are used. Keyhole fluctuation and energy absorption patterns are intimately connected.
3. The laser-intensity profile for laser keyhole welding is very complex.
4. Non-uniform localized heating by the laser beam on the front keyhole wall causes formation of humps on the front wall.

Numerical simulations of the laser keyhole welding process have been formulated. Takahashi et al (2002) developed a comprehensive numerical code that took into account surface evaporation, surface tension, transient behaviour of the molten pool and the diffusion process. Experimental results were used to validate the numerical code. Karkhin et al (2002) solved the inverse heat conduction equation in order to find suitable welding conditions from desired weld features. The weld interface, molten pool boundary and weld texture orientation were used as input. A novel spot laser penetration spot weld method was developed by Dijken et al (2003) in the area of microlaser welding. This technique which is well suited for the welding of very thin materials enables novel product designs. Jin and Li (2003) formulated a conduction model for deep penetration laser welding. An actual keyhole profile was used to develop the model under the assumption of the keyhole being cylindrical. The mechanism of energy balance on the keyhole walls was investigated.

Laser keyhole welding is therefore a complex process.

2.4.1.1. Laser Absorption

There are certain absorption phenomena that take place in the keyhole during laser keyhole welding. These are, as mentioned earlier on:

- Inverse Bremstrahllung absorption – A phenomenon that involves the absorption of photons by electrons.
- Fresnel absorption – Absorption that results from multiple laser beam reflections along the sides of the keyhole.

Around the mouth of the keyhole, there are fluid flow effects and above the mouth of the keyhole, the plasma in the metallic plume is sometimes hot enough to defocus the laser beam (Ducharme et al, 1994). In addition to the absorption mechanisms mentioned, there are loss mechanisms that occur due to reflection outside the keyhole and radiation leaving the keyhole after multiple reflections (Kaplan, 1994). Studies investigating laser beam absorption by plasma indicate that (Tix et al, 1995):

(i) The mean plasma temperature increases strongly with incident laser power due to the high charge state of ions.

(ii) The degree of absorption remains approximately the same for increasing laser power.

(iii) The Peclet number for which the absorbed laser energy is able to maintain a keyhole increases strongly with the incident laser power.

The Peclet number is a form of dimensionless velocity (ratio of convection to conduction) (Steen, 1998).

(iv) The energy absorption is enhanced for higher modes of the laser intensity distribution.

Laser beam absorption in the plasma has a significant effect on the relationship between penetration depth and focus position. Semak et al (2000) formulated a

model to investigate the absorption of laser beam energy by plasma during laser welding. Maximum penetration occurred at different focus positions depending on whether the absorption was low or high. If the absorption were low, then the maximum penetration would correspond to a focus position just below the sample substrate. On the other hand, a high absorption would correspond to a focus position above the sample substrate.

Absorption of laser power in a keyhole is much higher than direct absorption on a flat surface (Kroos, 1993).

2.4.1.2. Energy and Pressure Balances

The forces operative during keyhole welding are as follows (Duley, 1999):

- Forces tending to form and maintain the keyhole, i.e., recoil/hydrodynamic pressure (p_h), vaporization pressure (p_v), and beam/radiation pressure (p_r).
- Forces tending to close the keyhole, i.e., gravitational/hydrostatic pressure (p_g) and surface tension (p_γ).

In a keyhole the vaporization pressure, p_v tends to push back its walls and decreases from the bottom of the keyhole (where the temperature is highest) dropping to about zero a short distance from the top of the keyhole. The hydrodynamic pressure is due to fluid (molten metal) flow. The hydrostatic pressure increases with depth of the keyhole due the height and density of the molten metal surrounding the keyhole. Surface tension tends to minimise the surface area of the weld by either acting upwards against the radiation and hydrodynamic pressures or pulling back molten metal back to the parent metal depending on whether the keyhole is closed or open (Lancaster, 1986). Radiation pressure has to do with pressure exerted by the laser beam on the molten material.

Putting these pressures in the form of an equation gives (Duley, 1999)

$$p_v + p_r = p_g + p_\gamma + p_h \qquad (2.4)$$

$p_g = \rho gh$ and $p_\gamma = 2\gamma/r$ where g = gravitational force, ρ = molten metal density, h = depth/height of keyhole, r = radius of keyhole assuming hemispherical geometry and γ = surface tension.

$$p_v + p_r = 2\gamma/r + \rho gh + p_h$$

$$h = (p_v + p_r - 2\gamma/r - p_h)/\rho g \qquad (2.5)$$

The number of keyhole models that take energy and pressure balances into consideration demonstrates the importance of these phenomena. Semak (1994) considered the vapour recoil pressure as the driving force for keyhole formation and melt motion. The top and middle sections of the keyhole were assumed to be held open by the recoil vapour pressure, equal to the sum of surface tension and hydrostatic pressures. The recoil pressure at the bottom of the growing keyhole was estimated to be 10-100 times greater than the surface tension or hydrostatic forces. Clucas et al (1995) considered pressure balances at different depths of the keyhole. At both ends of the keyhole, the ablation pressure is significant but it is negligible along most of the length of the keyhole where a rapid build-up of hydrodynamic pressure balances surface tension pressure. Forsman et al (2001) represented the pressure balance as follows:

$$p_v = p_h + p_\lambda$$

which is illustrated by figures 2.3

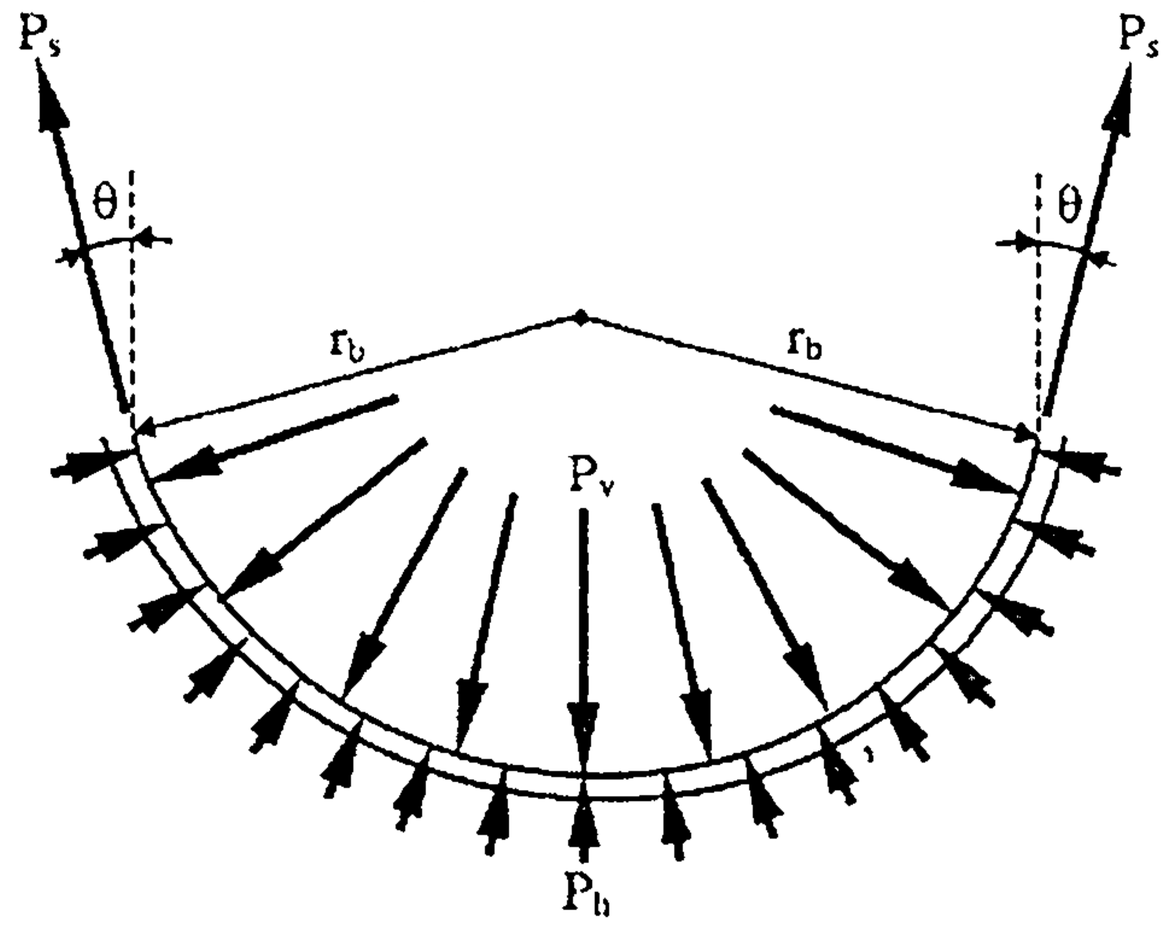

Figure 2.4 Balance of vapour pressure and surface tension at the bottom of the keyhole (from Forsman, 2001)

Kroos (1993) used an energy balance equation in investigating the stability of a cylindrical keyhole. The absorbed energy (q_{abs}) was equated to the sum of the energy carried away by ablation of particles (q_{abl}) and heat conduction losses (q_λ).

Thus

$$q_{abs} = q_{abl} + q_\lambda \qquad (2.6)$$

Clucas et al (1998) described energy input in the keyhole by the Fresnel absorption at the keyhole walls and the inverse Bremsstrahlung absorption in the plasma. The energy output was derived from conduction into the workpiece and ablation at the keyhole walls.

Thus

$$q_B + q_F = q_{abl.} + q_\lambda \qquad (2.7)$$

q_F is the power absorbed per unit depth at the keyhole wall due to Fresnel absorption, q_B represents the inverse Bremmstrahlung absorption. Numerical simulations carried out by Semak et al (1997) produced results that are summarized below:

(i) the recoil pressure can play a significant in ejection of the melt from the interaction zone even for low melt surface temperatures close to the melting point

(ii) high-velocity melt flow is generated during laser welding when the typical laser beam intensities are taken into consideration; thus the melt-flow pattern cannot be considered to be the motion of a cylinder in an infinite liquid pool.

(iii) 70-90% of the laser intensity absorbed in the beam interaction zone is carried away by the melt flow. Thus, convection in the interaction zone cannot be ignored.

(iv) The velocity of the keyhole wall front is determined by the absorbed laser intensity and can be either smaller or higher than the beam's translation energy.

These findings showed the inadequacy of the assumption that the evaporation-induced recoil pressure is equal to the surface tension pressure. Solana et al (1997) formulated a comprehensive model that determined 3D keyhole geometry by taking into account heat conduction, ablation losses and evaporation effects at the keyhole open surfaces, as well as the inverse Bremssstrahlung and Fresnel absorption mechanisms. Ablation and surface tension pressures were also considered. With regard to energy losses, the most significant mechanism was considered to be the amount of laser intensity hitting the upper keyhole surface. These losses became

larger as the welding speed increased because of the increasing shift between the beam axis and the centre of the keyhole.

2.4.1.3. Keyhole, Weld pool shape and motion

Matsuiro et al (1992) developed a method for the prediction of laser welding pool profile. Combining a pressure balance equation with an energy deposition in the form of a line source whose finite depth was equal to the keyhole depth, pool widths and depths approximating experimental values were obtained. Three forces, gravity force, surface tension and the recoil pressure were considered responsible for the weld pool surface profile. Trappe (1994) solved the heat conduction equation with a free keyhole boundary, which was calculated self-consistently. A near circular keyhole with its centre moving in the direction of the translation was obtained. Results obtained indicated that the temperature at the keyhole wall was nearly constant, by virtue of the pressure balance. Semak et al (1995) carried out high contrast and high spatial resolution camera observations of the keyhole during laser welding and arrived at the following conclusions:

(i) For typical welding conditions, either the keyhole opening size exceeds the laser spot size so that the wall is not exposed to the laser beam or only the front part of the keyhole wall is exposed to the laser beam with the sides and back being outside the laser spot.

(ii) The assumption that the keyhole opening is coaxial to the laser spot and approximately equal in size to it is only satisfied for low power and low translation speed.

(iii) High speed photography and Schlieren imaging of fast translation speed welding indicate the existence of high velocity flow originating from the front

part of the keyhole and directed down the weld pool. This flow affects thermal distribution in the sample and induces weld pool instabilities that may cause porosity and spattering.

Ducharme et al (1994) found that weld pool shapes varied with the ease of ionization of shroud gases used during laser welding. Helium with the highest ionization potential produced a teardrop shaped weld pool while argon with ionization energy of about two-thirds that of helium gave larger teardrop-shaped weld pools. In an attempt to investigate keyhole shapes in laser deep penetration welding, Jin et al (2003) carried out camera observations during keyhole welding of glass GG17. The following is a summary of the results:

(i) The keyhole is bent in the direction opposite to the welding speed. Most parts of the rear wall are hidden from the laser beam. The top part of the keyhole is irradiated directly by the laser beam while the multiple reflections of the laser beam on the walls can only influence the laser intensity distribution on the bottom part of the keyhole. Strong convection currents in the melt pool bring the absorbed laser intensity from the front part to rear part.

(ii) The keyhole is cone-shaped. Its diameter is dependent on the laser power density and the diameter of the laser beam spot.

(iii) The greater the welding speed, the greater the curvature of the keyhole.

The above shows that keyhole shape and motion is dependent on a number of intricately linked factors which include welding speed and laser beam intensity amongst others. Keyhole welding is a very complex and dynamic process and

research is still going on with regard to gaining a deeper understanding of the process.

2.4.2. Instability of the Laser Keyhole Welding

The complexity of laser keyhole welding has been demonstrated by the dynamic nature of the keyhole. Kroos et al (1993) studied the dynamic behaviour of the keyhole theoretically and concluded that the collapse of a keyhole after sudden laser shutdown was related to the balance between the surface tension and inertia of the molten metal. Calculations showed that fluctuations in laser power and assist gas jet/pressure could cause the keyhole to oscillate at about 500Hz. The theoretical studies of Klein et al (1994) showed that the keyhole is able to perform radial, axial and azimuthal oscillations. Instabilities can occur for finite amplitudes that may subsequently lead to such welding defects as spiking, or ripple formation. Diagrammatic representations of the three modes of oscillation are shown below. The keyhole was assumed to be cylindrical.

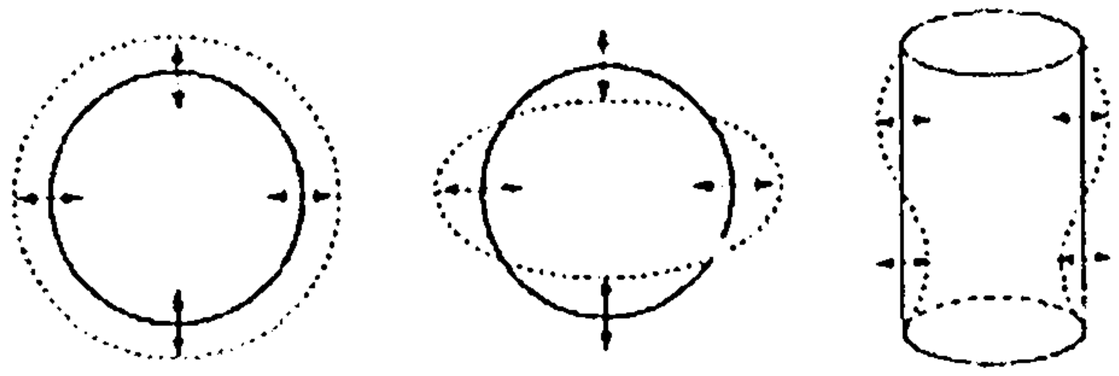

Figure 2.5 The three oscillation modes of a keyhole (from Klein et al)

Semak et al (1995) observed the keyhole using high-speed camera photography and obtained results that supported the following assumptions:

- The recoil pressure has a pulsating character that drives the high-amplitude, low frequency volumetric oscillations of the melt pool. The laser-induced vaporization

gives rise to the recoil pressure that exceeds surface tension and hydrostatic pressure in the weld pool. This gives rise to a high-velocity, high-amplitude melt flow round the keyhole.

- There exist long-wavelength melt oscillations whose frequencies increase during solidification.

Dowden and Kapadia (1996) linked pore formation in the keyhole to instability in the keyhole, brought about by interaction between the forces of surface tension and excess pressure produced by ablation of material from the keyhole walls. It was found that pores seem to form more readily in a blind keyhole than in an open one because it is difficult for pressure to build up in an open keyhole since both ends are at atmospheric pressure. On the other hand, it is far much easier for pressure to build up in a blind keyhole. A simulation of front keyhole wall behaviour was done numerically by Matsunawa and Semak (1997) and the calculations showed that depending on the process conditions, the absolute value of the keyhole wall velocity component parallel to the translation velocity could be higher than, equal to or smaller than the beam translation speed. Humps were produced in the keyhole wall when the component of the keyhole wall velocity vector was greater than the beam translation speed. It has found that when high irradiance is applied to metals with low surface tension and viscosity, the instability of the weld pool increases. This is reflected in the difficulty usually encountered in CO_2 laser welding of aluminium and magnesium. Spatter, undercut, drop-out and porosity are produced when high irradiance is applied to low viscosity and surface tension alloys.

Matsunawa et al carried out extensive observations of the keyhole during laser welding in both the pulsed and continuous wave modes, using high-speed videos.

The results obtained and conclusions made are quite revealing and a summary is given below:

1. In the spot welding mode, keyhole fluctuated frequently in size and shape in spite of almost constant peak power during spot welding. The fluctuation period was different depending on the type of metal used.
2. The keyhole collapsed within one-tenth of the time it took the weld pool to solidify and a large cavity always formed at the bottom of the keyhole.
3. In continuous welding mode, the keyhole was less unstable but it also changed its shape and size with time. The depth of the keyhole also changed with time. A deep depression which formed at the rear wall of the keyhole moved from top to bottom periodically and SEM and gas analysis of porosity showed that bubbles comprised evaporated metal vapour and shielding gas.
4. The keyhole and the whole melt pool were strongly perturbed by dynamic pressure of the metallic vapour jet. The motion of small tungsten particles (that had been sandwiched between thin plates before the application of the laser beam energy) revealed that there was a very complex flow in the molten pool. Figure 2.5 shows a schematic of the keyhole.

Two types of porosity were identified (i) that induced by hydrogen and (ii) that caused by the fluctuation of the keyhole due to intense evaporation of the metal.

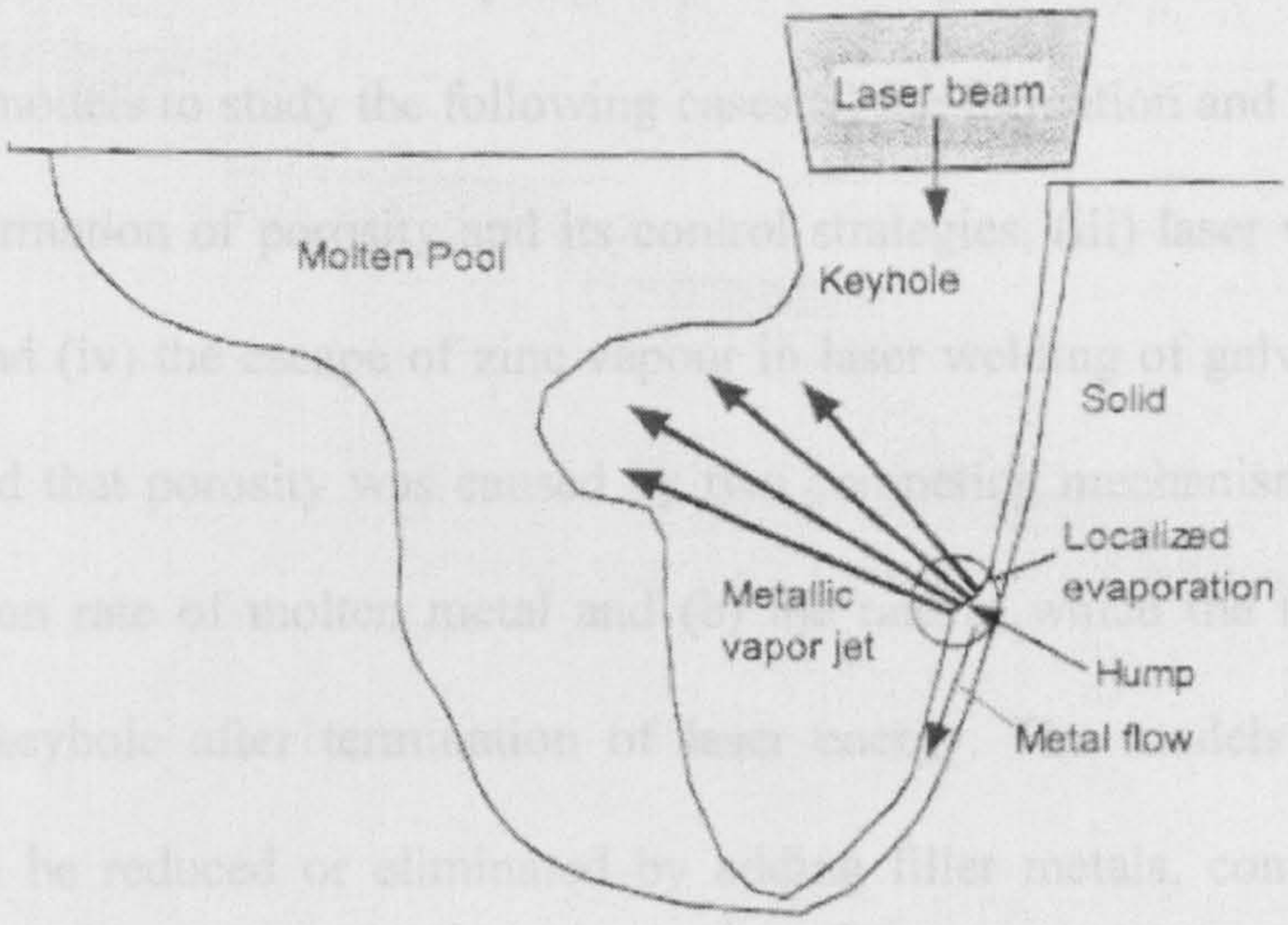

Figure 2.6 Keyhole illustrating localized evaporation of metal from front keyhole wall (from Matsunawa et al., 1998)

In order to characterise Nd:YAG keyhole dynamics , Martin et al (2001) used a CCD camera placed coaxially to the laser beam and recorded keyhole images that were compared with those obtained from numerical modelling. Results indicated two distinct behaviours of the keyhole namely:

- Good welding results that were reflections of a 'pseudo-steady' state that produced a 'pseudo-constant' keyhole shape. This behaviour was characterised by low frequency in the plume current.
- Poor welding results identified with a highly dynamic keyhole mode associated with irregular and rapidly varying keyhole shapes exhibiting high frequencies in the plume current.

It has been shown that Marangoni effect (effect of temperature-dependent coefficient of surface tension) is an important factor in deep penetration welding of steel

(Fuhrich et al, 2001). Variation of chemical elements such as sulphur, phosphorus, oxygen, etc contributes to this phenomenon. Zhang et al (2002) developed mathematical models to study the following cases (i) the formation and collapse of a keyhole (ii) formation of porosity and its control strategies, (iii) laser welding with filler metals and (iv) the escape of zinc vapour in laser welding of galvanized steel. Results showed that porosity was caused by two competing mechanisms which are (a) solidification rate of molten metal and (b) the rate at which the molten metal backfills the keyhole after termination of laser energy. The models showed hat porosity could be reduced or eliminated by adding filler metals, controlling laser tailing power or applying an electromagnetic force during keyhole collapse process. However, it was more difficult to obtain uniform weld pool composition in laser welding than in arc welding. Amara et al (2003) modelled compressible vapour flow during laser welding. It was observed that friction phenomena occurred between the vapour and keyhole walls which in turn resulted in a more uniform distribution of pressure.

Keyhole welding and the formation, maintenance and collapse of the keyhole are indeed very complex phenomena, which from all indications require further investigation.

2.5. Physics of Laser Conduction Welding

Compared to laser keyhole welding, conduction limited welding is more stable and ideally there should be no vaporization at all, since temperatures are usually below boiling point and more specifically within the melting regime. Conduction welding takes place when the power density is low and a melt depression does not occur

(LIA, 2000). Heat conduction takes place not only in the vertical direction but also in the horizontal direction and the weld are semi-circular in shape (Schuocker, 1999). The weld pool has strong Marangoni forces resulting from the variation of surface tension with temperature (Steen, 1998). The heat flow is three-dimensional and is carried out by conduction into the workpiece material. Depending on the total amount and rate of energy deposition, as well as the thermal conductivity and mass of the workpiece, the heat energy is shared between melting to form a fusion zone and just heating to produce a heat-affected zone (Messler, 1999).

2.5.1. Studies on Laser Conduction Welding

Cline and Anthony (1977) studied heat treatment and melting with a scanning laser beam. The maximum temperature in the case of laser melting (which is in a similar regime as laser conduction welding) is between the melting point and boiling point. The melt pool moves with the laser beam and latent heat absorbed at the melting interface is liberated at the solidifying interface. Esposito and Daurelio (1982) conducted studies into the conduction welding of steel. Amongst their findings was the surprise discovery that penetration depth decreased with increasing power density and the effect was so strong that penetration depth was decreased by a factor of two when the laser beam was directly focused on the workpiece. This phenomenon is investigated in this work.

Chen and Lee (1983) studied transient temperature profiles in solids during laser scanning and identified two important parameters namely, beam diameter and scan velocity. Russo et al (1984) formulated a numerical model for conduction-mode laser welding that ignored the weld pool motion. There was a fair agreement between calculations and experimental data on temperature-dependent absorption and weld

shapes for aluminium and nickel. Wake et al (1992) studied temperature distribution and its influence to the metal surface induced by a scanning laser beam. It was considered that such a study would shed more light on the optimisation of the laser teat treatment process. Good agreement was found between theoretical and experimental results.

DebRoy and Paul (1988) studied free surface flow and heat transfer in laser conduction welding with high manganese stainless steel. Results obtained show that the surface topography of the weld pool was significantly uneven. The surface deformity became less pronounced during solidification and computed surface topography agreed well with experimental results. The theoretical computations took cognisance of the surface tension being the driving force behind fluid flow in the weld pool. Bos and Chen (1996) formulated a practical method for the prediction of weld pool dimensions in laser conduction welding. Weld pool sizes were predicted using the aspect ratio of the welds as a variable parameter. The weld aspect ratio was dependent on the weld pool convection while the weld pool dimensions were determined from heat conduction from the weld pool into the base metal. Pitscheneder et al (1997) studied laser conduction weld pools in order to achieve a comprehensive understanding of the combined role of sulphur content and laser-material interaction parameters. A numerical model was formulated based on the concept of surface tension-driven fluid flow. Two types of fluid flow were identified, (i) radially inward flow and (ii) radially outward flow and the aspect ratio of the welds depended on the type of flow. Xie and Kar (1999) employed laser conduction welding to investigate the welding of thin (0.6mm gauge) steel sheets with and without surface oxidation. As in all the previous studies a low-power focused laser beam (400W CO_2 laser beam) was used. Tsai and Kannatey-Asibu (2000) modelled

the laser conduction welding process for feedback control using a low-power focused beam on a thin workpiece.

Zhao and DebRoy (2001) studied the weld metal composition change during laser conduction welding of aluminium alloy 5182. In this study, the laser beam was defocused by up to a maximum of ± 2mm above the focus. The peak temperature recorded was slightly above the boiling point of the alloy and was for a small region near the centre of the weld pool surface. Williams, Scott and Calder (2001) used diode lasers for laser conduction welding of aluminium alloys. Good quality welds were obtained as a result. However, thin sprayed graphite coatings were used to enhance coupling in aluminium alloys. Graphite has an adverse effect on laser welds by way of reducing corrosion resistance of the workpiece or material. Berthe et al (2002) studied the control of laser welding in the conduction regime. A fast-response system was developed that made monitoring of the different phases of interaction resulting from millisecond pulse interactions such as pure conduction, vaporization and/or plasma, possible. In a study of high power diode laser welding of metal catalytic converters, Salimen et al (2002) found that heat conduction limited welding turned out to be more suitable than the keyhole welding mode. Qin et al (2002) developed a 3D analytical model during the study of temperature field produced during laser heat conduction welding of thin parts. Experimental results used for the verification of the model were obtained using a Nd:YAG laser and theoretical results were identical to experimental results. Interest in laser conduction welding is increasing but presently the use of this mode of welding is limited to very thin materials and the use of defocused laser beams has not really been considered. Laser power coupling efficiency for laser conduction welding and laser keyhole welding were compared by Nath et al (2002) from experimental results and it was found that

generally the power coupling efficiency was lower for conduction welding than for keyhole welding.

2.6. Contrast between Laser Keyhole Welding and Conduction Welding

It is obvious from the foregoing that keyhole welding is far more complex than conduction welding. The following table gives the relative advantages and disadvantages of both processes.

Process	Advantages	Disadvantages
Keyhole Welding	• Low heat input per unit length • Small weld bead • Low distortion • High aspect ratio • Very fast speeds	• Tends to be unstable • Spatters, pores, drop-outs and undercuts • Requires good fit-up • Requires laser with reasonable beam profile
Conduction Welding	• Very stable process • Larger beam reduces fit-up problems	• Relatively slow • Higher heat input • Higher distortion

Conduction welding is free from complex keyhole phenomena such as inverse Bremsstrahlung and Fresnel absorptions, recoil pressure, and vaporization pressure. Melting in conduction welding is achieved by heat conduction through the workpiece but absorption techniques need to be employed in order to achieve laser absorptivity,

especially for highly reflective materials such as aluminium.. The high power density in keyhole welding usually makes this step unnecessary for it, as the workpiece gets heated up rather quickly to form a keyhole.

2.7. Laser welding of aluminium alloys

It has been shown that some characteristics of aluminium that affect its weldability are (i) reflectivity (ii) oxide layer (iii) material properties such as thermal conductivity and specific heat capacity. Alloying elements such as Mg, Si, Mn, Zn and Cu also affect the weldability of aluminium alloys in that they can give rise to the occurrence of solidification cracks, segregations, etc (Ricciardi et al, 1986). The welds often contain pores that are caused by hydrogen precipitation and/or the dynamic motion of the keyhole. The pores produced in the former case are spherical while those produced in the latter case are elliptical (Forsman, 2000)

Interest in the welding of aluminium has continued to increase and over the years studies have been conducted into the laser welding of aluminium alloys. Jones et al (1992) carried out 5kW CO_2 welding of some 5000 and 6000 series aluminium alloys. In all cases pores were observed in the welds and all welds failed at the weld metal during tensile strength tests. Rapp et al (1994) found that the quality of aluminium welds improved if lasers of high output (e.g. 4-5kW) and high quality laser beams were used. Another way of achieving high quality welds was the simultaneous usage of two CO_2 lasers. The use of filler wires was explored and it was found to enhance flexibility and reliability of the welding process. However, porosity was not totally eliminated.. Defects that occur during aluminium welding are (Dausinger, et al, 1996):

1. Sagging seam

2. Undercut
3. Hot cracks
4. Hydrogen pores
5. Cavities
6. Irregular roots
7. Blowholes

The first four are caused by characteristics of the metal while the last three are caused by process instability. Similar findings to that of Rapp et al (1994) have been achieved (Behler et al, 1997; Pohl et al, 1997; Li and Gobbi, 1997). Weston et al (1998) welded five different aluminium alloys using pulsed and high powered continuous CO_2 and Nd:YAG lasers. Results showed that for AA5083, AA7475, AA8090 and AA2219 the pulsed Nd:YAG welds showed less cracking than the continuous Nd:YAG laser. Only AA6061 samples showed a higher cracking for pulsed laser welding. High quality welds were produced but an average power of 5kW was used for the welding. Katayama and Matsunawa (1998) carried out a study of defect formation conditions and causes during CO_2 welding of AA5052, AA5083, AA6061 and AA7N01 and some of the results obtained are summarised below:

- During welding of as-received alloy specimens with unpolished surfaces, heavier porosity occurs than when the surfaces are polished.
- The alloy grade, shielding gas type and flow rate, laser power, welding speed and defocusing distance affect the number and size of pores.
- In alloys, which are hard to fuse, porosity increases with laser power. In easily fusable alloys, large pores occur at a high rate, but the total number found decreases.

- The porosity of all alloys and the total volume of pores decrease with an increase in welding speed. However, at low welding speeds typical of arc welding, very little porosity is found.
- Porosity decreases with increasing defocusing distance and with shallower penetration depth.
- During high-speed welding solidification cracking occurs and the solidification cracking susceptibility of the alloys was ranked in the following order

AA5182, AA5083 < AA5052 < AA7N01 < AA6061

It was accepted, in this study, that generally heat conduction type welds show little porosity. Forsman et al (1999) studied factors affecting absorptivity in Nd:YAG laser welding of aluminium and concluded that

- Surface finish has a negligible effect on the absorption of aluminium when it is welded by an Nd:YAG laser. If melting does not occur then absorption is greater for rougher surfaces than for smoother surfaces.
- The number of internal reflections of the laser beam determines the level of absorption in the keyhole. The absorption tends to decrease with increasing welding speed.
- The melting efficiency of the welding process tends to decrease with speed as a result of a decrease in thermo-capillary stirring.

Other factors that influence absorption in aluminium alloys are as follows (Forsman, 2000):

- A reduction in wavelength generally yields higher absorption because the photons are more energetic and are therefore more readily absorbed by electrons. For example absorption is higher for a Nd:YAG laser beam than a CO_2 laser beam.

- Increased surface roughness yields higher absorption because of the greater effective area for absorption and an increased number in undulations. This is especially true before the formation of the keyhole.
- Increased temperature yields higher absorption.
- Absorption increases when there is a phase change.

In highlighting the advantages of direct diode lasers over traditional CO_2 and Nd:YAG lasers, Herfurth et al (2001) stated that diode lasers weld in the conduction limited mode and though the base metal melts, there is insufficient heat input to vaporise the material. This produces afar less violent action in the weld zone with no spatter and no potential for optics contamination.

Palanco et al (2001) conducted real-time spectroscopic monitoring of the occurrence of weld defects in CW laser welding of aluminium alloys found out that blow-holes and notch defects are preceded by a sudden alteration of plasma emission characteristics. They suggested that this led to the formation of a strong plasma shock wave that could not be absorbed by the molten pool. The excess momentum is released through an ejection of the material surrounding the plasma. Katayama, Mizutani and Matsunawa (2002) studied porosity formation and mechanism during laser welding of aluminium alloys. It was found that porosity formation is affected by welding speed, type of nozzle, etc. Kutsuna et al (2002) studied the crack susceptibility of aluminium alloys and found that by using an adaptive mirror that produced a change in focal point of the laser beam, there was a reduction in crack susceptibility and consequently the weld pool and keyhole were stabilized. Gref et al (2002) carried out double focus welding of aluminium alloys and results obtained indicated that welding depth, efficiency and quality could be increased thereby. Haboudou, Peyre and Vannes (2002) studied the keyhole and melt pool oscillations

in dual beam welding of aluminium alloys. Porosity was reduced and more stable weld pools were achieved. Takahashi et al (2002) performed welding of thin aluminium alloy sheets with welding speeds up to 20 m/min. However solidification cracks formed in the weld bead centres resulting in decreased strength. Cheng et al (2002) performed high-power CO_2 laser welding of aluminium alloys up to 4mm thick. Effects of processing parameters (beam quality, laser power, welding speed, etc) were studied using a new technique called 'artificial keyhole'. The technique made it possible to break through the high reflectivity of the alloys. Zhao and DebRoy (2003) developed a numerical model for laser keyhole welding of aluminium alloys. The model was used to predict the mode of welding, the keyhole geometry and weldment temperature.

The above studies indicate that there is always a possibility of weld defects in laser keyhole welding of aluminium, those occurring most often being porosity and solidification cracking. Ways of reducing defects have been studied for keyhole welding but conduction limited welding remains a far more stable process especially for materials in the 2mm-3mm gauge.

References

- Akhter,R., Davis, M., Dowden, J., Kapadia, P., Ley, M., and Steen, W.M., *'A Method for Calcutaling the Fused Zone Profile of Laser Keyhole Welds'*, J.Phys.D.,: Appl. Phys. 21 , pp.23-28, 1989
- Amara, E.H., Fabbro, R., Bendib, A., *'Modelling of the compressible vapour flow induced in a keyhole during laser welding'* Journal of Applied Physics, v. 93, n 7, (2003), pp.4289-4296
- Andrews, J. G., and Atthey,D.R., *'Hydrodynamic Limit to Penetration of a Material by a High-power Beam'* J.Phys.D.: Appl. Phys., Vol9, pp. 2181-2194, 1976
- Behler, K., Berkmanns, J., Ehrhardt, A., and Frohn, W., *'Laser Beam Welding of Low Weight Materials and Structures'* Materials & Design, Vol. 18, Nos. 4/6 pp.261-267, 1997
- Berthe, L., Delage, D., Lepretre, D., Bacinello, L., Knapp, W., Dumont, N., Durand, F., *'Study and control process in laser conduction welding for millisecond pulse duration range'*, Proceedings of SPIE – The International Society for Optical Engineering, v 4830, p.69-72, 2002
- Bos, J.A., and Chen, M.A., *'On the Prediction of Weld Pool Size and Heat Affected Zone in Shallow-Pool Welding'*, HTD-Vol. 336/FED-Vol. 240, Transport Phenomena in Materials Processing and Manufacturing ASME, 1996
- Chen, I., and Lee, S., *'Transient Temperature Profiles in Solids heated with Scanning Laser'* J. Appl. Phys. 54 (2), pp. 1062-1066, 1983
- Cheng, Z., Xu, G., Zhao, Q., and Lu, Y., *' High power CO_2 welding of AL alloy plates'*, Proceedings of SPIE – The International Society for Optical Engineering, v 4831, pp. 332-335, 2002

- Cline, H.E., and Anthony, T. R., *'Heat Treating and Melting with a Scanning Laser or Electron Beam'* Journal of Applied Physics, Vol. 48, No.9, pp.3895-3900, 1977
- Clucas,D.A.V., Ducharme,R., Kapadia, P. D., Dowden, J.M., and Steen, W.M., *' A Mathematical Model of the Flow within the Keyhole during Laser welding'*, ICALEO, pp. 989-998, 1995
- Crafer,R.C., and Oakley, P., *Laser Processing in Manufacturing*, Chapman and Hall, 1993
- Dawes, C., *Laser Welding*, Abington Publishing, 1992
- DebRoy, T., Basu, S., and Mundra, K., *'Probing Laser Induced Metal Vaporization by gas Dynamics and Liquid Transport Phenomena'* J.Appl. Phys. 70(3), pp.1313-1319, 1991
- Dijken, D. K., Hoving, W., De Hosson, J. Th. M., *'Laser penetration spike welding: A microlaser welding technique enabling novel product designs and constructions'* Journal of Laser Applications, v 15, n 1, pp. 11-18, 2003
- Dowden, J., Kapadia, P., Clucas, A., Ducharme, R., and Steen, W.M., *'On the Relation between Fluid Dynamic Pressure and the Formation of Pores in Laser Keyhole Welding'*, Journal of Laser Applications, Vol. 8, pp. 183-190, 1996
- Dowden, J., Postacioglu, N., Davis,M., and Kapadia, P.,*'A Keyhole Model in Penetration Welding with a Laser'*, J.Phys.D.,: Appl. Phys. 20 , pp.36-44, 1987
- Ducharme, R., Williams , K., Kapadia, P.,Steen, B.,and Glowacki, M., *'The Laser Welding of Thin Metal Sheets:An integrated Keyhole and Weld Pool Model with Supporting Experiments'*J.Phys.D:Appl.Phys.27, pp.1619-1627, 1994
- Dumord, E.,Jouvard, J.M., and Grevey, D.,*'Modeling of Keyhole during cw Nd:YAG Laser Welding'* ICALEO, pp. 951-960, 1995

- Esposito, C., Daurelio, G., and Cingolani, A., *'On the Conduction Welding Process of Steels with the CO_2 Laser'* Optics and Lasers in Engineering, Vol. 3, pp. 139-151, 1982
- Fabbro, R., and Chouf, K., *'Keyhole Modeling during Laser Welding'* Journal of Applied Physics, Vol. 87, No.9, pp.4075-4083, 2000
- Forsman, T., *'Laser Welding of Aluminium Alloys'* PhD Thesis, University of Technology, Lulea, 2000
- Forsman, T., Kaplan, A.F.H., Powell, J., and Magnusson, C., *'Nd:YAG Laser Welding of Aluminium: Factors Affecting Absorptivity'* Lasers in Engineering, Vol. 8, pp.295-309, 1999
- Forsman, T., Powell, J., and Magnusson, C., *'Process Instability in Laser Welding of Aluminium Alloys at the Boundary of Complete Penetration'* Journal of Laser Applications, Vol. 13. No. 5, pp. 193-198, 2001
- Fuhrich, T., Berger, P., and Hugel, H., *'Marangoni Effect in Laser Deep Penetration Welding of Steel'* Journal of Laser Applications, Vol. 13, N0. 5, pp. 178-186, 2001
- Gref, W., Russ, A., Leimser, M., Dausinger, F., Hugel, H., *'Double focus technique – Influence of focal distance and intensity distribution on the welding process'* Proceedings of SPIE – The International Society for Optical Engineering, v 4831, pp. 289-294, 2002
- Haboudou, A., Peyre, P., and Vanes. A. B., *'Study of keyhole and melt pool oscillations in dual beam welding of aluminium alloys: Effect of porosity formation'* Proceedings of SPIE – The International Society for Optical Engineering, v 4831, pp. 295-300, 2002

- Herfurth, H.J., Cryderman, M., and Clarke, J.A., *'Diode Laser Welding of Aluminium'* Industrial Laser Solutions, pp.29-31, 2001
- Jin, X. and Li, L., *'A conduction model for deep penetration laser welding based on an actual keyhole'* Optics and Laser Technology, v 35, n 1 , pp. 5 -12, 2003
- Jin,X., Li, L., *'An Experimental Study on the Keyhole Shapes in Laser Deep penetration Welding'*, Optics and Lasers in Engineering, 2003
- Jones,I., Riches, S., Yoon,J.W., and Wallach,E.R., *'CO_2 Laser Welding of Aluminium Alloys'* Proccedings of LAMP '92, Nagaoka, June 1002, pp. 523-527
- Kaplan, A. *'A Model of Deep Penetration Laser Welding based on Calculation of The Keyhole Profile'* J.Phys. D:Appl. Phys. 27, pp. 1805-1814, 1994
- Karkhin, V. A., Plochikhine, V.V., Ilyin, A.S., Bergman, H.W., *'Inverse modelling of fusion welding processes'* Welding in the World, Le Soudage Dans Le Monde, v 46, n 11-12, pp. 2-13, 2002
- Katayama, S., Matsunawa, A., and Kojima, K., *'CO_2 Laser Weldability of Aluminium Alloys (2^{nd} Report): Defect Formation Conditions and Causes'* Welding International, Vol.12, No.12, pp. 44-59, 1998
- Katayama, S., Mizutani, M., Matsunawa, A., *'Development of porosity prevention procedures during laser welding'*, Proceedings of SPIE – The International Society for Optical Engineering, v 4831, (2002), pp. 281-288
- Ki,H., Mohanty, P. and Mazumder, J., *'Modeling of Laser Keyhole Welding: Part I,* Metallurgical and Materials Transactions A, Vol. 33A, p.1817-1830, 2002
- Ki,H., Mohanty, P. and Mazumder, J., *'Modeling of Laser Keyhole Welding: Part II,* Metallurgical and Materials Transactions A, \vol. 33A, p.1831-1842, 2002

- Klein, T., Vicanek, M., Kroos, J.,Decker,I., and Simon, G.,.,' *Oscillations of the Keyhole in Penetration Laser Beam Welding'*, J.Phys.D:Appl.Phys. 27, pp. 2023-2030, 1994
- Kroos, J., Gratzke,U., Simon, G.,. *'Towards a Self-consistent Model of the Keyhole in Penetration Laser Beam Welding'*, J.Phys. D:Appl. Phys. 26, pp. 474-480, 1993
- Kroos. J.,Gratzke, U.,Vicanek, M., and Simon, G.,' *Dynamic Behaviour of the Keyhole in Laser Welding'*, J.Phys.D:Appl.Phys. 26, pp. 481-486, 1993
- Kutsuna, M., Shido, K., Okada, T., *'Fan shaped cracking test of aluminium alloys in laser welding'* Proceedings of SPIE – The International Society for Optical Engineering, v 4831, (2002), pp. 230-234
- Laser Institute of America (ed. Ready, J.,), *'LIA Handbook'* , Laser Institute of America, 2001
- Leong, K.H., and Geyer, H.K.,' *Laser Beam Welding of any Metal*, ICALEO, pp. 242-250, 1998
- Li, Z., and Gobbi, S.L., *'Laser Welding for Lightweight Structures'* Journal of Materials Processing Technology 70, pp.137-144, 1997
- Martin. B., Loredo, A., Pilloz, M., and Grevey, D., *'Characterisation of cw Nd:YAG Laser Keyhole Dynamics'*, Optics & Laser technology 33, pp.33.207, 2001
- Matsuhiro, Y., Inaba, Y., and Ohji, T., *'Mathematical Modelling of Molten Pool in Laser Welding'*, Proceedings ogf LAMP '92, pp. 381- 386, 1992
- Matsunawa, A., and Semak, V., '*The Simulation of Front Keyhole Wall Dynamics during Laser Welding'*, J.Phys.D:Appl.Phys. 30, pp. 798-809, 1997

- Matsunawa, A., Kim, J., Seto, N., Mizutani, M., and Katayama, S., *'Dynamics of Keyhole and Molten Pool in Laser Welding'* Journal of Laser Applications, Vol. 10, No. 6, pp. 247-254, 1998
- Mazumder,J., and Steen, W.M., *'Heat Transfer Model for cw Laser Material Processing'* J.Appl. Phys. 51(2), pp.941-947, 1980
- Metzbower, E.A., *'On the Formation of the Keyhole and its Temperatures'* Journal of Laser Applications 9, pp. 23-33, 1997
- Nath, A. K., Sridhar, R., Ganesh, P., and Kaul, R., *'Laser power coupling efficiencyin conduction and keyhole welding of austenitic stainless steel'* Sadhana – Academy Proceedings in Engineering Sciences, v 27, n 3, pp. 383 – 392, 2002
- Ohji, T., Murakami, E., Matsubayashi, K. and Matsuhiro, Y., *' A Mathematical Model for Laser Welding with Keyhole'*, ICALEO, pp. 471 –475, 1994
- Palanco, S., Klassen, M., Skupin, J., Hansen, K., Schubert, E., Sepold, G., and Laserna, J. J., *'Spectroscopic Diagnostics on CW-Laser Welding Plasmas of Aluminium Alloys'* Spectrochimica Acta Part B 56, pp.651-659, 2001
- Paul, A., and DebRoy, T., *'Free Surface Flow and Heat Transfer in Conduction Mode Laser Welding'* Metallurgical Transactions B, Vol. 19B, pp. 851-858, 1988
- Pitscheneder, W., Grubock, M.,Mundra, K., DebRoy, T., and Ebner, R., *'Numerical and Experimental Investigation of Conduction–Mode Laser Weld Pools'*, Mathematical Modelling of Weld Phenomena 3, IOM Communications Ltd., pp.41-63, 1997
- Pohl, T., and Schultz M., *'Laser Beam Welding of Aluminium Alloys for Light Weight Structures using CO_2 and Nd:YAG Laser Systems'* Proceedings of the LANE'97, pp. 181-192, 1997

- Qin, G., Yang, Y., Lin, Y., Qin, X., Wang, X., and Lin, S., *'Nd:YAG CW laser heat-conduction welding (Paper 1),* , Transactions of the China Welding Institution, v 23, n 6, pp.13 -16, 2002
- Rapp,J., Glumann, C., Dausinger, F., and Hugel,H., *'Laser Welding of Aluminium Lightweight Materials: Prpblems, Solutions, Readiness for Application'* Optical and Quantum Electronics 27 pp.1203-1211, 1995
- Ricciardi,G., Cantello, M., and Micheletti, G.F., *'Light Alloys and SuperAlloys Laser Welding'* Advanced Manufacturing Processes 1 (2), pp.223-243, 1986
- Russo, A. J., Benson, D. A., Hadley, R. G.,' *Two-Dimensional Modeling of Conduction-Mode Laser Welding*, ICALEO, Vol. 44, pp. 8-16, 1984
- Salimen, A., Lylykangas, R., and Tuomola, H., *'High power diode laser welding of metal catalytic converters'*, Proceedings of SPIE – The International Society for Optical Engineering, v 4831, pp. 32-37, 2002
- Schoucker, D., *'High Power Lasers in Production Engineering'*, Imperial College Press, 1999
- Semak, V., V., Hopkins, J. A., M$_c$Cay, M. H., and M$_c$Cay, T. D.,' *A Concept for a Hydrodynamic Model of Keyhole Formation and Support During Laser Welding'*, ICALEO, pp. 641-650, 1994
- Semak, V., V., Hopkins, J. A., M$_c$Cay, M. H., and M$_c$Cay, T. D.,' *Melt Pool dynamics during Laser Welding'*, J.Phys.D:Appl.Phys. 28, pp. 2443-2450, 1995
- Semak, V., V., West, J.C., Hopkins, J. A., M$_c$Cay, M. H., and M$_c$Cay, T. D.,' *Shape and Position of Keyhole During Laser Welding'*, ICALEO, pp. 544-552, 1995

- Semak,V., Matsunawa, A., '*The Role of Recoil Pressure in Energy Balance during Laser Materials Processing*', J.Phys.D: Appl.Phys. 30, pp. 2541-2552, 1997
- Semak,V.V., Steele, R.J., Fuerschbach, P.W., and Damkroger, B.K., '*Role of Beam Absorption in Plasma during Laser Welding*', J.Phys.D:Appl.Phys. 33, pp. 1179-1185, 2000
- Steen, W.M., *Laser Material Processing'* , Springer Verlag London Limited, 1998
- Sudnik, W., Radj, D., and Erofeew,W., *'Computerized Simulation of Laser Beam Welding, Modelling and Verification'* J.Phys.D.,: Appl. Phys. 29 , pp.2811-2817, 1996
- Takahashi, K., Kumagai, M., Katayama, S and Matsunawa, A., *'CO_2 laser welding of aluminium alloys at high speeds up to 20m/min'* Proceedings of SPIE – The International Society for Optical Engineering, v 4831, (2002), pp. 319-324
- Takahashi, N., Fujii, S., Yasuda, K., *'Development of numerical simulation technique for laser welding'* , Proceedings of SPIE – The International Society for Optical Engineering, v 4830, p.203-207, 2002
- Tix,C., Gratzke, U., and Simon, G., '*Absorption of the Laser Beam by the Plasma in Deep Laser Beam Of Metals'* J. Appl. Phys. 78 (11), pp.6448-6453, 1995
- Trappe, J., Kroos, J., and Simon, G., *'On the Shape and Location of the Keyhole in Penetration Laser Welding'*, J.Phys.D.,: Appl. Phys. 27 , pp.2152-2154, 1994
- TRUMPF GmBH & Co., *Technical Information: Laser Processing*, TRUMPF GmBH & Co., 1994
- Tsai, F., and Kanntey-Asibu, E., *'Modeling of Conduction Mode Laser welding Process For Feedback Control'* Transactions of the ASME, Vol. 122, pp.420-428, 2000

- Wake, M., Hasegawa, M., Konishi, Y., and Kakunai, S., *'Temperature Distribution and Influence to Metal surface Induced by a Scanning Circular Laser Beam'*, Proceedings of Lamp '92, Nagaoka, pp. 347-352, 1992
- Weston, J. P., Jones, I.A., and Wallach, E.R., *'Laser Welding of Aluminium Alloys using Different Laser Sources'* CISFFEL6, 6th International Conference on Welding and Melting by Electron and Laser Beams, Toulon, France 15-19 June 1998
- Williams, S. W., Scott, G., and Calder, N.J., *'Direct Diode Laser Welding of Aerospace Alloys'* LaserOpto 33(4), pp.50-54, 2001
- Xie, J., and Kar, A., *'Laser Welding of Thin Sheet Steel with Surface Oxidation'*, Welding Research Supplement, pp. 343s-348s, 1999
- Zhao, H., and DebRoy, T., *'Macroporosity free aluminium alloy weldments through numerical simulation of keyhole mode laser welding'* Journal of Applied Physics, v 93, n 12, pp. 10089-10096, 2003
- Zhao, H., and DebRoy, T., *'Weld Metal Composition Change during Conduction Mode Laser Welding of Aluminium Alloy 5182 '* Metallurgical and Materials Transactions B, Vol. 32B, pp. 163-172, 2001

3. Theoretical Aspects and Modelling of Process

In this chapter some theoretical aspects of conduction welding and 1D and 2D analytical/semi-quantitative analysis are discussed. Numerical modelling of the process is also discussed.

3.1 Semi-Quantitative Analysis Of Penetration Depth/Spot Radius Phenomenon – 1D

It has been observed that penetration depth increases with spot radius during low-speed laser welding in the conduction mode regime. The laser beam is defocused. Below is a 1D semi-quantitative analysis of the phenomenon.

The basic equation for heat flow in one direction with no convection or heat generation is (Wilson and Hawkes, 1987; Steen, 2003):

$$\frac{\partial^2 T}{\partial z^2} = \frac{1}{\alpha}\frac{\partial T}{\partial t}$$

Constant thermal properties are assumed and the following boundary conditions:

At $z = 0$, constant flux $H = -k\left[\frac{\partial T}{\partial z}\right]_{surf}$

At $z = \infty$, $\frac{\partial T}{\partial z} = 0$

At $t = 0$, $T = T_0$

The temperature at a depth z below the surface of a semi-infinite solid at a time t after heat flow starts is then given by

$$T(z,t) = \frac{2H}{K}(\alpha t)^{\frac{1}{2}} ierfc\left(\frac{z}{2(\alpha t)^{\frac{1}{2}}}\right) \qquad (3.1)$$

where

$H = I(1 - R_s)$

I, H is beam intensity (Wm^{-2})

R_s is surface reflectance

α is thermal diffusivity (m^2s^{-1})

K is thermal conductivity ($Wm^{-1}K^{-1}$)

t is time (s)

The function ierfc is given by

$$ierfc(x) = \frac{1}{\sqrt{\pi}}[\exp(-x^2) - x(1 - erf(x))]$$

where $erf(x) = \frac{2}{\sqrt{\pi}} \int_0^x e^{-\xi^2} d\xi$

From (3.1)

$$T(0,t) = \frac{2H}{K}(\frac{\alpha t}{\pi})^{\frac{1}{2}} \qquad (3.2)$$

Let z_m be depth at which temperature reaches melting point, T_m when the surface temperature has just reached the boiling temperature, T_b.

From equations (3.1) and (3.2)

$$\frac{T(z_m,t)}{T(0,t)} = \frac{T_m}{T_b} = \pi^{\frac{1}{2}} ierfc(\frac{z_m}{2(\alpha t)^{\frac{1}{2}}}) \qquad (3.3)$$

From (3.1.2)

$$(\alpha t)^{\frac{1}{2}} = \frac{T_b K \pi^{\frac{1}{2}}}{2H}$$

Putting this in (3.3), we obtain

$$ierfc(\frac{Hz_m}{KT_b\pi^{\frac{1}{2}}}) = \frac{T_m}{\pi^{\frac{1}{2}}T_b} \qquad (3.4)$$

Equation (3.4) shows that the product Hz_m is constant as long as the surface temperature is at boiling temperature.

Thus $z_m \alpha \frac{1}{H}$. This means that the welding depth will increase with decreasing intensity for as long as the surface temperature remains at boiling. This result is comparable to that obtained by Duley(1976) and Prokhorov(1990).

$$z_m = \frac{1.2KT_m}{H}\left(\frac{T_b}{T_m} - 1\right) \tag{3.5}$$

Equation (3.5) shows that z_m is inversely proportional to H.

As the intensity decreases, a point is reached where the boiling temperature can no longer be sustained. Let the temperature at this point be T_p.

Then $T_m < T_p < T_b$

Equation (3.4) becomes

$$ierfc\left(\frac{Hz_m}{KT_p\pi^{\frac{1}{2}}}\right) = \frac{T_m}{\pi^{\frac{1}{2}}T_p} \tag{3.6}$$

But from (3.2), $T_p = \frac{2H}{K}\left(\frac{\alpha t}{\pi}\right)^{\frac{1}{2}}$ (3.7)

$$\therefore \quad \left(\frac{Hz_m}{KT_p\pi^{\frac{1}{2}}}\right) = \left\{\frac{z_m}{2(\alpha t)^{\frac{1}{2}}}\right\}$$

Therefore, $ierfc\left(\frac{Hz_m}{KT_p\pi^{\frac{1}{2}}}\right) = ierfc\left\{\frac{z_m}{2(\alpha t)^{\frac{1}{2}}}\right\}$

and $\frac{T_m}{\pi^{\frac{1}{2}}T_p} = ierfc\left\{\frac{z_m}{2(\alpha t)^{\frac{1}{2}}}\right\}$ (3.8)

Now, $t = \frac{2R}{v}$

For small values of x, $ierfc(x) \approx \frac{1}{\sqrt{\pi}} - x \approx 0.56 - x$

Combining (3.7), (3.8) with the above relations we have

$$z_m = 2(\alpha t)^{\frac{1}{2}}[0.56 - \frac{\pi T_m v^{\frac{1}{2}} R^{\frac{3}{2}} K}{2^{\frac{3}{2}} \alpha^{\frac{1}{2}} P}] = 1.12.\sqrt{2}.\alpha^{\frac{1}{2}} \frac{R^{\frac{1}{2}}}{v^{\frac{1}{2}}} - \frac{\pi T_m K R^2}{P} \qquad (3.9)$$

Equation (3.9) may be written as

$$z_m = AR^{\frac{1}{2}} - BR^2 \qquad (3.10)$$

for constant P ,K, T_m, v and α

where $A = 1.12\sqrt{2}\frac{\alpha^{\frac{1}{2}}}{v^{\frac{1}{2}}}$ and $B = \frac{\pi T_m K}{P}$

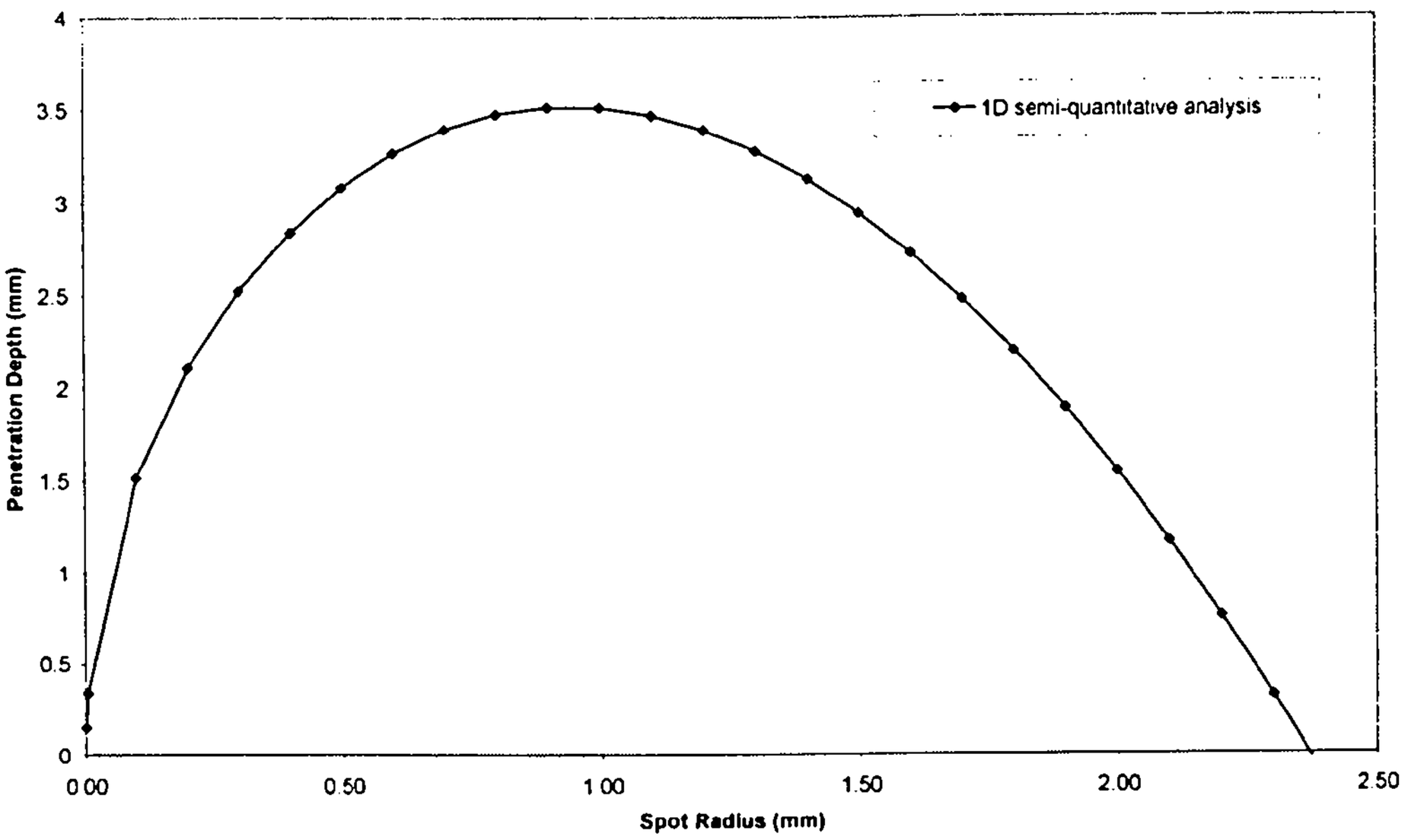

Figure 3.1. – Result of semi-quantitative simulation of laser conduction welding process

Figure 3.1 shows the result of a simulation using values, $P=500W$, $v = 10mm/s$ and K, T_m and α remaining constant. The important thing here is the penetration depth/spot radius variation.

This phenomenon is only observable at relatively low welding speeds. Thus the choice of welding speed is critical depending on the type of laser and the laser power involved. At greater speeds the reduced interaction time results in a relatively lower heat absorption by the workpiece.

3.2 Semi-Quantitative Analysis of Laser Conduction Welding (LCW) – 2D

The equation for temperature distribution by a circular disc source, of radius r, moving with velocity v in the x direction across the surface of a thick plate (see figure 3.2) is given by (Ion., et al 1984):

$$T = T_0 + \frac{q/v}{2\pi K[t(t+t_0)]^{1/2}} \exp - \frac{1}{4a}\{\frac{(z+z_0)^2}{t} + \frac{y^2}{(t+t_0)}\} \qquad (3.11)$$

where $t_0 = \frac{r^2}{4a}$, $z_0{}^2 = [\frac{r}{e}(\frac{\pi a r}{v})^{1/2}]$, $t = \frac{2r}{v}$

Boundary conditions are as follows:

At $z = 0$, $\frac{\partial T}{\partial z} = 0$ (no heat losses to the surroundings)

At $z = \infty$, $T = T_0$;

a = thermal diffusivity (m^2s^{-1})

q = power (W)

v = welding speed (ms^{-1})

t = interaction time (s)

K = thermal conductivity (W/mK)

T_b = boiling temperature (K)

T_m = melting temperature (K)

T_0 = ambient temperature (K)

T = temperature (K)

r = spot radius (m)

Take a point P(y,z) with its temperature at boiling temperature, T_b and let the temperature that represents that of the melting isotherm be T_m.

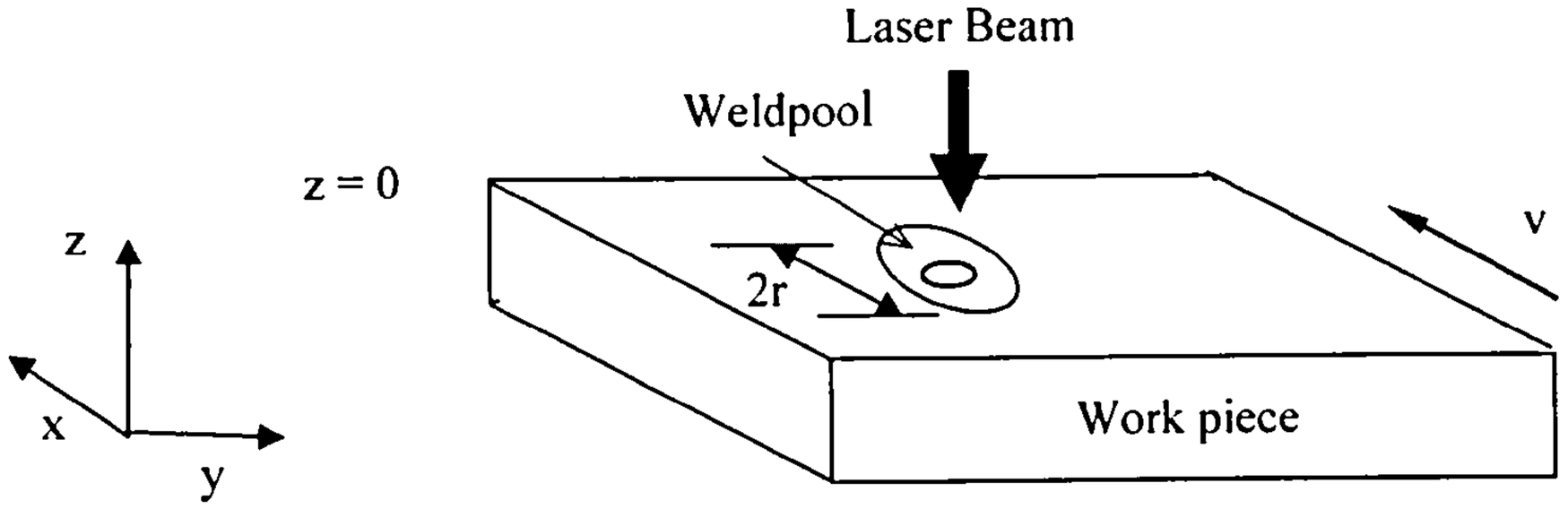

Figure 3.2 Laser conduction welding coordinate system and geometry

Then

$$T_b = T_0 + \frac{q/v}{2\pi K[t(t+t_0)]^{1/2}} \exp - \frac{1}{4a}\{\frac{{z_0}^2}{t} + \frac{y^2}{(t+t_0)}\} \tag{3.12}$$

$$T_m = T_0 + \frac{q/v}{2\pi K[t(t+t_0)]^{1/2}} \exp - \frac{1}{4a}\{\frac{(z_m+z_0)^2}{t} + \frac{y^2}{(t+t_0)}\} \tag{3.13}$$

Re-arranging and dividing (3.13) by (3.12) we have:

$$\frac{T_m - T_0}{T_b - T_0} = \exp - \frac{1}{4a}[\frac{(z_m+z_0)^2 - {z_0}^2}{t}] \tag{3.14}$$

$$\therefore -\ln(\frac{T_m - T_0}{T_b - T_0}) = \frac{1}{4a}[\frac{(z_m+z_0)^2 - {z_0}^2}{t}] \tag{3.15}$$

Then

$$4a\ln(\frac{T_b - T_0}{T_m - T_0}) = \frac{(z_m + z_0)^2 - {z_0}^2}{t} \tag{3.16}$$

since $-ln(x) = ln(1/x)$

Re-arranging equation (3.16) gives

$$z_m = \sqrt{4at\ln(\frac{T_b - T_0}{T_m - T_0}) + {z_0}^2} - z_0 \tag{3.17}$$

Putting in expressions for t and z_0^2 in equation (3.17) gives

$$z_m = \sqrt{\frac{8ar}{v}\ln(\frac{T_b - T_0}{T_m - T_0}) + [\frac{r}{e}(\frac{\pi ar}{v})^{1/2}]} - \sqrt{\frac{r}{e}(\frac{\pi ar}{v})^{1/2}} \tag{3.18}$$

Equation (3.18) gives the variation of penetration depth z_m with spot radius r when the surface temperature is at the boiling point. It shows that the penetration depth increases with spot radius in this regime.

The relation between penetration depth and spot radius for the whole range of surface temperature from boiling and then the subsequent decrease to below boiling (due to decreasing intensity) now follows:

Rearranging equation (3.11) we have:

$$\frac{2\pi K[t(t+t_0)]^{1/2} v(T_m - T_0)}{q} = \exp -\frac{1}{4a}\{\frac{(z_m + z_0)^2}{t} + \frac{y^2}{(t+t_0)}\} \tag{3.19}$$

$$-\ln[\frac{2\pi K[t(t+t_0)]^{1/2} v(T_m - T_0)}{q}] = \frac{1}{4a}\{\frac{(z_m + z_0)^2}{t} + \frac{y^2}{(t+t_0)}\} \quad (3.20)$$

$$\therefore 4a\ln[\frac{q}{2\pi K[t(t+t_0)]^{1/2} v(T_m - T_0)}] = \{\frac{(z_m + z_0)^2}{t} + \frac{y^2}{(t+t_0)}\} \quad (3.21)$$

From equation (3.21) it is easily shown that

$$z_m = \sqrt{4at\ln[\frac{q}{2\pi K[t(t+t_0)]^{1/2} v(T_m - T_0)}] - [\frac{y^2 t}{(t+t_0)}]} - z_0 \quad (3.22)$$

When the expressions for t and z_0^2 are inserted in equation (3.22),we have

$$z_m = \sqrt{\frac{8ar}{v}\ln[\frac{q}{2\pi K[\frac{2r}{v}(\frac{2r}{v} + \frac{r^2}{4a})]^{1/2} v(T_m - T_0)}] - [\frac{y^2 \frac{2r}{v}}{(\frac{2r}{v} + \frac{r^2}{4a})}]} - \sqrt{\frac{r}{e}(\frac{\pi ar}{v})^{1/2}} \quad (3.23)$$

$$z_m = \sqrt{\frac{8ar}{v}\ln[\frac{q}{2\pi K[r(\frac{8ar + r^2 v}{2a}]^{1/2}(T_m - T_0)}] - [\frac{16ary^2}{(8ar + r^2 v)}]} - \sqrt{\frac{r}{e}(\frac{\pi ar}{v})^{1/2}} \quad (3.24)$$

Equation (3.24) gives a 2D expression for the variation of penetration depth with spot radius, power and distance *y* from the *x* direction (i.e. centre of weld pool or the direction of welding).

Plots obtained from equation (3.24) (keeping K and a constant) are shown below.

Values used for the calculations are those for mild steel and are given below:

$a = 1.38 \times 10^{-5}\ m^2s^{-1}$

$K = 50 W/mK$

$T_m = 1500^0C$

$T_0 = 25^0C$

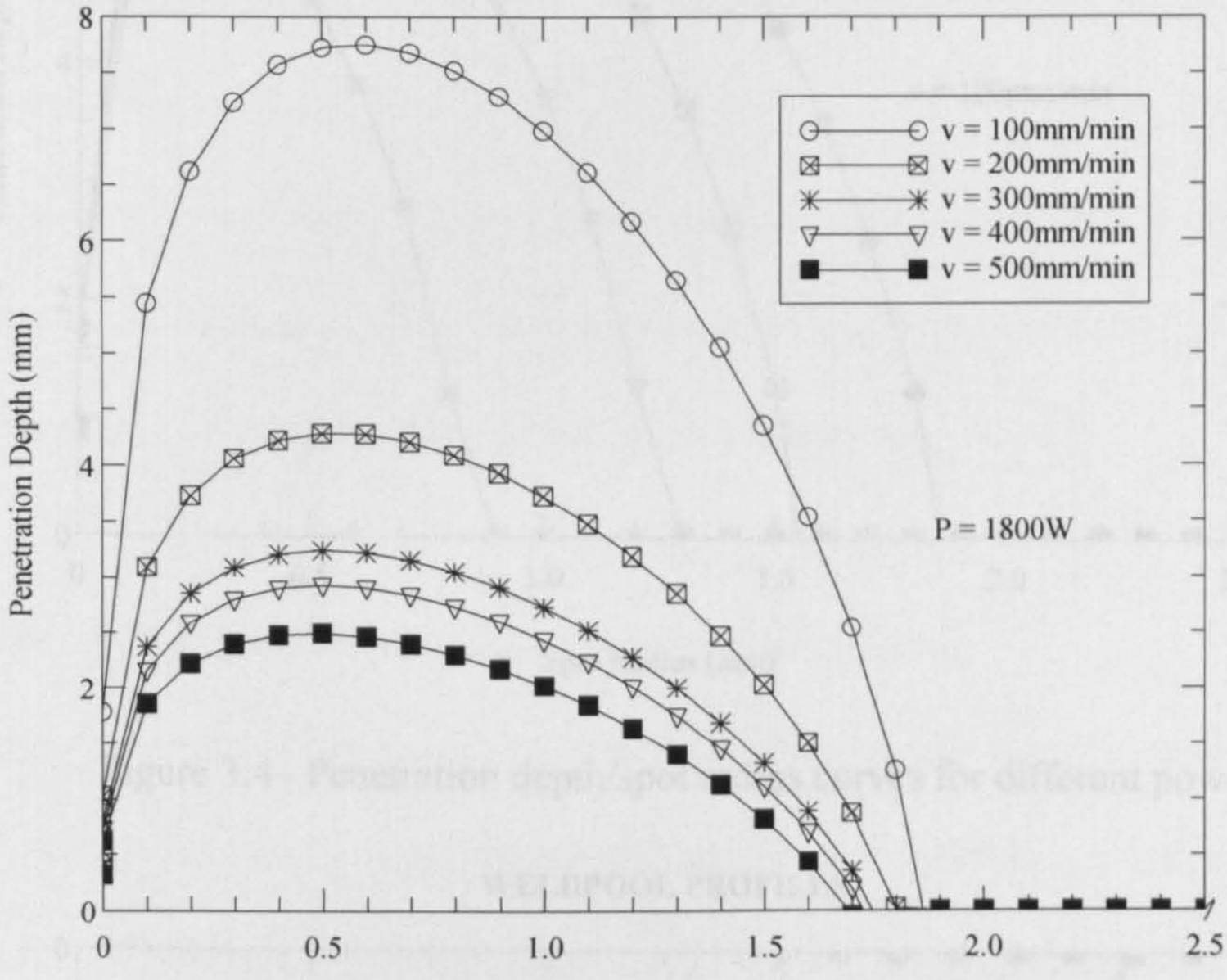

Figure 3.3 – Penetration depth/spot radius curves for different welding speeds

Figure 3.3 shows that as the spot radius increases, the penetration depth increases up to a maximum and then decreases. As would be expected, an increase in welding speed at constant power produces a decrease in penetration depth.

Figures 3.4 shows the effect of laser power on penetration depth. At constant welding speed, penetration depth is directly proportional to laser power. For this simulation, laser power of 1800W produces the greatest penetration depth and laser power of 800W produces the smallest penetration depth.

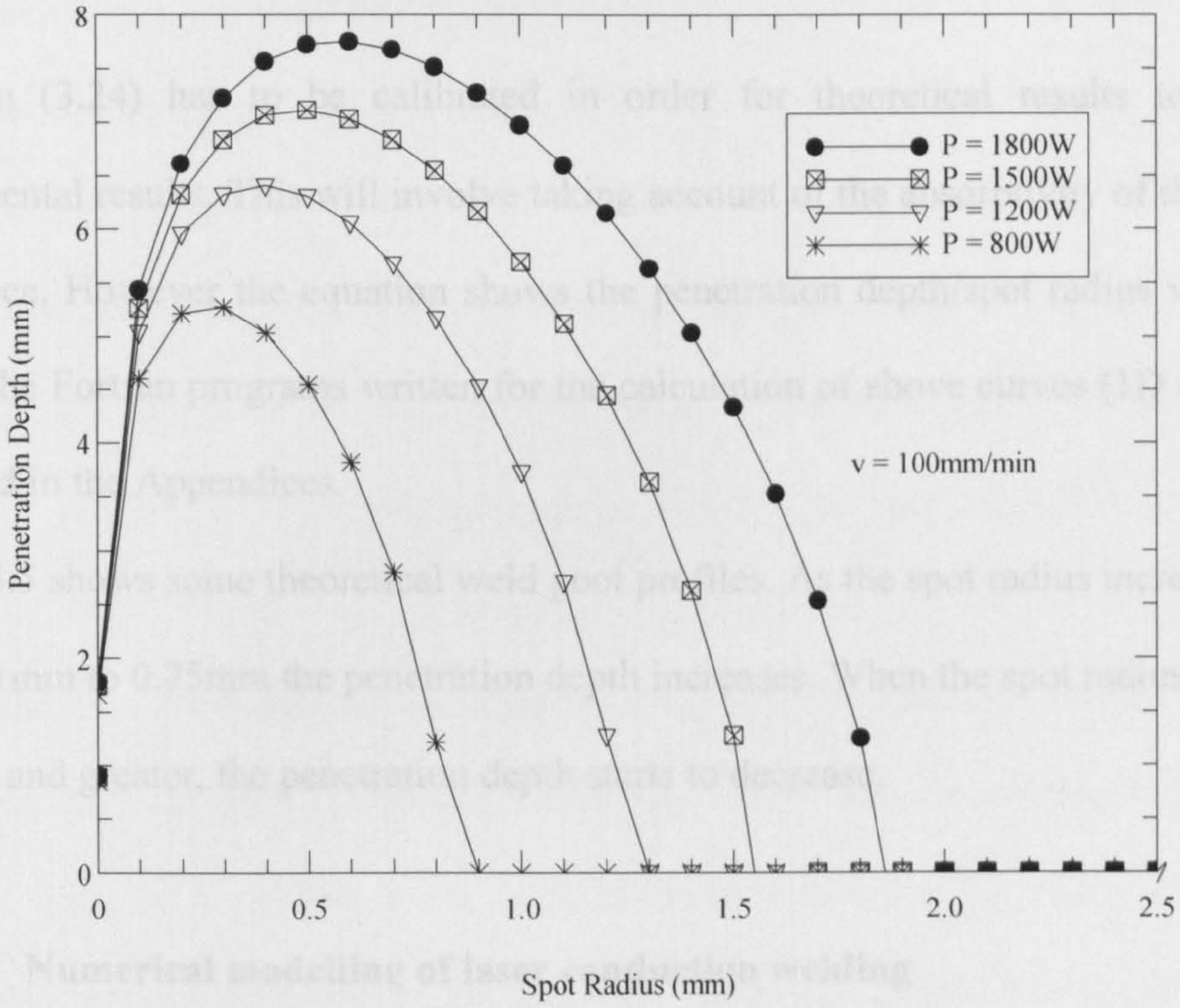

Figure 3.4– Penetration depth/spot radius curves for different powers

WELDPOOL PROFILES

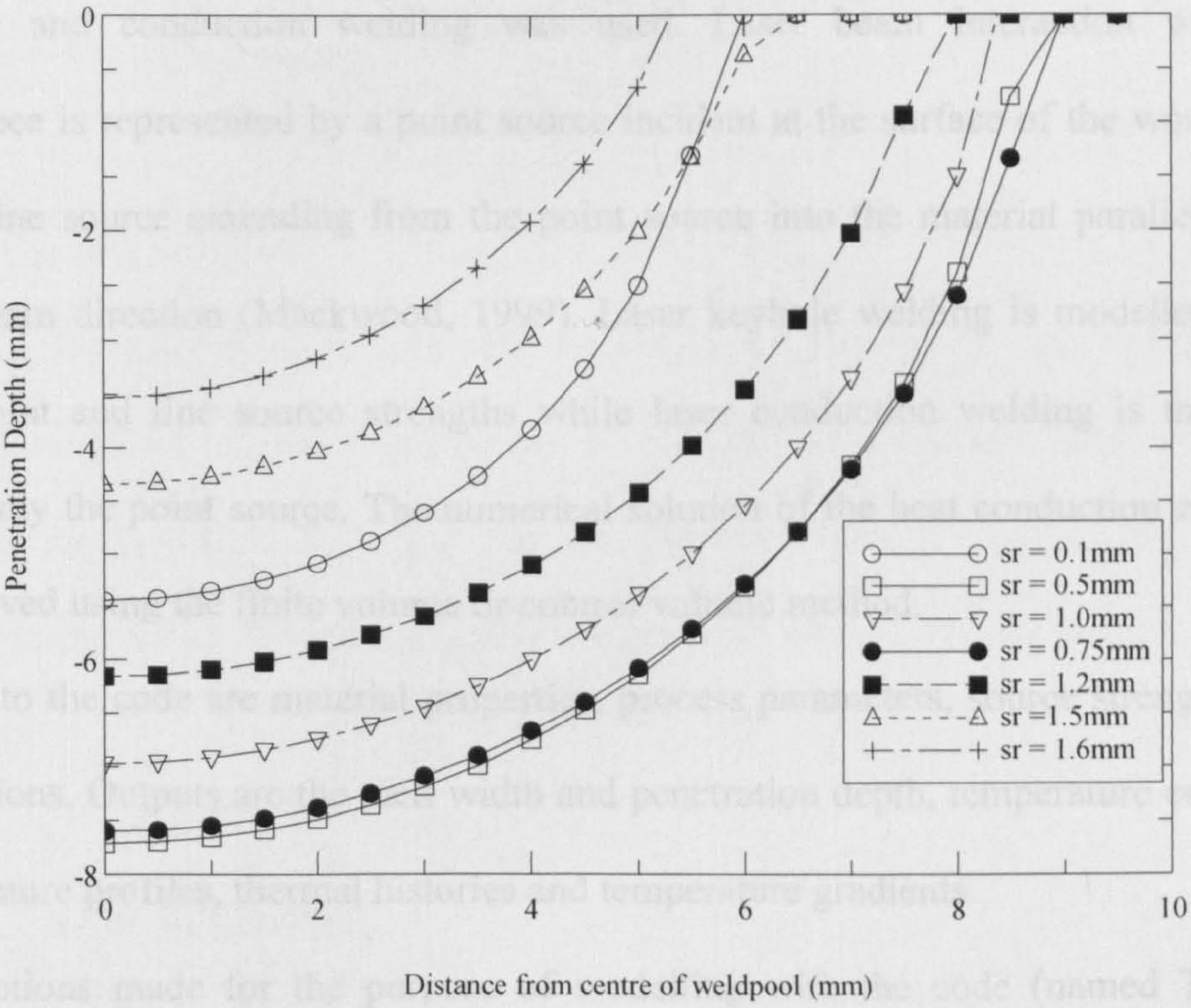

Figure 3.5 – Weld pool profiles for different distances from the focus

Equation (3.24) has to be calibrated in order for theoretical results to match experimental results. This will involve taking account of the absorptivity of the metal workpiece. However the equation shows the penetration depth/spot radius variation trend. The Fortran programs written for the calculation of above curves (1D and 2D) are listed in the Appendices.

Figure 3.5 shows some theoretical weld pool profiles. As the spot radius increases from 0.1mm to 0.75mm the penetration depth increases. When the spot radius rises to 1mm and greater, the penetration depth starts to decrease.

3.3. Numerical modelling of laser conduction welding

A computer programme designed to make predictions of the temperature for a variety of laser weld geometries through the medium of thermal modelling both for keyhole and conduction welding was used. Laser beam interaction with the workpiece is represented by a point source incident at the surface of the workpiece, and a line source extending from the point source into the material parallel to the laser beam direction (Mackwood, 1999). Laser keyhole welding is modelled using both point and line source strengths while laser conduction welding is modelled using only the point source. The numerical solution of the heat conduction equation is achieved using the finite volume or control volume method.

Inputs to the code are material properties, process parameters, source strengths and dimensions. Outputs are the melt width and penetration depth, temperature contours, temperature profiles, thermal histories and temperature gradients.

Assumptions made for the purpose of modelling with the code (named TS4D – thermal simulation in four (4) dimensions) are as follows:

- The welding set-up must be symmetrical about the weld line.
- Convection in the weld pool is neglected.
- Distortion is neglected.
- Convective and radiative heat loss can only take place from the top and bottom surfaces of the workpiece and not from the regions of the workpiece to the air.
- Forces due to gravity are neglected since they are assumed negligible compared to surface tension forces.
- No heat loss conditions are assumed on the *y* boundary and downstream (part of workpiece that has already passed under the laser beam) x boundary. For the upstream (part of workpiece yet to pass under laser beam) x boundary, there is a choice between a no heat loss condition and an ambient temperature boundary.
- For simulation of surface treatment and conduction welding, it is assumed that the temperature will not exceed boiling point.
- Power is absorbed evenly

3.3.1. Use of TS4D code

TS4D requires experimental weld pool cross-sections. The point source strength, line source strengths and power source are all adjusted until the predicted weld pool cross-section is a good fit to the experimental one. Then the temperature field is obtained from which the thermal histories, temperature profiles and contours can be generated.

3.3.1.1. Solution domain

The solution is calculated in the domain

$$-\frac{1}{2}Length \le x \le \frac{1}{2}Length$$

$$0 \le y \le \frac{1}{2}Width$$

$$0 \le z \le Total\ \ Depth$$

The solution domain is kept as small as possible to increase the accuracy of computation but large enough so that the temperatures on its boundaries do not rise appreciably above the ambient temperature. A choice for Length and Width of 80mm each would suffice for most situations.

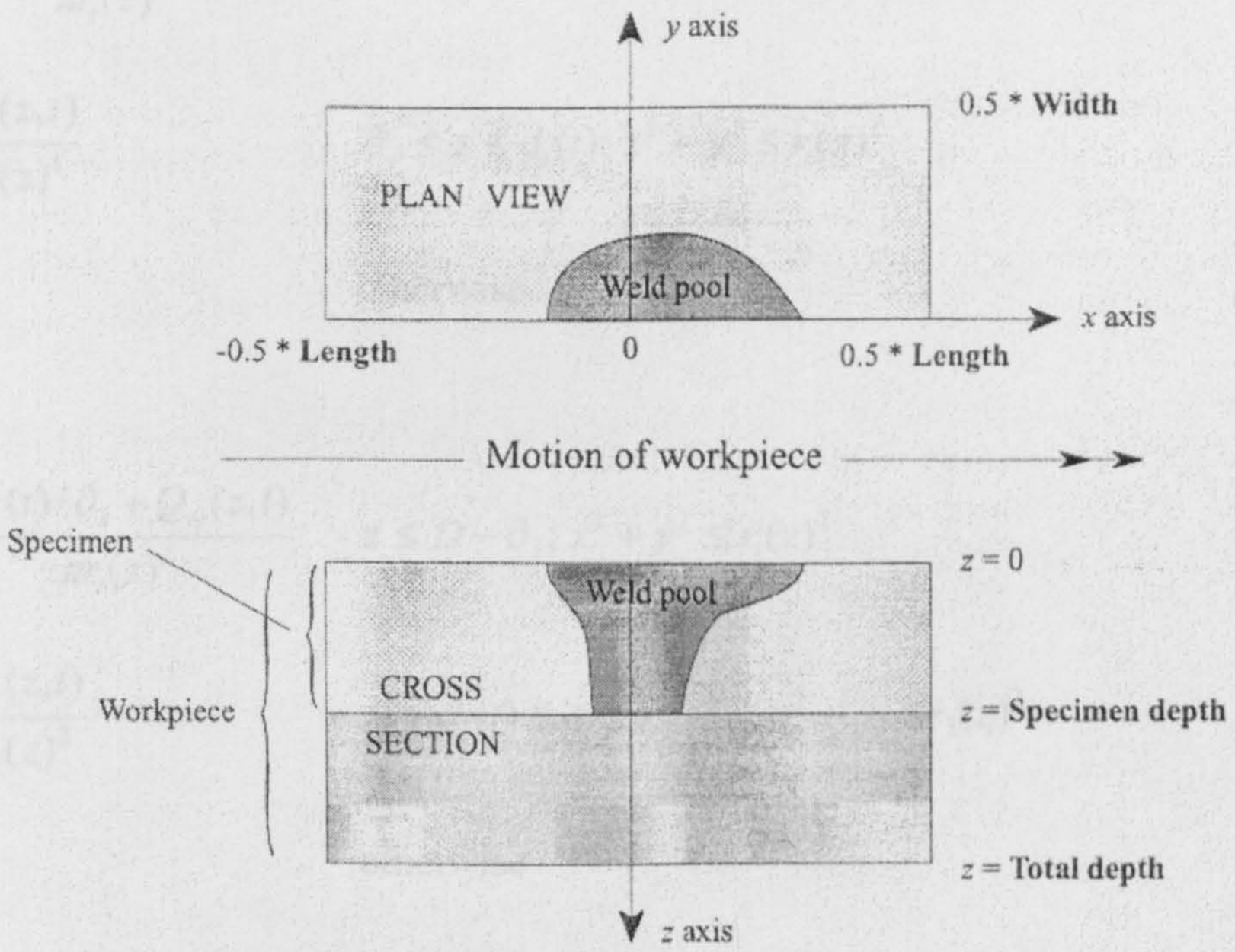

Figure 3.6 Solution domain for TS4D

3.3.1.2 Heat Source

Up to 11 heat sources can be incident on the workpiece. Let $f(x-x_i, y, t)$ represents energy flux attributable to a single source at time t on the top surface.

x_i is the x-coordinate of the centre of the source i where

$$-0.5 * Length < x_i < 0.5 * Length$$

The plume for each source is represented by a surface heat source of strength $Q_{S_i}(t)$ of radius $r_i(z)$ and the keyhole by a volume source of strength $Q_{v_i}(z,t)$ and length $d_i(t)$ with $0 \le d_i(t) \le D$ (where D is the workpiece depth).

Let $S_{T_i}(z,t)$ and $S_{B_i}(z,t)$ be defined as

$$S_{T_i} = \frac{Q_{S_i}(t)/\partial_z + Q_{v_i}(z,t)}{\pi r_i(z)^2} \qquad z \le \partial_z;\ x^2 + y^2 \le r_i(z)^2$$

$$S_{T_i} = \frac{Q_{v_i}(z,t)}{\pi r_i(z)^2} \qquad \partial_z \le z \le d_i(t);\ x^2 + y^2 \le r_i(z)^2$$

$$S_{T_i} = 0 \qquad \text{otherwise}$$

$$S_{B_i} = \frac{Q_{S_i}(t)/\partial_z + Q_{v_i}(z,t)}{\pi r_i(z)^2} \qquad z \le D - \partial_z;\ x^2 + y^2 \le r_i(z)^2$$

$$S_{B_i} = \frac{Q_{v_i}(z,t)}{\pi r_i(z)^2} \qquad D - d_i(t) \le z \le D - \partial_z;\ x^2 + y \le r_i(z)^2$$

$$S_{B_i} = 0 \qquad \text{otherwise}$$

In the program, the quantity δ_z is assigned a finite value, that is a tiny fraction of D that has a negligible effect on the predicted temperatures.

The function $f(x\text{-}x_i, y, t)$ can be expressed as

$$f(x - x_i, y, z) = (S_{T_i}(0,t) + S_{B_i}(0,t)) * q(x - x_i, y, 0)$$

For the numerical simulations undertaken in this work, $q(x-x_i,y,z)$ takes the following form:

$$q(x-x_i,y,z) = e^{-((x-x_i)^2+y^2)/Srad_i^2(z)} \qquad 0 \le z \le d_i(t)$$

so that

$$q(x-x_i,y,z) = 1 \qquad at \;\; x = x_i, y = 0$$

and $q(x-x_i,y,z) = e^{-2}$ at $(x-x_i) = S_{rad_i}(z)$, $y = S_{rad_i}$

$$q(x-x_i,y,z) = 0 \qquad \text{otherwise.}$$

$S_{rad_i} = Radius\ of\ spot$

3.3.1.3 Boundary Conditions

The steady-state heat conduction equation that is being solved is

$$\rho(T)C_p(T)u\frac{\partial T}{\partial x} = k(T)(\frac{\partial^2 T}{\partial x^2}+\frac{\partial^2 T}{\partial y^2}+\frac{\partial^2 T}{\partial^2 z}) + \sum_1^{NSS} S(z)$$

For the time-dependent heat conduction equation

$$\rho(T)C_p(T)\,(\frac{\partial T}{\partial t}+u\frac{\partial T}{\partial x}) = k(T)(\frac{\partial^2 T}{\partial x^2}+\frac{\partial^2 T}{\partial y^2}+\frac{\partial^2 T}{\partial^2 z}) + \sum_1^{NSS} S(z,t)$$

where NSS is the number of sources or sinks incident on the workpiece where

x, y, z	are	cartesian coordinates [m]
t	is	time [s]
T(x, y, z)	is	time-independent temperature [K]
T(x, y, z,t)	is	time-dependent temperature [K]
$\rho(T)$	is	mass density [kg/m^3]
$C_p(T)$	is	specific heat capacity [J/kg/K]
K(T)	is	thermal conductivity [W/m/K]
u	is	translation speed of workpiece (welding speed) [m/s]

S(z) is time-independent heat source

S(z, t) is time varying heat source

- **Top Boundary (z= 0)**

(i) For surface treatment and conduction welding sources:

$$k\frac{\partial T}{\partial z} = Q_T(x,y,t) \qquad T(x,y,0,t) \le T_{boiling}$$

$$T = T_{boiling} \qquad \text{otherwise}$$

$T_{boiling}$ is the boiling point of workpiece.

(ii) For laser keyhole sources:

$$k\frac{\partial T}{\partial z} = Q_T(x,y,t)$$

$$Q_T(x,y,t) = \sum_i^{11} f_{T_i}(x-x_i,y,t) + A_T(T-T_0) + \varepsilon_T\sigma(T^4 - T_0^4)$$

- **Bottom boundary (z = Total depth)**

(i) For surface treatment and conduction welding sources:

$$k\frac{\partial T}{\partial z} = Q_B(x,y,t) \qquad T(x,y,Total\ depth,t) \le T_{boiling}$$

$$T = T_{boiling} \qquad \text{otherwise}$$

$T_{boiling}$ is the boiling point of workpiece.

(iii) For laser keyhole sources:

$$k\frac{\partial T}{\partial z} = Q_B(x,y,t)$$

$$Q_B(x,y,t) = \sum_i^{11} f_{B_i}(x-x_i,y,t) + A_B(T-T_0) + \varepsilon_B\sigma(T^4 - T_0^4)$$

σ = Stefean-Boltzmann constant = 5.66961 x 10^{-8} $Wm^{-2}K^{-4}$

ε_T and ε_B are emissivity for top and bottom surfaces respectively

A_T and A_B are coefficients of convective loss from top and bottom surfaces respectively.

- **Downstream and y boundaries**

$k\frac{\partial T}{\partial x} = 0;$ $k\frac{\partial T}{\partial y} = 0$. There is no heat loss through the edge boundaries.

- **Upstream boundary**

Here a choice is made between

$k\frac{\partial T}{\partial x} = 0;$. (no heat loss)

or alternatively

T = Ambient (i.e. temperature remains at ambient temperature)

- **Symmetry condition**

$$k\frac{\partial T}{\partial y} = 0 \quad at\ y = 0$$

This assumes that $T(x, y, z, t) = T(x, -y, z, t)$ for all y. Only symmetric configurations are considered.

3.3.2 Control Volume Method

In the control volume method, the differential equation governing the problem is examined as it relates to the underlying conservation principle (Ketkar, 1999). Every discrete grid point or node has the conservation principle that is used in deriving the differential equation, applied to it. The control volume method leads quickly to

mathematical expressions that have a physical basis and are therefore very versatile when it comes to applying simple or complex boundary conditions.

3.3.2.1 One-Dimensional Steady State Problem

The steady state heat conduction equation in one-dimension is given by

$$\frac{d}{dx}(k\frac{dT}{dx})+S=0 \tag{3.25}$$

where k is the thermal conductivity and S is the source term. Figure 3.7 shows a one-dimensional control volume. P identifies a general nodal point, and its neighbours, nodes to the east and west, are identified by E and W respectively (Versteeg and Malalasekera, 1998). The west side face of the control volume is referred to by 'w' and the east side face by 'e'. The distances between the nodes W and P and between nodes P and E are δx_{WP} and δx_{PE} respectively. Distances between face w and point P and between P and face e are denoted by δx_{wP} and δx_{Pe}.

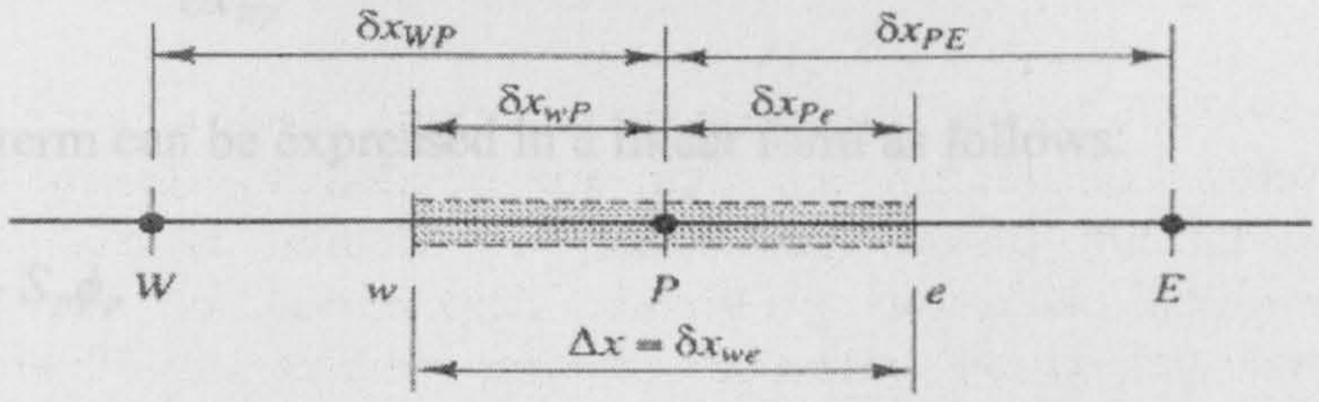

Figure 3.7 One-dimensional control volume (from Versteeg and Malalasekera, 1998)

The key step of the finite volume method is the integration of the governing equation(s) over a control volume to yield a discretised equation at its nodal point P. Integrating equation (3.25) gives

$$\int_{\Delta V} \frac{d}{dx}(k\frac{dT}{dx})dV + \int_{\Delta V} SdV = (kA\frac{dT}{dx})_e - (kA\frac{dT}{dx})_w + \bar{S}\Delta V = 0 \qquad (3.26)$$

A is the cross-sectional area of the control volume face, ΔV is the volume and $\bar{S}$ is the average value of source S over the control volume.

T and k are defined at nodal points. In order to calculate values at the control volume faces, linear approximations are used in the method of central differencing. Therefore

$$k_w = \frac{k_W + k_P}{2}$$

$$k_e = \frac{k_P + k_E}{2}$$

and

$$(kA\frac{dT}{dx})_e = k_e A_e(\frac{T_E - T_P}{\partial x_{PE}}) \qquad (3.27)$$

$$(kA\frac{dT}{dx})_w = k_w A_w(\frac{T_P - T_W}{\partial x_{WP}}) \qquad (3.28)$$

The source term can be expressed in a linear form as follows:

$$\bar{S}\Delta V = S_u + S_P\phi_P \qquad (3.29)$$

Substituting equations (3.27), (3.28) and (3.29) into (3.26) gives

$$k_e A_e(\frac{T_E - T_P}{\partial x_{PE}}) - k_w A_w(\frac{T_P - T_W}{\partial x_{WP}}) + (S_u + S_P T_P) = 0 \qquad (3.30)$$

This can be arranges as

$$(\frac{k_e}{\partial x_{PE}} A_e + \frac{k_w}{\partial x_{WP}} A_w - S_P)T_P = (\frac{k_w}{\partial x_{WP}} A_w)T_W + (\frac{k_e}{\partial x_{PE}} A_e)T_E + S_u \qquad (3.31)$$

Equation (3.31) can then be written as

$$a_P T_P = a_W T_W + a_E T_E + S_u \tag{3.32}$$

where

$$a_W = \frac{k_w}{\partial x_{WP}} A_w$$

$$a_E = \frac{k_e}{\partial x_{PE}} A_e$$

$$a_P = a_W + a_E - S_P$$

Equations (3.32) and (3.29) represent the discretised form of the equation (3.25)

3.3.2.2 Two-dimensional Steady State Problem

The two-dimensional steady state conduction equation is given by

$$\frac{\partial}{\partial x}(k\frac{\partial T}{\partial x}) + \frac{\partial}{\partial y}(k\frac{\partial T}{\partial y}) + S = 0 \tag{3.33}$$

A two-dimensional (2D) grid is shown below:

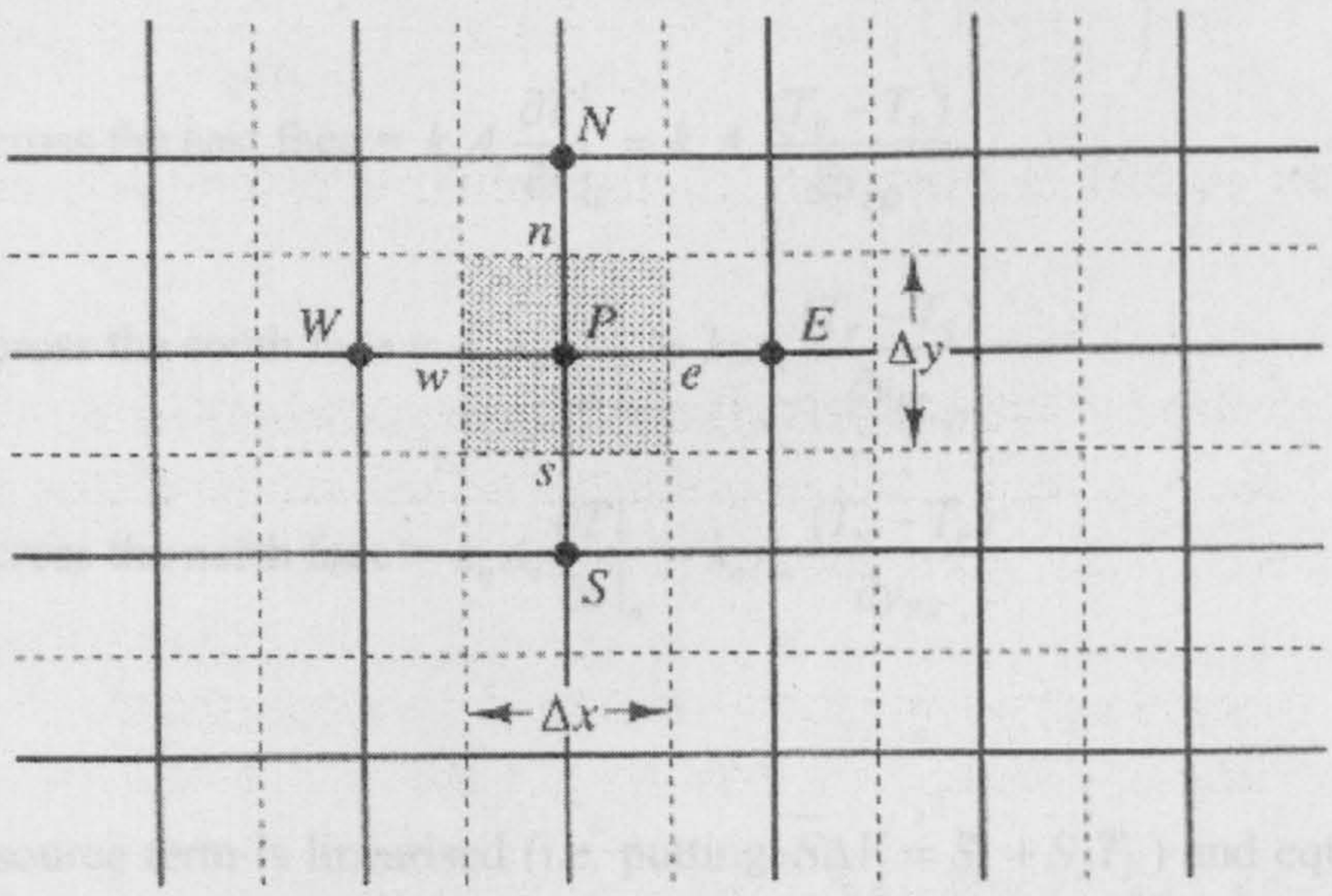

Figure 3.8 Two-dimensional grid (from Versteeg and Malalasekera, 1998)

The nodal point P has not only east (E) and west (W) neighbours but also north (N) and south (S) neighbours. Integrating equation (3.32) over the control volume yields

$$\int_{\Delta V} \frac{\partial}{\partial x}(k\frac{\partial T}{\partial x})dx.dy + \int_{\Delta V} \frac{\partial}{\partial y}(k\frac{\partial T}{\partial y})dx.dy + \int_{\Delta V} S_T dV = 0 \qquad (3.34)$$

$A_e = A_w = \Delta y$ *and* $A_n = A_s = \Delta x$

Equation (3.34) becomes

$$\left[k_e A_e(\frac{\partial T}{\partial x})_e - k_w A_w(\frac{\partial T}{\partial x})_w\right] + \left[k_n A_n(\frac{\partial T}{\partial y})_n - k_s A_s(\frac{\partial T}{\partial y})_s\right] + \bar{S}\Delta V = 0 \qquad (3.35)$$

Expressions for the flux through control volume faces are:

$$\text{Flux across the west face} = k_w A_w \left.\frac{\partial T}{\partial x}\right|_w = k_w A_w \frac{(T_P - T_W)}{\partial x_{WP}} \qquad (3.36)$$

$$\text{Flux across the east face} = k_e A_e \left.\frac{\partial T}{\partial x}\right|_e = k_e A_e \frac{(T_E - T_P)}{\partial x_{PE}} \qquad (3.37)$$

$$\text{Flux across the south face} = k_s A_s \left.\frac{\partial T}{\partial x}\right|_s = k_s A_s \frac{(T_P - T_S)}{\partial y_{SP}} \qquad (3.38)$$

$$\text{Flux across the north face} = k_n A_n \left.\frac{\partial T}{\partial x}\right|_n = k_n A_n \frac{(T_N - T_P)}{\partial y_{PN}} \qquad (3.39)$$

Is the source term is linearised (i.e. putting $\bar{S}\Delta V = S_u + S_P T_P$) and equations (3.36), (3.37), (3.38) and (3.39) are put into equation (3.35) , then we have

$$(\frac{k_w A_w}{\partial x_{WP}} + \frac{k_e A_e}{\partial x_{PE}} + \frac{k_s A_s}{\partial y_{SP}} + \frac{k_n A_n}{\partial y_{PN}} - S_P)T_P = (\frac{k_w A_w}{\partial x_{WP}})T_W + (\frac{k_e A_e}{\partial x_{PE}})T_E + (\frac{k_s A_s}{\partial y_{SP}})T_S + (\frac{k_n A_n}{\partial y_{PN}})T_N + S_u \quad (3.40)$$

Equation (3.40) can be expressed in the general form below:

$$a_P T_P = a_W T_W + a_E T_E + a_S T_S + a_N T_N + S_u \quad (3.41)$$

where

$$a_W = \frac{k_w A_w}{\partial x_{WP}}$$

$$a_E = \frac{k_e A_e}{\partial x_{PE}}$$

$$a_S = \frac{k_s A_s}{\partial y_{SP}}$$

$$a_N = \frac{k_n A_n}{\partial y_{PN}}$$

and $a_P = a_W + a_E + a_S + a_N - S_P$

3.3.2.3 Three-Dimensional Steady State Problem

The discretised equations for a 3D steady state heat conduction equation can be obtained in a similar manner. For the 3D derivation the nodal point P has six neighbouring nodes identified as west, east, south, north, bottom and top nodes (W, E, S, N, B, T). The cell faces are identified by w, e, s, n, b, and t, which refer to the west, east, south, north, bottom and top cell faces.

The discretised equation is given by

$$a_P T_P = a_W T_W + a_E T_E + a_S T_S + a_N T_N + a_B T_B + a_T T_T + S_u \quad (3.42)$$

where

$$a_W = \frac{k_w A_w}{\partial x_{WP}}$$

$$a_E = \frac{k_e A_e}{\partial x_{PE}}$$

$$a_S = \frac{k_s A_s}{\partial y_{SP}}$$

$$a_N = \frac{k_n A_n}{\partial y_{PN}}$$

$$a_B = \frac{k_b A_b}{\partial z_{BP}}$$

$$a_T = \frac{k_t A_t}{\partial z_{PT}}$$

$$a_P = a_W + a_E + a_S + a_N + a_B + a_T - S_P$$

The 3D control volume is as illustrated below

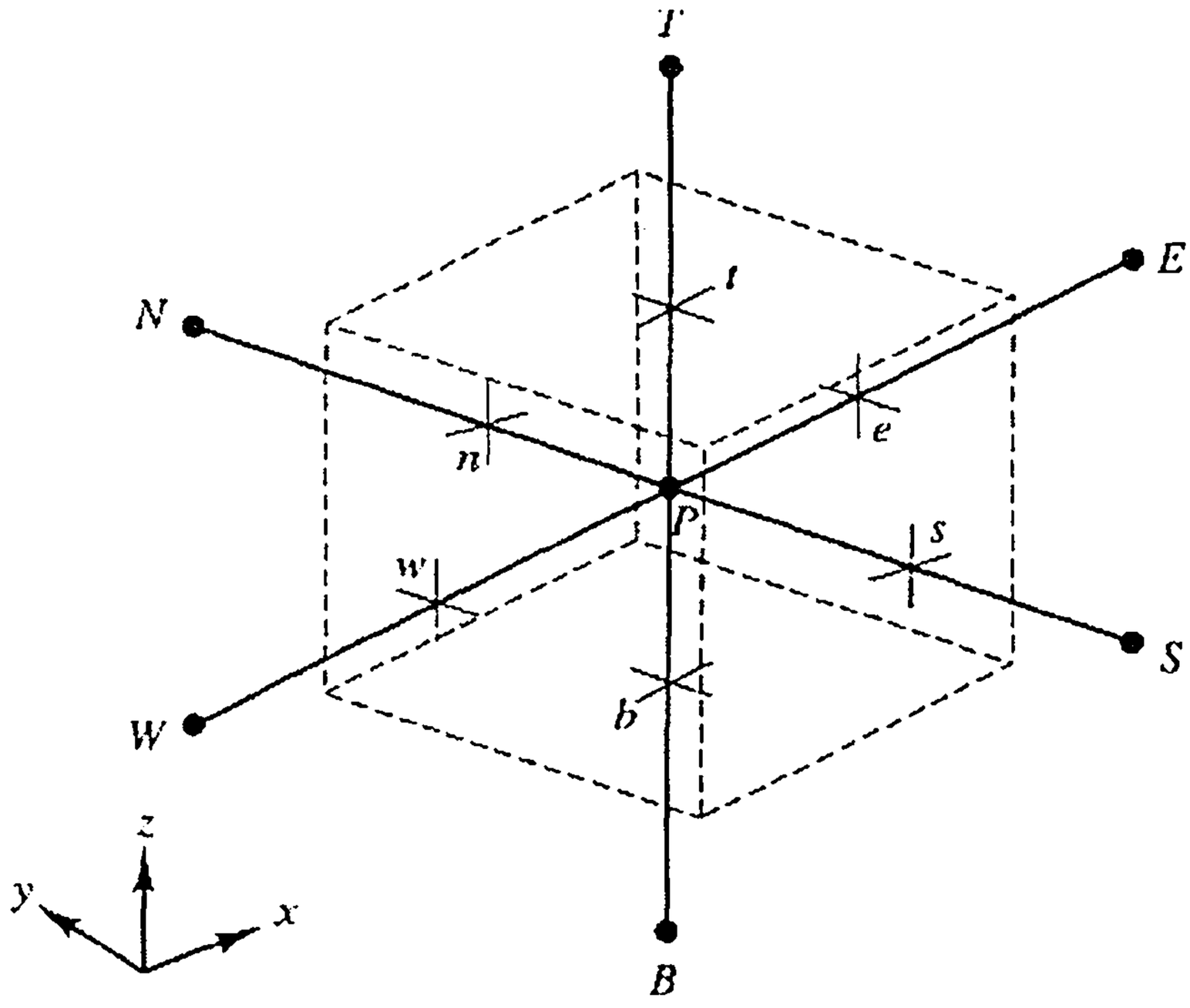

Figure 3.9 Three-dimensional grid (from Versteeg and Malalasekera, 1998)

The control volume method of solving the heat conduction equation makes it possible to incorporate a number of laser beam profiles and spot profiles (square, circular and of course Gaussian) in the code TS4D.

The steady state option was used during TS4D modelling, hence the 1D, 2D and 3D steady state control volume derivations.

Details of simulation results with TS4D are given in chapter 5. The penetration depth/spot radius variation was obtained with the code.

3.4 Other theoretical considerations

In this section, the theory behind spot radius calculations (for both CO_2 and Nd:YAG lasers) and absorptivity measurements is discussed.

3.4.1 Spot radius calculations

As highlighted in chapter 2, the variation of the laser beam diameter with distance in the direction of propagation is given by

$$w = w_0\sqrt{1+(\frac{\lambda z}{w_0{}^2\pi})^2} \tag{3.43}$$

where

w_0 is the beam radius at the focus, λ is the laser beam wavelength and z is distance in the z direction, i.e. perpendicular to the top surface of the workpiece. This equation was used to calculate the spot radii of the laser beam corresponding to distance between the focus and workpiece.

3.4.2 Absorptivity Measurements

If a piece of metal sample is irradiated with laser energy, it becomes heated and the net flux entering it is given by

$$Q_h = mc_p(T)\frac{dT_h(T)}{dt} = AP_{inc} - P_{l.h} \tag{3.44}$$

where m is the mass of the sample, c_p is the specific heat, dT_h/dt the heating rate, AP_{inc} the incident power multiplied by the absorptivity and $P_{l.h}$, the losses due to natural convection. Once the beam is switched off, the heat flow leaving the system is:

is:

$$Q_c = mc_p(T)\frac{dT_c(T)}{dt} = -P_{l.c} \tag{3.45}$$

Since the sample and its surroundings remain physically unchanged in a still atmosphere it can be assumed that the power loss on heating and cooling is equal as long a s there are no surface modifications.

Subtracting equation (3.45) from equation (3.44) gives

$$Q_h - Q_c = mc_p(T)\left[\frac{dT_h(T)}{dt} - \frac{dT_c(T)}{dt}\right] = AP_{inc} - P_{l,h} + P_{l,c} \tag{3.46}$$

This gives

$$A = \frac{mc_p(T)}{P_{inc}}\left[\frac{dT_h(T)}{dt} - \frac{dT_c(T)}{dt}\right] \tag{3.47}$$

3.5 Numerical Analysis using ABAQUS

A point source model can represent the LCW process. The commercial finite element package ABAQUS/Standard (version 5.8) was used to simulate LCW in a 2D axisymmetric element model. A 2D model was adopted due to the large amount of CPU time, space and memory required for a 3D solid element model simulation. The heat flux was represented by a Gaussian beam formulation and simulated using a user-subroutine DFLUX within ABAQUS. If the welding speed is v and the laser beam diameter at a distance h above the focus is D, then the time, t_p taken for the laser beam spot to cross a particular point on the surface in the direction of welding is given by

$$t_p = \frac{D}{v} \tag{3.48}$$

A schematic of 3D solid with shaded area that is modeled using ABAQUS is shown in figure 3.10.

Heat flow in the welding direction (x) is neglected.

Boundary conditions for the simulation are as follows:

$$\text{Temperature, } T \leq T_b \tag{3.49}$$

This was achieved by placing a limit on the maximum intensity incident on the work-piece. At the top and bottom of the work-piece convection boundary conditions are applied as follows:

$$q = -H(T - T_0) \tag{3.50}$$

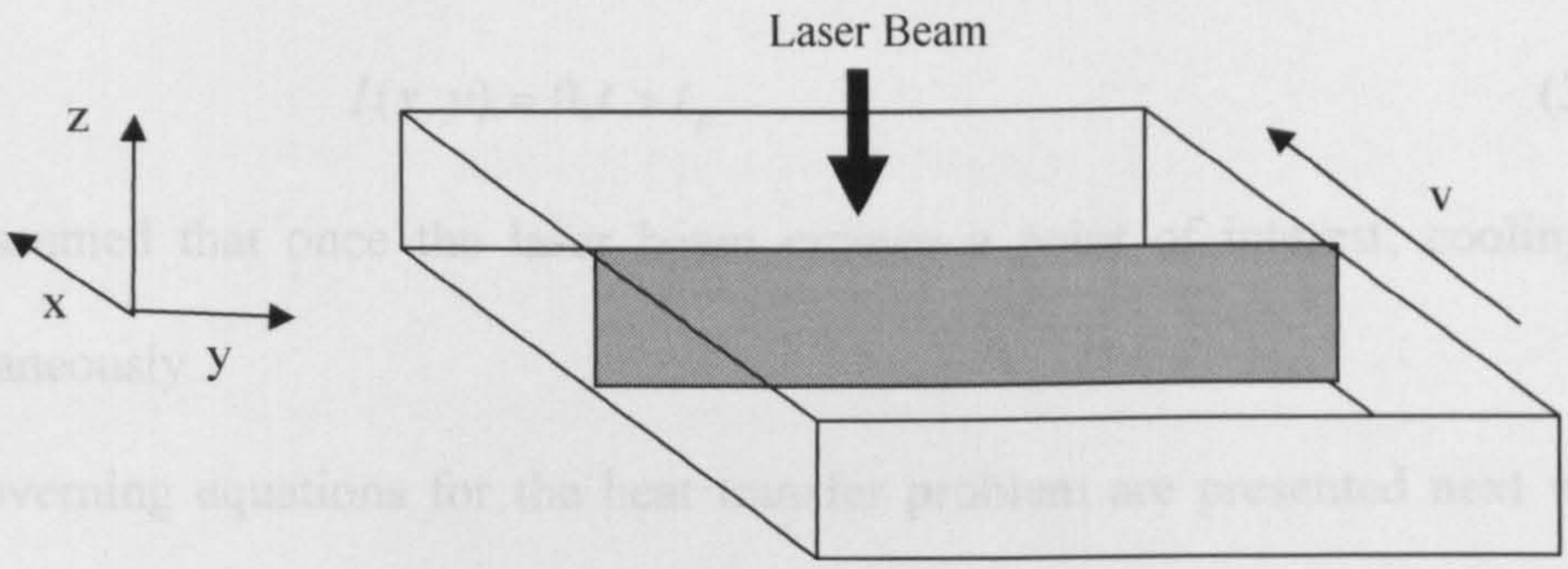

Figure 3.10 – Schematic of 3D workpiece with 2D area of interest highlighted

In the melt pool area,

$$q = AI(x,y) - \sigma\varepsilon(T^4 - T_0^4) - H(T - T_0) \tag{3.51}$$

where $q = -K\nabla T$, according to the Fourier law

T = Temperature

T_0 = Ambient temperature

T_b = Boiling temperature

h = heat transfer co-efficient

I = Intensity

A = absorption co-efficient

σ = Stefan Boltzmann's constant

ε = emmissivity

The Gaussian beam is represented by the following distribution:

$$I(x,y) = \frac{P}{\pi r_0^2}\exp(\frac{-2r^2}{r_0^2}) \tag{3.52}$$

$r^2 = x^2 + y^2$

r_0 = laser beam spot radius and is defined as the radius within which the intensity, I, does not vary by more than $1/e^2$ of its peak (central) value.

$$I(x,y) = 0, t > t_p \tag{3.53}$$

It is assumed that once the laser beam crosses a point of interest, cooling starts instantaneously

The governing equations for the heat transfer problem are presented next with the appropriate boundary conditions described previously.

The basic energy balance equation is given by (Hibbit, Karlsson ans Sorensen, 1998)

$$\int_S qdS + \int_V rdV = \int_V \rho \dot{U}\, dV \tag{3.55}$$

where S and V denote surface and control volume respectively

q = heat flux per unit area crossing surface S from environment to body

r = heat flux per unit volume generated within body

ρ = material mass density

$U(\theta)$ = internal energy per unit mass

$\dot{U}$ = material rate of change of U per time

$$q = -\underset{\sim}{q}.\underset{\sim}{n} \tag{3.56}$$

$\underset{\sim}{q}$ = heat flux vector

$\underset{\sim}{n}$ = unit outward normal to the surface

$\underset{\sim}{x}$ = displacement vector

$$\int_V \rho \dot{U}\, dV = -\int_S \underset{\sim}{q}.\underset{\sim}{n}\, dS + \int_V r dV \tag{3.57}$$

Substitute (3.56) into (3.57) and apply divergence theorem

$$\int_V \rho \dot{U}\, dV = -\int_V \frac{\partial}{\partial \underset{\sim}{x}}.\underset{\sim}{q}\, dV + \int_V r dV \tag{3.58}$$

This is the strong form of the thermal equilibrium that cannot be enforced numerically. Therefore a 'weak' form is required.

Multiply (3.58) by an arbitrary variational temperature,$\delta\theta$ and integrate over the volume

$$\int_V \rho \dot{U}\, \delta\theta dV = -\int_V \delta\theta \frac{\partial}{\partial \underset{\sim}{x}}.\underset{\sim}{q}\, dV + \int_V \delta\theta r dV \tag{3.60}$$

Applying the chain rule

$$\int_V \rho \dot{U}\, \delta\theta dV = \int_V -(\frac{\partial}{\partial x}.(\underset{\sim}{q}\, \delta\theta) + \underset{\sim}{q}.\frac{\partial \delta\theta}{\partial x})dV + \int_V \delta\theta r dV \tag{3.61}$$

Applying the divergence theorem and equation (3.56)

$$-\int_V \frac{\partial}{\partial \underset{\sim}{x}}.(\underset{\sim}{q}\, \delta\theta)dV = \int_S -\underset{\sim}{n}.\underset{\sim}{q}\, \delta\theta dS = \int_S q\, \delta\theta dS \tag{3.62}$$

$$\int_V \rho \dot{U}\, \delta\theta dV - \int_V \frac{\partial \delta\theta}{\partial \underset{\sim}{x}} . \underset{\sim}{q}\, dV = \int_S \delta\theta q dS + \int_V \delta\theta r dV \qquad (3.63)$$

This is the 'weak' form of the thermal energy balance equation that is discretized. Temperature-dependent values of thermal conductivity and specific heat capacity for mild steel were used for the ABAQUS simulation. The simulation was undertaken in order to investigate the LCW process for weldpool temperatures that are difficult to measure experimentally. Figure 3.11 shows the mesh used for the simulation and figures 3.12(i) - 3.12(iii) show weld zones from ABAQUS simulation results. The variation of penetration depth with spot radius obtained from the simulation is shown in figure 3.13. Figure 3.13 illustrates the results obtained when the maximum surface temperature was kept at boiling temperature and also when it was allowed to rise to above boiling temperature during the ABAQUS simulation. To keep the maximum temperature at the boiling temperature, the heat flux was adjusted accordingly within the user subroutine, DFLUX.

ABAQUS results indicated that when the maximum surface temperature was kept at boiling temperature, the penetration depth increased with increase in spot radius of the laser beam. The penetration depth decreased when the surface temperature decreased to below boiling temperature. The results also showed that after maximum penetration depth had been reached, points of all curves coincided irrespective of whether the intensity was restricted or not.

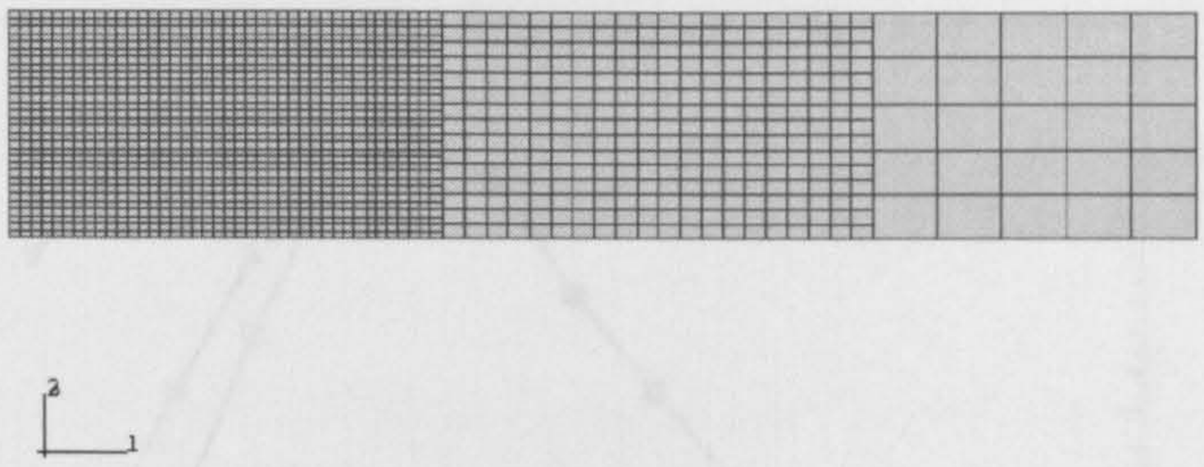

Figure 3.11 - Mesh used for ABAQUS numerical simulation

This result would suggest that maximum penetration depth may be achieved during LCW when the surface temperature is at boiling point of the material such that any further increase in spot radius (achieved by increasing the distance from the focus), would produce a decrease in the surface temperature.

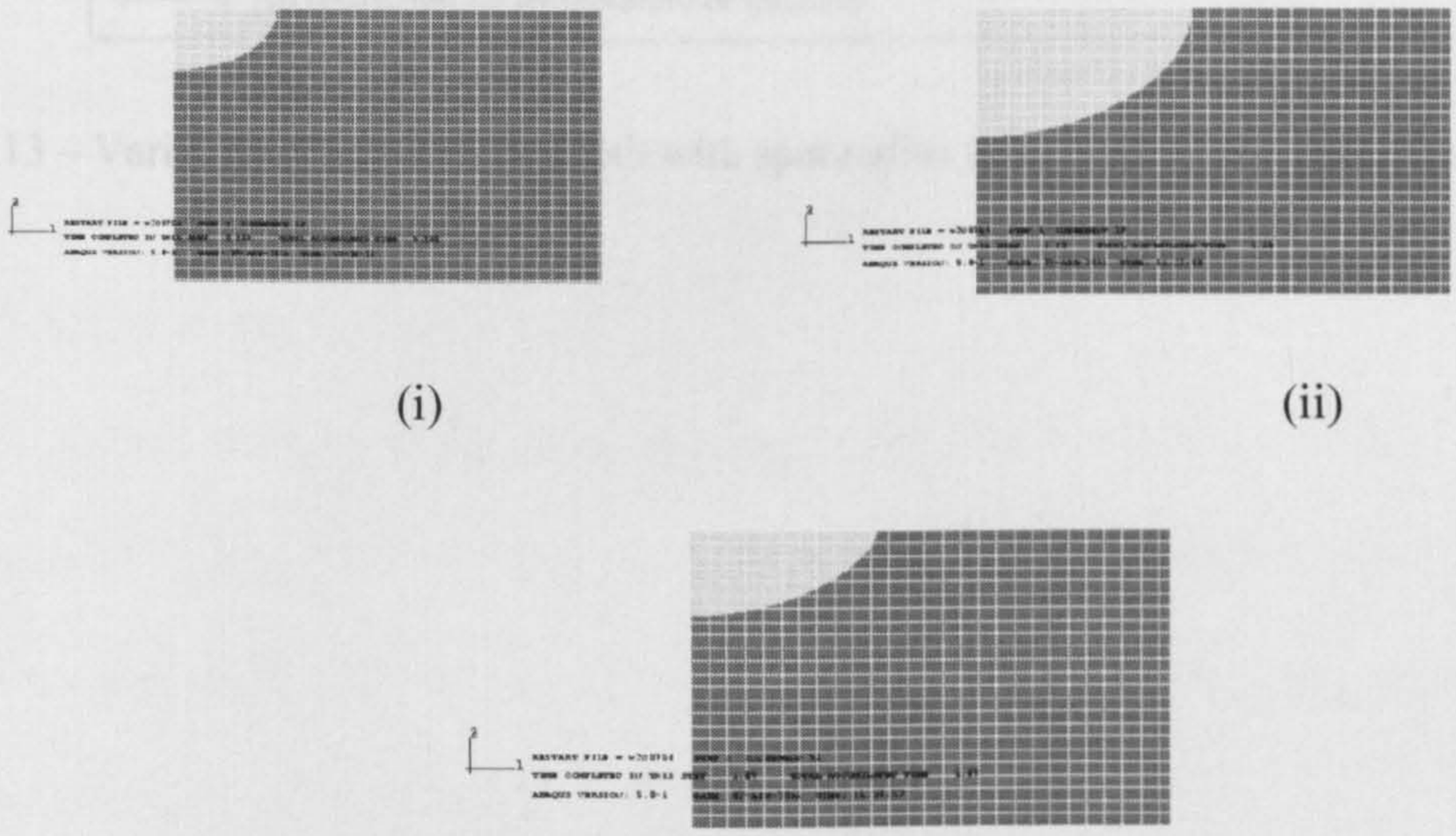

(i) (ii)

(iii)

Figure 3.12 - ABAQUS simulation result showing weldpool profiles for (i) spot radius equal to 0.294mm, (ii) spot radius equal to 0.805mm and (iii) spot radius equal to 1.331mm

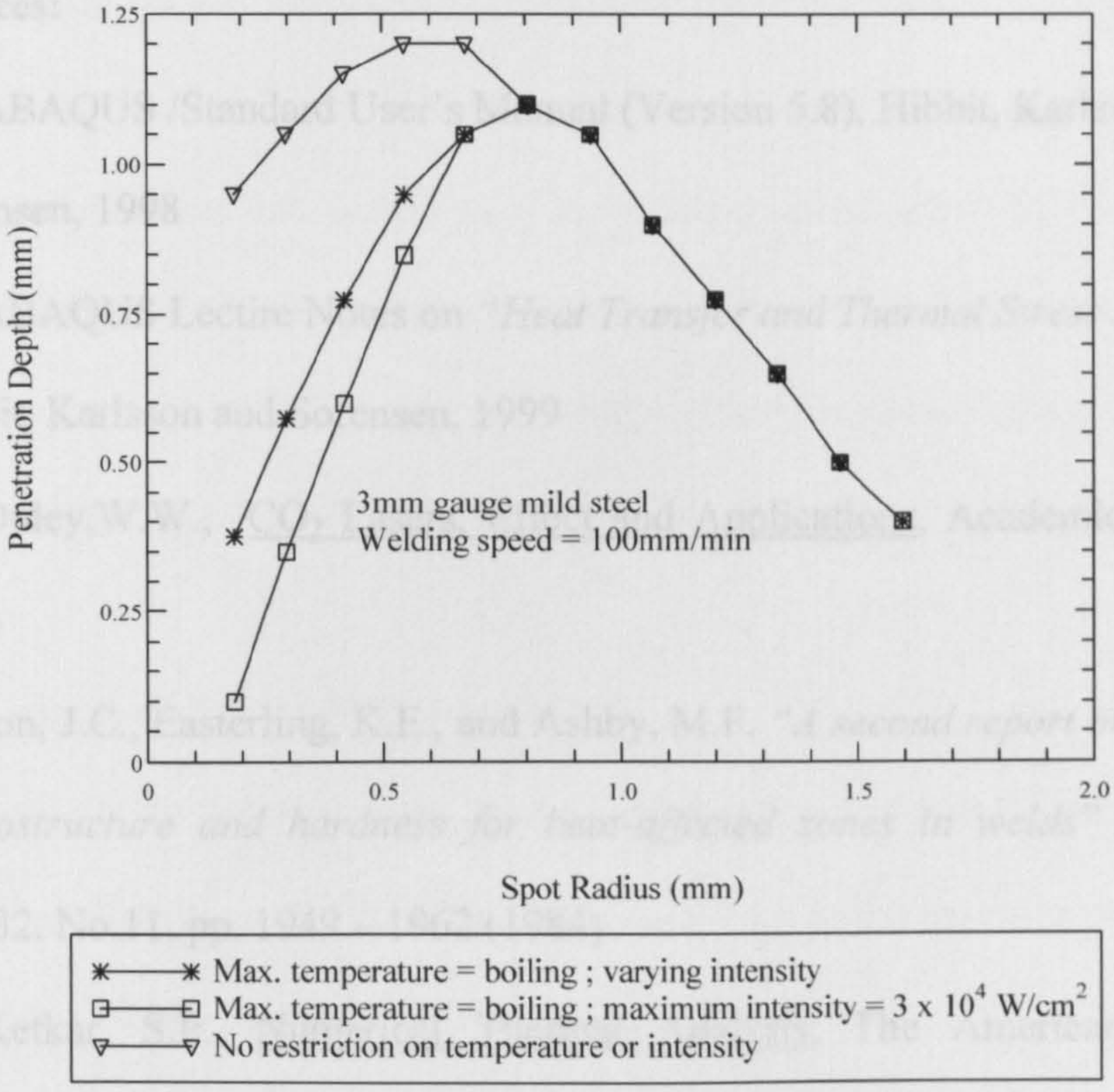

Figure 3.13 – Variation of penetration depth with spot radius from ABAQUS simulation

References:

- ABAQUS /Standard User's Manual (Version 5.8), Hibbit, Karlsson and Sorensen, 1998
- ABAQUS Lectire Notes on *"Heat Transfer and Thermal Stress Analysis"*, Hibbit, Karlsson and Sorensen, 1999
- Duley,W.W., CO_2 Lasers, Effect and Applications, Academic, New York, 1976
- Ion, J.C., Easterling, K.E., and Ashby, M.F. *"A second report on diagrams of microstructure and hardness for heat-affected zones in welds"* Acta Metall. Vol.32. No.11, pp. 1949 – 1962 (1984)
- Ketkar, S.P., Numerical Thermal Analysis, The American Society of Mechanical Engineers, New York, 1999
- Mackwood,A., IMI-CEMWAM Project Team 5 Final Report, Department of Physics, University of Essex, 1999
- Prokhorov,A.M. et al, Laser Heating of Metals, IOP Publishing, 1990
- Steen. W., Laser Material Processing, Springer-Verlag London Limited, 2003
- Versteeg, H.K. and Malalasekera, W., An Introduction to Computational Fluid Dynamics -The Finite Volume Method, Longman, 1998
- Wilson,J., Hawkes,J.F.B., Lasers, Prentice Hall, 1987

4. Experimental

The power of the laser beam is an important factor in the laser conduction welding process. Other factors that are essential are welding speed, gas flow rate, focal length of lens, jigging configuration, and distance of focus above the work piece (which determines the spot radius). In the following paragraphs, how these are combined to give the end results are discussed.

4.1. Laser Conduction Welding Set-Up

Two types of lasers were used for the laser conduction welding (LCW) experiments. The first laser used was a PRC/OPL CO_2 laser with a maximum power delivery of 1.8kW and a TEM_{01*} mode laser beam. Zinc Selenide lenses of focal length 127mm, 150mm and 254 mm were used to focus the laser beam. The PRC laser is a fast-axial flow, DC excited laser which can produce continuous wave, gated pulse, superpulse and hyperpulse operating modes.

This laser was used for the trial experiments on 2mm, 2.5mm and 3mm gauge mild steel. The workpiece which was mounted on an aluminium jig was moved relative to the laser beam using CNC programming. The CNC programs ensured that the welding speed and range of movement of the CNC table was controlled semi-automatically, given that each welding process was started by a manual operation which then activated the pres-set parameters of welding speed, stand-off distance, length of traverse and of course the points at which to open and close the laser cavity shutter. 127mm, 150mm (for mild steel) and 254mm focal length (for aluminium alloys) ZnSe lenses were employed for the purposes of focussing the laser beam onto the workpiece. 127 mm focal length ZnSe was used for the laser conduction welding of 3mm gauge mild steel because although the focused spot size was relatively small,

the defocused spot radii or diameters were greater for the 127mm lens than, say, for the 150mm lens. This is because, beyond the focus of a lens, the divergence of a laser beam passing through the lens is inversely proportional to its focal length. The average dimensions of the mild steel samples were 150mm by 80mm and the laser beam was directed along the centre of the sample lengthwise. The 254mm focal length lens was used for the welding of aluminium alloys due to its greater depth of focus which offered some protection of the optics against spatter and back reflections.

The other laser used was a Multi Wave-Auto^{TM} Lumonics AM356 continuous wave Nd:YAG laser that was utilised for the laser conduction welding of 3mm gauge aluminium alloys. The Nd:YAG laser was used because it produces laser beam of wavelength 1.06 microns which is more readily absorbed by aluminium than the 10.6 micron laser beam produced by a CO_2 laser. The maximum power that could be produced by the Nd:YAG laser was 3.5kW delivered by an fibre optic of diameter 600 microns. The beam exiting the fibre optic cable is divergent and is focused using a focus head mounted on the output end of the fibre optic cable. The focus head contains coated glass lenses, which first collimate and then focus the beam. A variety of standard lens combinations are available and the one used for the welding experiments produced a focused spot diameter of 0.48mm. This combination had a collimating lens of focal length 200mm and an objective focusing lens of focal length equal to 160mm. The workpiece was moved relative to the laser beam and fixturing was achieved using a copper base plate jig (see section 4.1.2). The shielding gas used was argon. To prevent spatter and fume from accumulating on the coverslide protecting the focusing lens, a high velocity, compressed air, cross jet was directed perpendicular to the beam path.

4.1.1. Mild Steel

Initially trial experiments were carried out on mild steel using the OPL/PRC CO_2 laser with a maximum laser power output of 1.8kW. Other parameters used for LCW experiments are shown below:

Parameter	Value
Laser Wavelength	10.6 microns (μm)
Lens Focal Length	127 mm, 150 mm, 254 mm
Average Laser Power	1800W
Traverse Speed	100mm/min – 175 mm/min
Laser Beam M^2	2.452
Laser Beam Mode	TEM_{01*}
Shielding Gas	Argon; 20l/min coaxial
Material	2mm, 2.5mm and 3mm gauge mild steel
Raw Beam Diameter	16.5mm
Distance from Focus (Standoff distance)	0 mm – 180 mm

Table 4.1 Parameters used during CO_2 laser conduction welding of mild steel

Theoretical spot sizes were calculated using the formula (Sun, 1998)

$$r_c = r_0\sqrt{1+(\frac{z\lambda M^2}{\pi r^2})^2} \qquad (4.1)$$

where

$$r_0 = \frac{2M^2F\lambda}{\pi D} \qquad (4.2)$$

r_c = calculated spot radius at distance z (mm)

D = raw laser beam diameter at lens (mm)

λ = Laser beam wavelength (mm)

F = focal length of lens (mm)

z = distance of focus from the workpiece (mm)

Laser burn prints obtained on Perspex indicated that the laser beam spot size increased with distance from the focus. Below is a graph (fig. 4.1) that shows the relationship between measured spot radii on Perspex and distance of focus from workpiece. A line of best fit is shown and from this line values for M^2 and focused spot radius were calculated as follows:

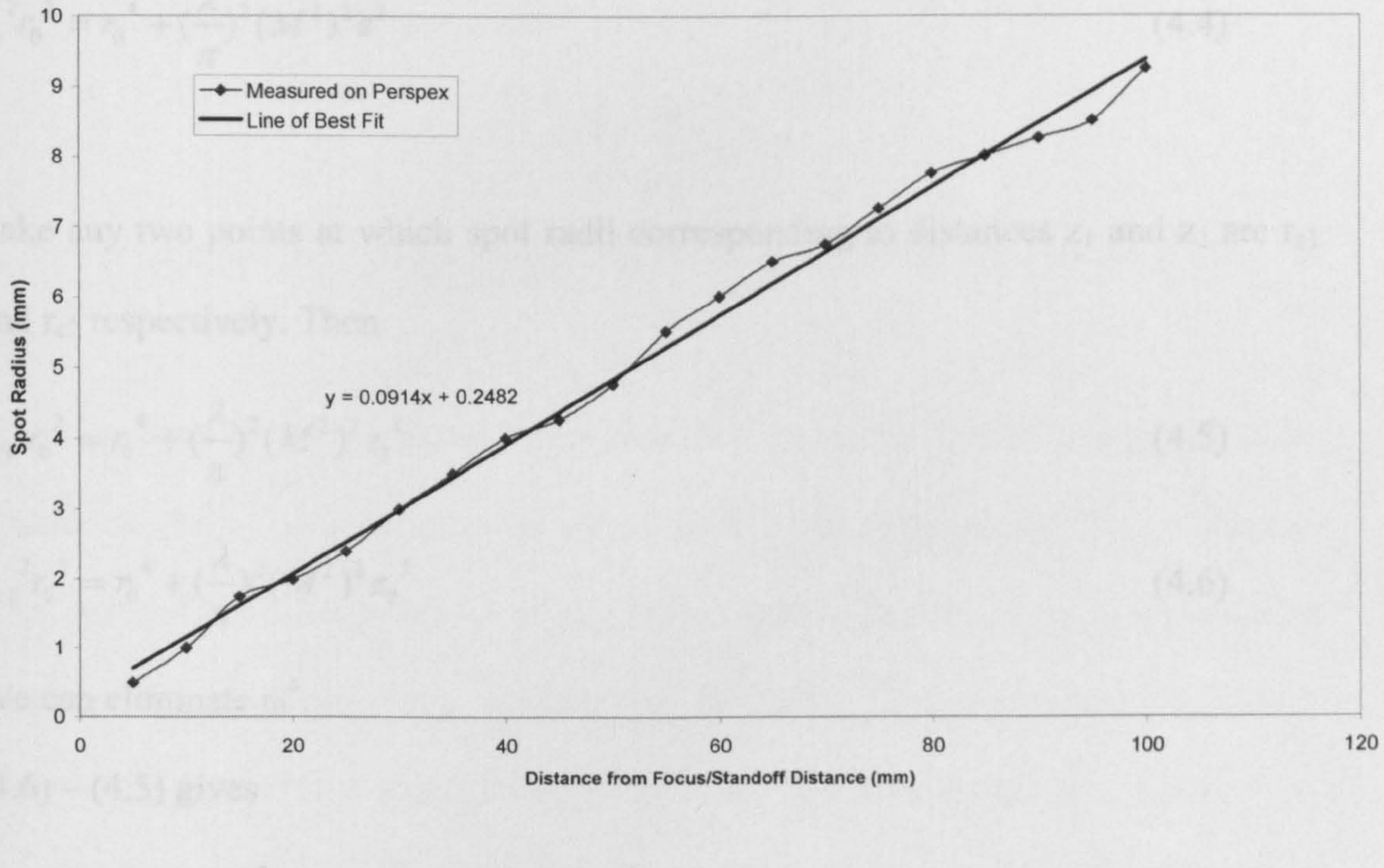

Figure 4.1 Relationship between distances from focus and measured spot radii on Perspex using a 127mm lens.

Diameters of CO_2 laser beams determined from Perspex have been found to give fairly accurate estimations of the real laser beam diameters (Miyamoto et al (1984) and Whitehouse, et al (1990)). Thus the diameters of CO_2 laser beam obtained on Perspex can be used as above to determine M^2.

It was found that there was a linear relationship between both measured spot radii and distances from the focus and the equation of the line of best fit was

$y = 0.0914x + 0.2482$.

From equation (4.1)

$$r_c^2 = r_0^2 + (\frac{M^2\lambda}{\pi r_0})^2 z^2 \qquad (4.3)$$

Multiplying equation (4.3) through by r_0^2, we have

$$r_c^2 r_0^2 = r_0^4 + (\frac{\lambda}{\pi})^2 (M^2)^2 z^2 \qquad (4.4)$$

Take any two points at which spot radii corresponding to distances z_1 and z_2 are r_{c1} and r_{c2} respectively. Then

$$r_{c1}^2 r_0^2 = r_0^4 + (\frac{\lambda}{\pi})^2 (M^2)^2 z_1^2 \qquad (4.5)$$

$$r_{c2}^2 r_0^2 = r_0^4 + (\frac{\lambda}{\pi})^2 (M^2)^2 z_2^2 \qquad (4.6)$$

We can eliminate r_0^4.

(4.6) – (4.5) gives

$$r_0^2 (r_{c2}^2 - r_{c1}^2) = (\frac{\lambda}{\pi})^2 (M^2)^2 (z_2^2 - z_1^2)$$

From this we obtain

$$r_0 = (\frac{\lambda}{\pi}) \sqrt{\frac{(z_2^2 - z_1^2)}{(r_{c2}^2 - r_{c1}^2)}} \quad (M^2) \qquad (4.7)$$

From values of r_c and z obtained from the line of best fit in figure 4.1, an average value of

$$(\frac{\lambda}{\pi})\sqrt{\frac{(z_2^{\,2}-z_1^{\,2})}{(r_{c2}^{\,2}-r_{c1}^{\,2})}}=0.036$$

$$\therefore r_0 = 0.036M^2 \qquad (4.8)$$

Equation of line of best fit from figure 4.1 is y = 0.0914x + 0.2482. The above equation means that at the focus (z = 0) the spot radius (r_0) = 0.2482. If this value of r_0 is put back into equation (4.8), $M^2 = 6.9$

$$\therefore r_0 = 0.2482 \; and \; M^2 = 6.9$$

The focused spot radius for other lenses namely 150mm and 254 mm were calculated using a linear proportion equation as follows:

$$r_l = \frac{0.2482}{127} x \; f_l$$

where r_l and f_l are focused spot radius and focal length of either 150mm or 254mm lens.

M^2 is a function of the laser beam diameter and laser beam divergence (LIA Handbook, 2001). It compares the actual laser beam divergence with a Gaussian laser beam of the same initial waist size (Steen, 2003), thereby giving a quantitative measure of laser beam mode quality. The M^2 factor is useful in analysing laser focusability and relates actual laser performance to an ideal standard, the lowest-order Gaussian mode, TEM_{00} (LIA Handbook, 2001).

Over 300 samples were welded in the trial experiments in order to test the hypothesis of using defocused laser beams for laser conduction welding.

After welding the samples were sectioned with a band saw and mounted with a Buehler Pneumet II mounting machine press machine. The hot mounting was

performed for about 15 minutes at a temperature of 100^0C. Each mount was ground using Struers Prepmatic polishing and grinding machine until the desired surface finish was achieved. The samples were then etched in Nital solution and in some cases ferric chloride solution. The etched samples were then examined under an optical microscope and from the micrographs produced measurements of the weld width and penetration depth were obtained. This could be done as the weld boundaries were clearly shown on the micrographs.

See Appendices for FORTRAN programme used for spot radii calculations.

4.1.2. Aluminium Alloys

The OPL/PRC CO_2 laser was used to weld 2mm AA5083 both in the keyhole welding mode and conduction welding mode using the 254mm lens. For aluminium welding the jig was tilted slightly so that along its length there was an angle between the base of the jig and the CNC table of 2^0. The aluminium alloy samples were mounted in the same way as the mild steel samples. However, the etchants used were different, namely sodium hydroxide solution and in some cases hydrogen fluoride-based solution.

Absorptivity of laser energy by aluminium posed a problem during laser conduction welding. Three options were tried (i) graphite coating (ii) laser-arc hybrid welding and (iii) sandblasting with aluminium oxide grit to enhance laser energy absorptivity.

(i) Graphite coating was administered by means of a spray can held at a distance from the workpiece. The use of graphite coating brought about an increase in absorptivity but the difficulty is producing an even spread of coating made

consistency very difficult. Furthermore, the weld quality was compromised due to the absorption of carbon in the weld pool. Carbon has the adverse effect of reducing the corrosion resistance of the weld. However interesting results were obtained.

(ii) The laser-arc hybrid process was utilized with the aim of providing some pre-heating during welding. The pre-heating produced by the TIG welder would then enhance absorptivity of the laser beam given that the temperature of the surface would have been raised to a much higher temperature than room temperature before the incidence of the laser beam. The distance between the arc and the laser beam (both focused and defocused) was varied between 5mm and 9mm. Any distance closer than 5mm resulted in the arc gas nozzle being overheated, which in turn shattered the ceramic gas nozzle. Synergic effects were observed with the laser-arc hybrid process.

A photograph of the laser-arc set-up is shown in figure 4.2. Figure 4.3 shows the cross section of the welding jig used for the experiments.

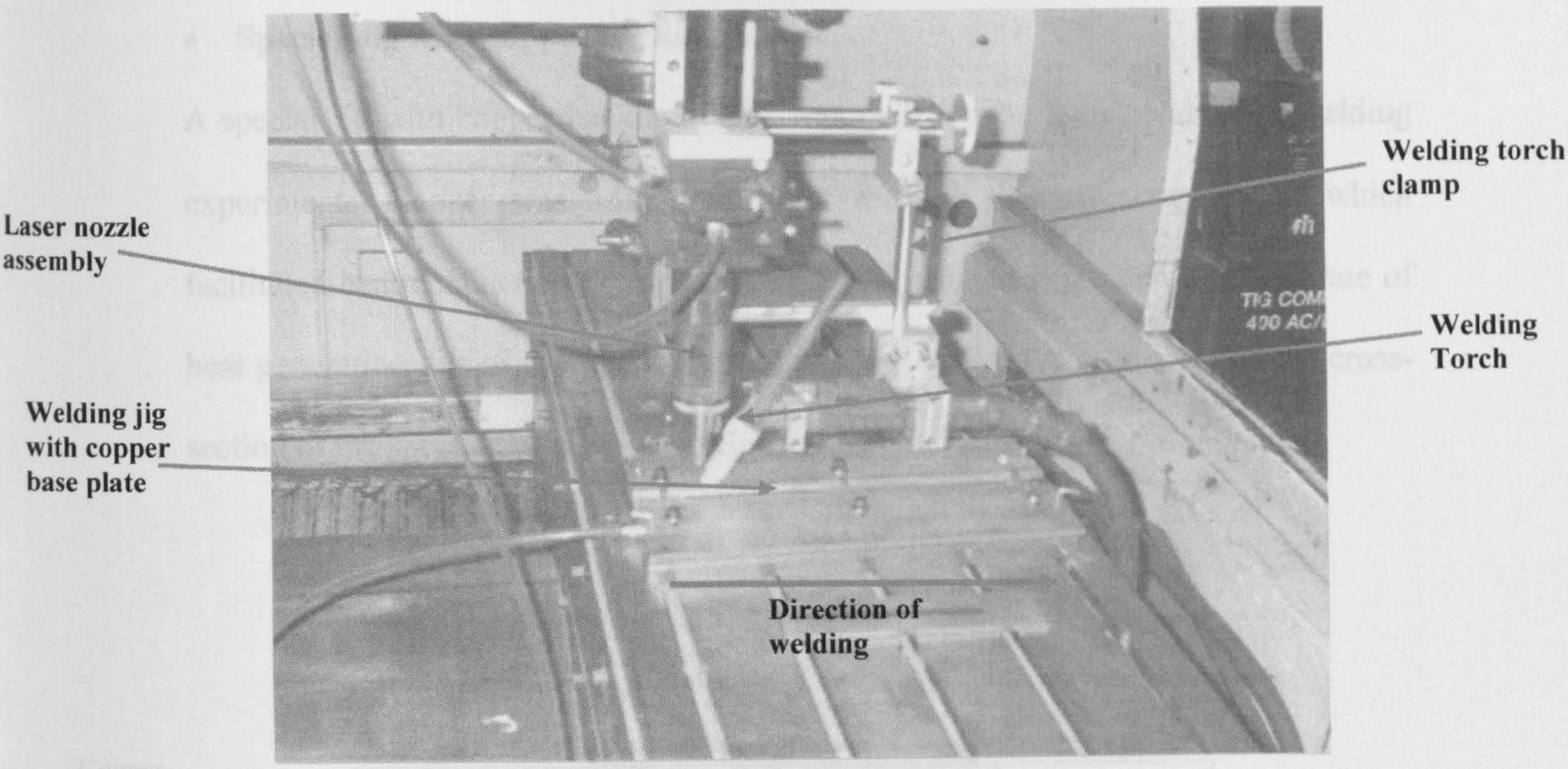

Figure 4.2 – Laser-Arc Setup

For the purposes of adjusting the position of the welding torch, a clamp was designed that allowed movement in the three orthogonal directions, x, y, and z. From figure 4.2, it can be seen that the welding torch was held at its natural angle of approximately 45^0 to the horizontal. The welding jig was fastened to the laser CNC table and the direction of welding is indicated an arrow in the diagram. The arc was initiated using the lift-off method initially and then finally the high frequency start method. In the former case the electrode was brought down to just touch the workpiece and then as soon as the electrode was lifted, the arc was initiated. The electrode-workpiece distance was approximately equal to the diameter of the electrode which in this case was 2.4mm. Zirconiated tungsten electrodes were used. Initially some time was spent in establishing some arc welding parameters for 3mm gauge AA5083 and chapter 5 contains results obtained from these trial experiments.

- **Special Jig with copper backing plates**

A special jig with copper backing plates was built for the laser conduction welding experiments. Copper was used because of its high thermal conductivity, which facilitated heat conduction from the welded samples that experienced a high rate of heat generation due to the relatively low welding speeds. A schematic of the cross-section of the special jig is shown in figure 4.3.

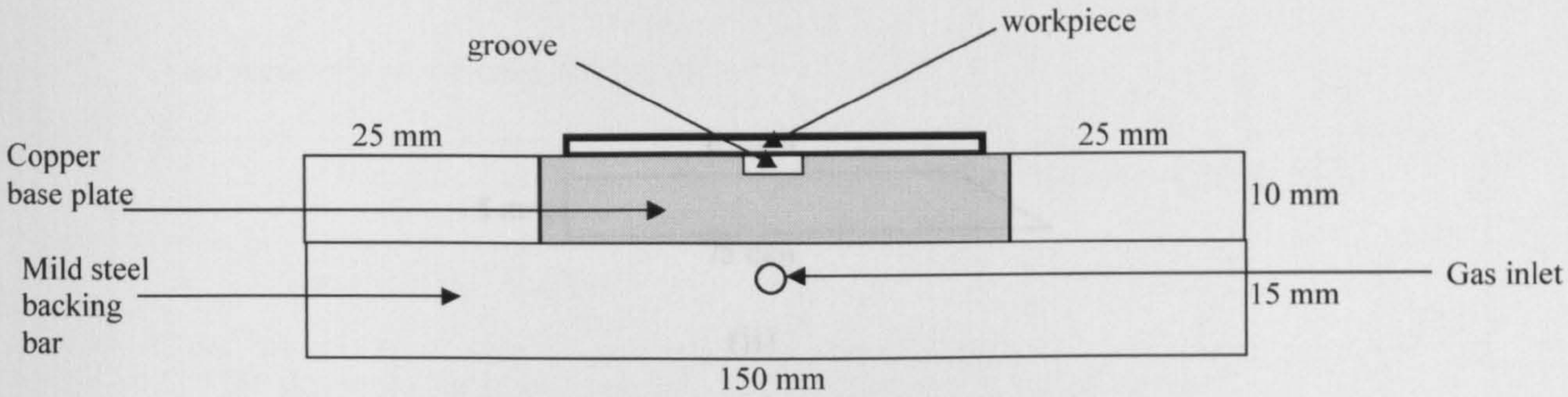

Figure 4.3 Schematic of copper-based welding jig

Figure 4.3 shows a cross-section of the jig without the clamps that are designed to hold the workpiece down on either side by virtue of screws. The copper base plate had little holes drilled into it so as to allow shielding gas put through the gas inlet to shield the bottom surface of the workpiece. The groove was about 12mm wide and about 1 mm deep.

A view of the copper base plate is shown below.

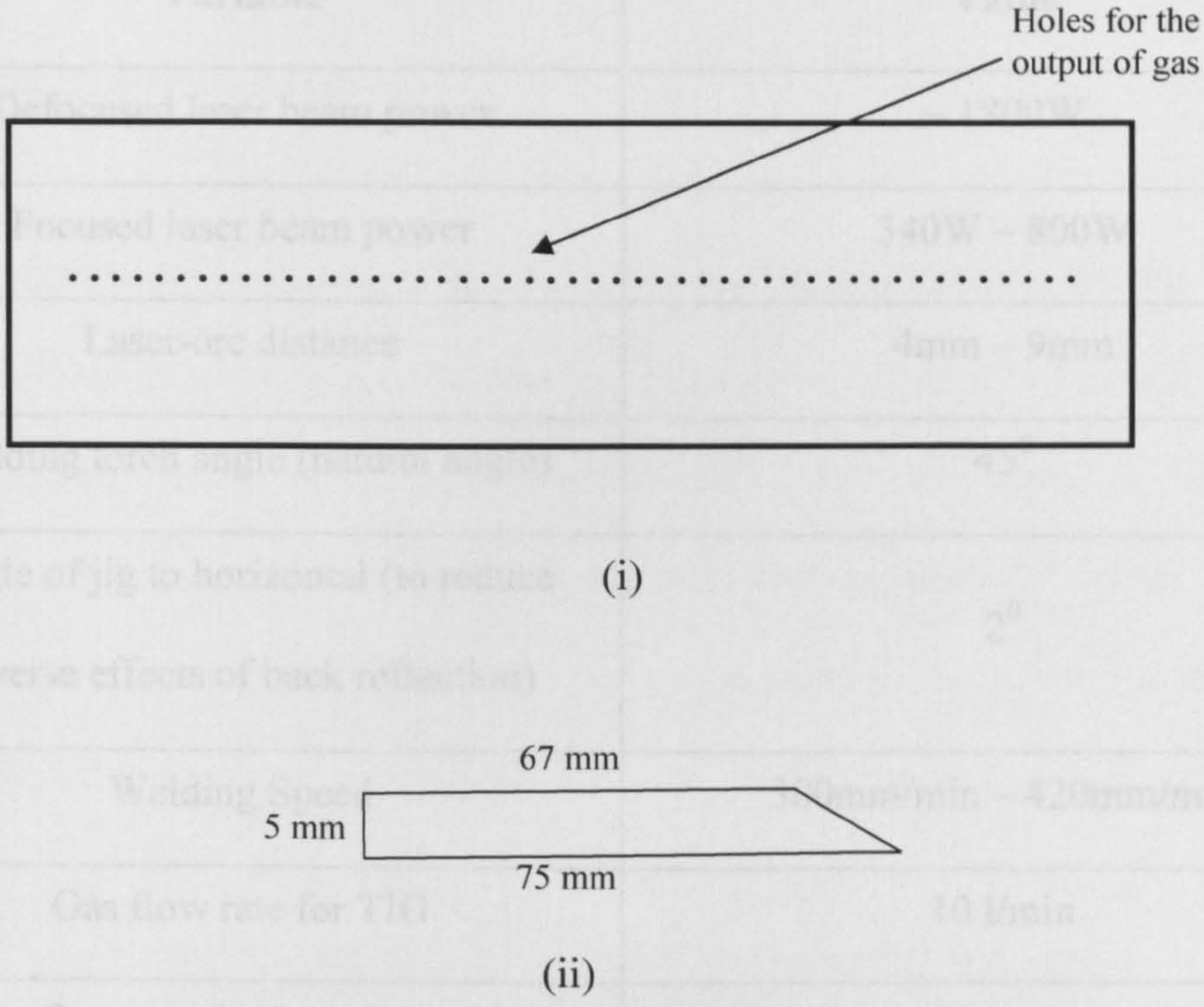

Figure 4.4 (i) View of copper base plate (ii) cross-section of the left clamp used for the jig.

The arc (TIG) welding equipment was a Migatronic 400 AC/ DC.

Figure 4.5– Migatronic 400AC/DC TIG Welder

Parameters used for the laser-arc (TIG) hybrid process are as shown below:

Variable	**Value**
Defocused laser beam power	~ 1800W
Focused laser beam power	340W – 800W
Laser-arc distance	4mm – 9mm
Welding torch angle (natural angle)	45^0
Angle of jig to horizontal (to reduce adverse effects of back reflection)	2^0
Welding Speed	300mm/min – 420mm/min
Gas flow rate for TIG	10 l/min
Gas flow rate for laser (coaxial)	10 l/min
Gas flow rate for bottom surface of workpiece	3 l/min
Electrode stick-out	6.5mm

Table 4.2 Parameters used during laser-arc welding of aluminium alloys

Figure 4.5 shows the TIG welding machine (Migatronic 400 AC/DC) used for the laser-arc welding experiments.

(iii) Sandblasting was carried out using aluminium oxide grit. This had the advantage of not only roughening up the surface of the sample but also increasing the effective surface area available for the incident laser beam. Sandblasting proved to be the most effective absorption enhancing technique

for laser conduction welding with a defocused beam in the case of aluminium alloys. The inconsistencies of the laser-arc process were avoided with the sandblasting option.

The sandblasted samples were used mainly, but not exclusively, for the Nd:YAG laser conduction welding experiments and below are photographs that show the set-up for this part of the experiments. The Nd:YAG had the advantage of the use of a robotic arm that gave it not only linear but rotational degrees of freedom. The fibre optic was attached to the robotic arm making it possible to deliver the laser beam energy in quite a number of positions.

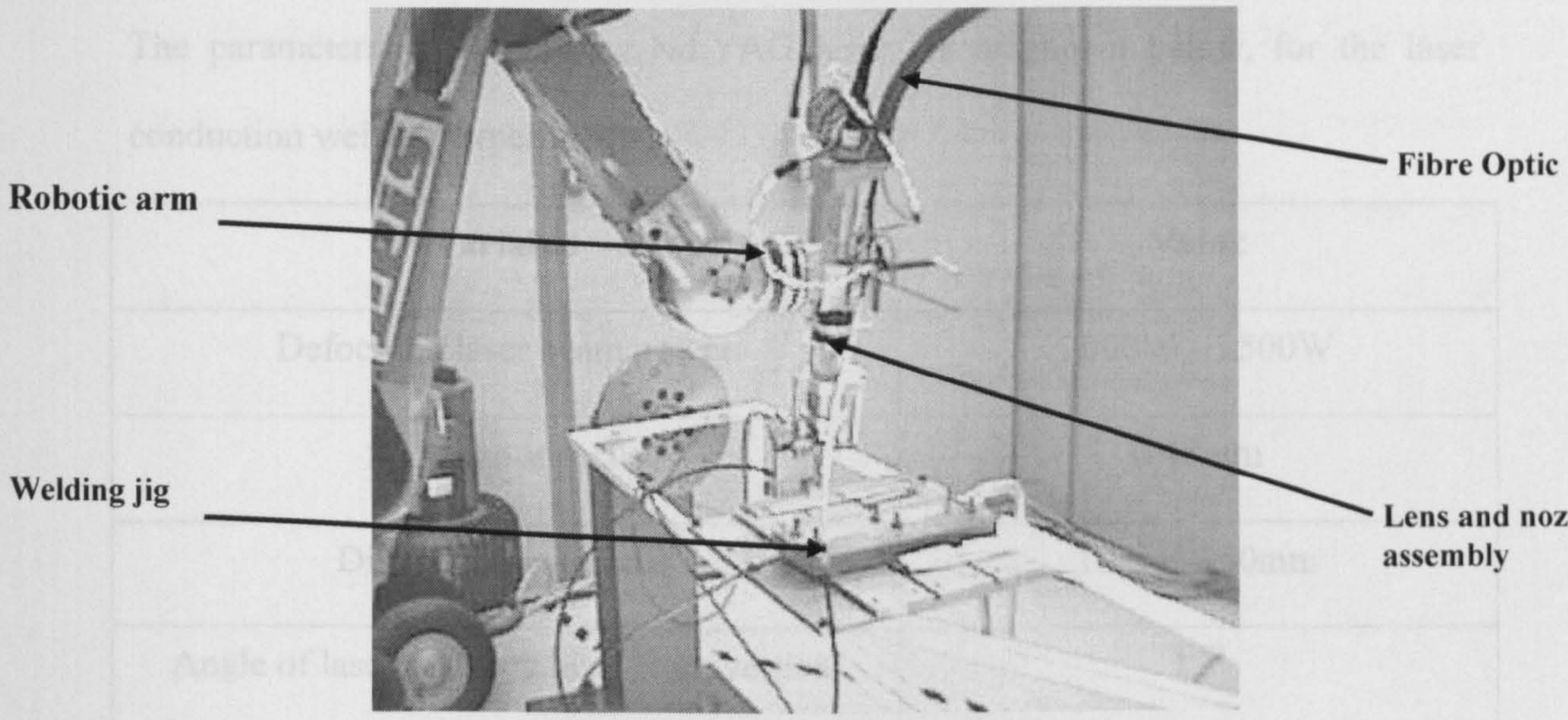

Figure 4.6 – Nd:YAG laser delivery system with robotic arm

The Nd:YAG laser delivery is as shown in figure 4.6. The lens nozzle assembly was tilted at an angle of 12^0 to the vertical sideways to the direction of translation.

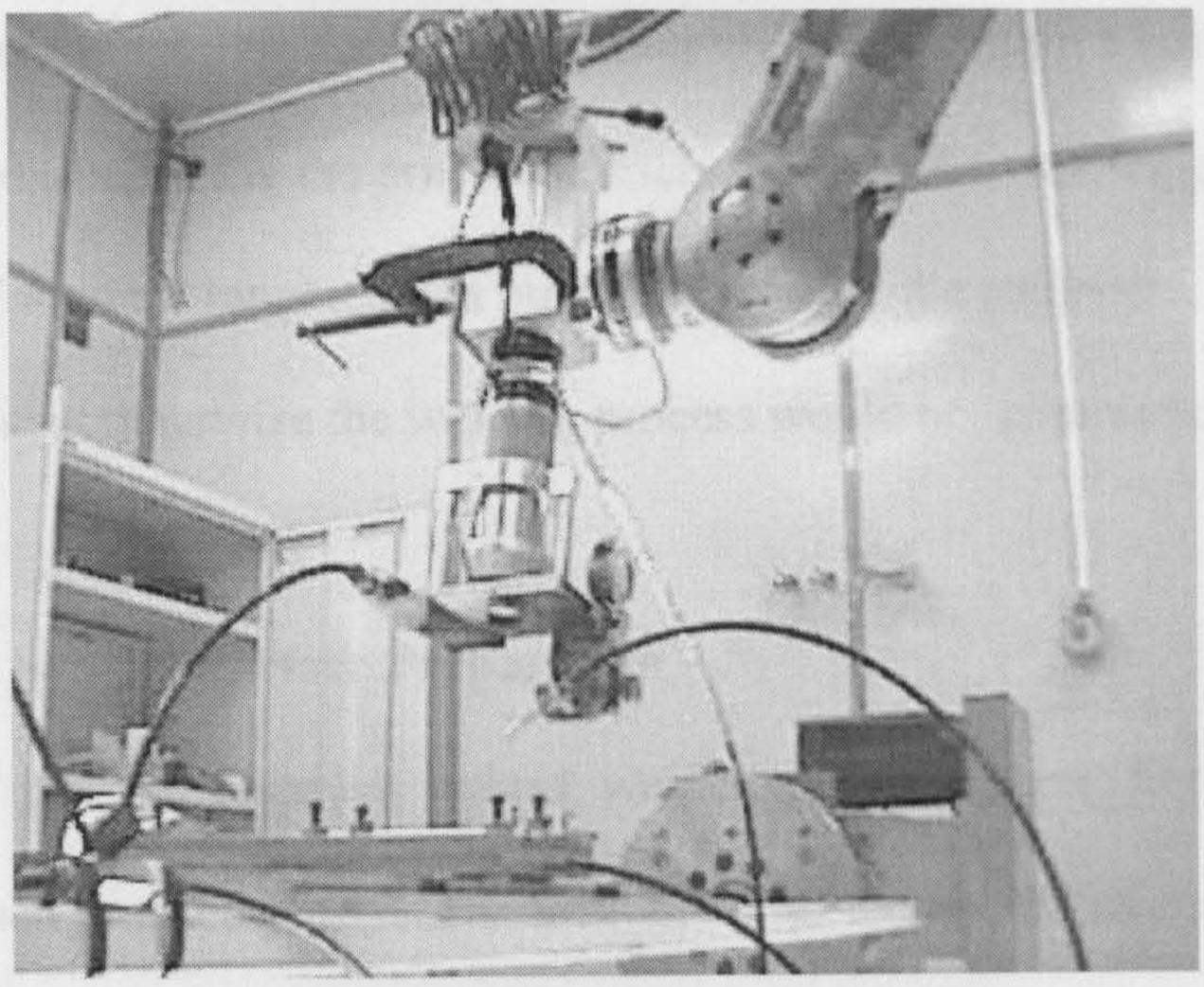

Figure 4.7 – Nd:YAG laser delivery system with robotic arm viewed from a different angle

Figure 4.7 gives different view of the Nd:YAG laser set-up.

The parameters used with the Nd:YAG laser are as shown below, for the laser conduction welding experiments.

Variable	**Value**
Defocused laser beam power	2000W – 2500W
Spot size at focus	0.48mm
Distance above focus	10mm – 50mm
Angle of laser focusing head from vertical	12^0
Welding Speed	600mm/min – 720mm/min
Gas flow rate	10 l/min
Gas flow rate for bottom surface of base plate	5 l/min

Table 4.3 Parameters used during Nd:YAG laser conduction welding of aluminium alloys

In order to ensure safety, the Nd:YAG welding took place within a built-up enclosure which remained shut during the process. Observations of the welding process could be via a CCTV monitor mounted just outside the door o the enclosure. The door had to be properly shut otherwise the welding process would not commence.

4.2. Sample Surface Preparation

Samples used for the laser-arc hybrid welding process were first cleaned with acetone and then brushed with a steel wire brush to reduce the thickness of the thin oxide layer that forms a corrosion-resistant covering for aluminium. After the brushing, the samples were once again cleaned with acetone and welding took place within 10 minutes of surface cleaning.

Samples that were welded using the Nd:YAG laser were sandblasted with aluminium oxide grit without necessarily brushing them first. The sandblasting not only roughened the surface of the samples but also simultaneously removed the tenacious oxide layer. The sandblasted surface had a dull matt finish. Samples were cleaned with acetone after sandblasting.

4.3. Laser Absorptivity/Reflectance Measurements

Absorptivity and reflectance tests were carried out for the sample surfaces encountered during the laser conduction welding experiments. These surfaces as mentioned earlier were

(i) As-received surface

(ii) Brushed surface

(iii) Sandblasted surface

Approximate absorptivity values were calculated for the above surfaces using small rectangular samples of 2mm AA5083. One of the reasons for embarking on this approximate calculation was to find the relative absorptivity for all surfaces. It was expected that results obtained would give an indication as to whether the sandblasted surface was a better one in terms of absorptivity.

The rectangular pieces were weighed and then with thermocouples attached to them, they were irradiated with a defocused CO_2 laser beam from the OPL/PRC laser. From basic heat conduction principles, and assuming that heat losses during the heating and cooling cycles are equal, the absorptivity is given by the equation

$$A = \frac{mc_p}{P_{inc}}[\frac{dT_h}{dt} - \frac{dT_c}{dt}] \qquad (4.9)$$

m = mass of sample

c_p = Specific heat capacity of material

P_{inc} = Incident power

$\frac{dT_h}{dt}$ = Heating rate

$\frac{dT_h}{dt}$ = Cooling rate

The heating and cooling rates were obtained from the slopes of temperature/time curves obtained from thermocouple readings. The heating rate is the slope of the rising part of the temperature curve while the cooling rate is the slope of the falling part of the temperature curve. Results obtained are given in Chapter 5.

Reflectance measurements were made using similar samples at National Physical Laboratory, London. Results were obtained for specular reflectance excluded (SCE) and specular reflectance included (SCI). Specular reflectance is the reflectance of a beam of radiant energy at an angle equal but opposite to the incident angle, i.e. mirror-like reflectance.

SCI therefore measures total reflectance from a surface, while SCE excludes the specular reflectance from the measurement. A 1064nm wavelength radiation was used for the purposes of reflectance measurements and four different surfaces were used namely (i) as-received (ii) sandblasted (iii) brushed and (iv) brushed and sandblasted. Results are shown in chapter 5.

4.4. Surface Profile Measurements

Surface profile measurements were carried out for the different sample surfaces at National University of Ireland, Galway. The technique used for this measurement is scanning white-light interferometry. The scanning white-light interferometer (Newview 100) provides surface topography and film thickness measurements to an accuracy of 0.1nm. The surface profiler has a variable field of view from 6 x 4.5 mm down to 0.18 x 0.14 mm. It has a vertical range of 100μm and it can measure roughnesses and step-heights in the range of 0.1nm up to 10's of microns. White light is split in a spectral interference microscope objective, where part of the light travels to a spot on the sample of interest and the remainder is directed to a reference mirror. When the two parts recombine, bright and dark lines or, interference fringes, appear at the point of focus. A piezoelectric stack moves the objective in the vertical direction through a scan of 5 and 100μm. Fourier transform algorithms convert the recorded data into surface topography information which is graphically displayed.

The profiles and surface roughness measurements obtained indicated that the sandblasted surface had the largest surface roughness values.

Optical microscope observations were carried out on the as-received and sandblasted surfaces in order to ascertain visually what alterations, if any, had been made on the sample surfaces as a result of sandblasting. The results obtained showed on a larger scale what was obtained from the interferometer measurements.

Scanning Electron Microscope (SEM) analysis of the sandblasted sample surface was made in order to verify whether some foreign body or other element had been deposited with the surface layer of the sample as to affect its absorptivity characteristics.

The scanning electron microscope has an electron gun that produces an electron beam of energy up to 40 keV. For the SEM experiments in this work, electron beams of energy equal to 25keV were utilised. Several electromagnetic lenses then focus a fine beam (~ 2nm in diameter) on to the specimen. The electron beam is scanned across the specimen by scan coils while a detector measures the radiation emitted from the specimen. At the same time the spot at the cathode ray tube (CRT) is scanned across the screen, while the amplified current from the detector modulates the brightness of the spot. In this way a picture of the variation of the detector signal across the specimen is built up (University of Liverpool, 1998).

Results indicate that the chemical composition of the sample remained unchanged.

Results are shown in chapter 5.

4.5. Tensile Strength Tests

Tensile strength tests were carried out on suitably shaped specimens on an Instron machine using a strain rate of 0.001mm/s and a crosshead speed of 4.5mm/s. The shape of the specimens is shown below in figure 4.8.

On the Instron machine, the specimen to be tested is clamped at its two ends by two grips. The upper grip is fixed although its vertical position can be adjusted so as to accommodate specimens of different sizes. A powerful hydraulic actuator drives the lower grip. Once the specimen has been attached to the grips, the vertical movement of the lower grip generates the desired loading of the specimen.

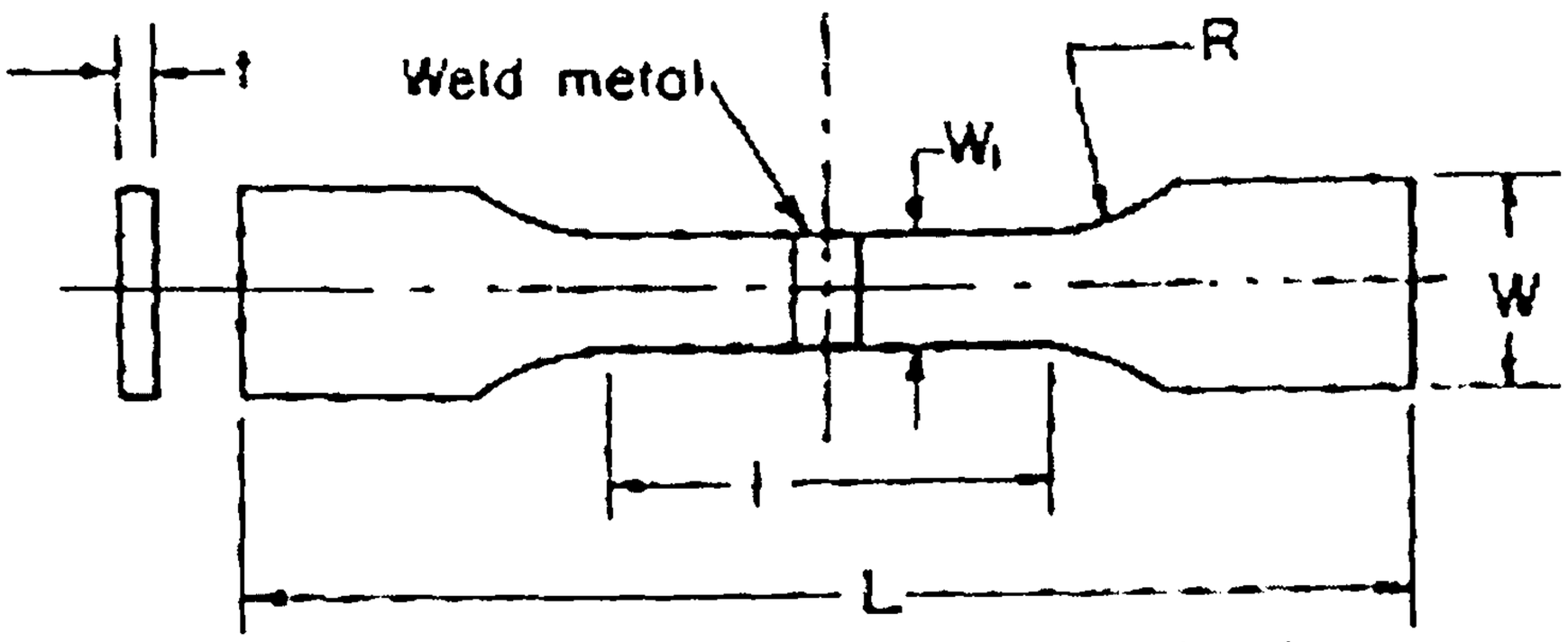

Figure 4.8 Shape for tensile strength testing

Dimensions used for both mild steel and aluminium are shown in table

	W_1 (mm)	W (mm)	t (mm)	l (mm)	L (mm)
Mild Steel	20	49	1.5	75	200
	18	49	2	75	200
Aluminium Alloys	12	24	2	75	200
	24	35	3	80	200

Table 4.4 Dimensions of samples used for tensile strength tests

4.6 Other considerations

In the case of laser conduction butt-welding, the edges of the samples used in the welding joint, were first of all milled and then brushed prior to welding. Stainless steel brushes were used in an attempt to reduce the aluminium oxide coating that could adversely affect the quality of the joint, given the difference in the melting temperatures of the oxide and the aluminium alloy. In some cases the brushing produced very small gaps along the weld line/joint but the defocused laser beam took care of that very adequately. While it is advisable to get the workpiece edges as close together as possible in the case of a butt-weld, this requirement is not as critical as in the case of keyhole welding which would not take place if there exists any gap wider that the laser beam spot size.

In the case of the laser-arc trial experiments, the welding sample surfaces had to be cleaned with acetone or methanol and then brushed before finally cleaned. Welding had to take place within ten minutes of the cleaning and brushing. For the laser conduction welding experiments the samples were cleaned and then sandblasted. There was no need for brushing since the sandblasting got rid of the tenacious oxide layer as well as increasing the absorptivity of the sample.

References:

- Miyamoto, I., Maruo, H., Arata, Y., *'Intensity Profile Measurement of Focussed CO_2 Laser Beam using PMMA'*, ICALEO, Vol. 44, pp. 313 – 320, 1984
- Whitehouse, D. R., and Nilsen, C. J., *'Plastic Burn Analysis (PBA) for CO_2 Laser Beam Diagnostics ', '* ICALEO, pp. 14 - 27, 1990

5. Results

This chapter contains results obtained from

(i) Laser conduction welding (LCW) trials of 2mm, 2.5mm and 3mm mild steel using CO_2 laser.

(ii) LCW trials of 3mm AA2014 using a CO_2 laser

(iii) Laser-arc welding results for 3mm AA5083

(iv) LCW of 2mm sandblasted AA5083 using CO_2 laser

(v) LCW of 3mm sandblasted AA5083 using Nd:YAG laser

(vi) Tensile strength tests results of 2mm and 3mm mild steel welds and also 2mm and 3mm AA5083, AA2024 and AA6061 welds.

(vii) Surface roughness analysis of sandblasted, brushed and as-received AA5083 samples

(viii) Absorptivity and reflectivity tests of sandblasted, brushed and as-received aluminium alloy AA5083

(ix) SEM analysis of sandblasted surface of AA5083

5.1. Welding trials using mild steel

Below are graphs that show the variation of penetration depth with spot radius which was varied by varying the distance of the laser beam focus to the workpiece.

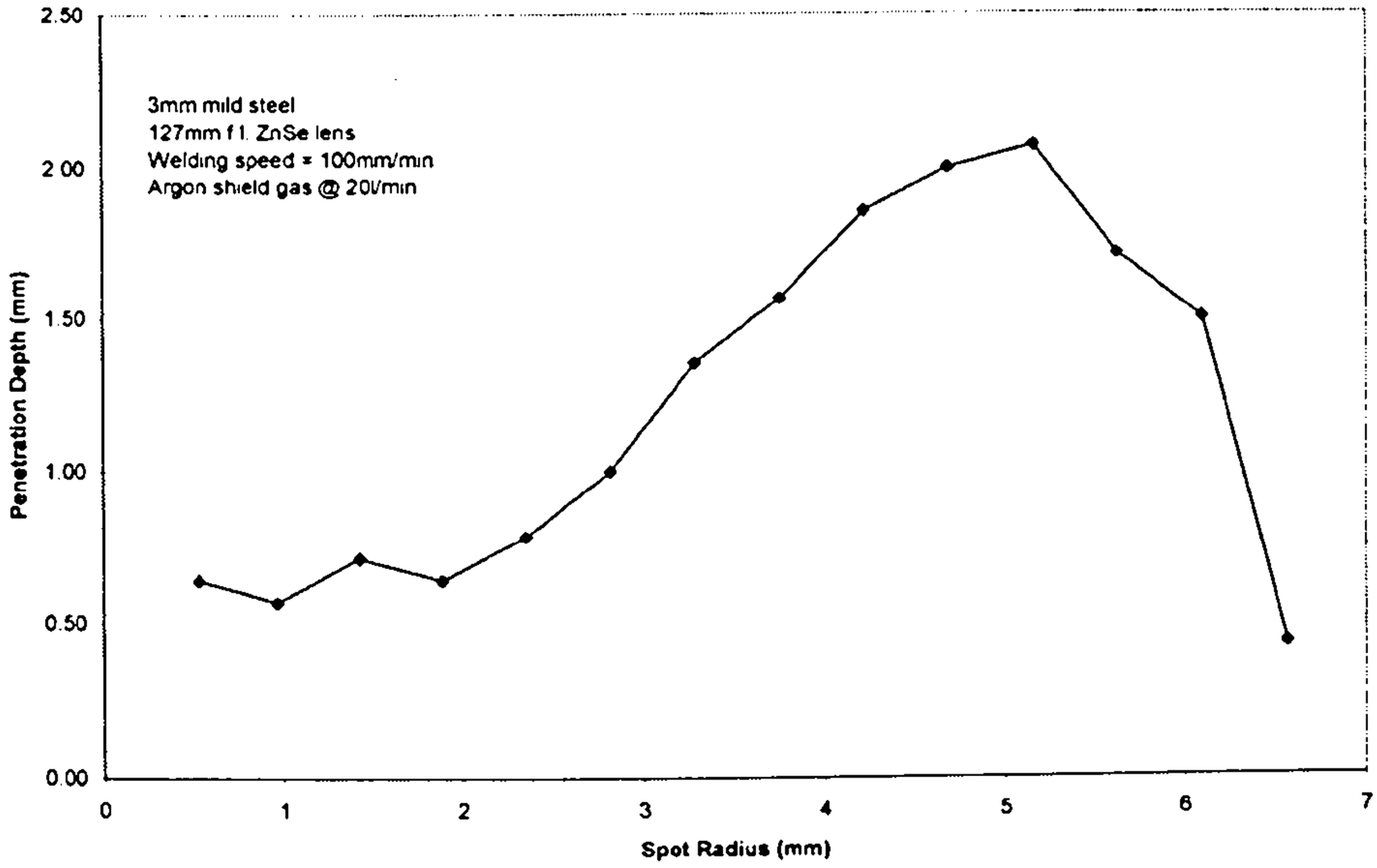

Figure 5.1 Graph showing penetration depth against spot radius from focus for 3mm gauge mild steel.

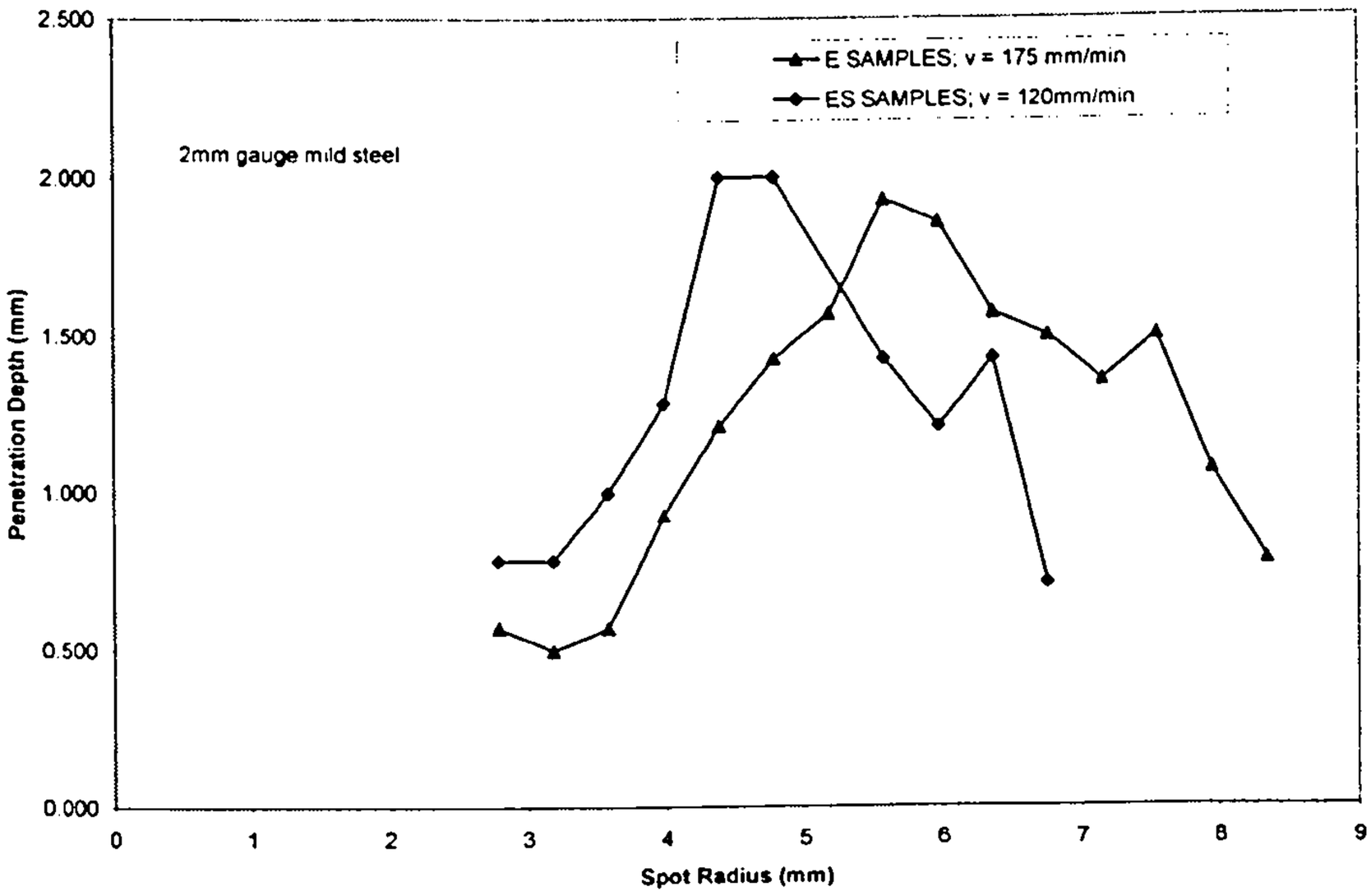

Figure 5.2 Graph showing penetration depth against spot radius from focus for 2mm gauge mild steel

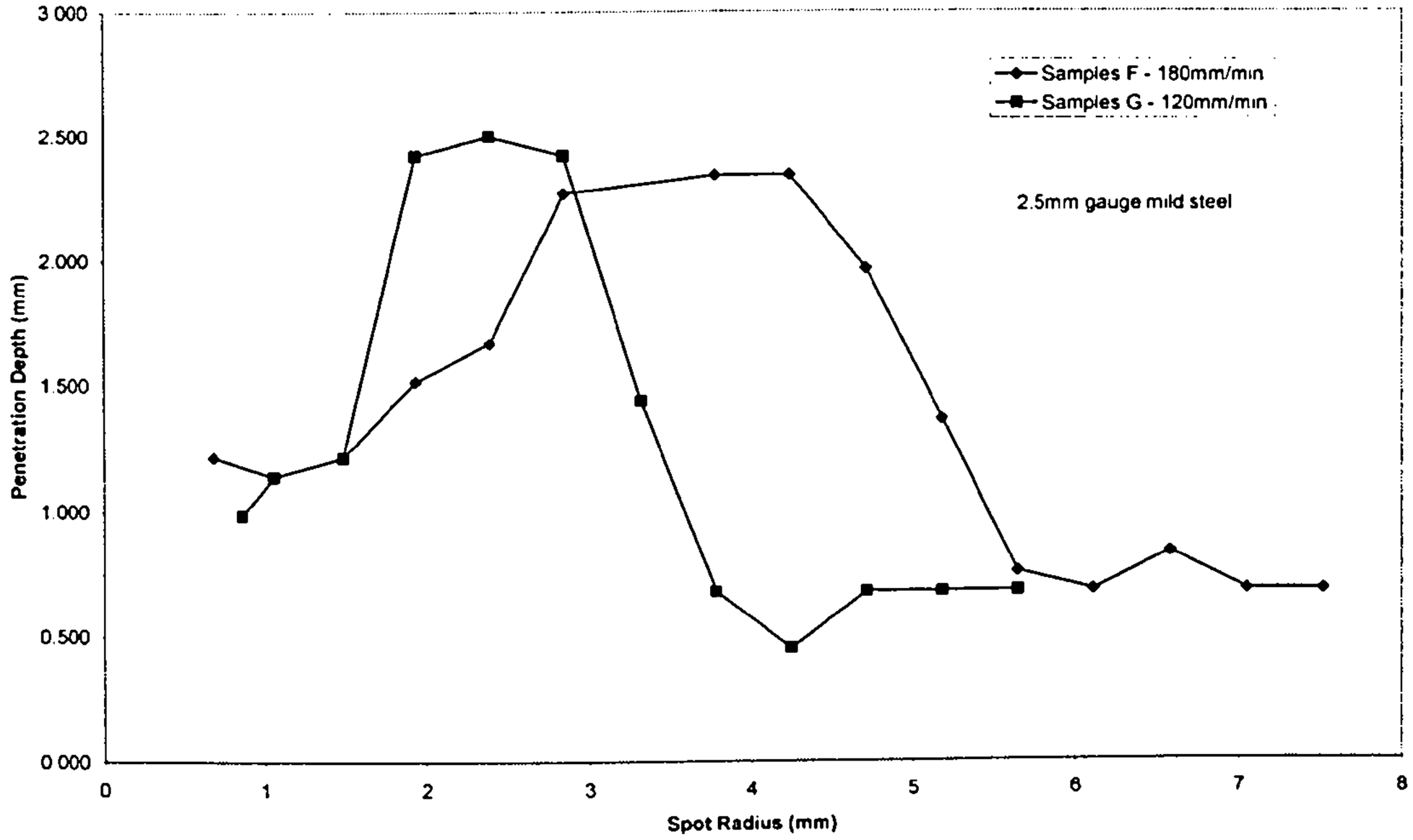

Figure 5.3 Graph showing penetration depth against spot radius for 3mm gauge mild steel

The graphs in figures 5.1 – 5.3 reveal a phenomenon for 2mm, 2.5mm and 3mm gauge mild steel and that is, during laser conduction welding using a defocused CO_2 laser beam, penetration depth increased up to a maximum and then decreased with distance from the focus. The trial experiments on mild steel showed that there was an optimum spot radius that produced maximum penetration during laser conduction welding with a defocused laser beam.

The curves for mild steel showed that the point of maximum penetration shifted to the right with an increase in welding speed. This is because as the welding speed increases more time is required to produce the amount of heat on the workpiece that will produce the maximum penetration depth. That increase in interaction time is reflected in an increase in spot radius and therefore a shift to the right. This phenomenon is peculiar to mild steel due to its material properties.

5.2. Welding trials using graphite-coated AA2014

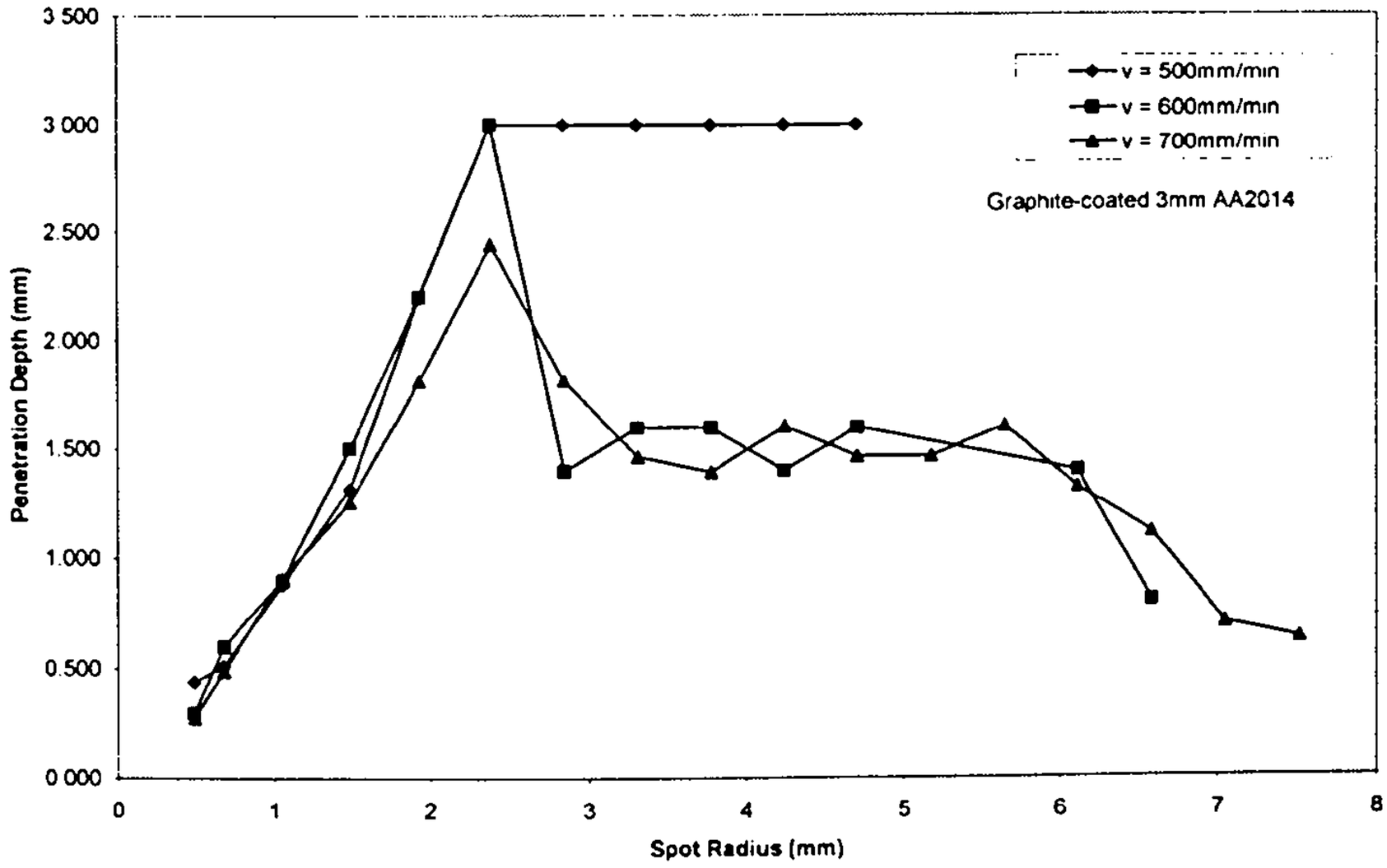

Figure 5.4 Graph showing penetration depth against distance from focus for graphite-coated 3mm AA2014

Figure 5.4 shows the variation of penetration depth with spot radius for 3mm gauge graphite-coated AA2014. Once again the same phenomenon was observed with AA2014. The detrimental effects of graphite, which included carbon absorption in the weld, rendered the use of graphite on aluminium unacceptable. On the graph the lines for both welding speeds seem to intertwine, a phenomenon that may be the result of uneven graphite coating spread that produced a non-uniform heating effect on the aluminium.

5.3. Laser-arc welding results

Results obtained using the TIG welder alone on 3mm gauge AA5083 indicate that, as expected, for constant arc currents penetration depth decreases with an increase in welding speed (figure 5.5).

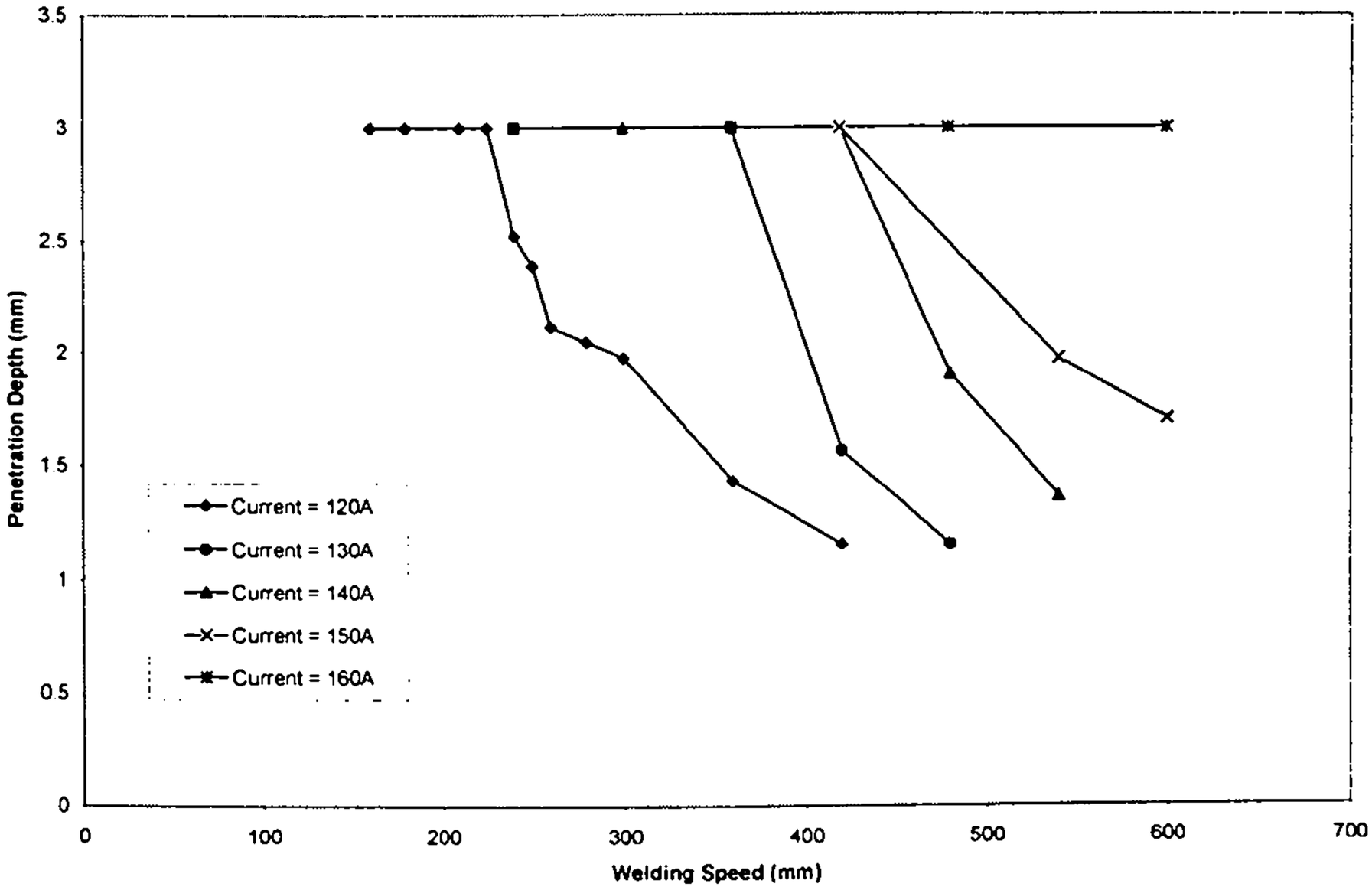

Figure 5.5 Graph showing variation of penetration depth with welding speed for TIG welded AA5083 at different arc currents and welding speeds

The laser-arc welding graphs in figures 5.6 and 5.7 show that the combination of the laser and arc gives rise to synergy, which increases the penetration depth of the welds. For example in figure 5.6 the penetration depth of the aluminium welds increased when the laser-arc (TIG) hybrid process was utilised, e.g. at a welding speed of 360mm/min and arc current of 130A, the penetration depth increased from approximately 2.2mm when TIG welded to 2.6mm when the laser-arc combination was used. The graph also shows that arc current and welding speeds influence penetration depth. Normally an increase in arc current at constant welding speed would increase the penetration depth, but an increase in arc current coupled with an increase in welding speed may cause the penetration depth to decrease as shown on graph 5.6. Penetration depths decreased from when arc current and welding speed were 130A and 360mm/min respectively to when they were 140A and 480mm/min

respectively. So arc current/welding speed combinations play a significant role in determining penetration depth.

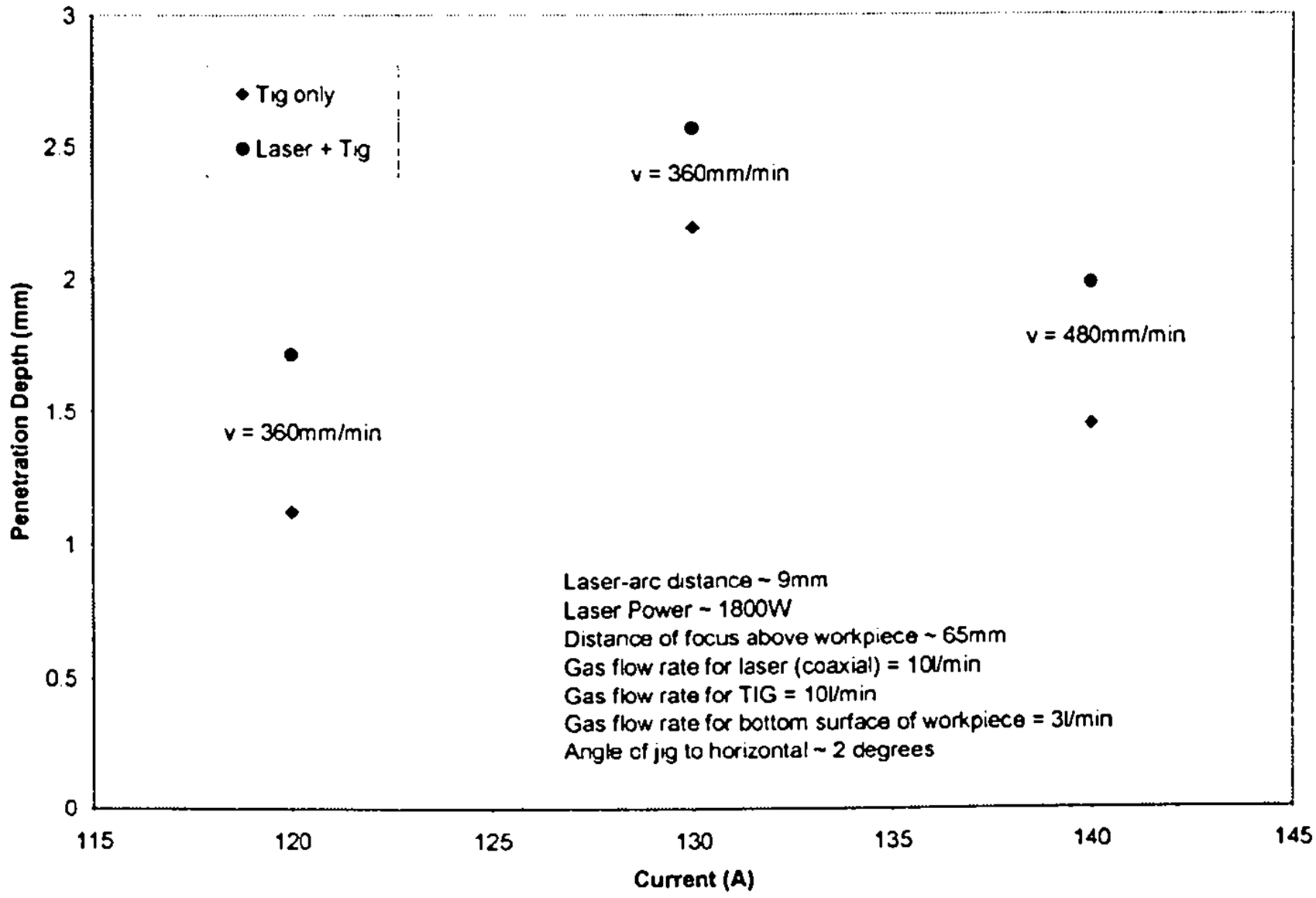

Figure 5.6 Graph showing penetration depth against arc current for laser-arc welded AA5083

Figure 5.7 shows the effect of an increase in distance from the focus on penetration depth. It should be noted that an increase in distance from the focus implies an increase in spot radius or spot size.

From figure 5.7, the penetration depth obtained for TIG-only weld s at 120A and 360mm/min was about 0.93mm while from figure 5.5. the same welding parameters produced a penetration depth of about 1.43mm. The disparity in results reflects the difficulty in reproducing TIG/arc weld results. Electrode length and contamination, start-up problems and gas pressure can all contribute to the variance in results. However, it is obvious that a laser-arc combination can produce an increase in

penetration depth, although such a process cannot be classified as laser conduction welding (LCW).

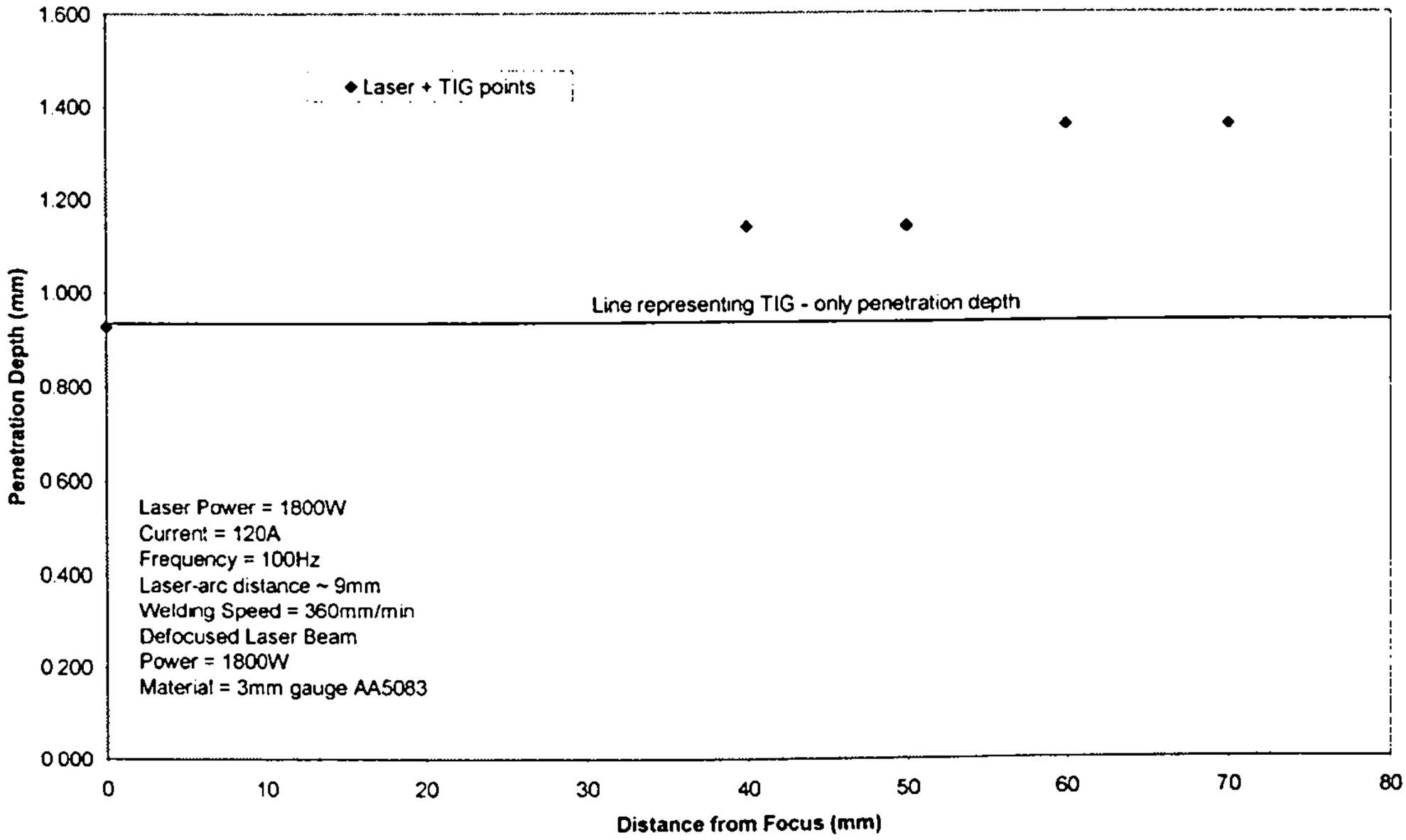

Figure 5.7 Graph showing penetration depth against distance from focus for laser-arc welded 3mm AA5083

Figure 5.8 shows the variation of penetration depth with laser power for laser-arc welded 3mm gauge AA5083 when arc current was kept constant at 120A. Laser-arc distance was kept at approximately 6mm. However in this case the laser beam was focused on the surface of the workpiece. It was observed that an increase in laser power led to an increase in penetration depth as would be expected. Although the welding speed for the laser-arc welding process was much lower at 360mm/min than for laser keyhole welding, it was evident that comparatively small contributions from both laser and arc could produce full penetration welds. The line drawn across the graph represents the penetration depth for TIG only welding at 120A.

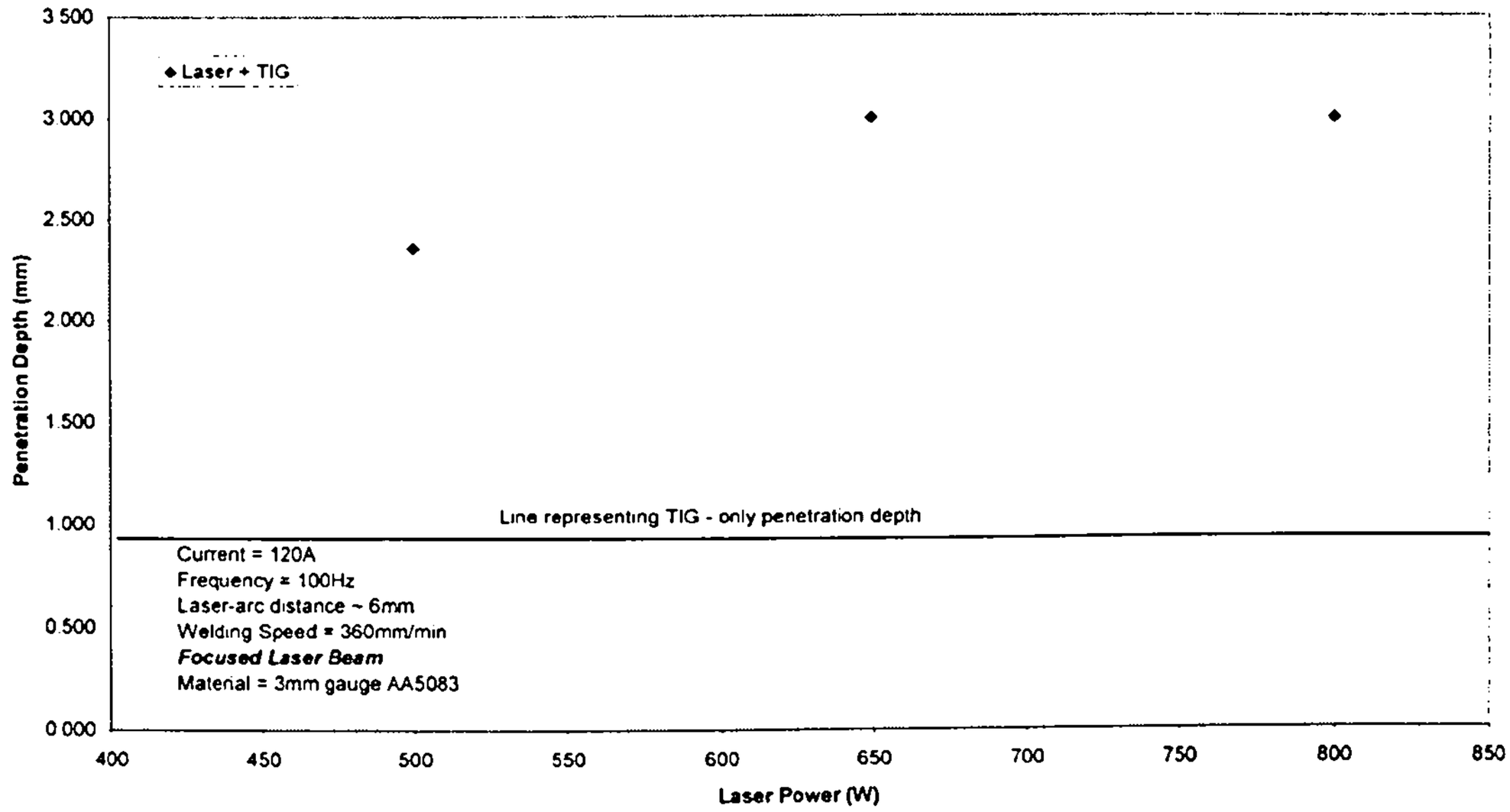

Figure 5.8 Graph showing penetration depth against laser power for laser-arc welded 3mm AA5083

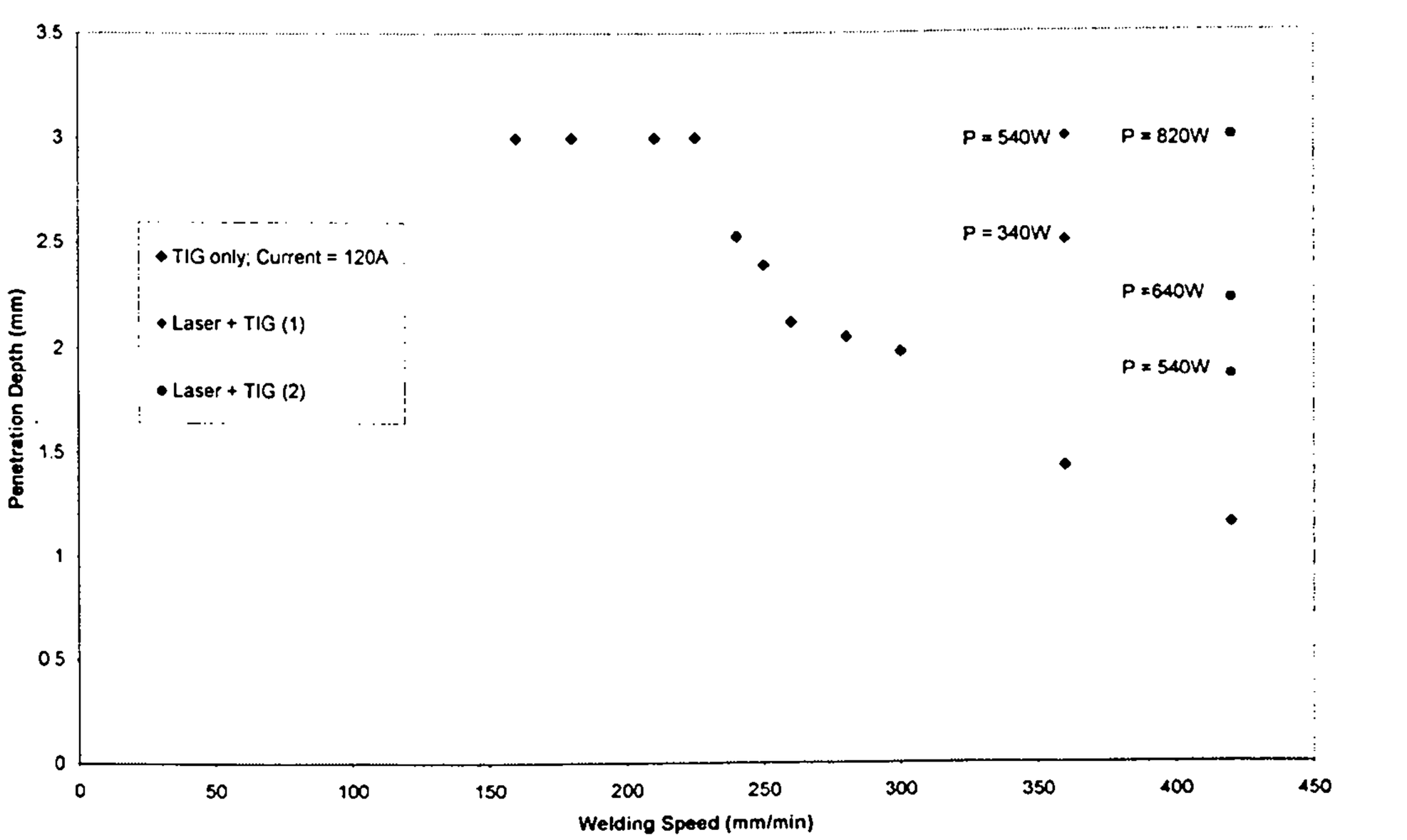

Figure 5.9 Graph showing variation of penetration depth against welding speed for laser-arc welded 3mm gauge AA5083

Figure 5.9 shows that as the welding speed increased, the penetration depth decreased for the only-TIG welding option. For the laser-arc process, this variation was also observed when the laser power was 540W. The arc current was kept constant at 120A. As would be expected, for speeds of 360mm/min and 420mm/min, the penetration depth increased when laser power was increased. The results from the laser-arc experiments indicate that

(i) It was not possible to use the arc purely as a pre-heating medium without interaction with the laser beam

(ii) Varying results obtained using the same parameters highlighted the difficulty in reproducing TIG results

(iii) Although an increase in penetration depth was achieved with the laser-arc combination process, the increases could also be obtained by slightly increasing the arc current.

5.4 CO_2 and Nd:YAG Laser Conduction Welding of Aluminium

Results obtained from the CO_2 laser conduction welding of 2mm gauge AA5083 are shown in figure 5.10 below. The workpiece was sandblasted in order to enhance absorptivity of the laser energy by the aluminium alloy.

Both welding widths and penetration depths increased initially up to a maximum and then decreased with increasing spot radius.

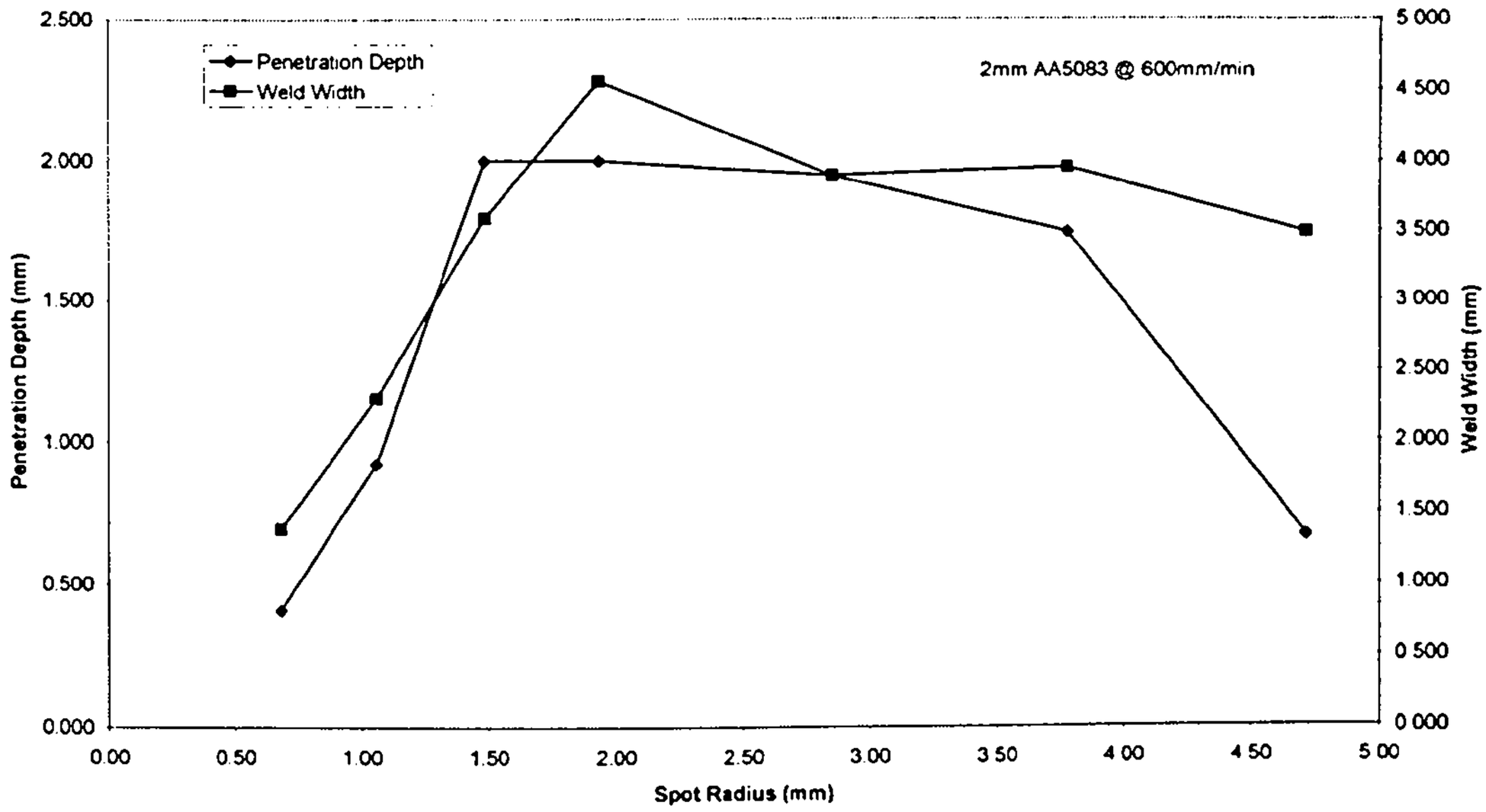

Figure 5.10 Graph showing variation of penetration depth and weld width with spot radius for CO_2 laser conduction welding of 2mm gauge AA5083

This trend that had been observed during the trial experiments with mild steel and graphite coated AA2014 was once again observed during the Nd:YAG laser conduction welding of 3mm gauge AA5083. Unlike the cases for mild steel, the maximum penetration depth for both welding speeds (600mm/min and 720mm/min) corresponded to the same spot radius as can be seen in figure 5.11a. For aluminium alloys, the optimum penetration depth is dependent on an optimum surface area of the laser beam on the workpiece that, of course, is dependent on the optimum spot radius. Beyond the point at which maximum penetration depth is obtained, the effective spot radius becomes less than the actual spot radius of the beam, and this gives rise to a decrease in penetration depth (see figures 5.11b and 5.11c). This is reflected in figure 5.4 with regard to graphite-coated 3mm AA2014. This optimum spot radius was about 2.4mm for the graphite-coated 3mm AA2014 samples and about 2.8mm for the sandblasted 3mm AA5083 samples. Figures 5.11b and 5.11c

also show the variation of weld width with increasing spot radius for 3mm AA5083 welded at 600mm/min and 720mm/min respectively. The graphs indicate that weld width increases up to a maximum and then decreases. This means that although there is an increase in spot radius, the effective spot radius varies in the same way as the penetration depth. As the spot radius increases beyond the optimum value, the laser energy concentrates in a gradually reducing inner area (area of the effective spot radius) of the laser beam whilst the outer fringes of the beam produce only a heating effect.

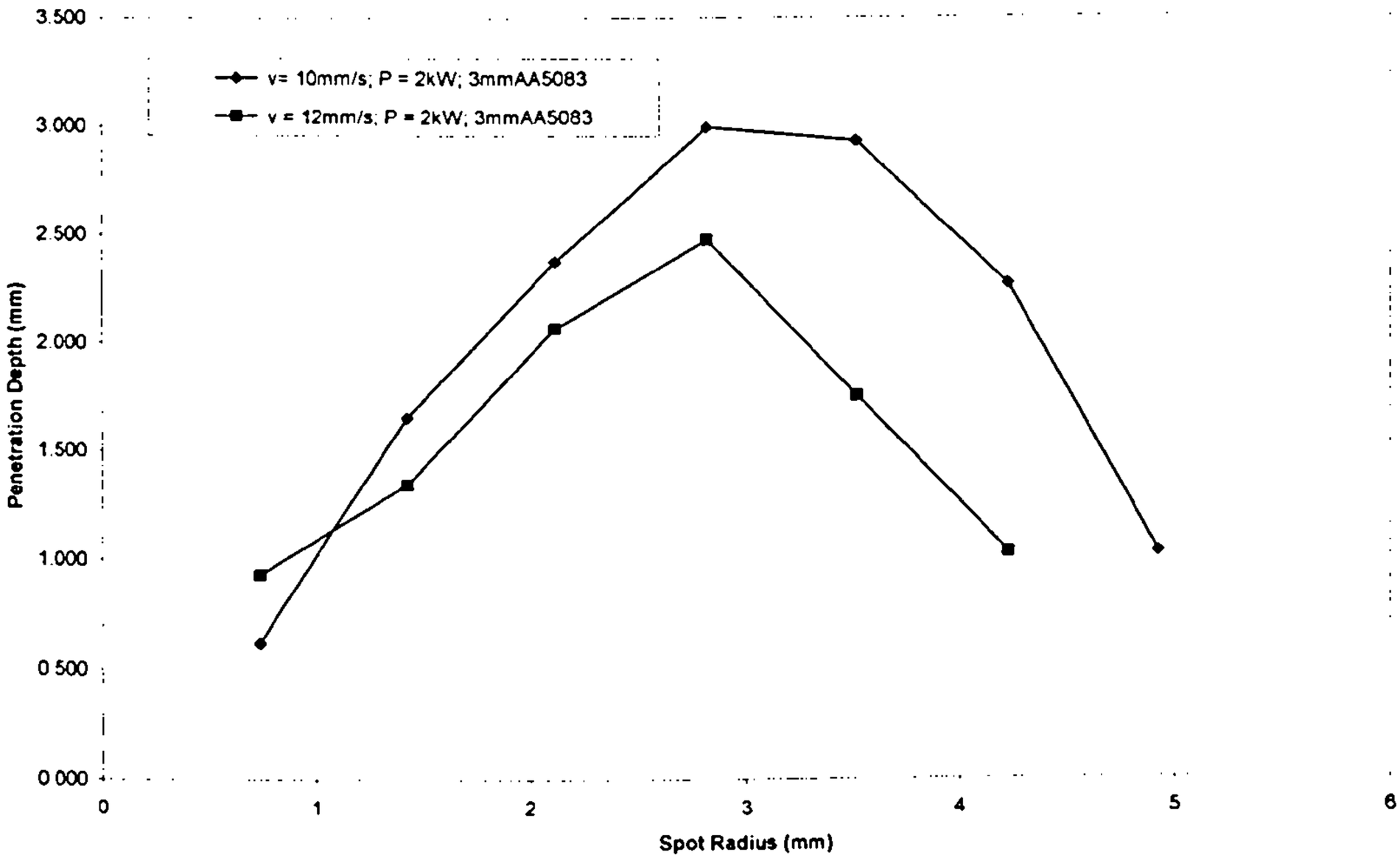

Figure 5.11a Graph showing variation of penetration depth with spot radius for Nd:YAG laser conduction welding of 3mm gauge AA5083 welded at 600mm/min and 720mm/min.

The penetration depth/spot radius curves were produced for only AA5083 since all the aluminium alloys used in this work exhibited the same phenomenon.

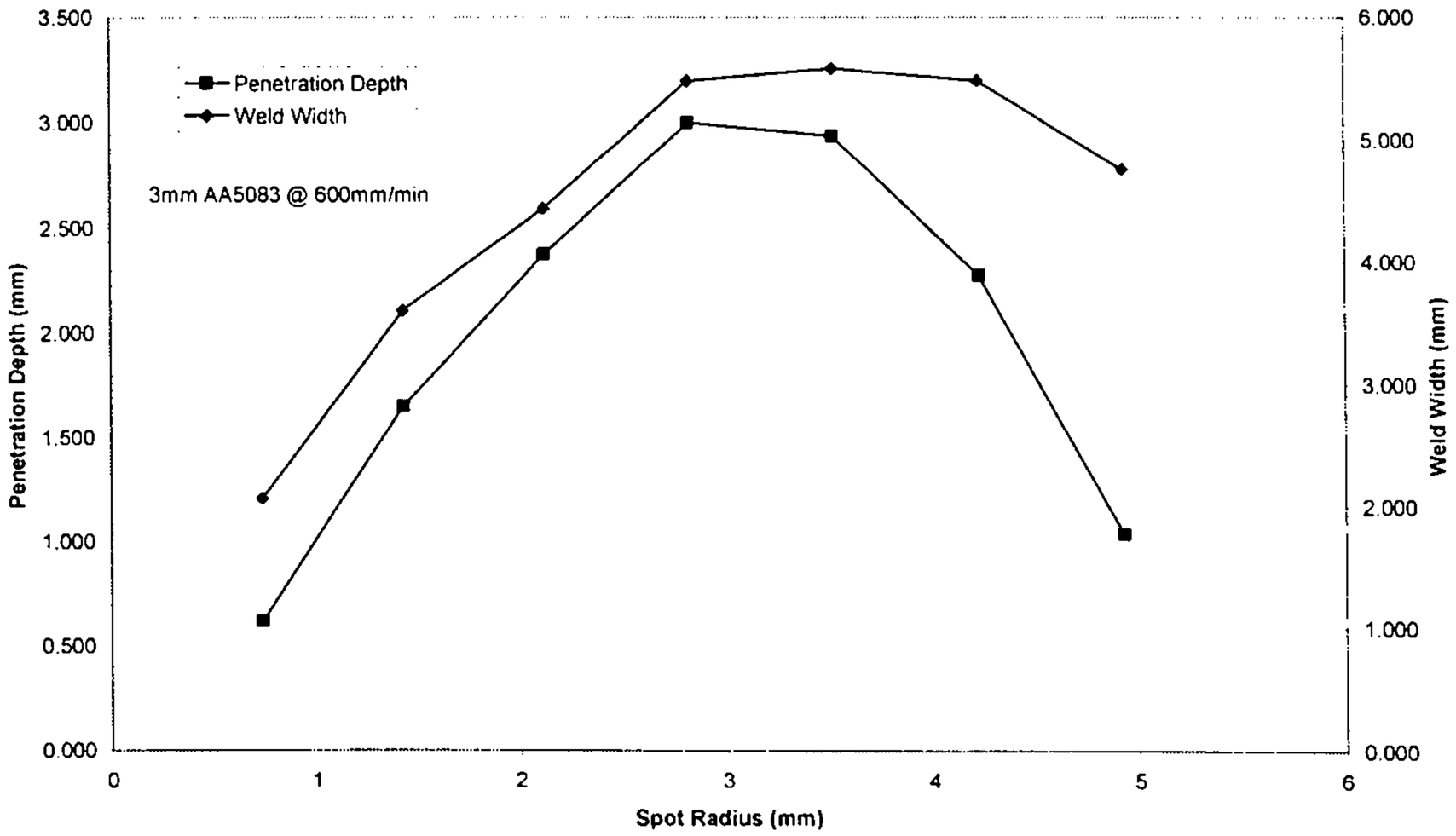

Figure 5.11b Graph showing variation of penetration depth and weld width with spot radius for Nd:YAG laser conduction welding of 3mm gauge AA5083 welded at 600 mm/min.

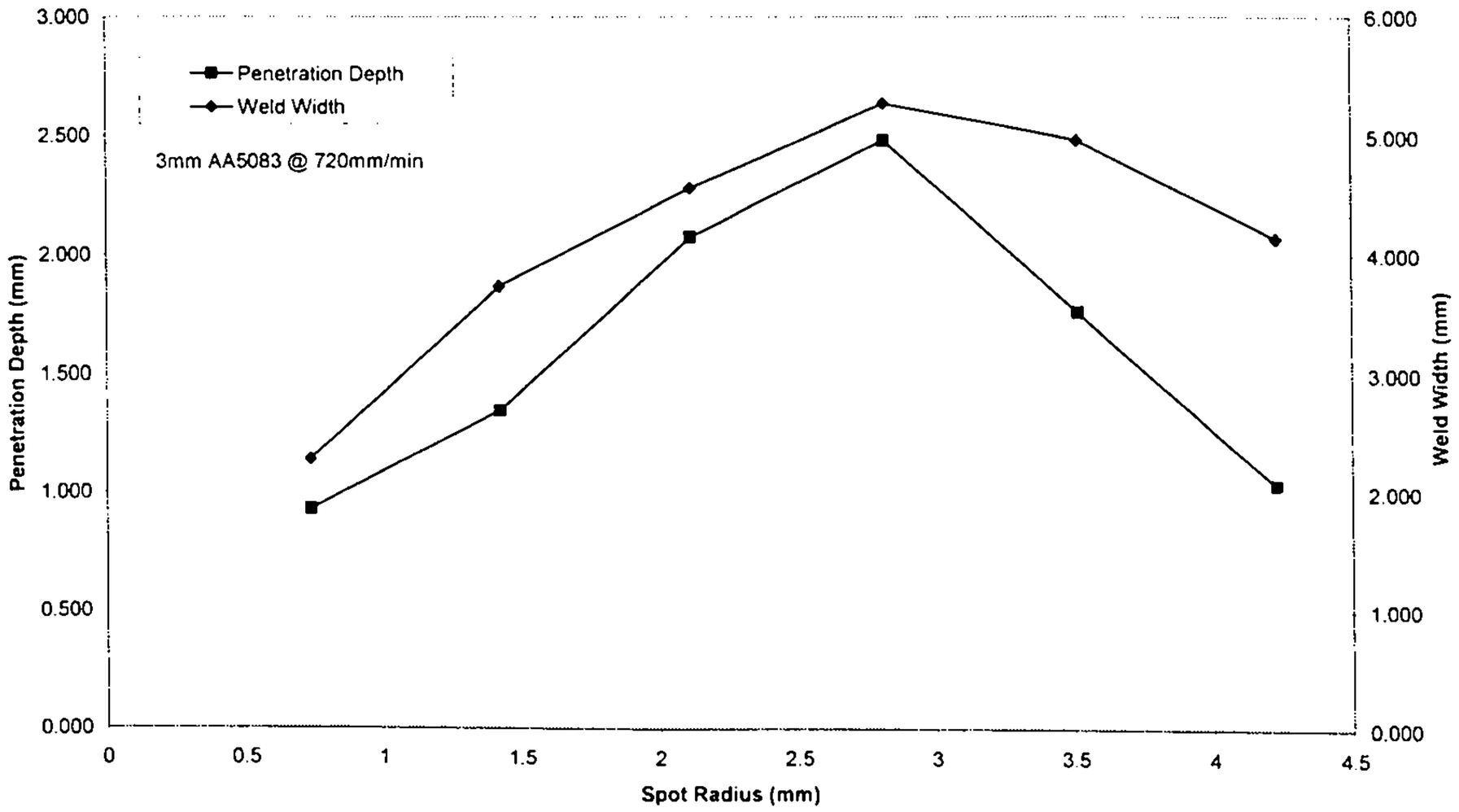

Figure 5.11c Graph showing variation of penetration depth and weld width with spot radius for Nd:YAG laser conduction welding of 3mm gauge AA5083 welded at 720 mm/min.

5.5. Tensile Strength Tests Results

Uniaxial tensile strength tests conducted for laser conduction butt-welded mild steel samples revealed that the fracture occurred at the base metal. This showed that the welds were as strong, if not stronger, than the base metal. Figure 5.12 illustrates this. The response of the conduction welds to the tensile strength tests was identical to that of keyhole welds.

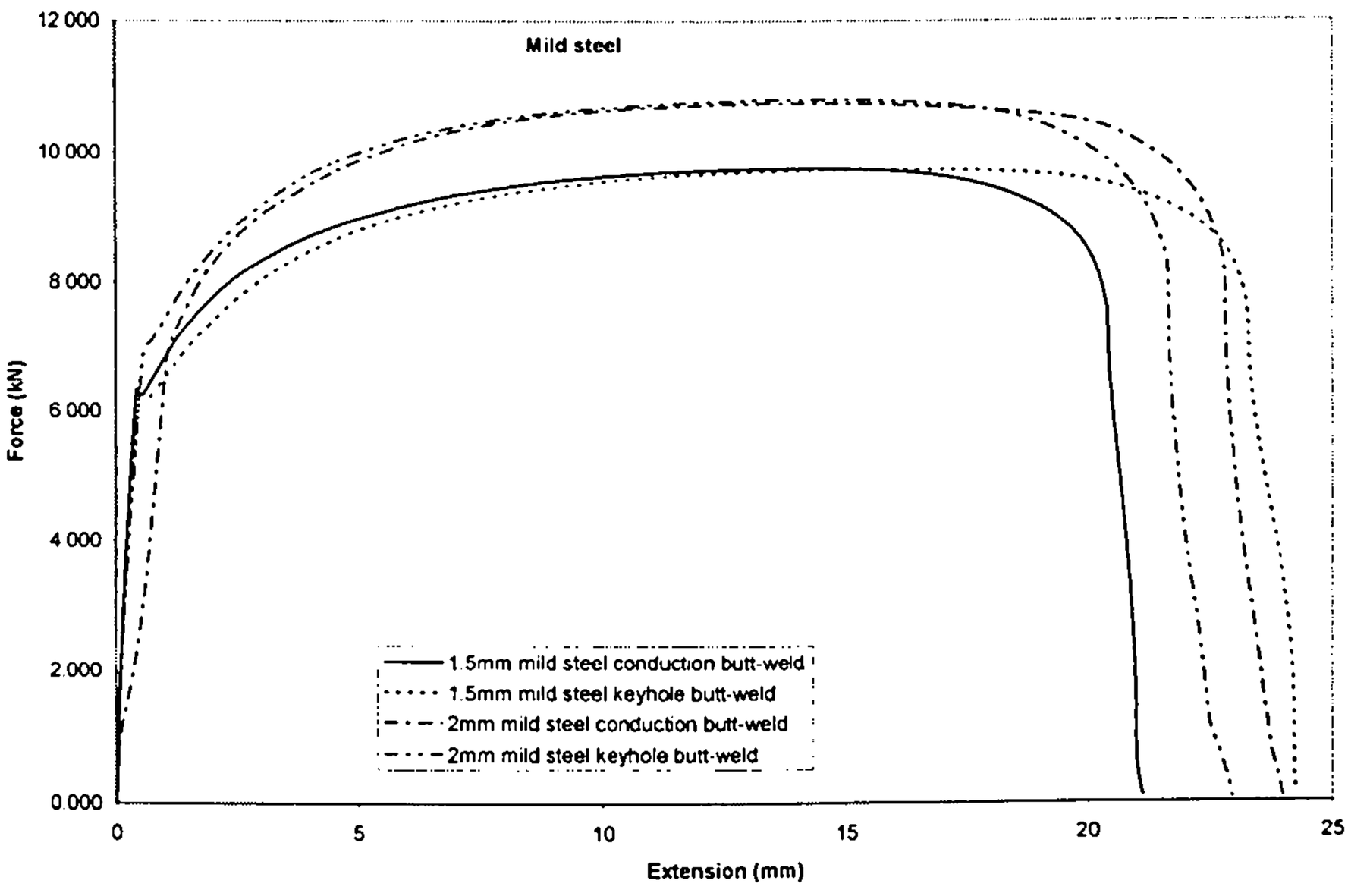

Figure 5.12 Graph showing tensile strength tests results for 1.5mm and 2mm gauge mild steel

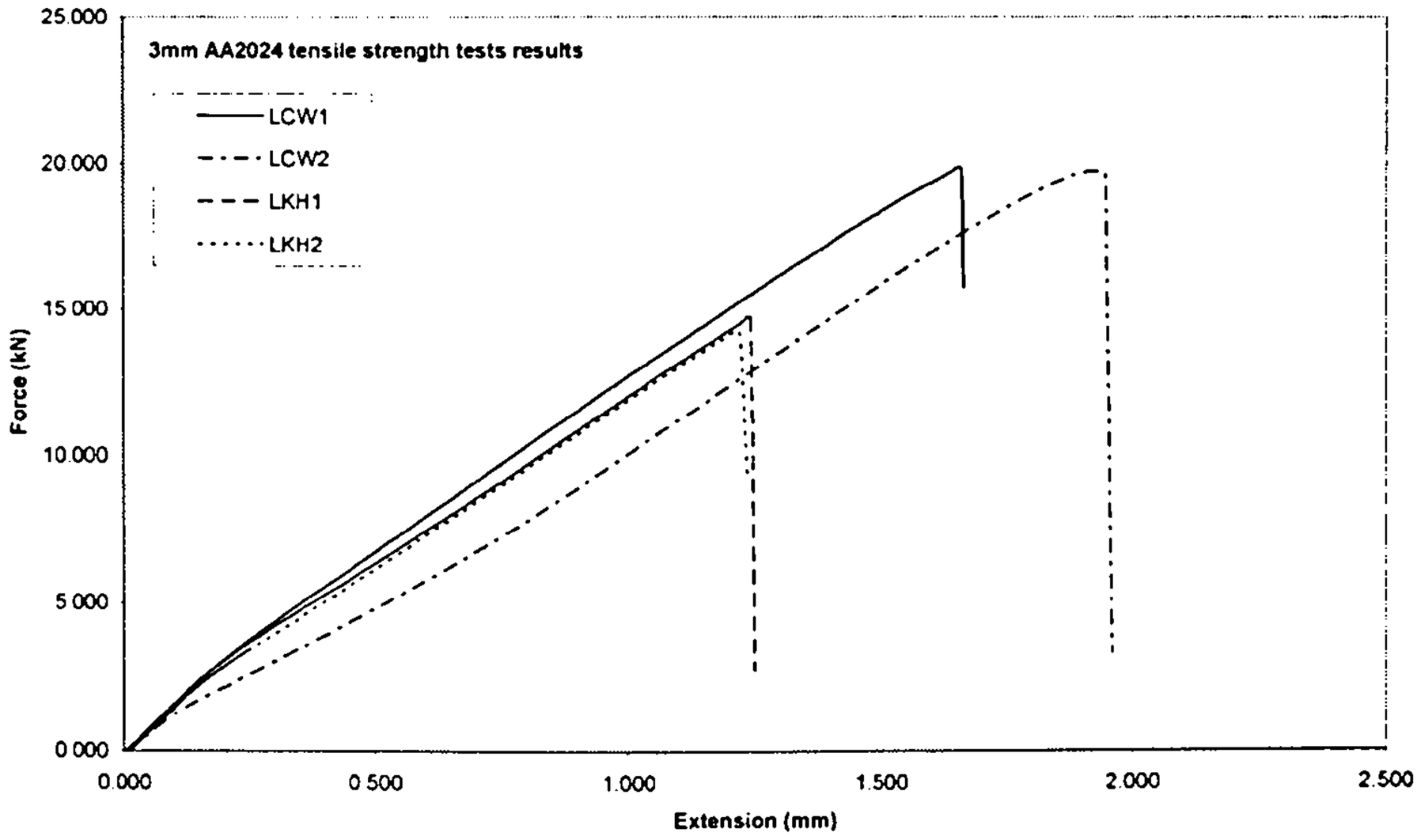

Figure 5.13 Graph showing tensile strength tests results for 3mm AA2024 keyhole and conduction welds

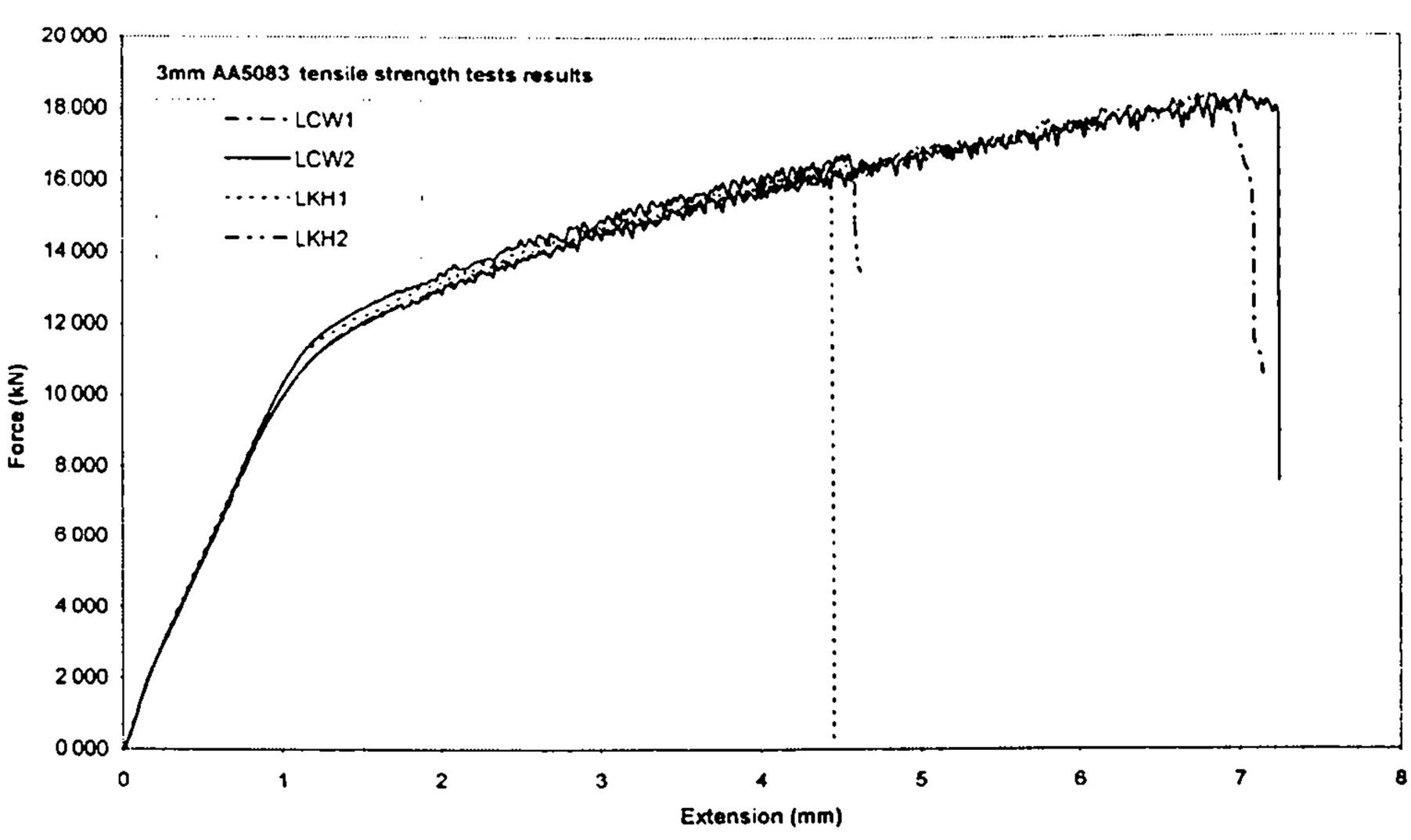

Figure 5.14 Graph showing tensile strength tests results for 3mm AA5083 keyhole and conduction welds

Figures 5.13 shows tensile strength tests results for conduction welds as well as keyhole welds for AA2024. It can be seen that the conduction welds achieve greater

extensions than the keyhole welds and the maximum force applied before fracture is greater for the conduction welds than for the keyhole welds.

In the case of AA5083 welds, the same trend occurs with the conduction welds requiring more force to fracture as shown in figure 5.14. All failures took place at the weld–base metal boundary of the butt welds.

However in the case of AA6061 the failure occurred at the base metal for both conduction welds and keyhole welds (see figure 5.15). The keyhole and conduction welds were both stronger than the base metal.

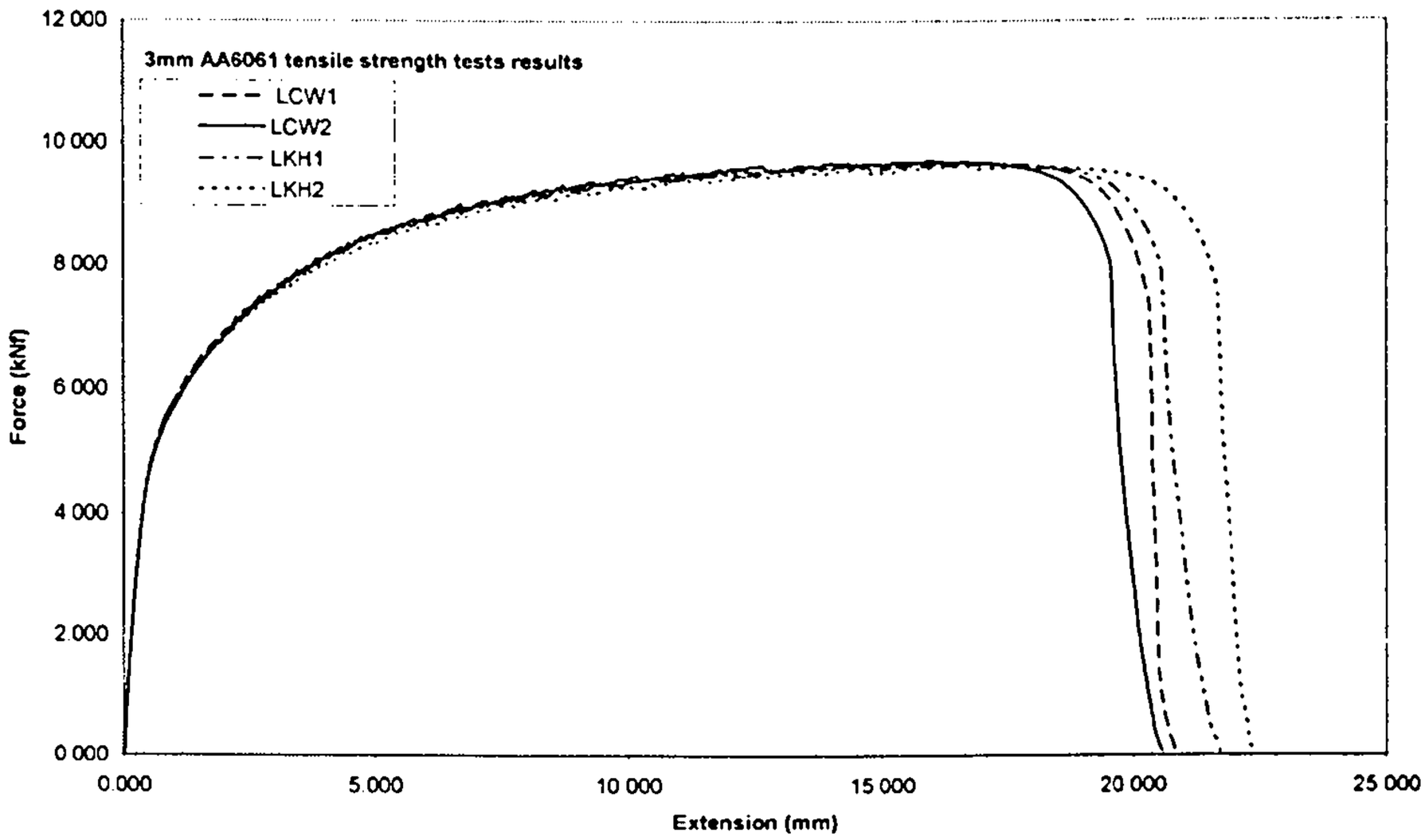

Figure 5.15 Graph showing tensile strength tests results for 3mm AA6061 keyhole and conduction welds

Results for the tensile strength tests are as follows:

	AA5083 (kN)	**AA2024 (kN)**	**AA6061 (kN)**
Laser Conduction Welds	18.48	19.83	9.70
Laser Keyhole Welds	16.53	14.57	9.64

The table shows that the fracture load for 3mm gauge AA5083 was 18.48kN and 16.53kN for laser conduction welds and laser keyhole welds respectively. For 3nm gauge AA2024, it was 19.83kN for laser conduction welds and 14.57kN for laser keyhole welds. In the case of 3mm AA6061, the fracture loads for laser conduction and laser keyhole welds were just about the same at 9.70kN and 9.64kN respectively. This confirms the fact that laser conduction welding by means of a defocused laser beam could produce welds that are of comparable and even higher tensile strength than laser keyhole welds.

5.6. Weld Profiles

During laser conduction welding, the process is quieter and fewer spatters leave the weld pool. Furthermore, porosity is reduced as evidenced by the comparison of micrographs in figures 5.16 and 5.17. The intense heat and high power density attained during keyhole welding (figure 5.16) forms a little groove on the weld surface, whereas the surface of the conduction weld is relatively smooth. Figure 5.17 is the micrograph of a bead-on-plate laser conduction weld of 2mm AA5083 at 500mm/min obtained using the PRC/OPL CO_2 laser. Figure 5.18 shows a butt-weld

for 2mm AA5083 achieved using a defocused CO_2 laser beam at welding speed of 450 mm/min. Again the weld is pore-free and smooth.

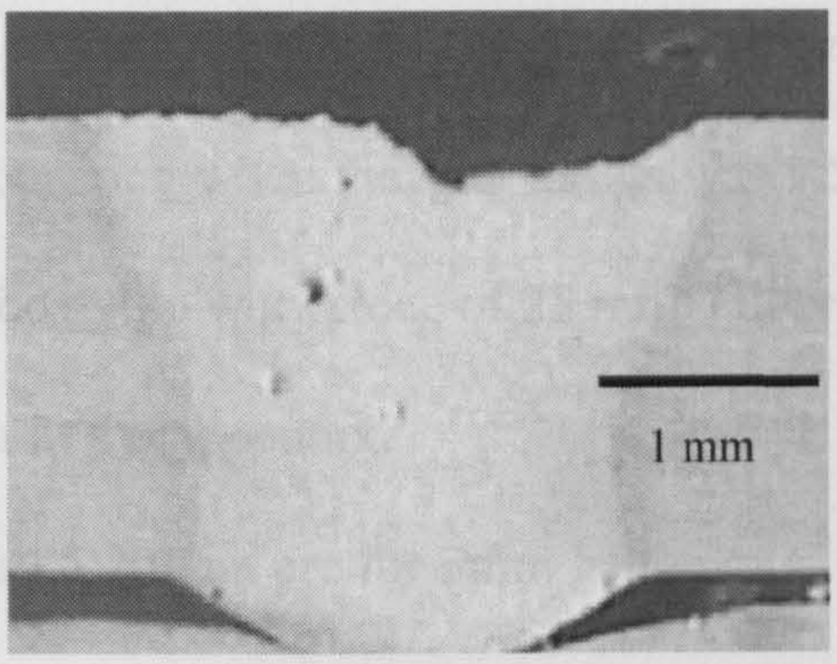

Figure 5.16 Micrograph of 2mm AA5083 keyhole weld showing pores that have formed inside; weld speed = 1100mm/min

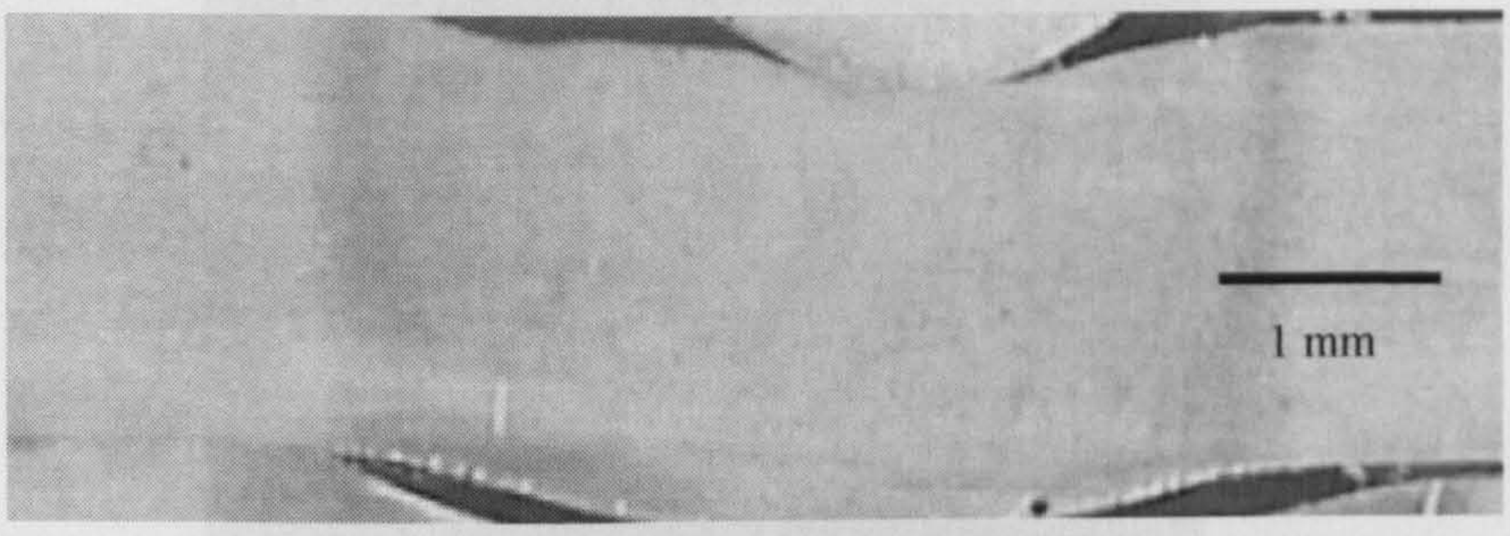

Figure 5.17 Micrograph of 2mm AA5083 bead-on-plate conduction weld with practically no pores; weld speed = 500 mm/min

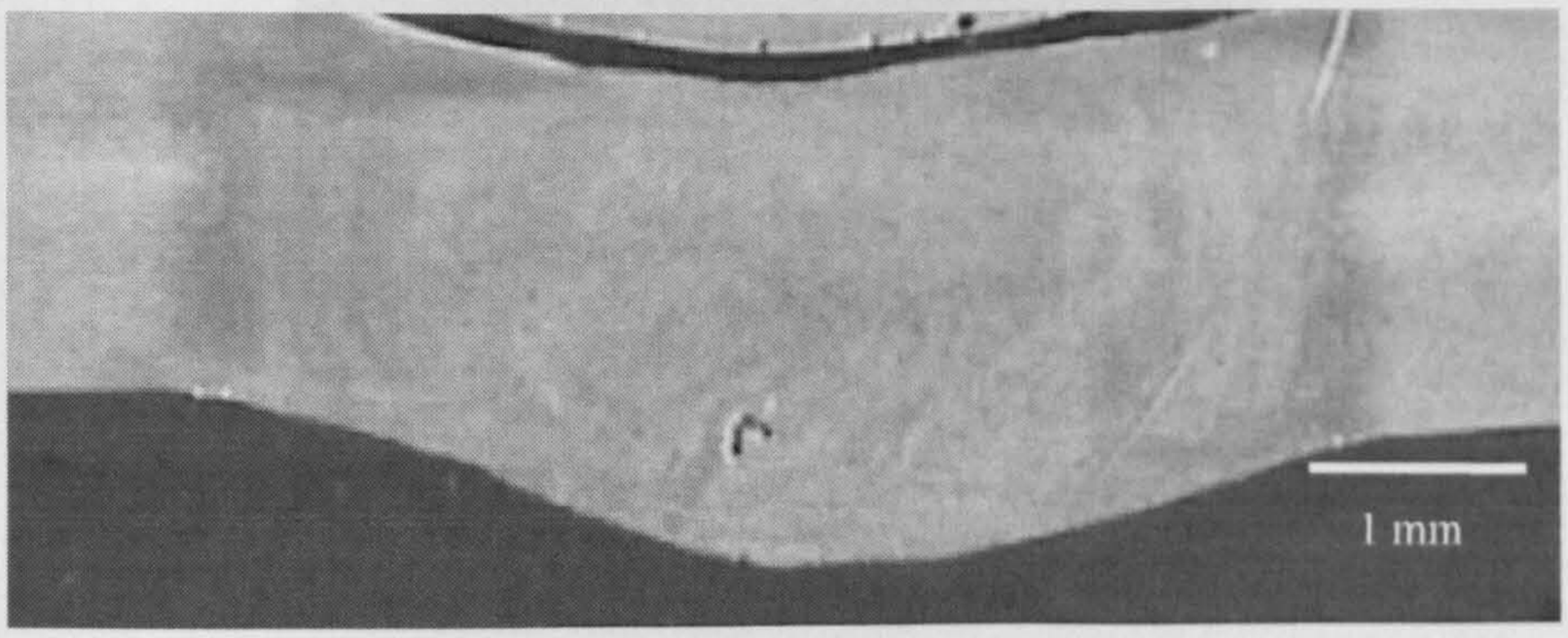

Figure 5.18 Micrograph of 2mm AA5083 conduction butt-weld; weld speed = 450 mm/min

Figures 5.19 show progressively the weld cross-sections obtained during the laser conduction welding of 3mm gauge AA5083 using the Nd:YAG laser. It can be seen that the penetration/spot radius variation mentioned above occurred; full and maximum penetration occurring when the spot radius was 3.52mm corresponding to a distance of the focus above the workpiece of 25 mm. Other aluminium alloy weld cross-sections are shown in the appendix.

The micrographs in figure 5.20 that are for 3mm gauge mild steel samples show the same trend i.e. increase in penetration depth up to a maximum and then a decrease, with increase spot radius.

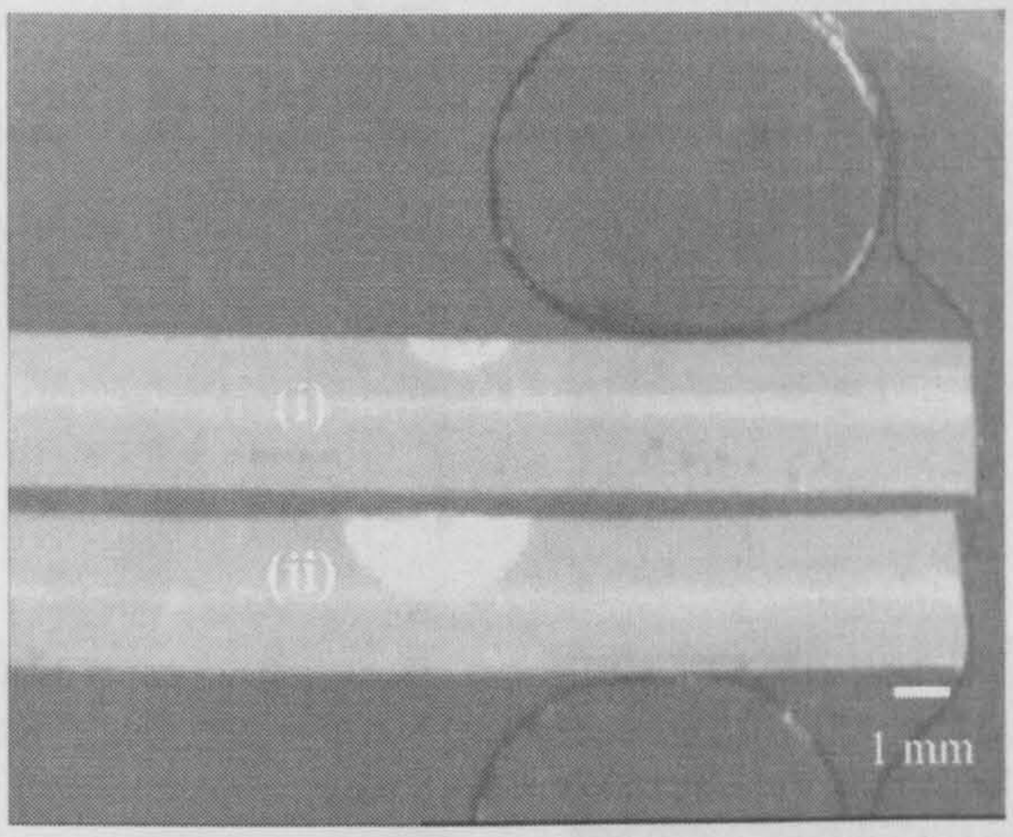

Figure 5.19 (a) (i) and (ii) show conduction welds for 3mm gauge AA5083 using Nd:YAG laser at distances 10 mm and 15 mm from focus; Average Power = 2kW

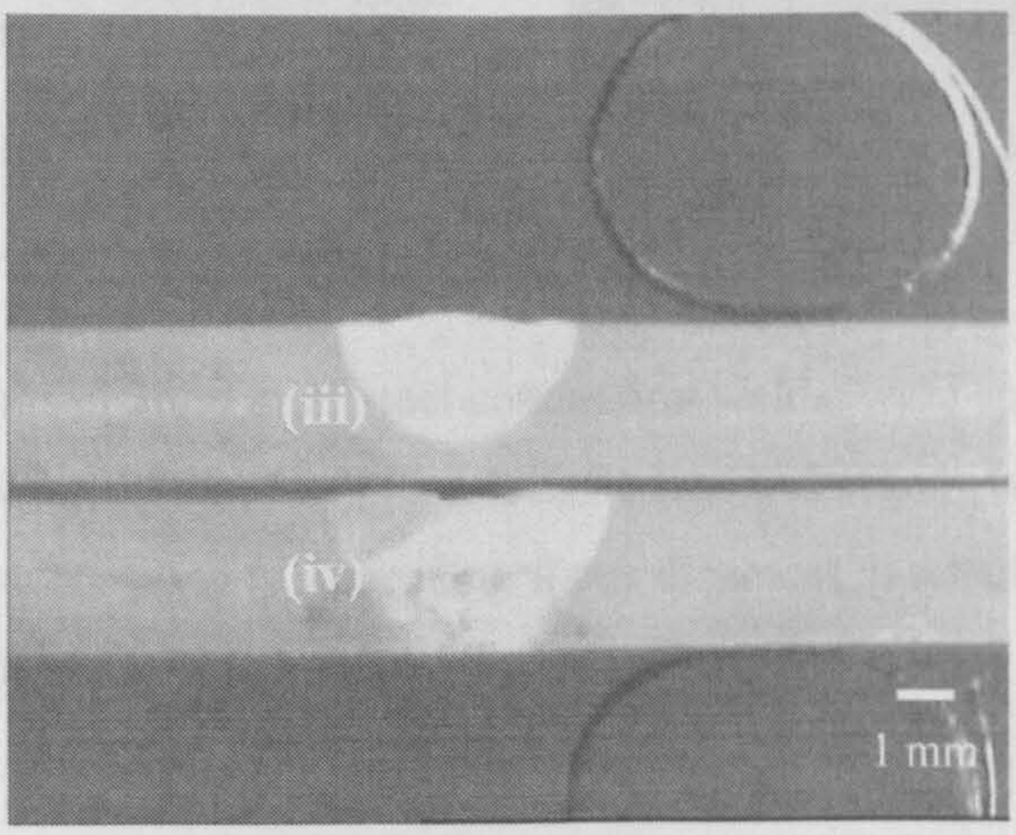

Figure 5.19 (b) (i) and (ii) show conduction welds for 3mm gauge AA5083 using Nd:YAG laser at distances 20 mm and 25 mm from focus; Average Power = 2kW

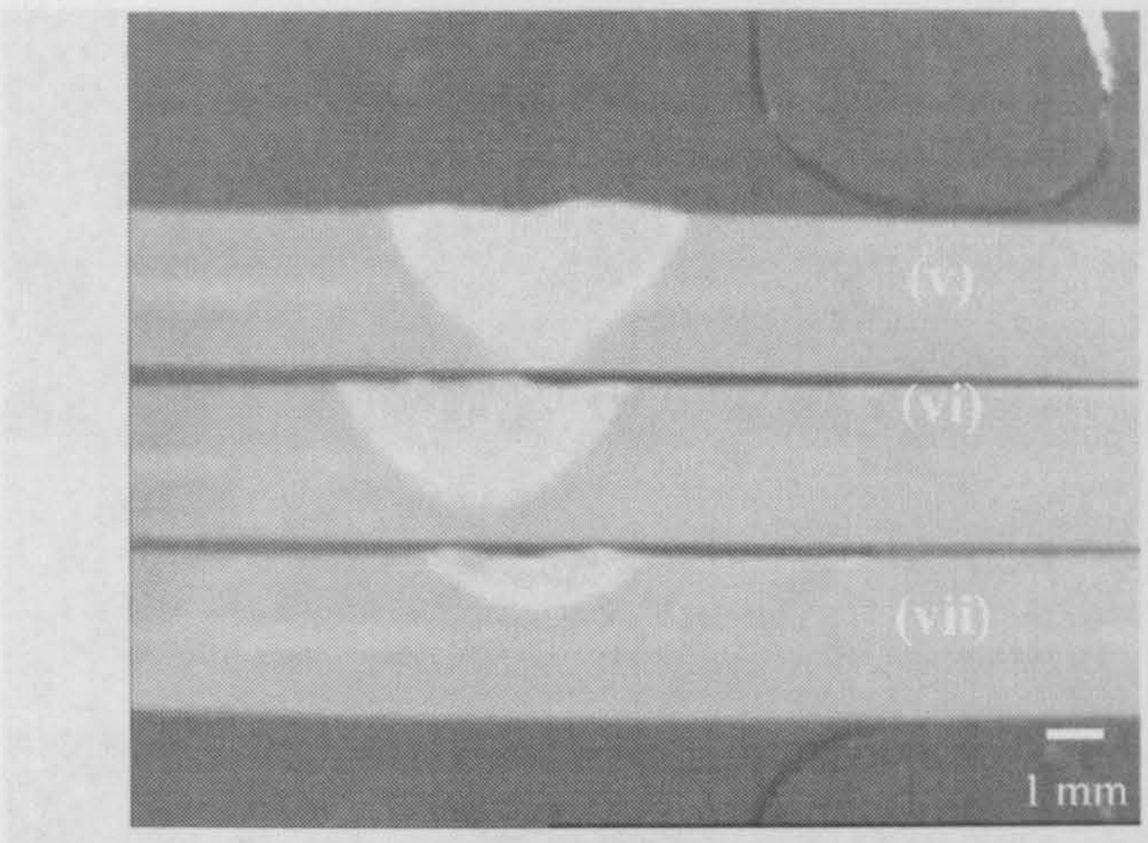

Figure 5.19 (c) (i) and (ii) show conduction welds for 3mm gauge AA5083 using Nd:YAG laser at distances 30 mm and 35 mm from focus; Average Power = 2kW

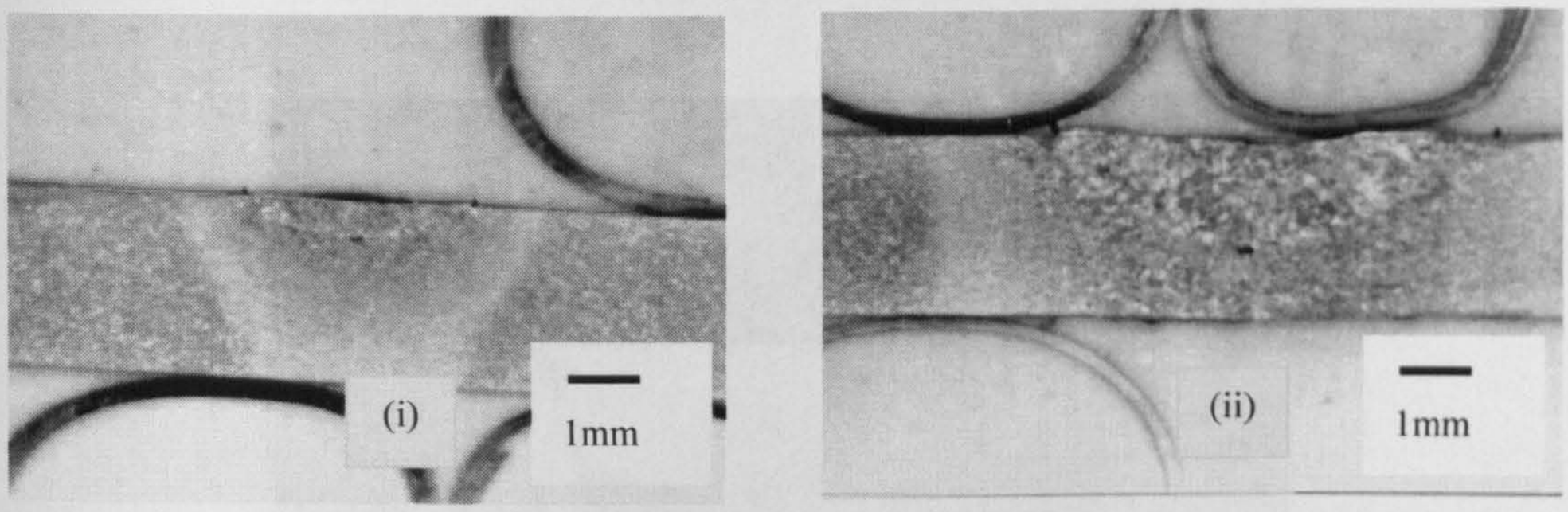

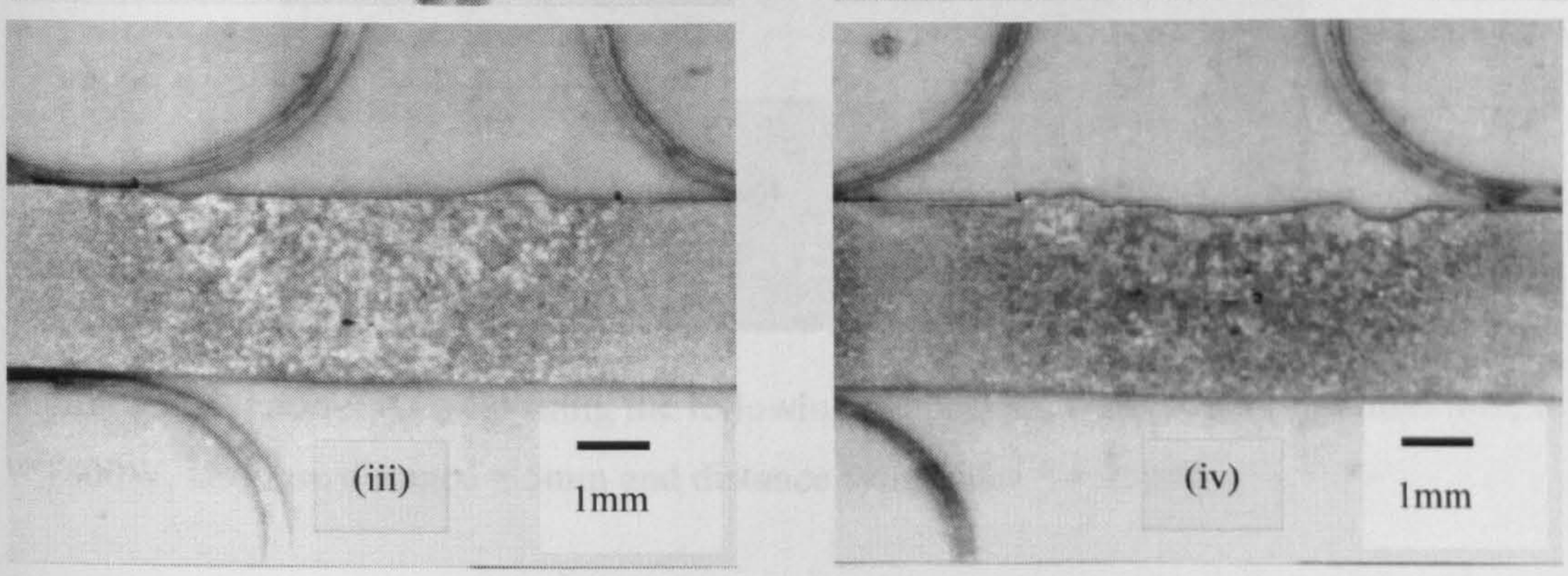

Figure 5.20 Micrographs of 3mm mild steel conduction welds; weld speed = 100 mm/min, Average power = 1800W, 127mm focal length ZnSe lens and argon pressure = 20l/min. The micrographs (i) – (iv) correspond to increasing focus distances at which the calculated spot radii are 1.89mm, 3.76mm, 5.18mm and 6.10mm respectively.

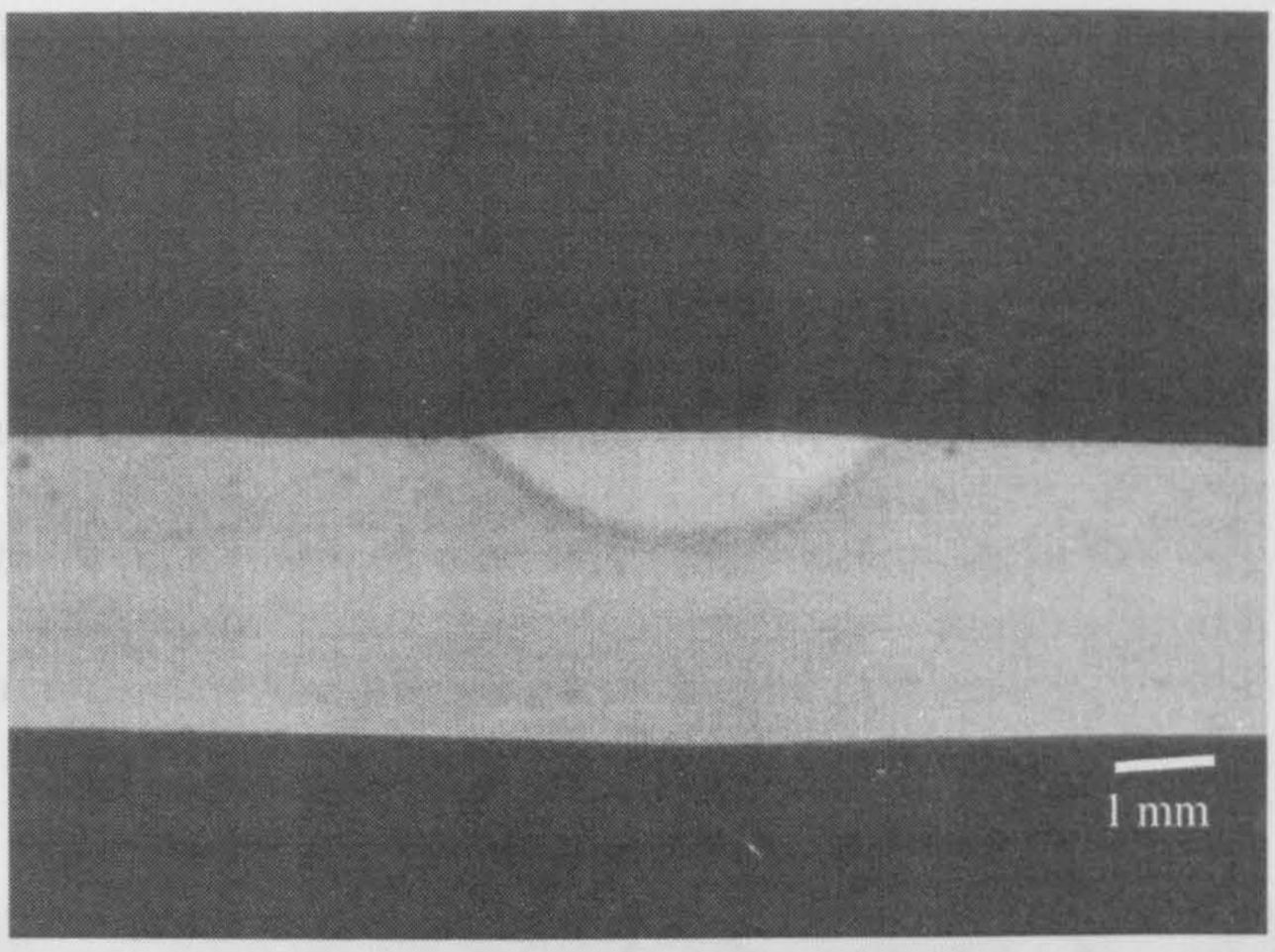

Figure 5.21 – TIG weld using the following parameters, I = 120A, v = 380mm/min

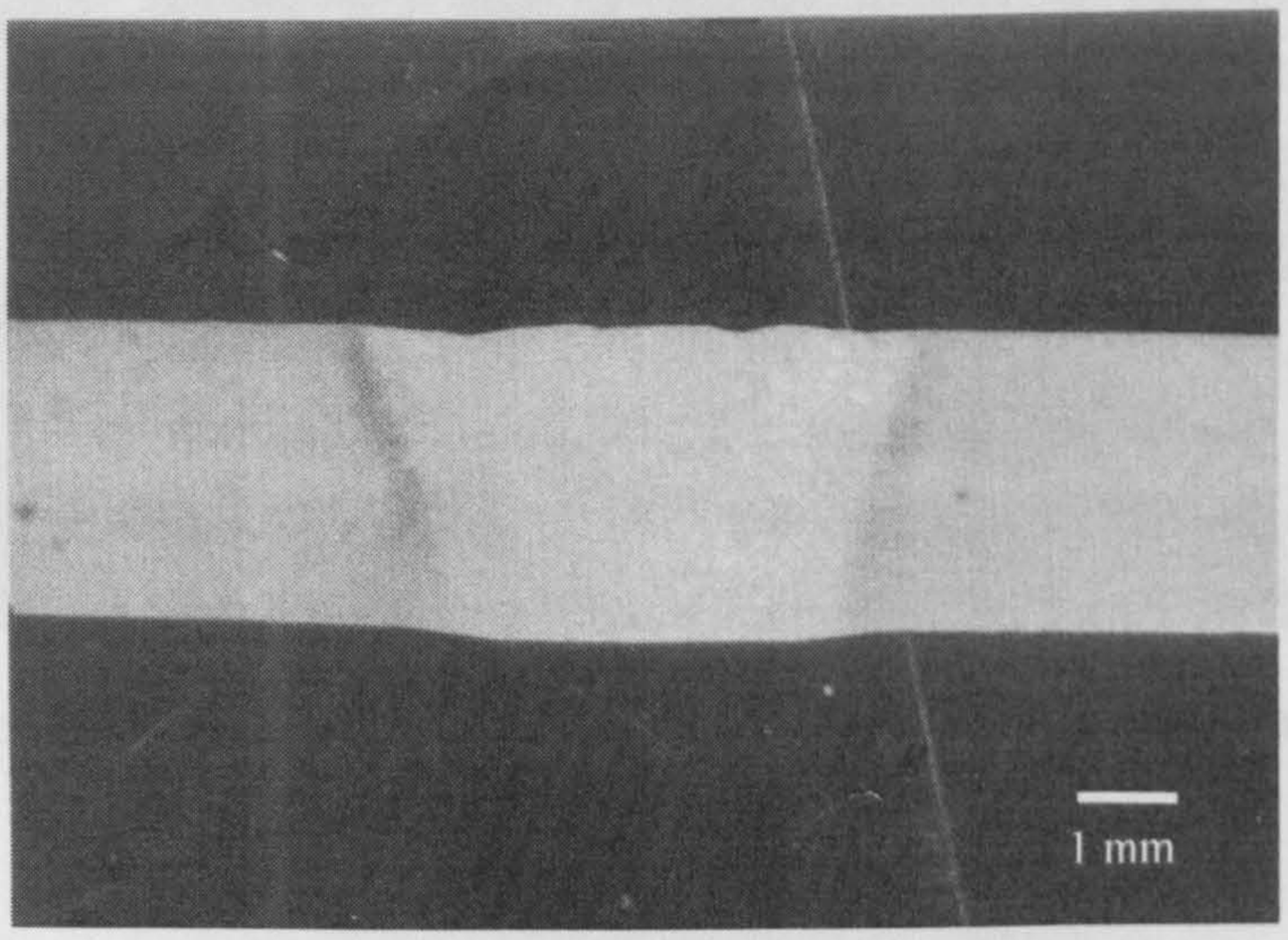

Figure 5.22 – Laser-TIG weld using the following parameters, I = 120A, v = 380mm/min, P = 1800W, laser-arc distance = 5mm and distance from focus = + 75mm

Figures 5.21 and 5.22 show the results of TIG-only and laser-arc welding of 3mm gauge AA5083 samples. The synergic effect produced as a result of the laser-arc combination gave rise to a full penetration weld, as shown in figure 5.22. However, the reason behind seeking to use the arc in the first place was to provide pre-heating as opposed to initiating a laser-hybrid process.

5.7 Surface Profile Analysis

Surface profile observations were made for sandblasted and as-received surfaces using both the SEM and an optical microscope. Figure 5.23 shows the optical microscope image of the sandblasted surface of an AA5083 sample. The dull parts of the micrograph are as a result of excessive light reflection in the tiny craters created by the aluminium oxide grit during the sandblasting process.

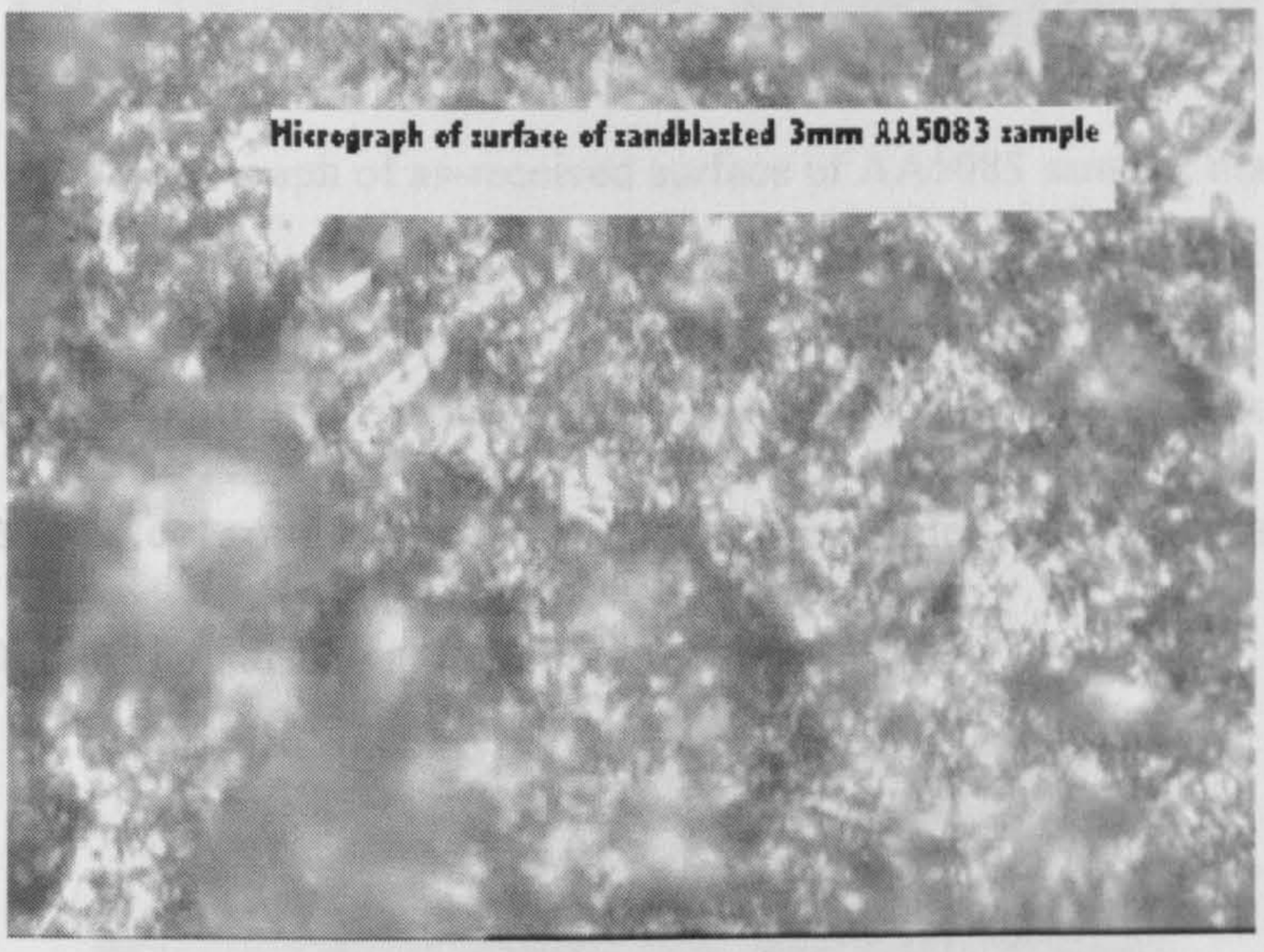

Figure 5.23 Micrograph of sandblasted surface of AA5083 sample; mag.x 50

The surface of the sandblasted sample enhanced laser beam absorptivity. The surface of as-received samples was examined under the optical microscope and the result is shown in figure 5.24.

It is evident from comparing figures 5.23 and 5.24 that for laser conduction welding with a defocused laser beam, surface profile is a significant factor.

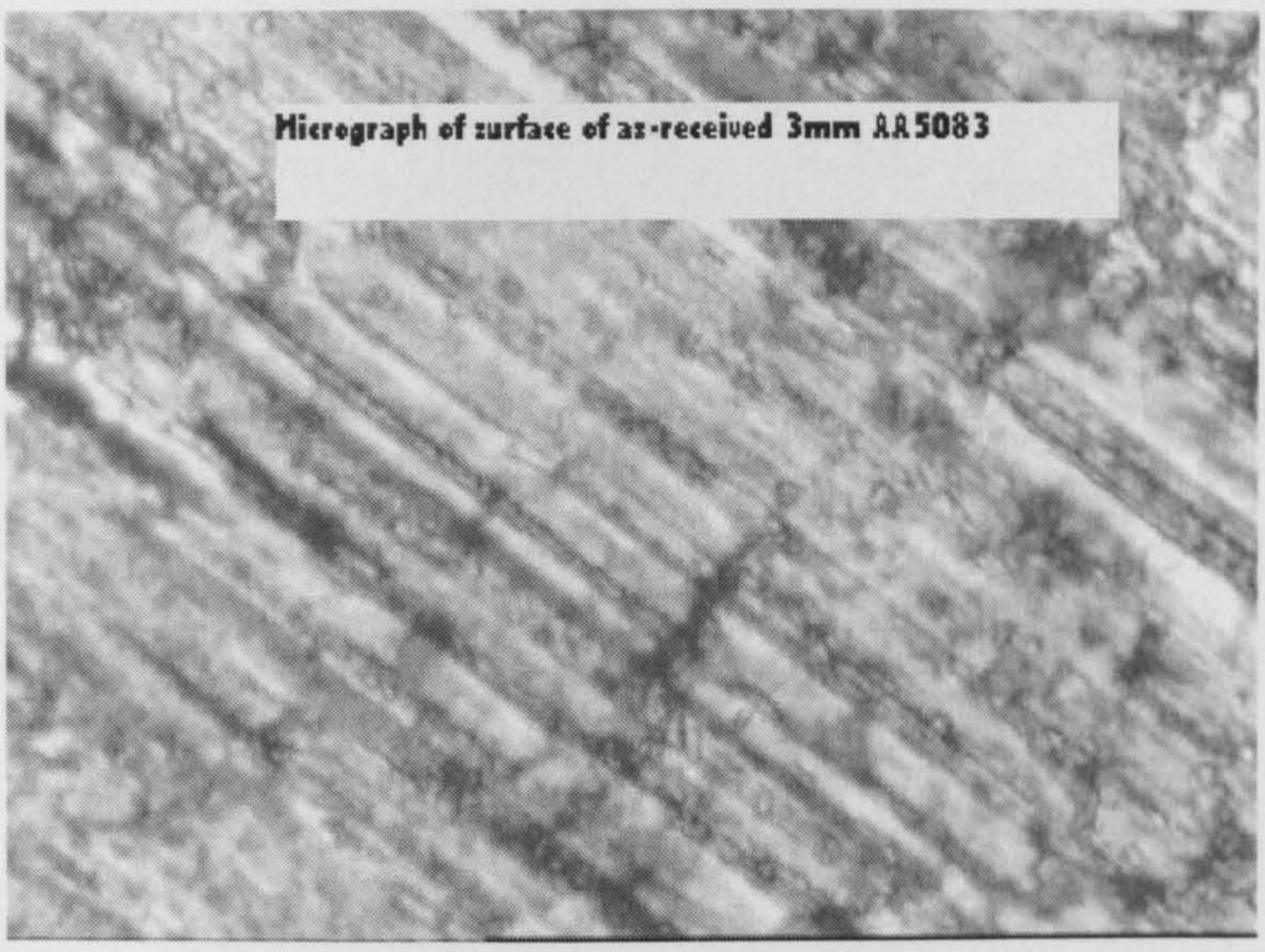

Figure 5.24 Micrograph of as-received surface of AA5083 sample; mag. x 50

It is clear that the aluminium oxide grit change the surfaces of samples drastically in such a way as to affect roughness. Tiny craters are created on the surface and a very large percentage of the surface area is covered.

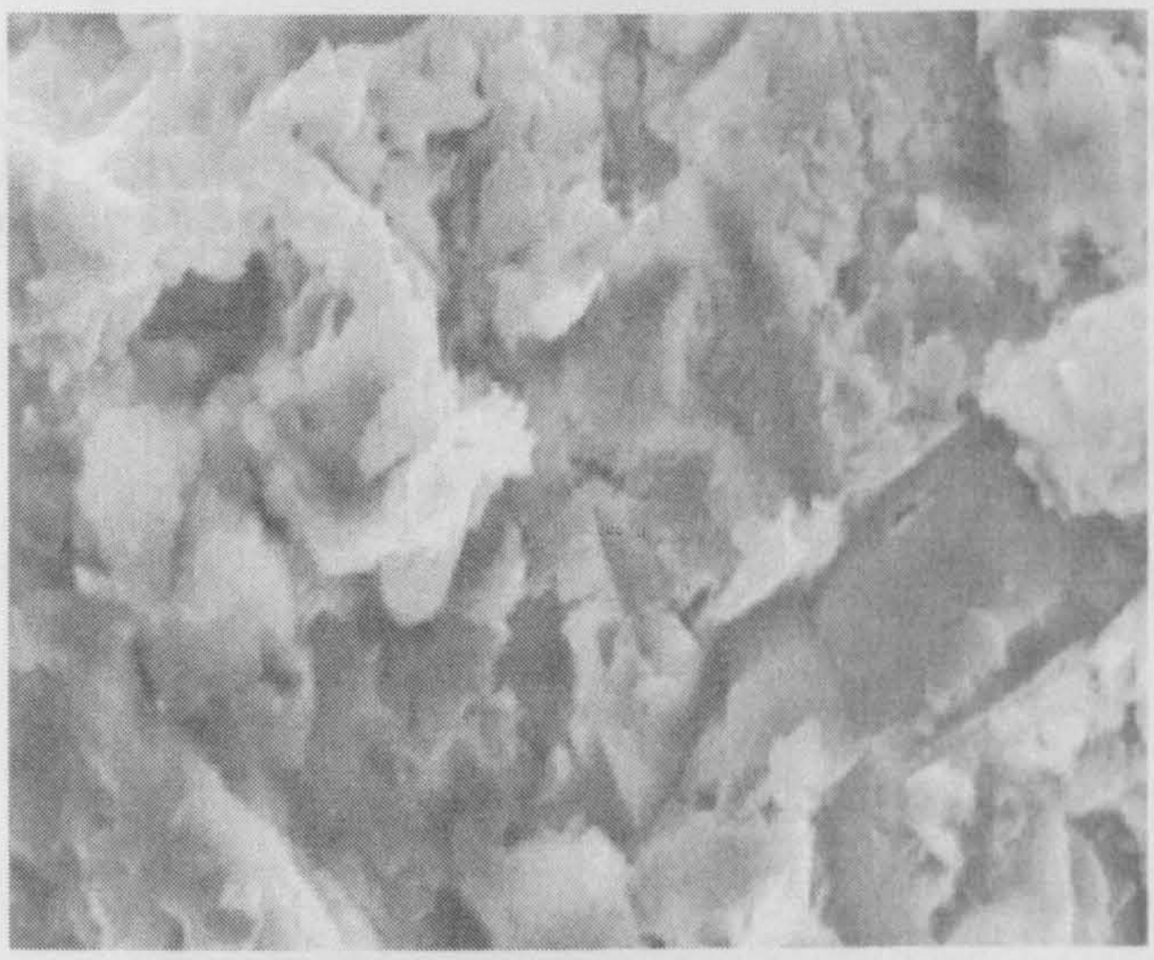

Figure 5.25 – SEM analysis of sandblasted surface of 3m AA5083 sample (x1.5k)

Figures 5.25 and 5.26 are SEM analysis results of the sandblasted surface and as-received surface respectively. This confirms results obtained through optical microscope observations.

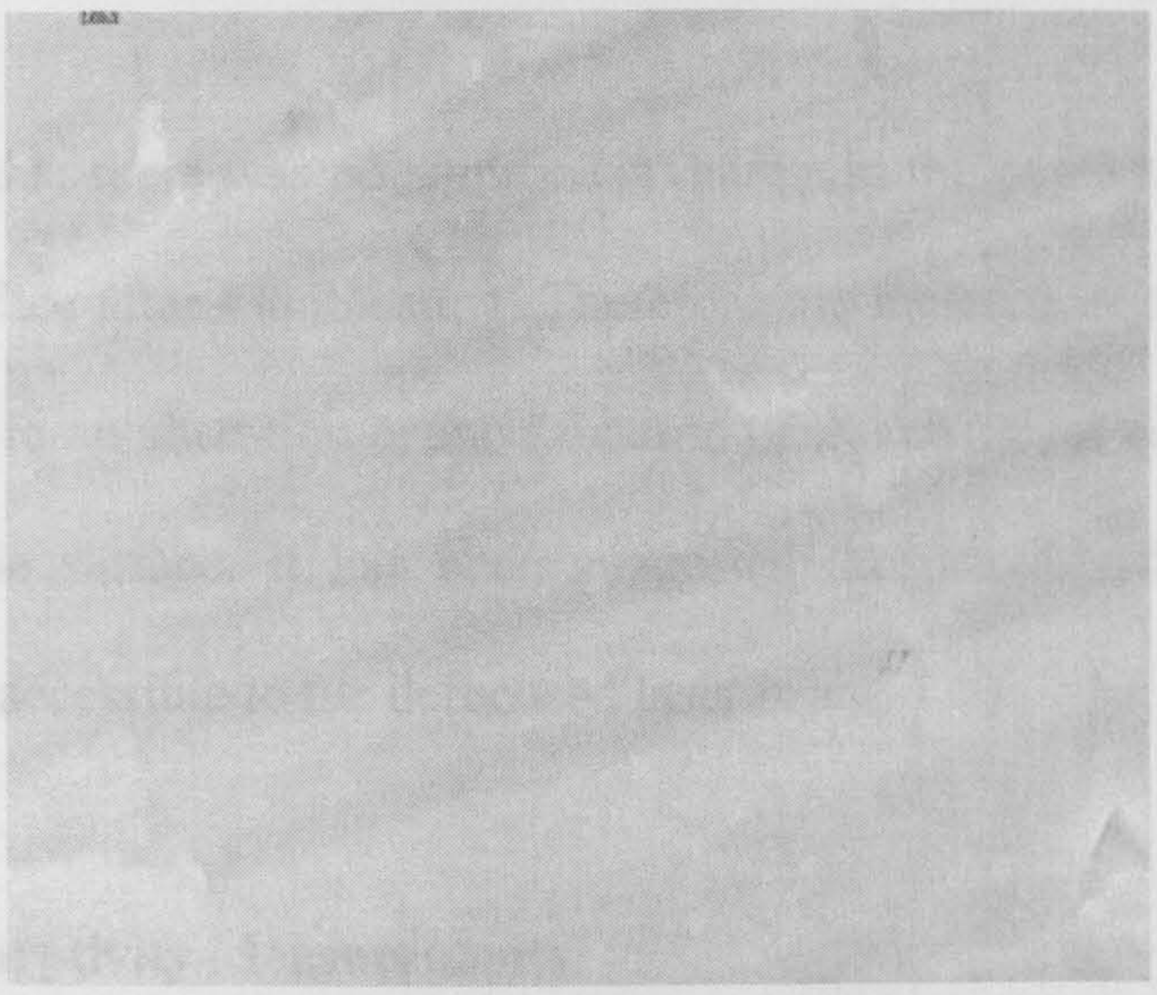

Figure 5.26 – SEM analysis of as-received surface of 3m AA5083 sample (x 1.25k)

An investigation into the chemical composition of the surface of an AA5083 sample was carried out using the SEM. As can be seen in figure 5.27, no other elements were imbedded in the surface of the sample and the chemical composition of the sample was basically unchanged.

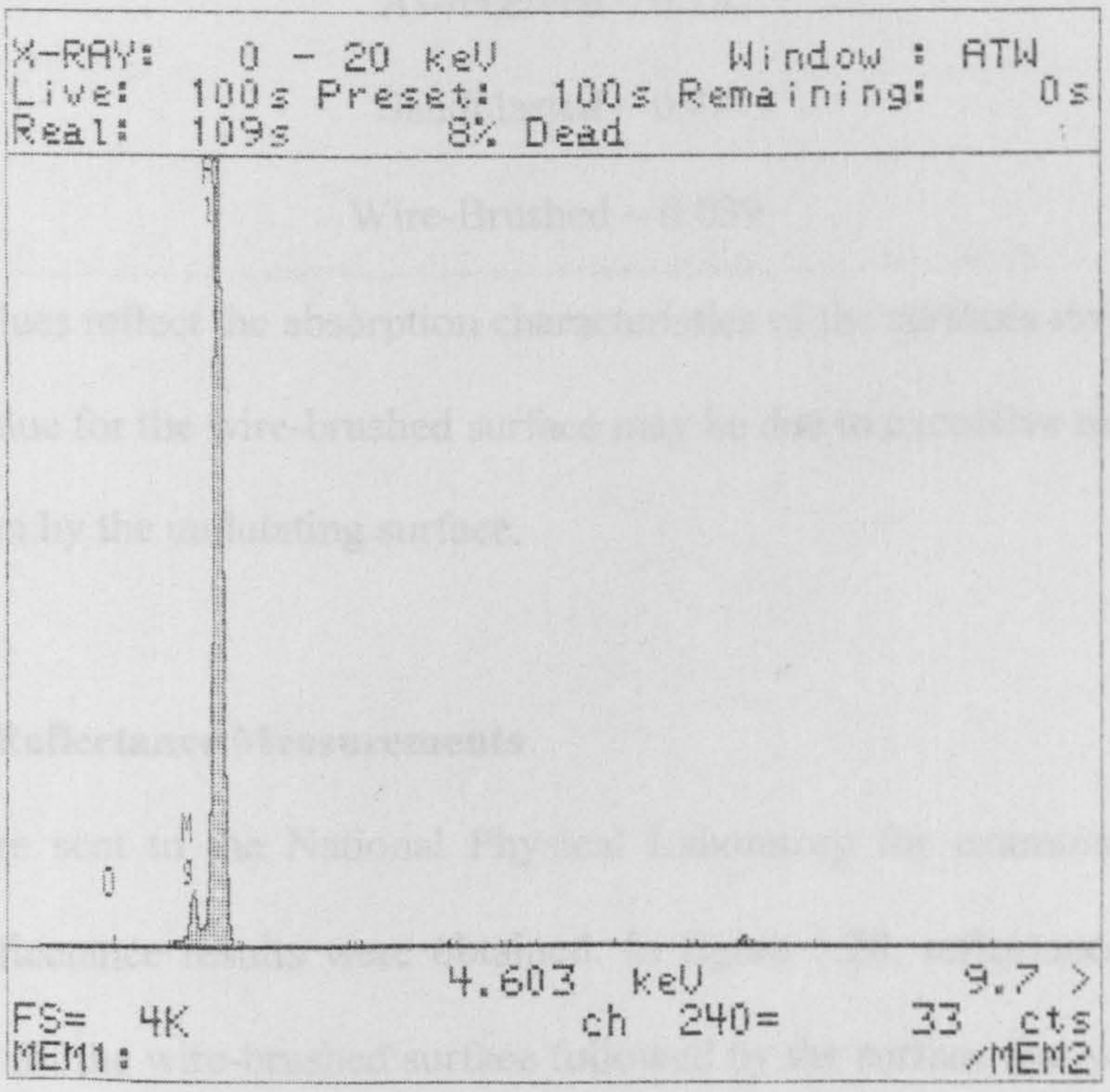

Figure 5.27 SEM analysis of sandblasted surface of AA5083 sample

It was observed that there was no significant change in the percentage of oxygen or oxide on the surface after sandblasting. Therefore the increase in absorptivity could not be attributed to an alteration or modification of the chemical composition of the sample or sample surface. It has been suggested that sandblasting increases the effective surface accessible to the defocused laser beam.

5.8. Absorptivity Measurements

Rough absorption calculations were made for the various sample surfaces of AA5083 with regard of CO_2 laser beams.

As explained in Chapter 4, the heating and cooling rates were found from the slopes of the temperature/time curves. Results obtained by substituting values into equation (4.1) gave the absorptions as follows:

As-received ~ 0.18

Sandblasted ~ 0.45

Wire-Brushed ~ 0.039

While the values reflect the absorption characteristics of the surfaces involved, the rather low value for the wire-brushed surface may be due to excessive reflections of the laser beam by the undulating surface.

5.9. Reflectance Measurements

Samples were sent to the National Physical Laboratory for examination and the following reflectance results were obtained. In figure 5.28, reflectance values (%) were highest for the wire-brushed surface followed by the surface that was first of all wire-brushed and then sandblasted. The grooves created during wire-brushing

produce diffuse reflections in all directions and this is probably what is responsible for the high reflectance.

The surface that was produced after sandblasting the as-received sample gave the least reflectance.

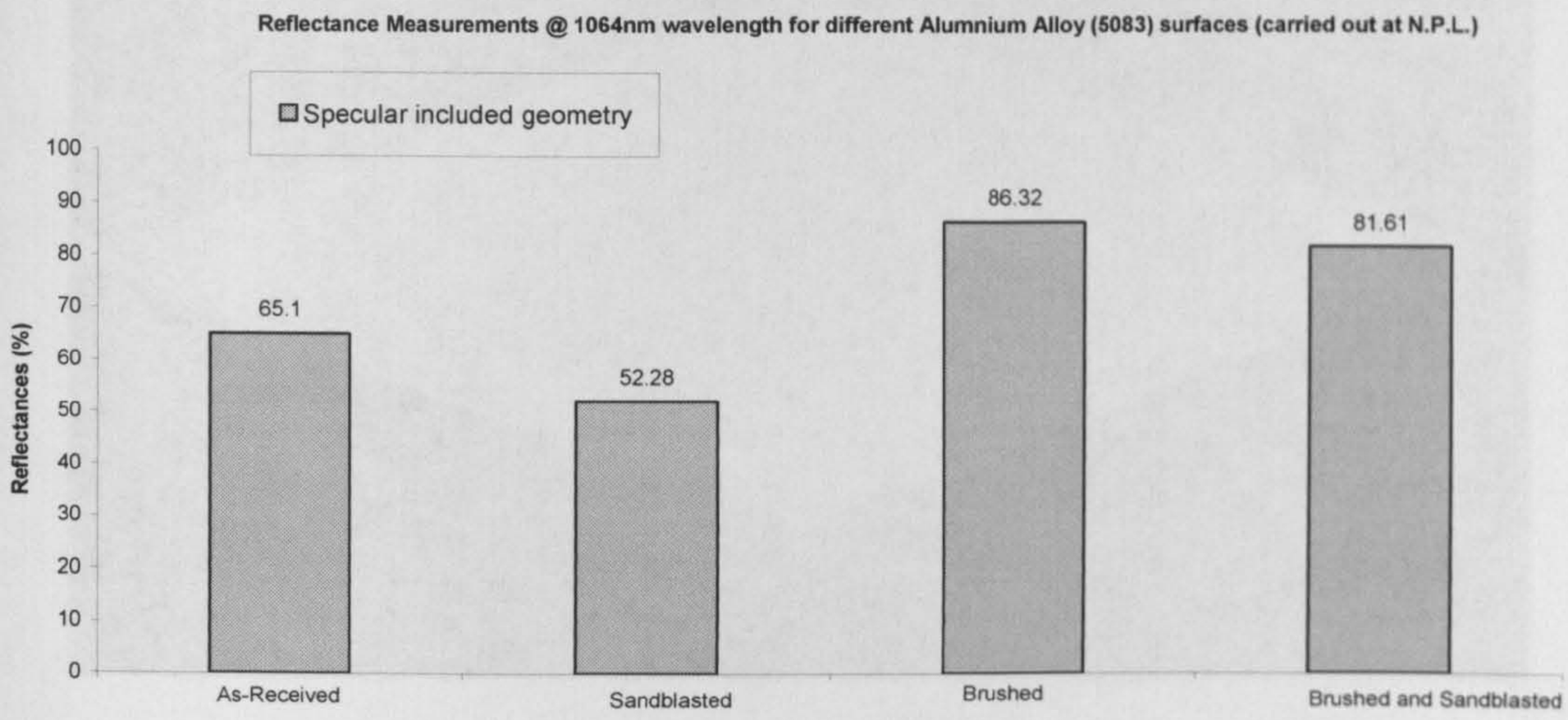

Figure 5.28 Reflectance bars for as-received, sandblasted, brushed and brushed & sandblasted

5.10. Surface Roughness Measurements

Surface roughness measurements were conducted at the National University of Ireland (NUI), Galway and the following visual profiles were obtained. Figures 5.29, 5.30 and 5.31 show the surface profiles for as-received, wire-brushed and sandblasted AA5083 sample surfaces.

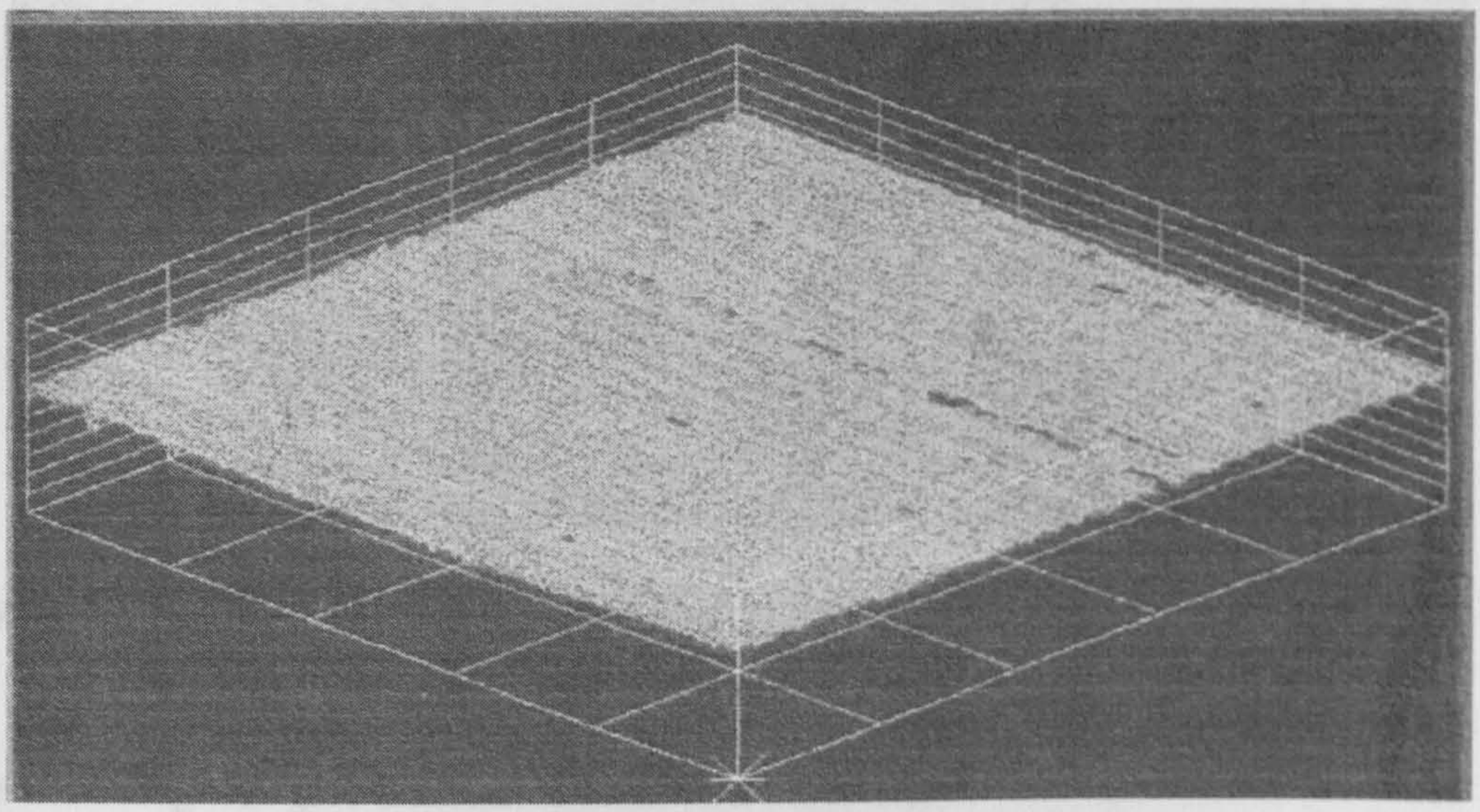

Figure 5.29 Surface roughness profile of surface of as-received AA5083 sample (x20)

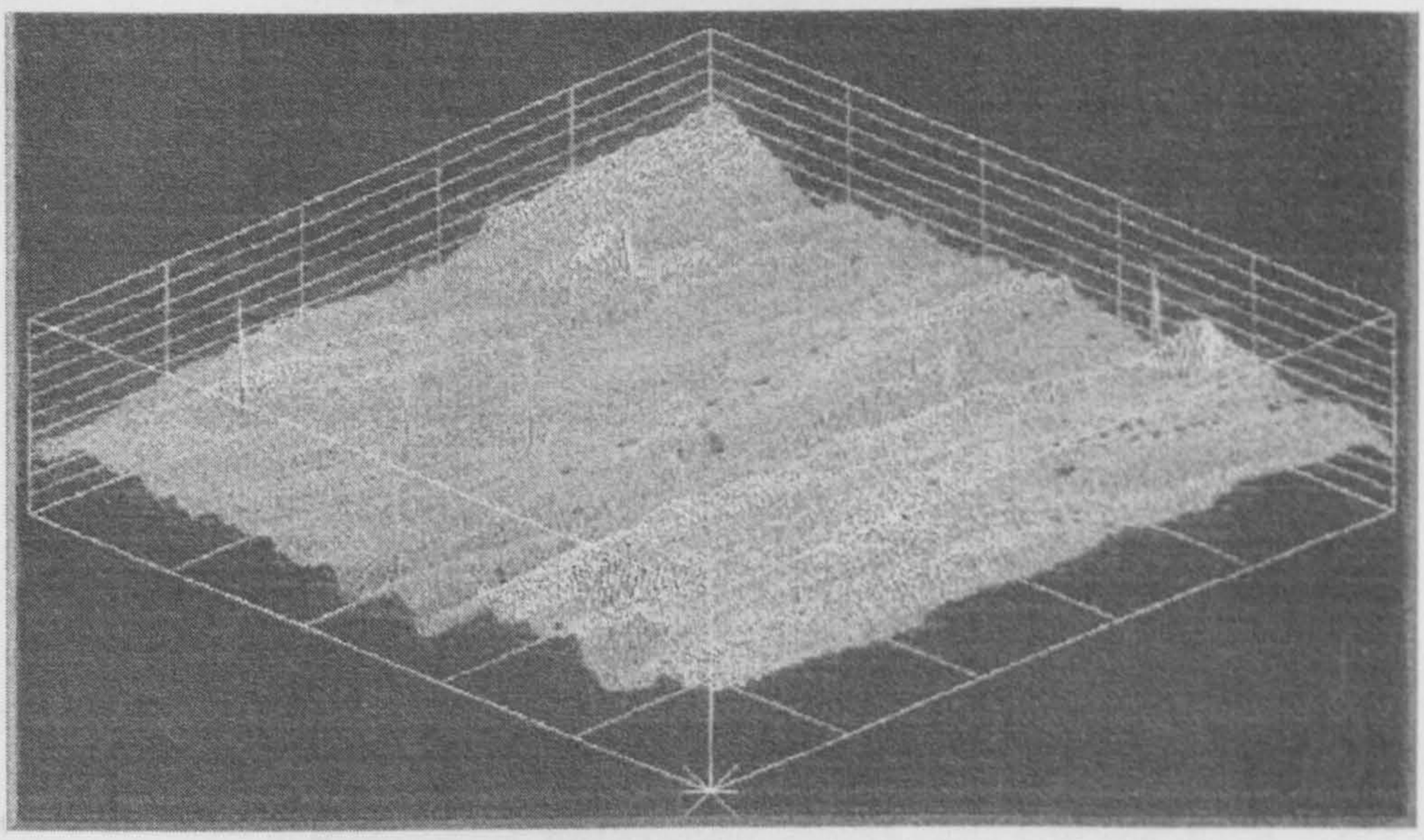

Figure 5.30 Surface roughness profile of surface of wire-brushed AA5083 sample (x 20)

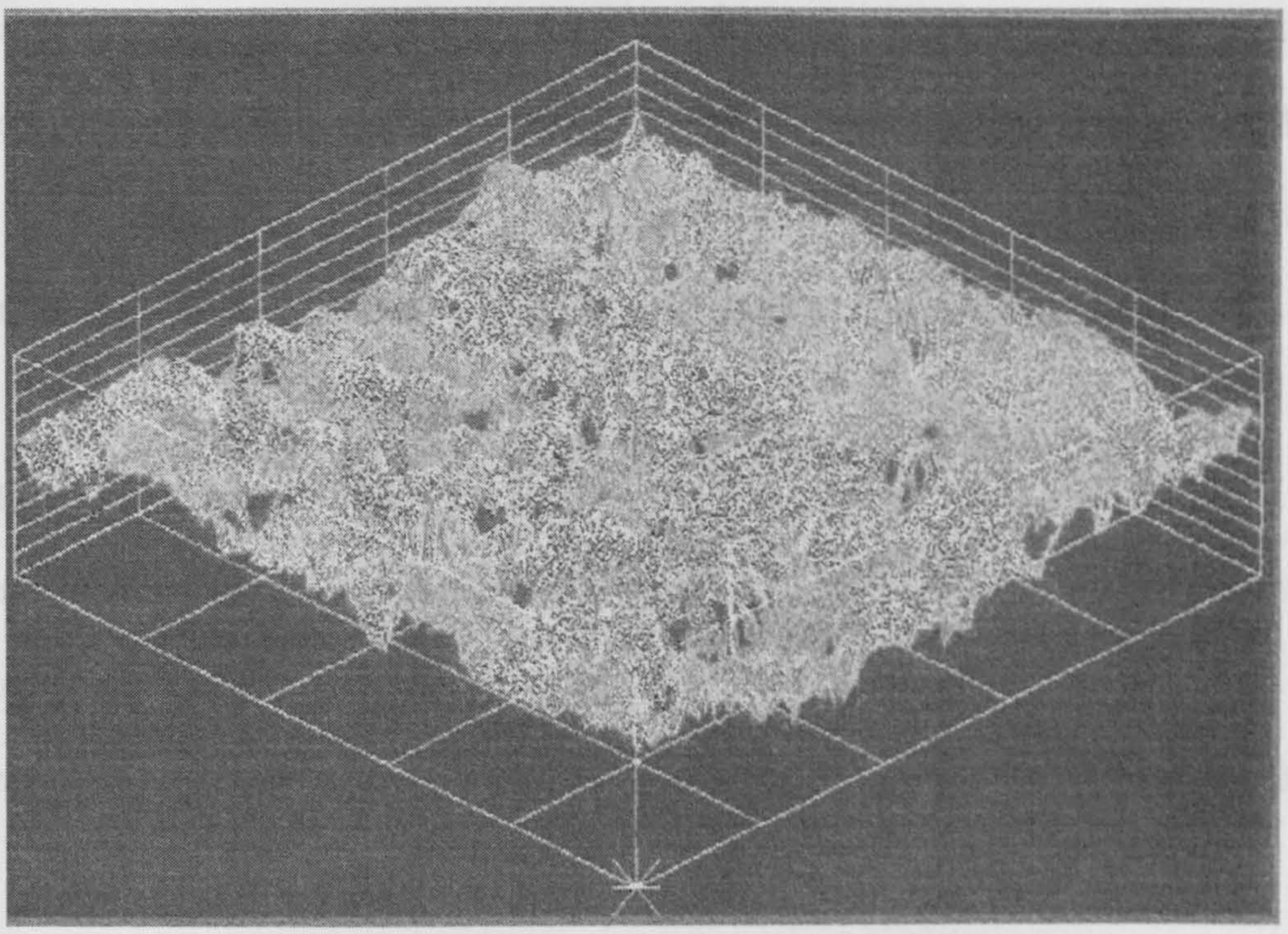

Figure 5.31 Surface roughness profile of surface of sandblasted AA5083 sample (x 20)

The above figures give a visual indication of the degree of roughness of the three surfaces. The surface roughness values were automatically calculated and the values are as follows:

- As-received = 45.099 μm
- Wire-brushed = 53.403μm
- Sandblasted = 57.853μm

It must be stressed that equality in surface roughness values may not necessarily produce the same degree of absorptivity. One surface pattern may generate more reflectivity than the other as is clearly the case here.

It should be stated that the surface roughness is not the only factor determining the absorptivity of a surface. Material properties also contribute to a large extent.

However, it can be seen that sandblasting increased surface roughness, reduced reflectance of the surface, increased effective surface area of the surface accessible to the laser beam and produced a dull matt finish as seen by the naked eye. Furthermore, the chemical composition of the material remained unchanged.

5.11 Weld Analysis

Comparisons of experimental results and results obtained from numerical simulations using the TS4D code were undertaken and figures 5.32 and 5.33 show the comparisons for 3mm AA5083 welded at 600mm/min and 720mm/min respectively.

5.11.1 TS4D Simulation Results

The graphs obtained from TS4D simulation results show the same trend as the experimental results.

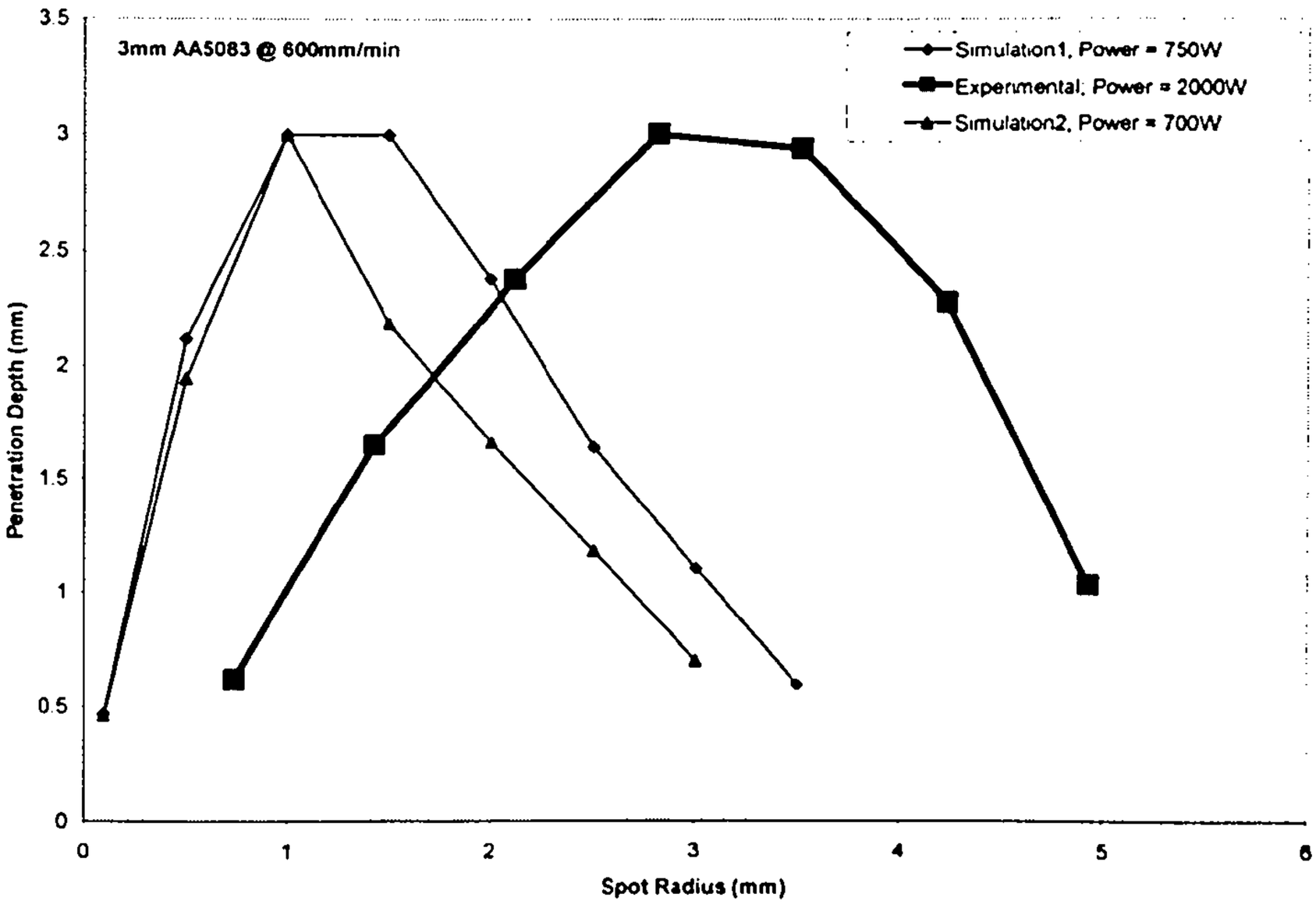

Figure 5.32 TS4D simulation and experimental results for laser conduction welding of 3mm gauge AA5083 welded at 600mm/min (showing variation of penetration depth with spot radius)

The penetration depth/spot radius variation is clearly visible from figure 5.32. The experimental curve (thick line) and the theoretical curves (thinner lines) do not coincide but penetration depth increases with increase in spot radius. This fact was utilised in producing butt-welds on 2mm gauge and 3mm gauge AA5083 sheets. Factors that could make the theoretical and experimental results agree better will be discussed in Chapter 6.

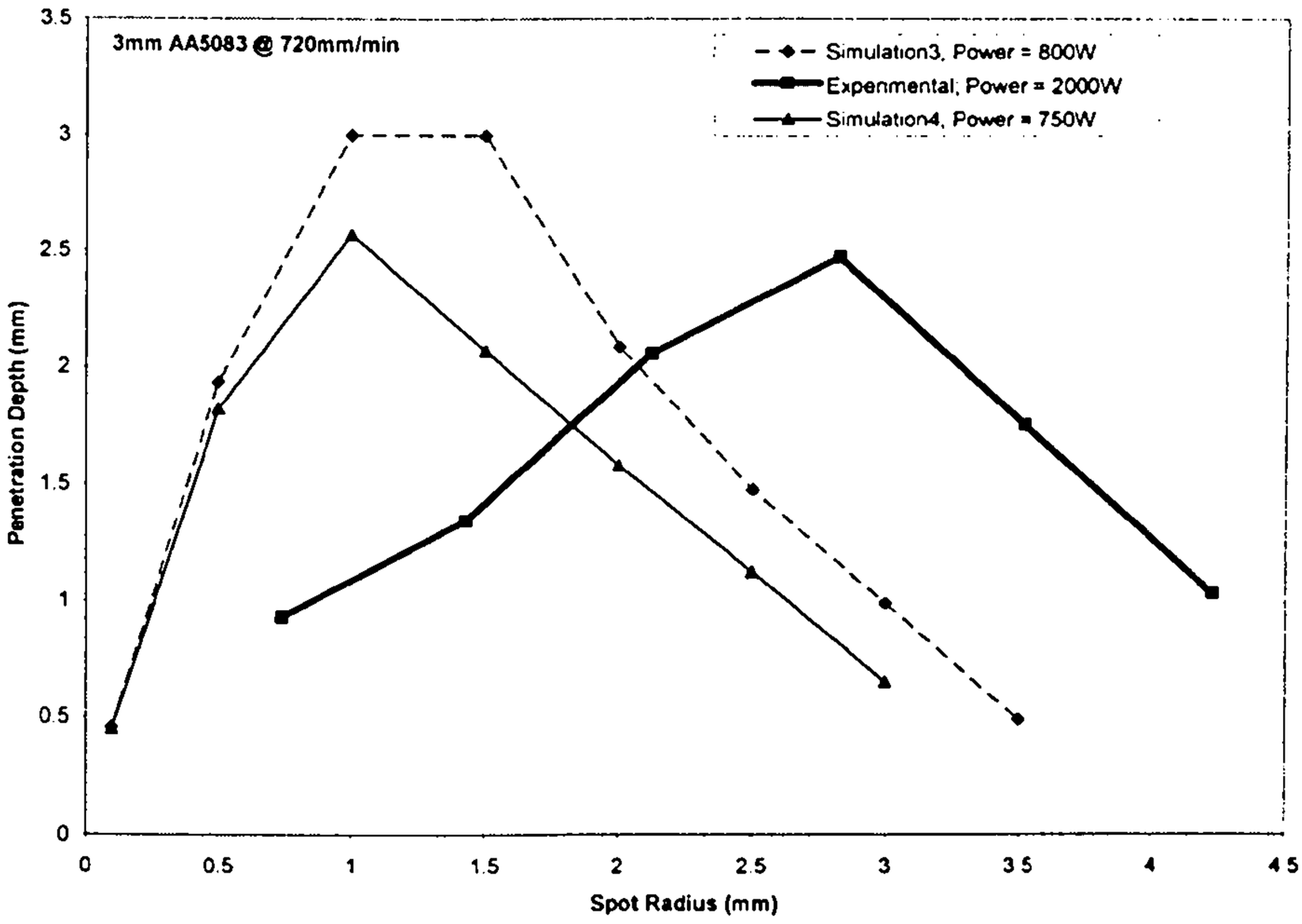

Figure 5.33 TS4D simulation and experimental results for laser conduction welding of 3mm gauge AA5083 at 720mm/min (showing variation of penetration depth with spot radius)

Figure 5.33 shows theoretical and experimental curves obtained for 3mm AA5083 welded at 720mm/min. The general shapes of the theoretical curves and experimental curve are similar although they do not coincide. Again, the TS4D simulations confirm the trend observed from experimental results.

Results obtained from semi-quantitative analysis, ABAQUS simulations, TS4D all confirm what has been obtained from welding experiments of aluminium alloys.

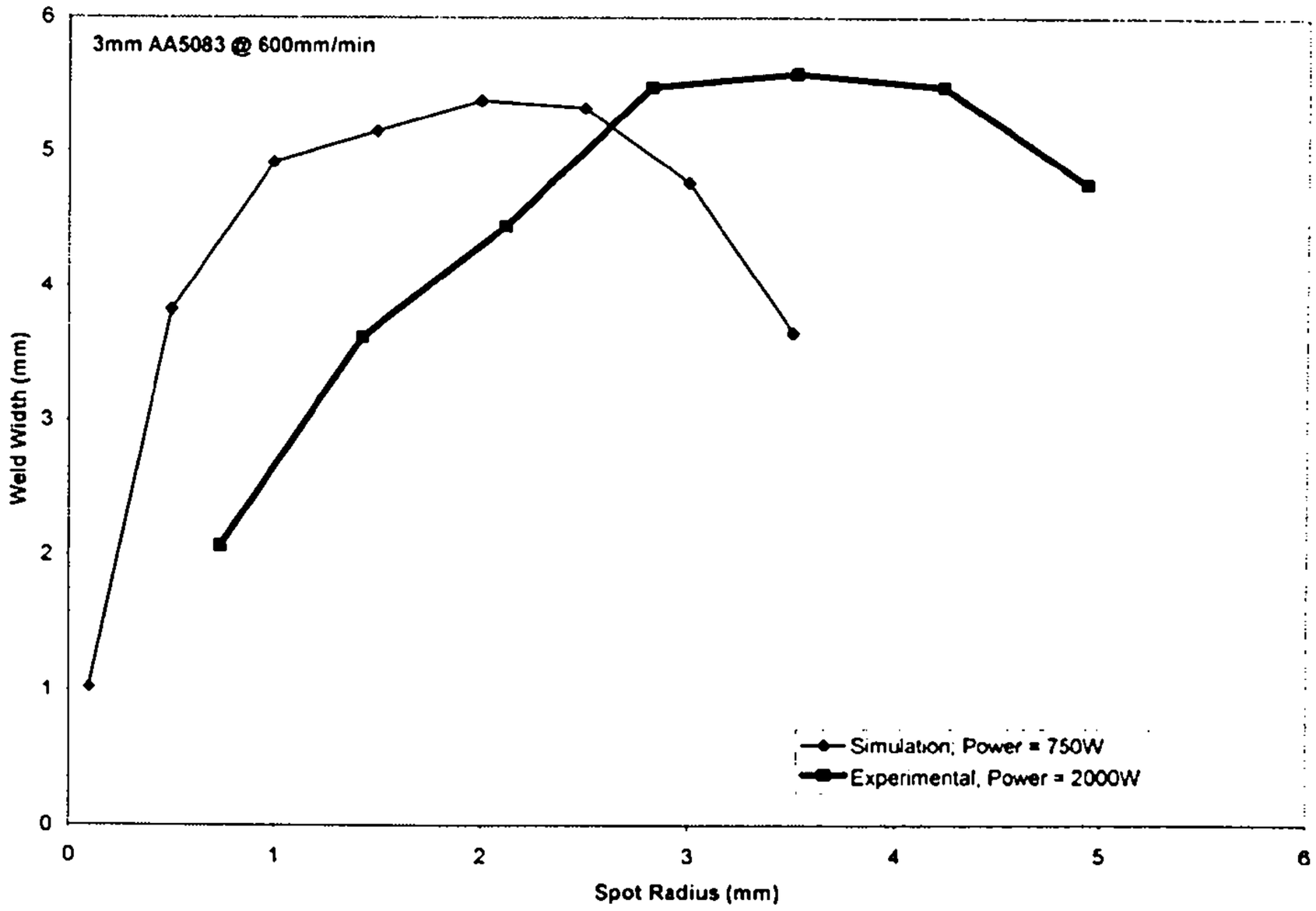

Figure 5.34 TS4D simulation and experimental results for laser conduction welding of 3mm gauge AA5083 at 600mm/min (showing variation of weld width with spot radius)

Figure 5.34 shows experimental results as well as TS4D simulation results for weld width/spot radius variation with regard to 3mm AA5083 welded at 600mm/min. The curves are similar in shape and confirm that as the spot radius increases beyond the optimum point (point of maximum penetration depth), the effective spot radius decreases.

The spot radius/penetration depth phenomenon can be attributed to the interplay between decreasing power intensity and increasing interaction time amongst other things. These interacting phenomena will be analysed in the following discussion chapter.

6. Discussion

6.1 Introduction

In this chapter some of the theoretical and experimental results presented in the previous chapter will be discussed and analysed. The first part of this chapter will concentrate on the formulation of a phenomenological model of the laser conduction welding process. The purpose of this model is to explain the variation of weld cross section with changes in laser beam diameter. The final part of this chapter will discuss the tensile test results presented earlier in this thesis.

6.2 The variation of weld cross section with laser beam diameter

6.2.1. Experimental results review

Figure 6.1 shows a typical set of results demonstrating the variation of weld depth with increasing laser spot radius.

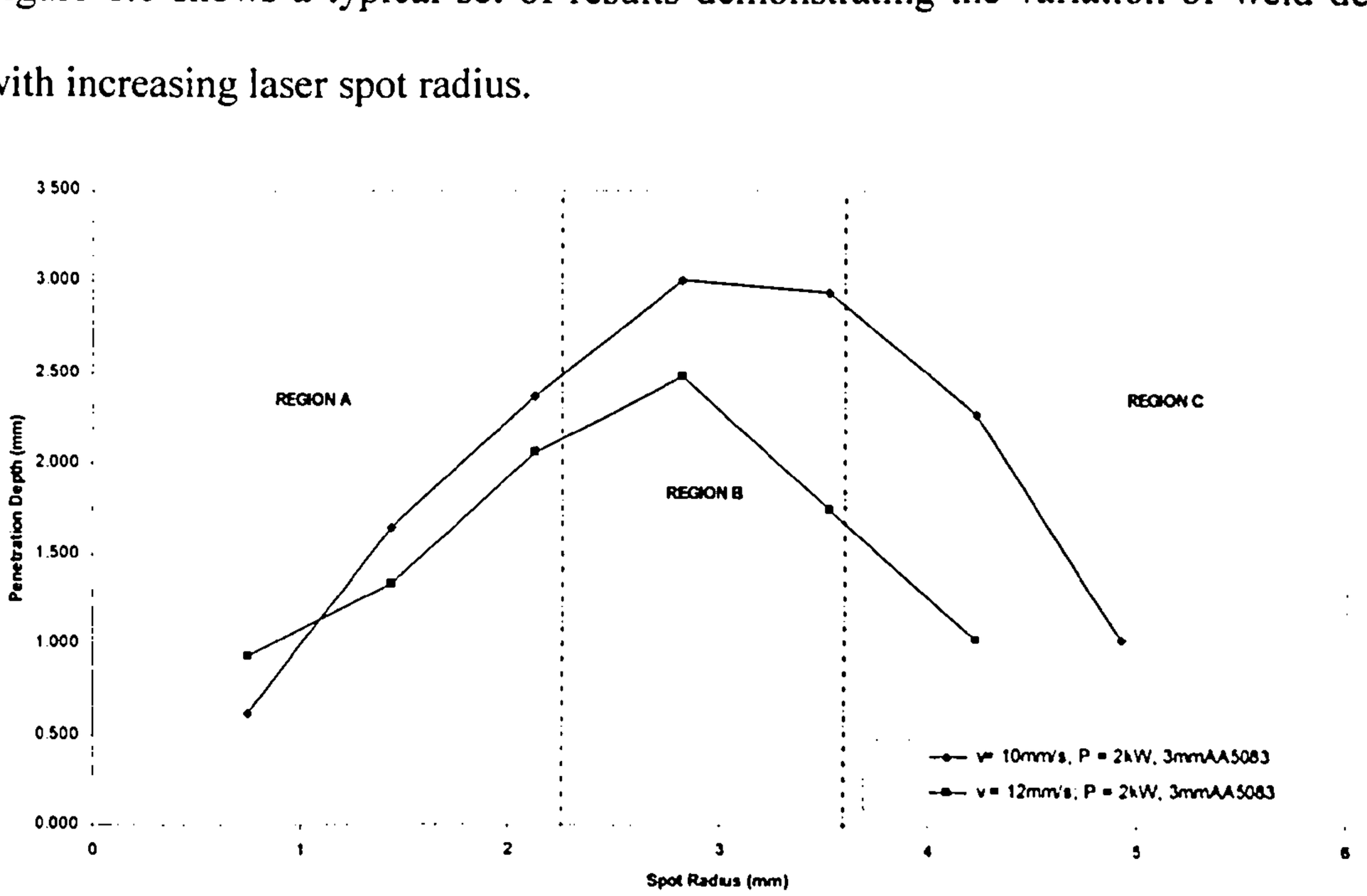

Figure 6.1 – Graph showing the variation of weld depth for Nd:YAG laser conduction welding of 3mm gauge AA5083

Figure 6.2 shows similar results relating to the variation in weld width on the top surface of the material. It is clear from these results that there is an optimum laser beam diameter (for these experimental conditions) for maximum weld penetration and width.

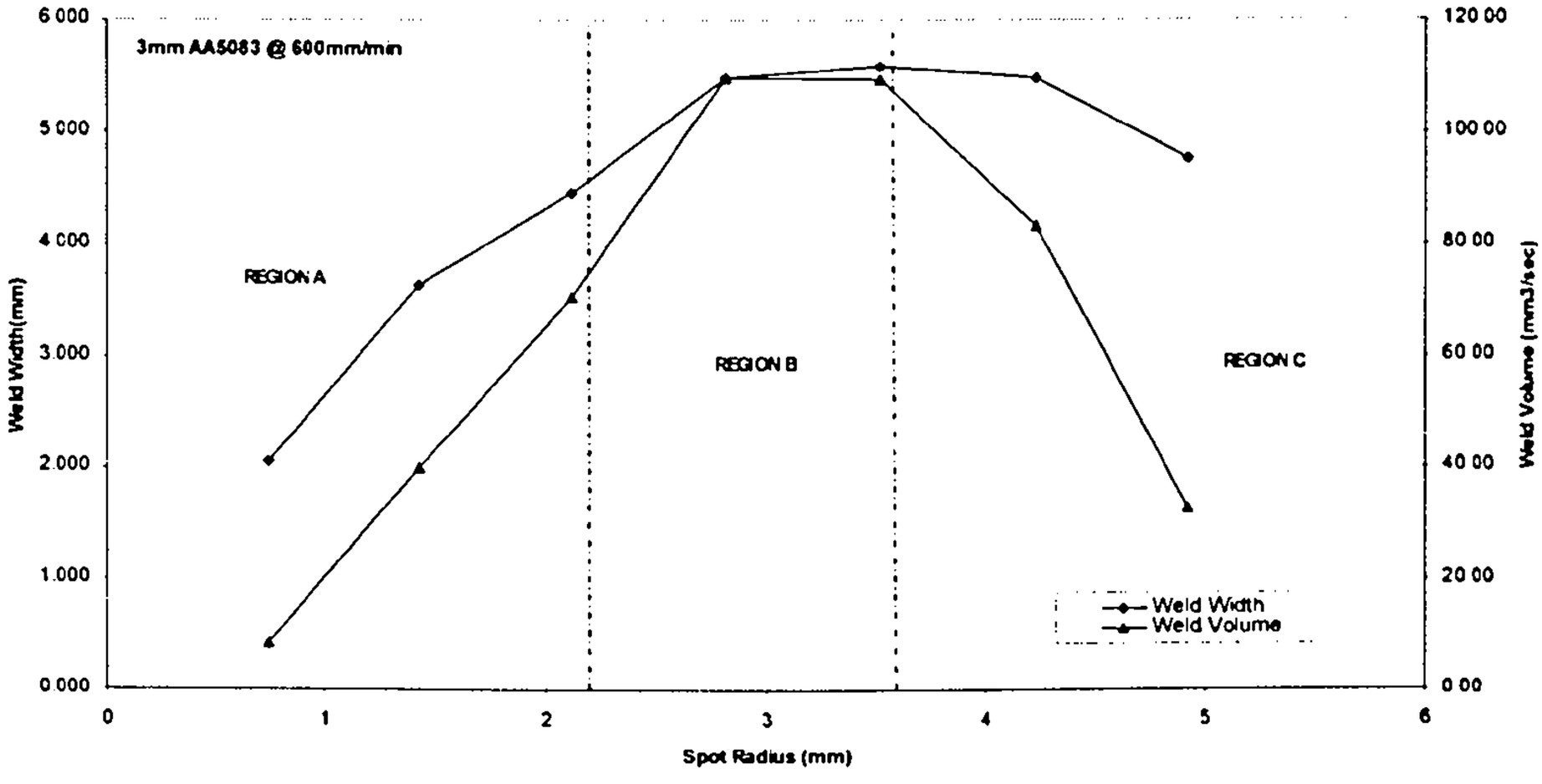

Figure 6.2 – Graph showing the variation of weld width (top surface) for laser conduction welding of 3mm gauge AA5083

This, of course, indicates that there is an optimum laser beam diameter for maximum melting efficiency. We need to consider why this should be the case and this is best done by dividing up the graphs into three regimes;

1. Region A; where the laser beam is below the optimum radius range for maximum melting efficiency,
2. Region B; where the laser beam radius is close to optimum for maximum melting efficiency and
3. Region C; where the beam radius is too large for maximum melting efficiency.

Optimum melting efficiency is obviously of great interest as it gives us an insight into the fundamentals of laser-material interaction. Also, an understanding of this optimum interaction could be useful in minimising the cost of the welding process.

Figure 6.3 shows that the optimisation of the melting efficiency occurs as the penetration depth and weld width are optimised. As the laser spot radius increases, two things happen in the laser-material interaction zone:

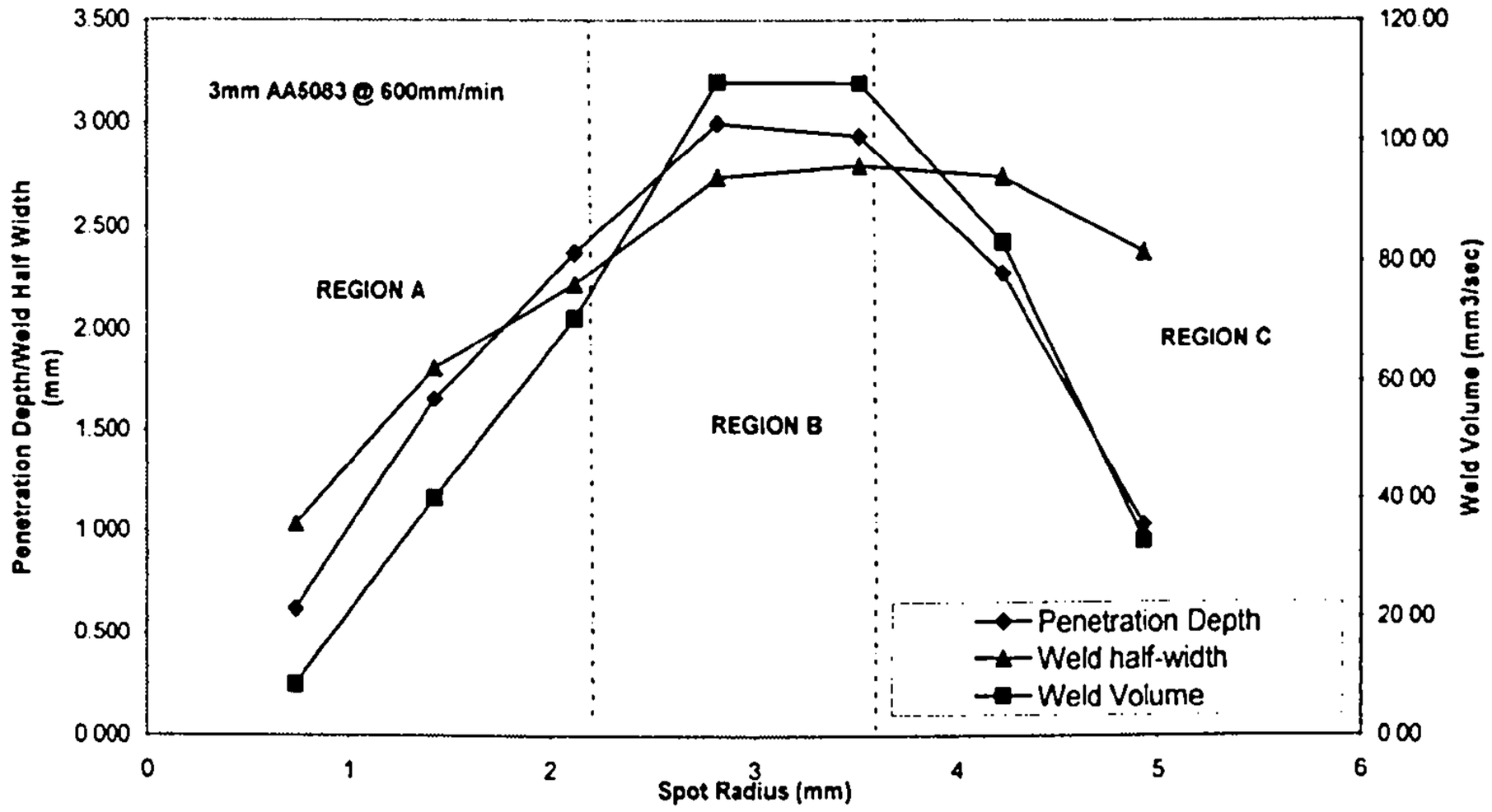

Figure 6.3 – Graph showing the variation of penetration depth/weld half width and weld volume with spot radius for 3mm gauge AA5083 welded at 600mm/min (N.B. Half width is shown here for direct comparison with the beam radius)

1. The intensity of the laser beam decreases. As the beam is circular in cross section this decrease in intensity is proportional to the square of the radius.
2. The interaction time between the material and the laser beam increases. This is because, at a given process speed, a larger diameter beam takes longer to move over any point on the material surface.

It is clearly the interplay between these two effects which leads to an optimisation in the laser-material interaction which, in turn, leads to a maximum melting efficiency.

6.2.2 Theoretical results review

Figures 6.4 and 6.5 show that the 1D and 2D theoretical analyses also demonstrate an optimisation of the melting depth with laser spot radius. Once again the graphical results can be divided up into three distinct regions with similar characteristics to the experimental results.

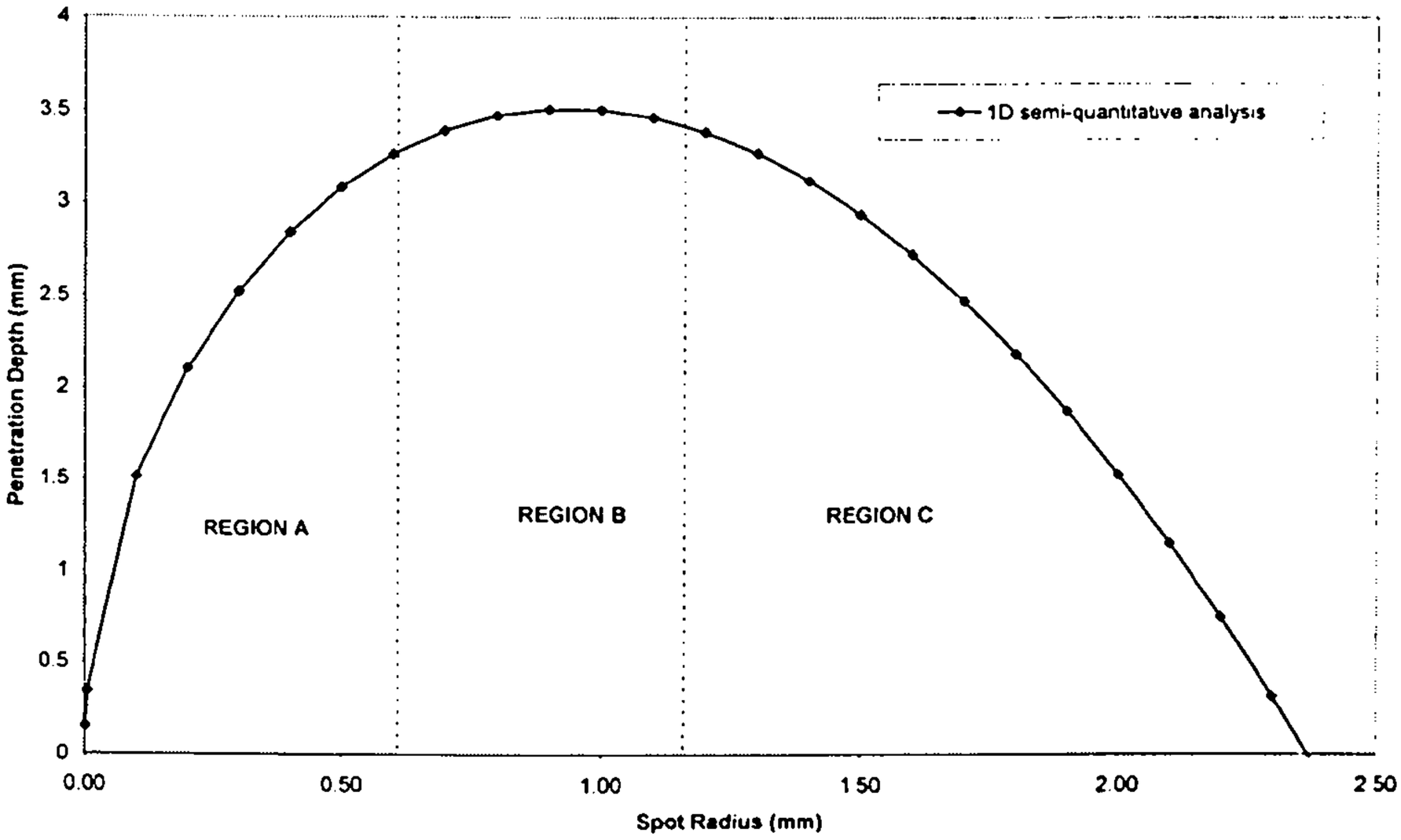

Figure 6.4 – Typical results of the 1D semi-quantitative simulation of the laser conduction welding process.

One important point which needs clarification is that these simple theoretical models produce unreliable results when the laser beam diameter is very small. This is for two main reasons:

1. At a small beam radius the interaction between the laser and the material is not conduction limited and involves a number of phenomena which are not accounted for in these simple models.
2. The theoretical calculations can produce results for beam diameters which are smaller than the physically possible minimum diameter.

This unreliability of the models is demonstrated by the results given in figures 6.6 and 6.7.

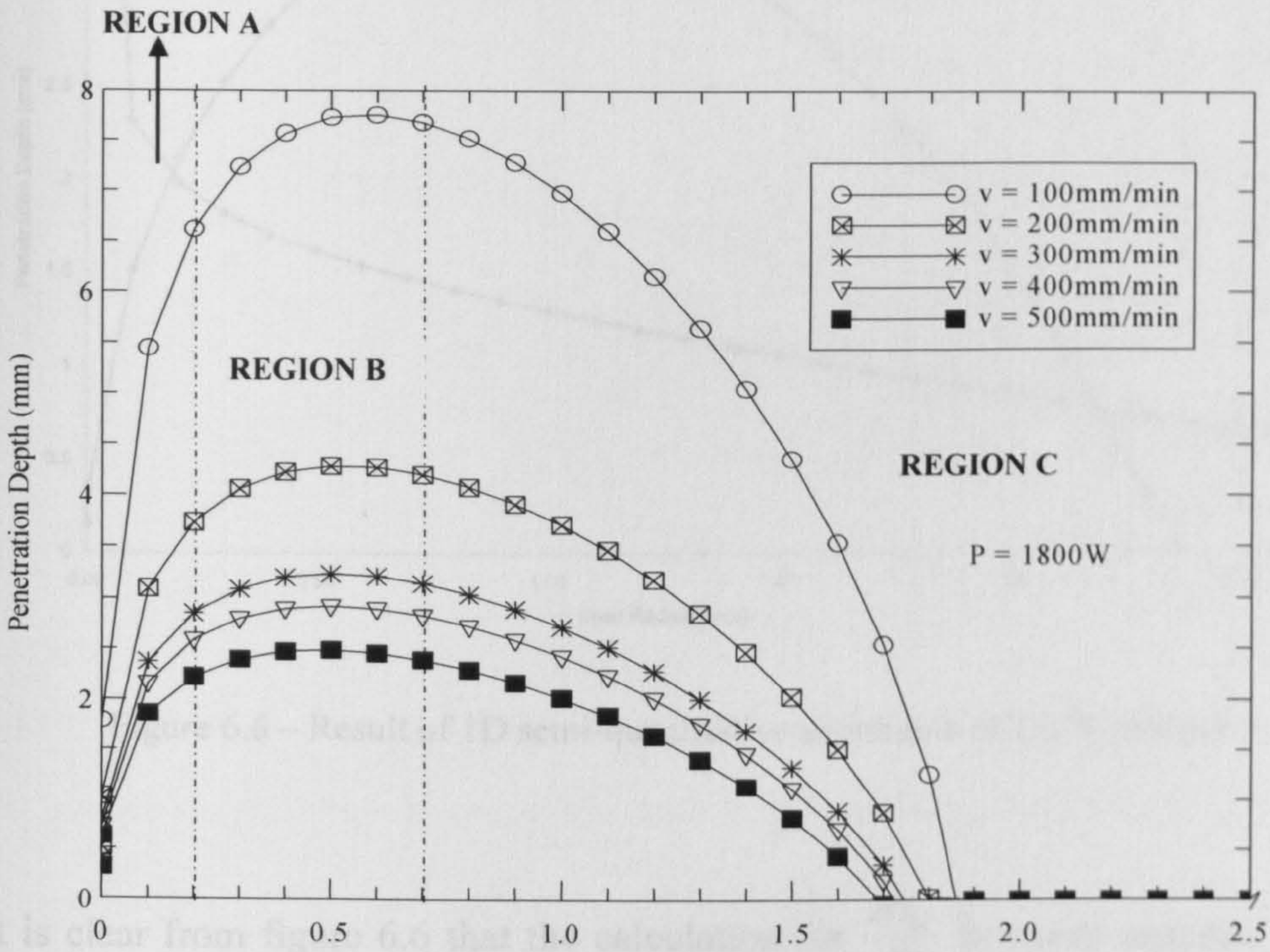

Figure 6.5 – Penetration depth/spot radius curves for different welding speeds obtained from 2D semi-quantitative analysis.

Figure 6.6 shows the result for the 1D semi-quantitative analysis. The penetration depth/spot radius curve is shown as well as a curve showing the variation of $\frac{dz_m}{dR}$ with spot radius. $\frac{dz_m}{dR}$ is the rate of change of penetration depth with spot radius.

From equation 3.10, $z_m = AR^{\frac{1}{2}} - BR^2$ where A and B are constants that depend on material properties. Differentiating z_m with respect to R, we have

$$\frac{dz_m}{dR} = \frac{A}{2\sqrt{R}} - 2BR \qquad (6.1)$$

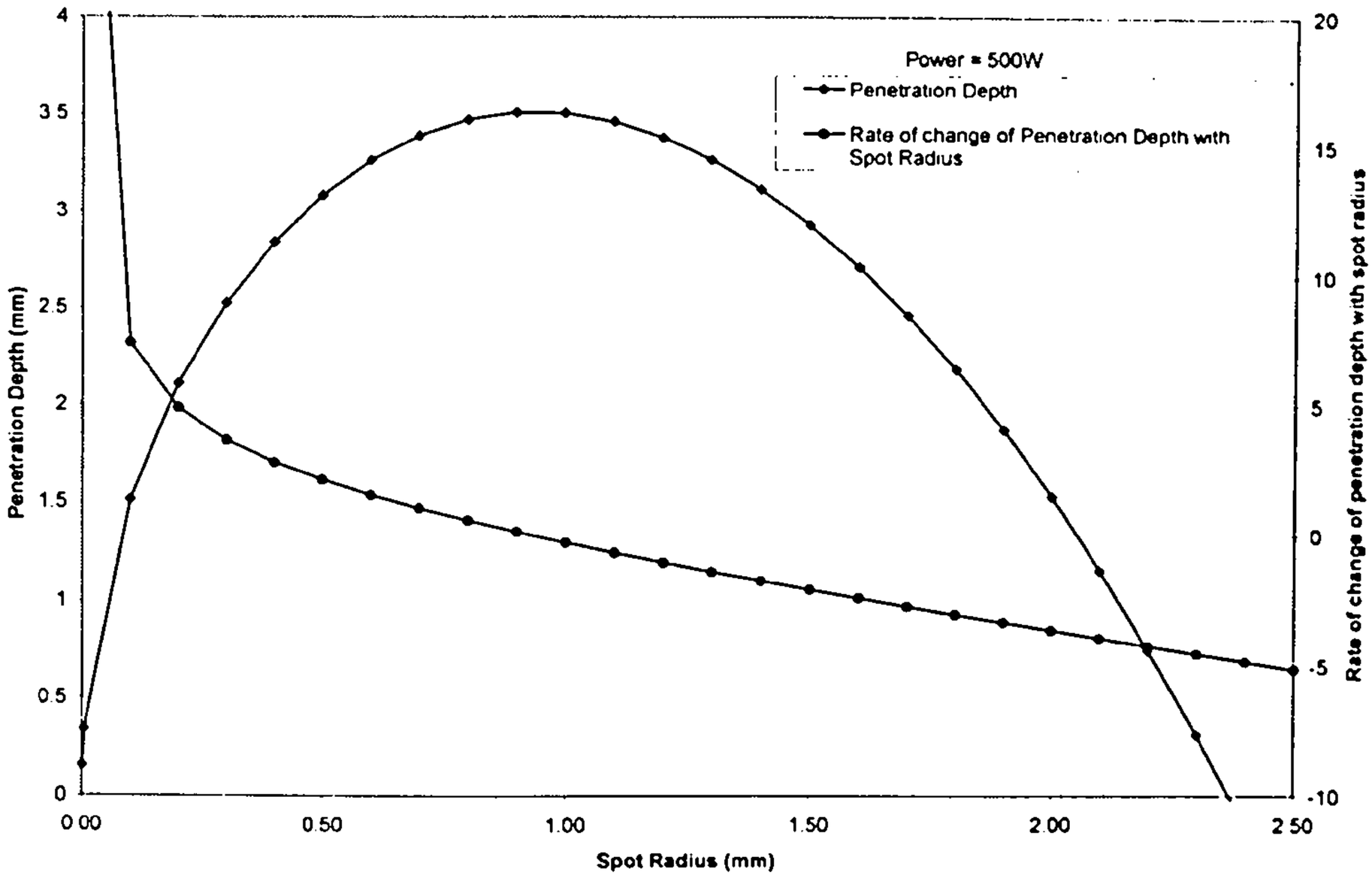

Figure 6.6 – Result of 1D semi-quantitative simulation of LCW process

It is clear from figure 6.6 that the calculation for $\frac{dz_m}{dR}$ becomes unstable when the spot radius is very small (in this case below 0.2 mm). At values of R above approximately 0.25 mm the calculation gives an approximately linear variation in the rate of $\frac{dz_m}{dR}$ which would be expected when the effects in question are being balanced against each other (i.e. the effects of reducing average intensity and increasing interaction time as a function of R). At small values of R the simple relationship expressed by equation 6.1 is no longer appropriate.

Figure 6.7 reveals the weakness in the TS4D simulation at small laser beam radii in that the surface temperature does not increase above its maximum allocated value of 2732K which is equivalent to the boiling point of the material.

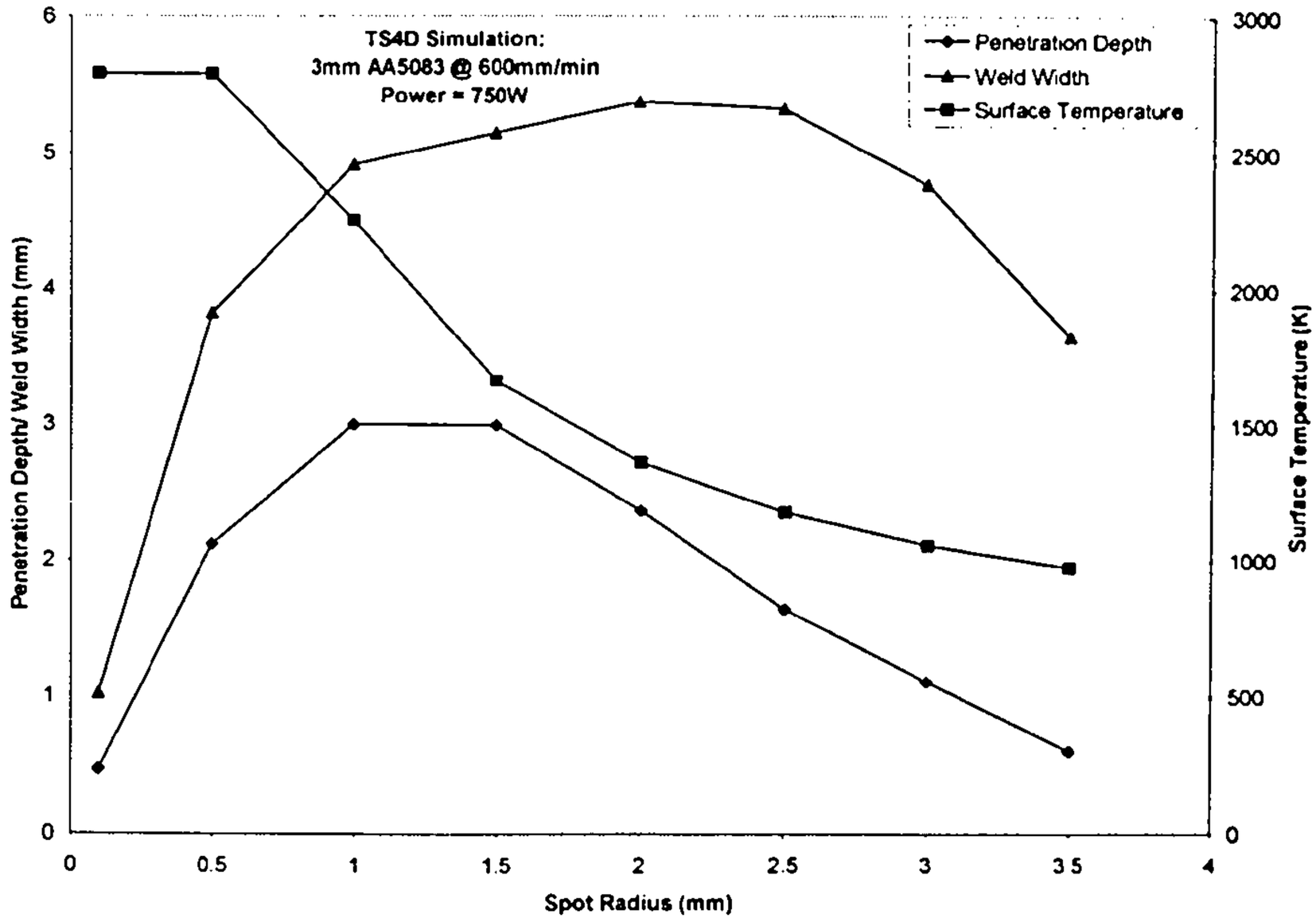

Figure 6.7 – Graph showing TS4D simulation for variation of penetration depth, weld width and surface temperature with spot radius for 3mm AA5083 welded at 600mm/min

Sub-surface boiling of the material and ionisation of the vapour are not considered in this model. In summary, the theoretical results mirror the experimental results in showing that there is an optimum laser beam radius for minimum melting. However the models used here are unreliable at very small beam radius values.

6.2.3 A phenomenological model of the variation of weld cross section with beam diameter

A phenomenological model of the change of melt cross section with laser spot diameter is presented in figure 6.8 which graphically describes the laser-melt combinations associated with regions A, B and C of the earlier graphs. The three types of interaction can be briefly explained as follows; (ignoring experimental and theoretical results for small spot radii where the process is not conduction limited):

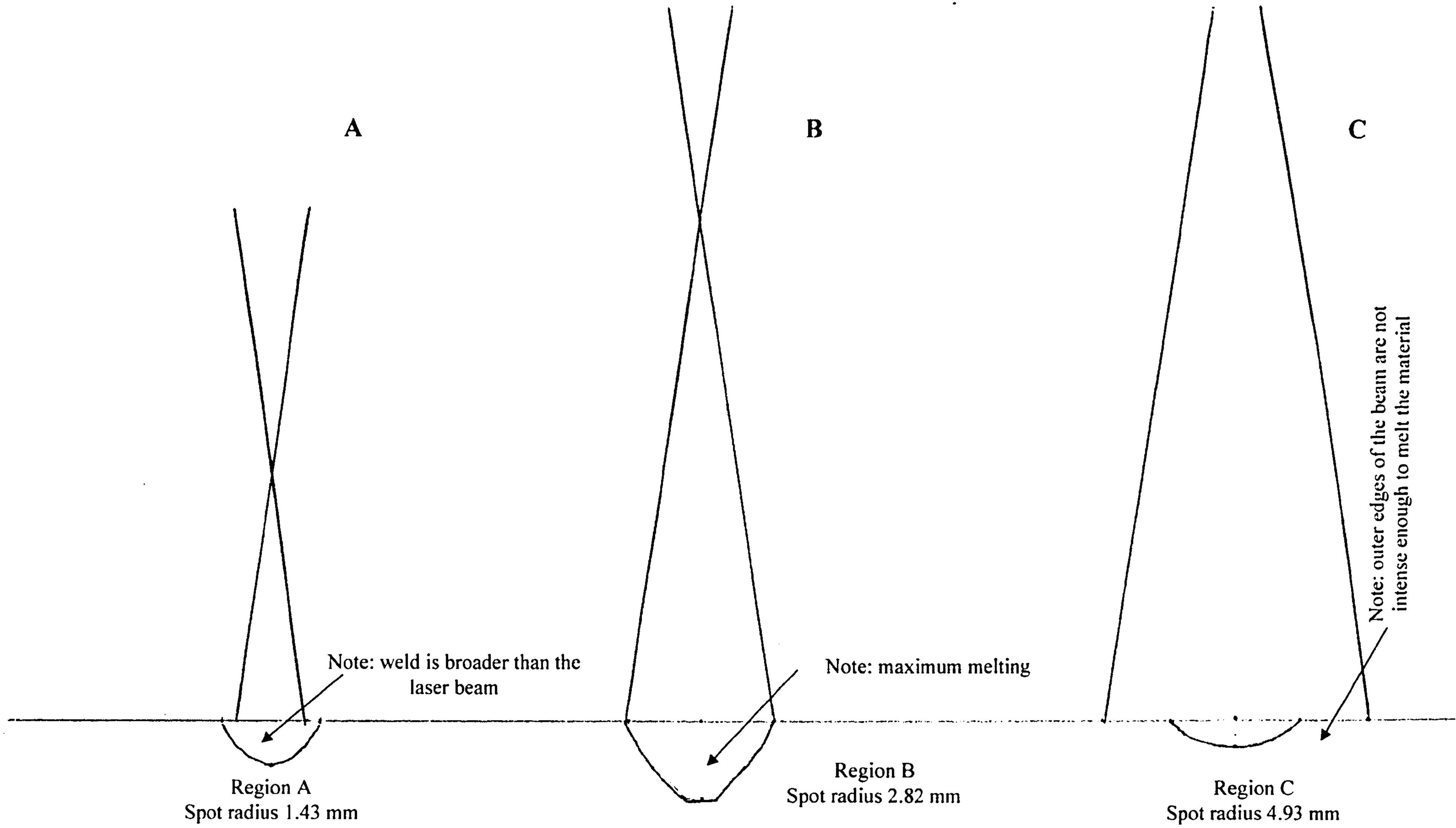

Figure 6.8 – A graphical description of the change in melt cross section with laser beam diameter (information taken from the measurements for figure 6.3)

Region A (see figure 6.8A) – In this case the melt diameter can exceed the beam diameter because the laser beam intensity is greater than that necessary to simply melt the material in the interaction zone. This point is confirmed in figure 6.9 which gives the values for the weld width/spot width ratios taken from figure 6.3

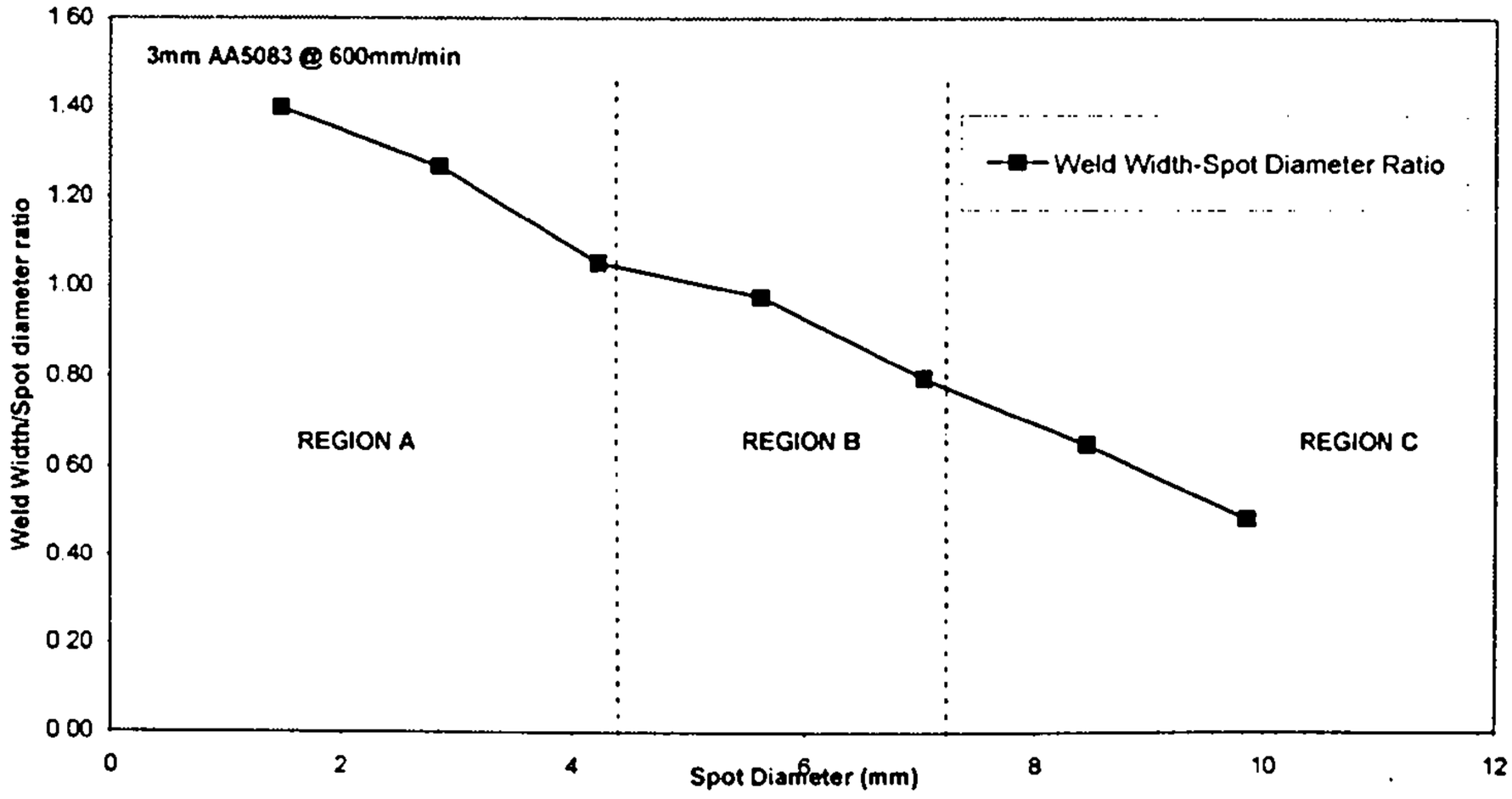

Figure 6.9 – The variation of the weld width/spot diameter ratio with increasing spot diameter

Figure 6.9 clearly demonstrates that in region A the ratio of weld width to laser beam width is greater than 1.0. This extension of the melt region beyond the boundaries of the incident beam is obviously a product of the rapid transfer of heat away from the laser generated melt into the surrounding material. This transfer takes place by two mechanisms:

1. Simple heat conduction from the weld pool (which because of the intense laser irradiation contains surplus heat).
2. Marangoni flow – This flow is a stirring action set up in the melt which tends to transfer hot melt from the centre of the weld to the cooler edges. This is demonstrated in figure 6.10.

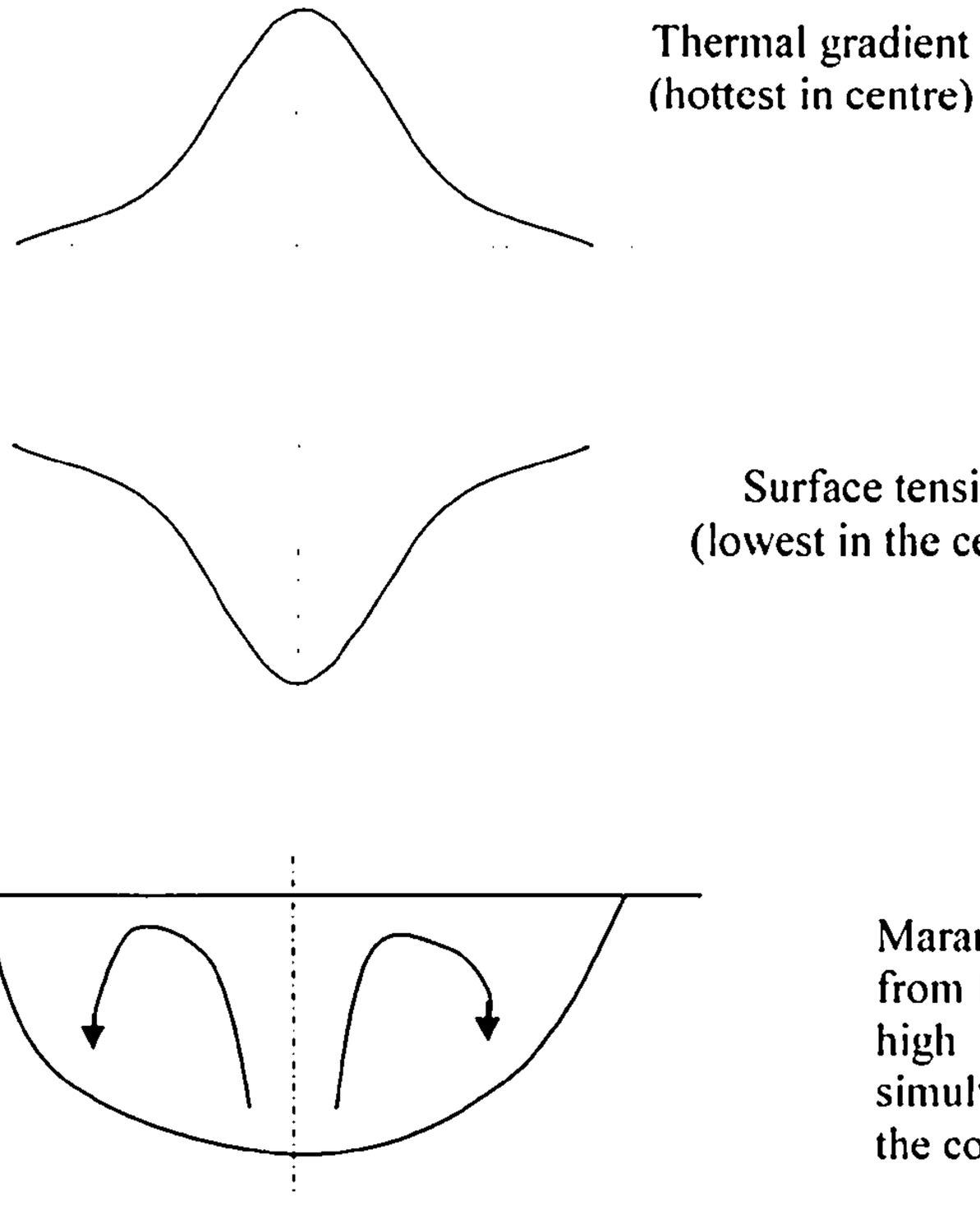

Figure 6.10 – A diagrammatic explanation of Marangoni flow

Marangoni flow is driven by the surface tension gradients within the melt pool. Generally, the surface tension of a liquid is inversely proportional to its temperature. This means that there is a tendency for hot (low surface tension) melt to migrate from the centre of the weld to the cooler (high surface tension) edges of the weld (as shown in figure 6.10). When the hot melt travels to the edges of the weld it carries some of its heat with it and this can melt the surrounding solid material. In this way the weld becomes wider than the incident laser beam.

In region A however the laser-material interaction is over too soon to allow the maximum amount of material melting to occur.

Region B: In this region of optimum melting the conductive heat flow, marangoni flow, laser intensity and interaction time all combine supportively to achieve the maximum amount of melting (see figure 6.8B).

Region C: In this region the laser-material interaction time is greater than was the case in regions A and B. However the laser beam intensity is reduced. This reduction in intensity means that melting only takes place near the centre line of the laser path where the interaction time is at a maximum and so is the laser beam intensity. These two points need some clarification:

a) Interaction time

The laser beam is circular in cross section and so those parts of the workpiece surface which are close to the centre line of travel will experience the laser for a longer time than those parts which are further from the centre line. This is demonstrated in figure 6.11.

In figure 6.11 f is a factor that is applied to the beam width to give the distance of travel of the laser beam away from the centre line. This is because the length of a chord of a circle can be expressed as the product of the diameter and a number. Alternatively if x is the distance from the centre line then the interaction time away from the centre line is $\frac{\sqrt{d^2-4x^2}}{v}$ or $\frac{2\sqrt{r^2-x^2}}{v}$ where r is the beam radius.

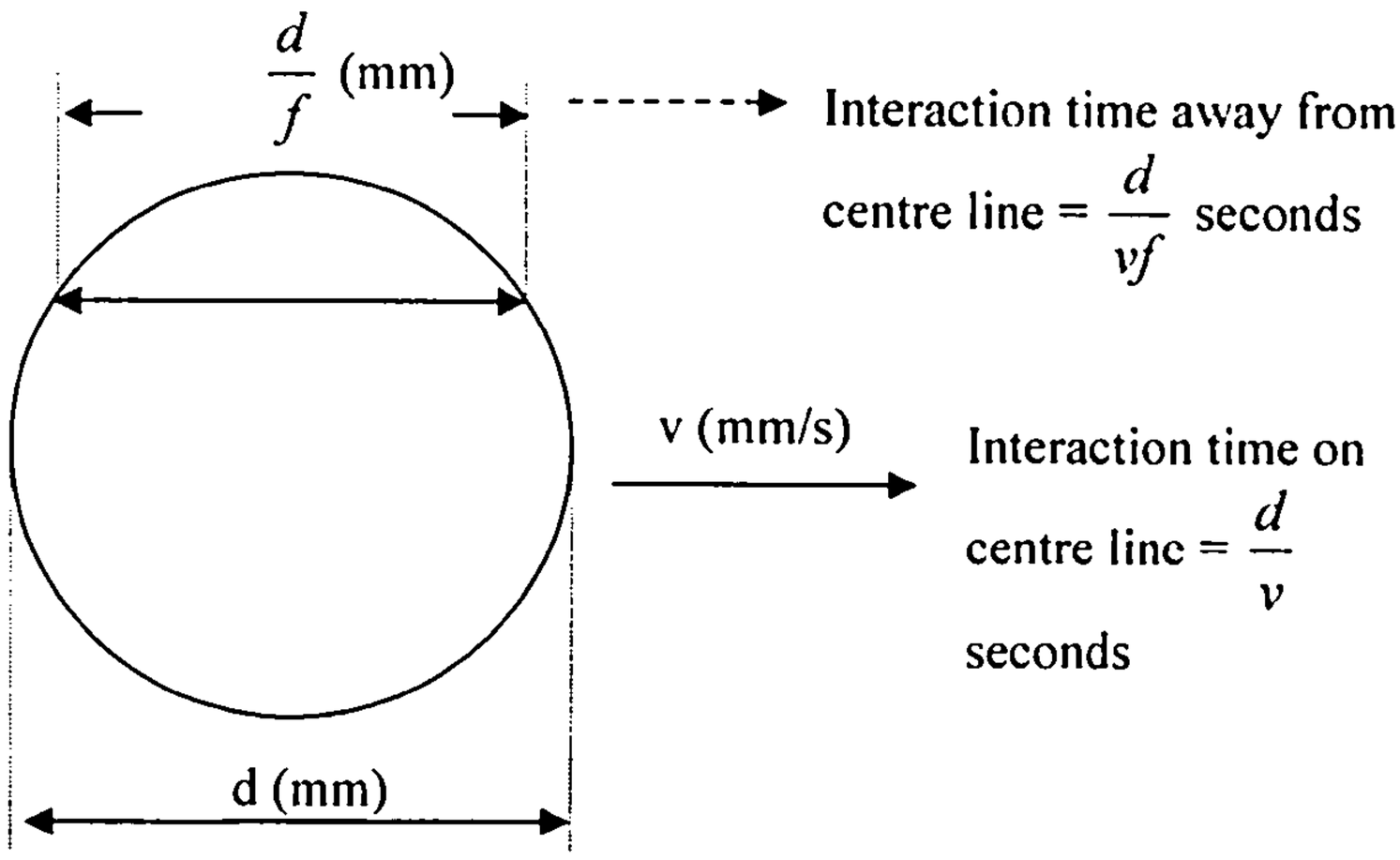

Figure 6.11 – The variation of laser-material interaction time with distance from the centre line of travel

b) Laser beam intensity

It was mentioned earlier in this thesis (section 2.3.2) that laser beams have a power intensity which is not constant across the beam cross section. The laser used in these experiments had a power distribution similar to that shown in figure 6.12 which is more intense towards its centre.

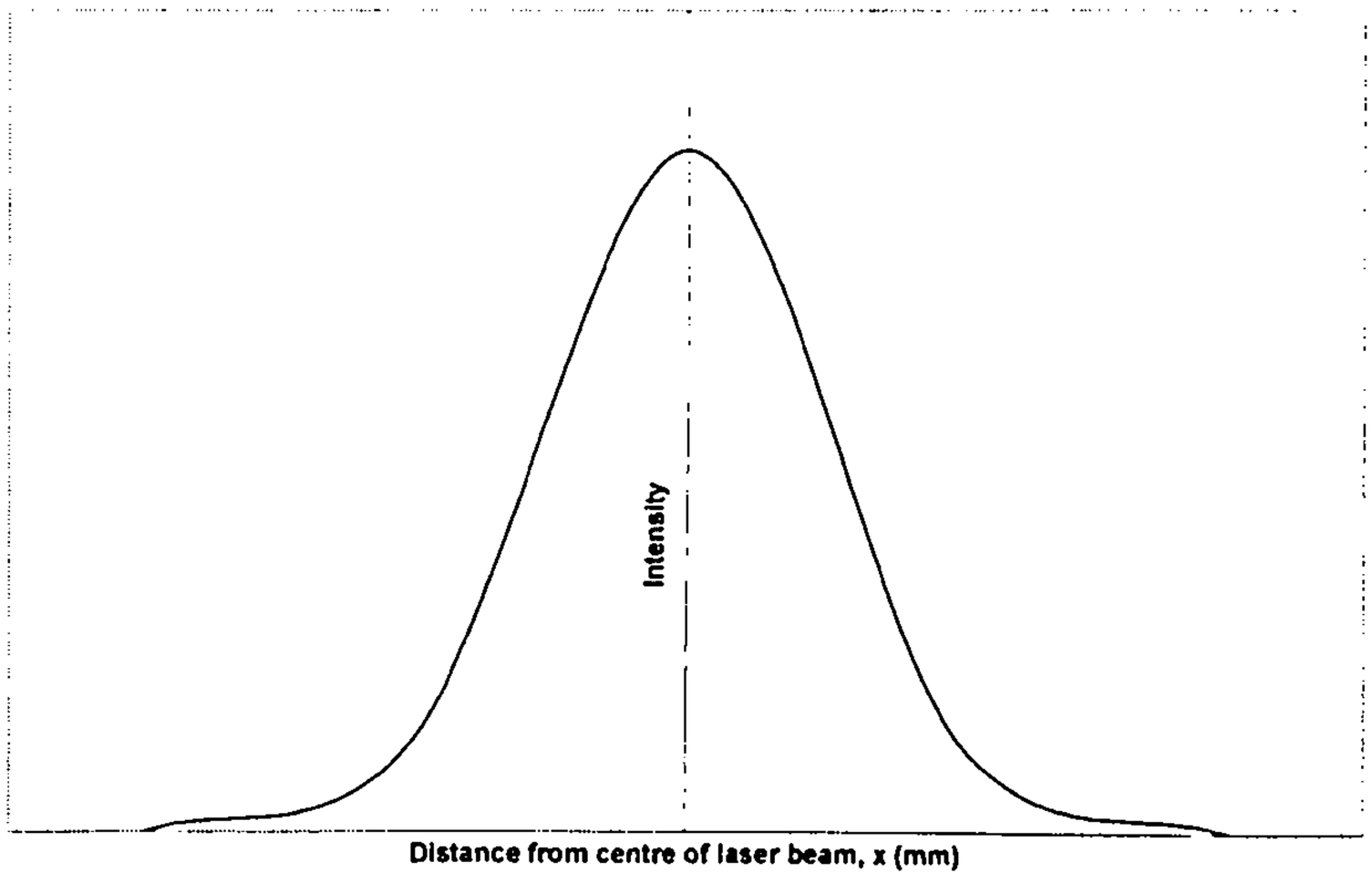

Figure 6.12 – A typical intensity distribution for the laser used in these experiments

This situation obviously combines with the interaction time argument shown in figure 6.11 to promote melting close to the centre line of the laser beam's travel.

As the spot radius is increased as we move across Region C the diameter and cross sectional area of the melt decreases. This is because the material requires a threshold power input to achieve melting. The zone in which this power input is available becomes ever smaller as the beam size is increased until, for very large diameter beams, the material is not melted at all.

To summarise this model briefly:

Region A – Very hot melt spreads sideways beyond the edge of the laser beam. Interaction times are short and melting efficiency is therefore low.

Region B – Maximum melting efficiency; widest and deepest welds are produced.

Region C – Energy inputs away from the centre line of movement are too low to achieve melting. Melting efficiency is low.

6.3 Tensile strength tests

True strain-true stress graphs obtained from transverse tensile strength tests results carried out for 3mm AA2024, AA5083 and AA6061 welds are shown below:

The graphs have been derived from tensile strength results shown in figures 5.13, 5.14 and 5.15. Figure 6.13 shows that the 3mm AA2024 samples fractured before there was any plastic deformation, suggesting that they were brittle.

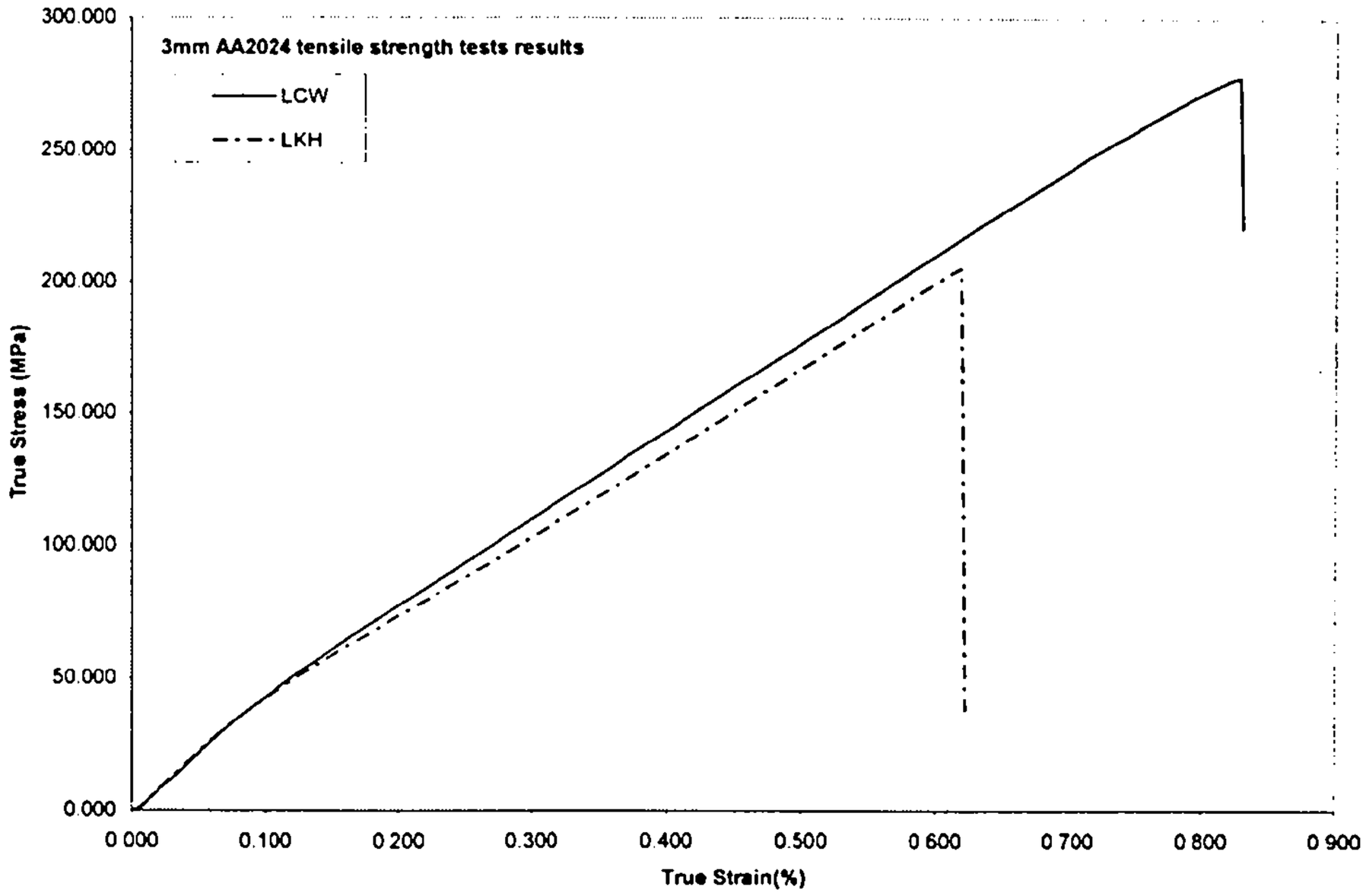

Figure 6.13 – Graph showing tensile strength test results for 3mm AA2024 laser conduction and laser keyhole butt-welds.

It should be noted that the tensile samples fractured in the weld zone, without any deformation.

The ultimate tensile strength for AA2024 is 475 MPa. The maximum stress applied was 275.4 MPa and 202.4 MPa for the laser conduction welding (LCW) and laser keyhole welding (LKH) samples respectively. This reveals that although both types of laser weld were weaker than the parent material, the laser keyhole welds were more brittle than the laser conduction welds.

The high power density during laser keyhole welding causes alloy composition changes (Zhao et al, 2001) due to vaporisation and results in the laser keyhole welds being the weaker of the two.

In the case of 3mm AA5083 (see figure 6.14) both the laser conduction and laser keyhole welds experienced plastic deformity. The samples stretched beyond the elastic zone into the plastic zone during the tensile tests.

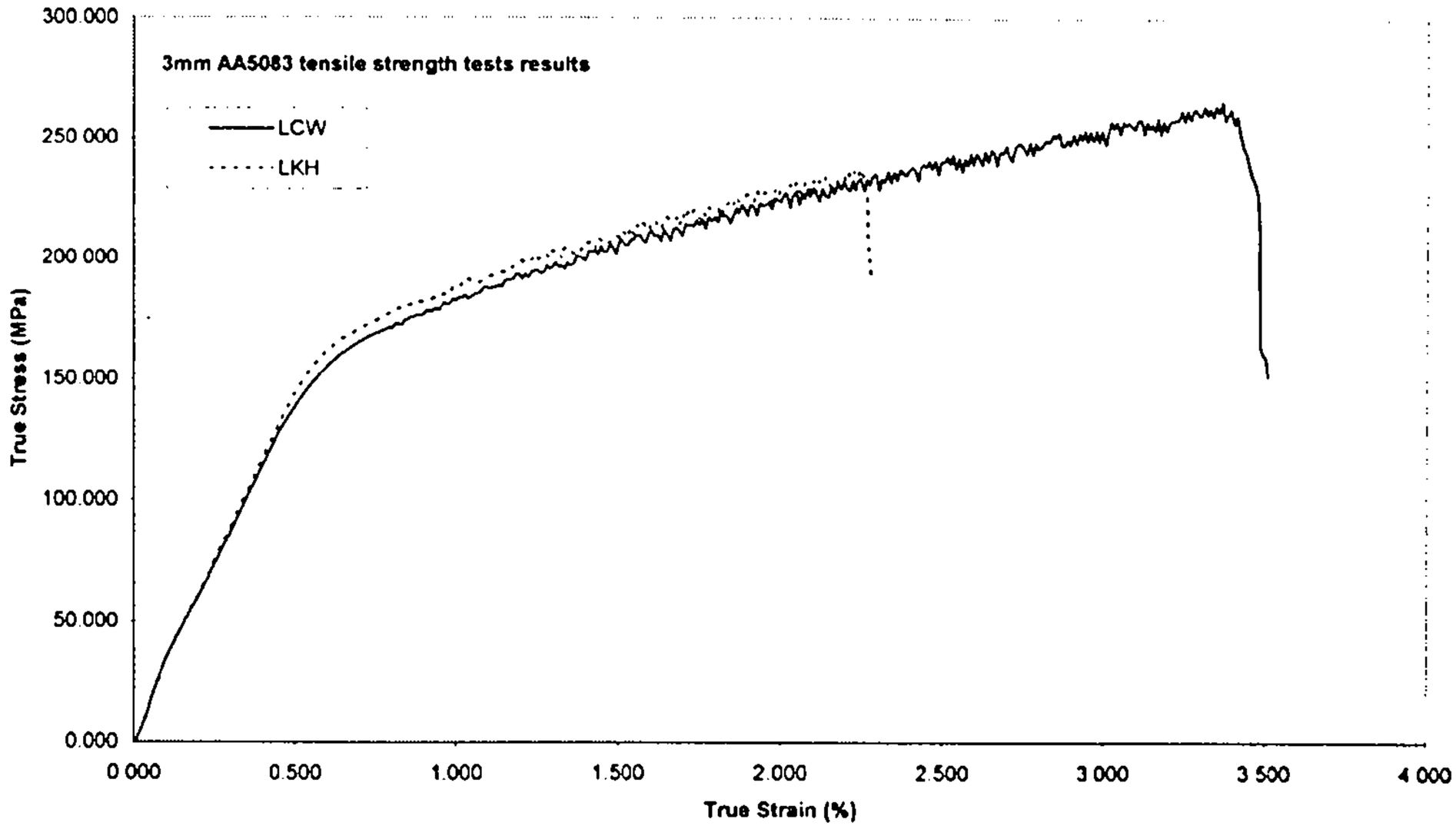

Figure 6.14 – Graph showing tensile strength test results for 3mm AA5083 laser conduction and laser keyhole butt-welds.

The AA5083 welds were more ductile than the AA2024 welds but with the laser conduction welds emerging stronger than the laser keyhole welds. Here again alloy depletion during keyhole welding caused a reduction in strength of the keyhole weld. Zhao et al found that during laser welding of AA5182 magnesium vaporisation occurred resulting in a lower magnesium concentration in the weld metal. This would definitely cause a weakening of the weld strength during laser keyhole welding. This was confirmed by the fact that the maximum loads applied were 256.7 MPa for laser conduction welds and 229.6 MPa for laser keyhole welds. The ultimate tensile strength (U.T.S.) for AA5083 is 300MPa. It should be noted that magnesium is the main alloy element (4 – 4.9%) apart from aluminium (94.8%) in AA5083.

Figure 6.15 shows the results true stress/true strain results for 3mm AA6061. In this case fracture occurred at the base metal and there was necking. The extension

continued well into the plastic zone culminating in the deformity of the tensile sample.

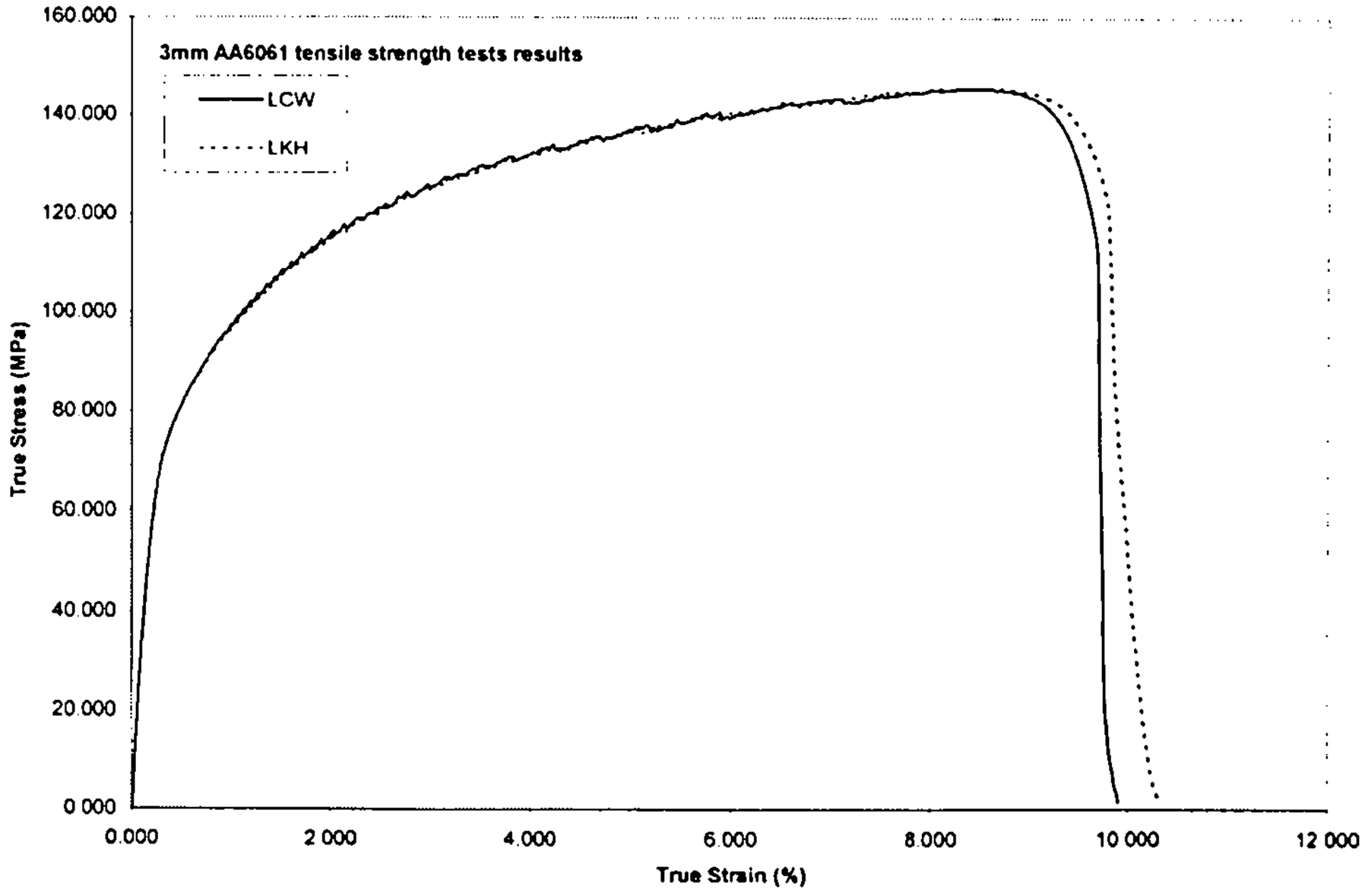

Figure 6.15 – Graph showing tensile strength test results for 3mm AA6061 laser conduction and laser keyhole butt-welds

In this case the changes in weld microstructure, both for keyhole and laser conduction welds, produced welds as strong if not stronger than the base metal. The maximum load for laser conduction welds was 134.7 MPa and 133.9 MPa for laser keyhole welds. The U.T.S for AA6061 is 125 MPa. It can be concluded that the tensile strength properties of the aluminium alloy welds varied in accordance with the strength of the base metal. The table below (6.1) illustrates the point. The stronger materials had the weakest welds (compared to the parent metal) of which the keyhole welds were the most brittle.

These results show that laser conduction welding may be a viable option for AA5083 and AA6061 but not for AA2024 if tensile strength is an issue. All the keyhole butt-welds had a tiny groove at the joint. However, the effect of the groove seems to be

Aluminium Alloy	U.T.S. (MPa)	Maximum Loads (MPa)	
		Conduction Welds	Keyhole Welds
AA2024	475	275.4	202.4
AA5083	300	256.7	229.6
AA6061	125	133.9	134.7

Table 6.1 – Tensile strength tests data

minimal bearing in mind the tensile strength response of AA6061. If the groove was to compromise significantly the strength of the keyhole welds, then the AA6061 would have responded differently, probably turning out far weaker than the base metal.

It is interesting to note that for AA5083 and AA6061 above the yield stress there are some fluctuations or serrations in the tensile test curve which indicate some form of discontinuous deformation. This occurs because there is some unyielded material in the test sample. It would be observed that these only occur for laser conduction welding and therefore it is safe to assume that the unyielded material is peculiar to laser conduction welds. The temperature range for laser conduction welding and the relatively wider area of laser conduction welds are probably responsible for this behaviour.

References:

Zhao, H. et al, *"Weld Metal Composition Change during Conduction Mode Laser Welding of Aluminium Alloy 5182"*, Metallurgical and Materials Transactions B, Vol 32B, pp.163 – 172, 2001

7. Conclusions

A method of laser conduction welding (LCW) using high-power defocused laser beams as opposed to industrial practice of focused laser beams was investigated. The results obtained were achieved for low speeds i.e. in the range of about 500 – 800 mm/min for aluminium alloys. The alloys used were 2mm gauge AA5083 and 3mm gauge AA5083-O, AA6061-O and AA2024-T3. Below is a summary of the findings:

- Theoretical and experimental results both demonstrated that the melting efficiency of the conduction limited laser welding process increased with laser beam radius until an optimum value was achieved. As the laser beam diameter increased beyond this optimum the melting efficiency (melt width and depth) decreased for any set of values of laser power and process speed etc.
- When the laser beam diameter was smaller than optimum the melt was of a larger diameter than the incident beam. This diameter spread was caused by the lateral transfer of surplus heat by Marangoni flow.
- When the laser beam diameter was larger than optimum the outer portions of the beam were insufficiently intense to cause melting. As the radius of the beam is further increased the proportion of the beam which is insufficiently intense increases and the weld diameter reduces further.
- Conduction limited welds were found to be generally stronger than their keyhole weld counterparts. This can be attributed to the fact that the boiling process inherent to keyhole welding tends to preferentially vaporise the alloying elements used to strengthen aluminium alloys.

Suggestions for future work:

- An improvement of the theoretical modelling of laser conduction welding to improve the agreement of the quantitative results with experimental measurements.
- Microstructural analysis of the metallurgical differences between keyhole and conduction limited welds.
- An extension of laser conduction welding research to a wide range of other alloys including steels.

Appendix A1

1D –SEMI-QUANTITATIVE ANALYSIS PROGRAM

```
program wmodelD
implicit none
integer,dimension(200)::fd
real,dimension(80)::sr
real,dimension(50)::pd
integer range,flag,k,j,z
real pi
character resp1,resp2,answer,mod

!*****************MAIN PROGRAM*****************************
      print*, 'Penetration Depth Program (1D)'
      pause

!************PENETRATION DEPTHS SECTION*********************

      open(10,file='srad.dat',status='old')    !spot radius file
      k=0
      flag=0

      do while(flag>=0)
            k=k+1
            read(10,*,iostat=flag) sr(k)
      end do

      close(10,status='keep')
      range=k-1


!*********PENETRATION DEPTHS FOR SPOT RADII****************

      open(6,file='srout1.dat',status='old')   !text output file for pd's
      open(7,file='srout2.dat',status='old')   !data output file for pd's


      call pendep(range,sr,pd)


      write(6,'(2X,"Spot Radius(mm)",2X,"Penetration Depth(mm)")')

      do j=1,range
      write(6,'(5X,F4.2,12X,F11.3)') sr(j),pd(j)
      write(7,'(5X,F4.2,12X,F11.3)') sr(j),pd(j)
      end do

      close(6,status='keep')
      close(7,status='keep')

      stop
```

```
        end

!*************************************************************************
!*************************SUBROUTINES*************************************
!*************************************************************************


!*********************Penetration Depth Subroutine*************************

        subroutine pendep(n,d,p)
        integer,intent(in)::n
        real,intent(in),dimension(n)::d
        real,intent(out),dimension(n)::p
        real alpha,TM,TB,TAMB,x,vel,pi,power,T
        real density,mass,sheat,absorp,constantA,constantB
        real ThermC

        ex = 2.718
        TM = 660
        TB = 2450
        density = 2.7 * 1e-6
        lheat = 3.97 * 1e5
        TAMB = 25
        sheat = 900
        absorp = 0.5
        vel = 10
        pi = 3.141592654
        ThermC = 226 * 1e-3

        print*,'Please enter Power in Watts'
        read*,power

        EP = absorp * power
        T = (TM - TAMB)/(TB - TAMB)
        alpha = ThermC/(density * sheat)

        constantA = 1.12 * sqrt(2 * alpha/vel)
        constantB = pi * TM * ThermC/EP

        do j=1,n

        p(j) = constantA * sqrt(d(j)) - constantB * d(j)**2

        end do

        end
```

Appendix A2

2D – SEMI-QUANTITATIVE ANALYSIS PROGRAM

```
program wmodel2DYAG
implicit none
integer,dimension(200)::fd
real,dimension(200)::sr2
real,dimension(50)::sr
real,dimension(50)::ww
real,dimension(80)::ym
      real,dimension(80)::pd
      integer range,flag,k,j,z
      real ss1,ss2,bb,spot_radius,pi,w,lamda,M_sq,focal_length
      real p,m,tes2,tes1,D,spot_radius_zero
      character resp1,resp2,answer,mod

!*****************MAIN PROGRAM*******************************
      print*, 'Spot radius(S)/Penetration depth(P)'
      read*,answer
!*****************SPOT RADIUS SECTION************************
  if(answer.eq.'S'.or.answer.eq.'s') then !beginning of 1st if block
      open(5,file='focal.dat',status='old')          !focal distance file
      j=0
      flag=0

do while(flag>=0)
        j=j+1
        read(5,*,iostat=flag) fd(j)
end do
close(5,status='keep')
range=j-1

open(3,file='outlist.dat',status='old')
call calc(range,fd,sr2)

write(3,'(6X,"Focal Distance(mm)",3X,"Spot Radius(mm)")')
do j=1,range
write(3,'(10X,I5,10X,F13.3)') fd(j),sr2(j)
end do

!***********PENETRATION DEPTHS SECTION*********************
      else if(answer.eq.'P'.or.answer.eq.'p') then !continuation of 1st if block
      print*,'PDs for spot radii(1)'
      print*,'PDs for y positions(2)'
      print*,'Weld widths(3)'
      read*,resp1
      if(resp1.eq.'1'.or.resp1.eq.'3') then     !2nd if,within 1st if block
      open(10,file='srad.dat',status='old')     !spot radius file
      k=0
      flag=0
```

```
        do while(flag>=0)
                k=k+1
                read(10,*,iostat=flag) sr(k)
        end do
        close(10,status='keep')
        range=k-1


!*********PENETRATION DEPTHS FOR SPOT RADII*******************
        if(resp1.eq.'1') then

        open(6,file='srout1.dat',status='old')   !text output file for pd's
        open(7,file='srout2.dat',status='old')   !data output file for pd's


        call pendep(range,sr,pd)
        write(6,'(2X,"Spot Radius(mm)",2X,"Penetration Depth(mm)")')

        do j=1,range
        write(6,'(5X,F4.2,12X,F11.3)') sr(j),pd(j)
        write(7,'(5X,F4.2,12X,F11.3)') sr(j),pd(j)
        end do

        close(6,status='keep')
        close(7,status='keep'
!*************WELD WIDTHS*****************************
        else if(resp1.eq.'3') then

        open(4,file='srout3.dat',status='old')   !output file for weld widths

        call width(range,sr,ww)

        do j=1,range
        write(4,'(9X,F4.2,4X,F10.6)') sr(j),ww(j)
        end do

        close(4,status='keep')
        end if

! *******PENETRATION DEPTHS FOR Y POSITIONS*****************

        else if(resp1.eq.'2') then

        open(8,file='ydist.dat',status='old')     !data file for y positions
        k=0
        flag=0
        do while(flag>=0)
                k=k+1
                read(8,*,iostat=flag) ym(k)
```

```
end do

close(8,status='keep')
range=k-1

open(9,file='yout.dat',status='old')      !output file for pd's of y positions

print*,'Enter spot radius in mm'
read*,spot_radius

call pendep2(range,spot_radius,ym,pd)

        do j=1,range
        write(9,'(9X,F8.6,4X,F9.6)') ym(j),pd(j)
        end do

        close(9,status='keep')
        end if
                end if  !end of 1st if

        stop
        end

!*****************************SUBROUTINES**************************
        subroutine      calc(n,b,a)
        integer,intent(in)::n
        integer,intent(in),dimension(n)::b
        real,intent(out),dimension(n)::a
        real spot_radius_zero, pi, lamda,M_sq,ss1,ss2
        real btemp,w,beam_diam
        character rep1*10
        integer p,m,focal_length

        write(3,'(20X,"RESULTS FOR YAG LASER")')

        pi = 3.141592654
        lamda = 1.06E-3
        M_sq = 100
        beam_diam = 45
        p = 0
        m = 0


        write(3,'(32X,"TEM",I1,I1)') p,m

!       TEMpm represents mode of laser beam

        spot_radius_zero = 0.240
        print*,'Enter calculation mode for spot radius(DIFL/BGAUSS)'
        read*,rep1
```

```
      print*,rep1

      write(3,'(20X,"CALCULATION MODE IS ",A10)') rep1

      do j=1,n

!     DIFFRACTION LIMITED SPOT RADIUS WITHOUT M SQUARED
      if(rep1.eq.'BGAUSS'.or.rep1.eq.'b')&
 &a(j) = spot_radius_zero*sqrt(1+(b(j)* lamda/(pi * (spot_radius_zero)**2))**2)

!     DIFFRACTION LIMITED SPOT RADIUS WITH M SQUARED
      if(rep1.eq.'DIFL'.or.rep1.eq.'d')&
&a(j)=spot_radius_zero*sqrt(1+(b(j)*lamda*M_sq/(pi*(spot_radius_zero)**2))*2)
      print*,a(j)
      end do

      end

      subroutine pendep(n,d,q)
      integer,intent(in)::n
      real,intent(in),dimension(n)::d
      real,intent(out),dimension(n)::q
      real alpha,TM,TB,TAMB,T,ex,vel,pi,ym,power,sheat
      real t1,p1,p2,p3,p4,p5,K,dd,ymm,t2,t3,z_sq

      ex = 2.718
      TM = 660
      TB = 2520
      TAMB = 25
      vel = 10
      sheat = 900
      density = 2.7 * 1e-6
      pi = 3.141592654
      K = 226 * 1e-3

      alpha = K/(density * sheat)

      T = (TM - TAMB)/(TB - TAMB)


      print*,'Enter power in Watts'
      read*,power

      print*,'Enter distance from weldpool centre'
      read*,ym


      do j=1,n

      z_sq = (d(j)/ex * sqrt(pi * alpha * d(j)/vel))
```

```
        t1 = d(j)**2/(4 * alpha)

        t2 = 2 * d(j)/vel

!       print*,z_sq


        p1 = 2 * pi * K * sqrt(t2 * (t2 + t1)) * vel * (TM - TAMB)

        p2 = log(power/p1)

        if(p2.lt.0) goto 10

        p3 = 4 * alpha * t2 * p2

        p4 = (ym**2 * t2/(t2 + t1))

        if((p3-p4).lt.0) goto 10

        p5 = sqrt(p3 - p4)

        q(j) = p5 - sqrt(z_sq)


10 end do

        end


        subroutine pendep2(n,c,d,q)
        integer,intent(in)::n
        real,intent(in),dimension(n)::d
        real,intent(out),dimension(n)::q
        real,intent(in)::c
        real alpha,TM,TB,TAMB,T,ex,vel,pi,power
        real t1,p1,p2,p3,p4,p5,K,dd,t2,t3,z_sq,qq


        ex = 2.718
        TM = 660
        TB = 2520
        TAMB = 25
        vel = 4.5
        sheat = 900
        density = 2.7 * 1e-6
        pi = 3.141592654
        K = 226 * 1e-3

        alpha = K/(density * sheat)
```

```
T = (TM - TAMB)/(TB - TAMB)


print*,'Enter power in Watts'
read*,power


do j=1,n

t1 = c**2/(4 * alpha)

t2 = 2 * c/vel

z_sq = (c/ex * sqrt(pi * alpha * c/vel))

!     print*,z_sq


p1 = 2 * pi * K * sqrt(t2 * (t2 + t1)) * vel * (TM - TAMB)

p2 = log(power/p1)

if(p2.lt.0) goto 10

p3 = 4 * alpha * t2 * p2

p4 = (d(j)**2 * t2/(t2 + t1))

if((p3-p4).lt.0) goto 10

p5 = sqrt(p3 - p4)

qq = p5 - sqrt(z_sq)

q(j) = (qq * -1)

10 end do

end


subroutine width(n,f,g)
integer,intent(in)::n
real,intent(in),dimension(n)::f
real,intent(out),dimension(n)::g
real alpha,TM,TB,TAMB,T,ex,vel,pi,power
real t1,p1,p2,p3,p4,p5,K,dd,ymm,t2,t3,z_sq

ex = 2.718
```

Appendix A2

```
TM = 660
TB = 2520
TAMB = 25
vel = 10
sheat = 900
density = 2.7 * 1e-6
pi = 3.141592654
K = 226 * 1e-3

alpha = K/(density * sheat)

T = (TM - TAMB)/(TB - TAMB)


print*,'Enter power in Watts'
read*,power


do j=1,n

z_sq = (f(j)/ex * sqrt(pi * alpha * f(j)/vel))

t1 = f(j)**2/(4 * alpha)

t2 = 2 * f(j)/vel
        p1 = 2 * pi * K * sqrt(t2 * (t2 + t1)) * vel * (TM - TAMB)
        p2 = log(power/p1)
        p3 = 4 * alpha * (t1 + t2)
        p4 = (z_sq * (t2 + t1)/t2)

        if(((p3*p2)-p4).lt.0) goto 10

        g(j) = sqrt((p3 * p2) - p4)


10 end do

        end
```

Appendix B – Table of Values

Sample	FD(mm)	SR (mm)	PD(mm)	WW(mm)	AR
PP1	5	0.531	0.643	1.786	0.360
PP2	10	0.97	0.571	2.143	0.267
PP3	15	1.429	0.714	2.429	0.294
PP4	20	1.892	0.643	3.429	0.188
PP5	25	2.358	0.786	3.857	0.204
PP6	30	2.825	1.000	4.500	0.222
PP7	35	3.292	1.357	5.143	0.264
PP8	40	3.76	1.571	5.357	0.293
PP9	45	4.228	1.857	6.500	0.286
PP10	50	4.697	2.000	6.571	0.304
PP11	55	5.175	2.071	7.143	0.290
PP12	60	5.633	1.714	6.500	0.264
PP13	65	6.102	1.500	6.857	0.219
PP14	70	6.571	0.429	5.214	0.082

Table A1 - Table showing penetration depths corresponding to distances from the focus for 3mm gauge mild steel samples; v = 100mm/min; 127mm f.l. ZnSe lens; samples PP

Certain abbreviations have been used namely:

FD = Distance above/below focus

PD= Measured penetration depth

WW =Measured weld width

AR = Aspect ratio

SR = Calculated Spot Radius

Appendix B

Sample	FD(mm)	SR(mm)	PD(mm)	WW(mm)	AR
F1	10	0.683	1.212	1.515	0.800
F2	20	1.061	1.136	2.348	0.484
F3	30	1.492	1.212	3.182	0.381
F4	40	1.941	1.515	4.545	0.333
F5	50	2.397	1.667	4.318	0.386
F6	60	2.857	2.273	4.545	0.500
F8	80	3.785	2.348	4.848	0.484
F9	90	4.25	2.348	4.545	0.517
F10	100	4.716	1.970	5.227	0.377
F11	110	5.183	1.364	5.303	0.257
F12	120	5.65	0.758	5.985	0.127
F13	130	6.117	0.682	6.212	0.110
F14	140	6.585	0.833	6.591	0.126
F15	150	7.052	0.682	6.061	0.113
F16	160	7.52	0.682	5.985	0.114

Table A2 - Table showing penetration depths corresponding to distances from the focus for 2.5mm mild steel samples welded at 180mm/min; 254mm f.l. ZnSe lens; samples F

Appendix B

Sample	FD(mm)	SR(mm)	PD(mm)	WW(mm)	AR
G1	15	0.861	0.985	1.818	0.542
G2	20	1.061	1.136	2.424	0.469
G3	30	1.492	1.212	3.712	0.327
G4	40	1.941	2.424	3.788	0.640
G5	50	2.397	2.500	4.848	0.516
G6	60	2.857	2.424	4.242	0.571
G7	70	3.32	1.439	4.242	0.339
G8	80	3.785	0.682	4.848	0.141
G9	90	4.25	0.455	5.152	0.088
G10	100	4.716	0.682	5.606	0.122
G11	110	5.183	0.682	6.061	0.113
G12	120	5.65	0.682	6.136	0.111

Table A3 - Table showing penetration depths corresponding to distances from the focus for 2.5mm mild steel samples welded at 120mm/min; 254mm f.l ZnSe lens; samples G

Appendix B

Sample	FD(mm)	SR(mm)	PD(mm)	WW(mm)	AR
E1	10	0.847	0.929	1.857	0.500
E2	15	1.227	1.214	2.000	0.607
E3	20	1.615	1.143	2.286	0.500
E4	25	2.007	1.286	2.500	0.514
E5	30	2.4	0.714	3.643	0.196
E6	35	2.795	0.571	3.714	0.154
E7	40	3.19	0.500	4.000	0.125
E8	45	3.586	0.571	4.500	0.127
E9	50	3.982	0.929	4.929	0.188
E10	55	4.378	1.214	5.500	0.221
E11	60	4.774	1.429	5.714	0.250
E12	65	5.17	1.571	6.000	0.262
E13	70	5.567	1.929	6.071	0.318
E14	75	5.964	1.857	6.286	0.295
E15	80	6.36	1.571	6.500	0.242
E16	85	6.757	1.500	6.571	0.228
E17	90	7.154	1.357	6.143	0.221
E18	95	7.55	1.500	6.500	0.231
E19	100	7.947	1.071	5.857	0.183
E20	105	8.344	0.786	5.714	0.138

Table A4 - Table showing penetration depths corresponding to distances from the focus for 2mm mild steel samples welded at 175mm/min; 150mm f.l. lens; sample E

Appendix B

Sample	FD(mm)	SR(mm)	PD(mm)	WW(mm)	AR
ES1	5	0.494	1.286	2.214	0.581
ES2	10	0.847	1.214	2.357	0.515
ES3	15	1.227	1.214	2.071	0.586
ES4	20	1.615	1.571	3.429	0.458
ES5	25	2.007	1.214	3.000	0.405
ES6	30	2.4	1.071	3.143	0.341
ES7	35	2.795	0.786	3.357	0.234
ES8	40	3.19	0.786	4.071	0.193
ES9	45	3.586	1.000	4.429	0.226
ES10	50	3.982	1.286	4.643	0.277
ES11	55	4.378	2.000	5.071	0.394
ES12	60	4.774	2.000	5.643	0.354
ES14	70	5.567	1.429	5.429	0.263
ES15	75	5.964	1.214	4.929	0.246
ES16	80	6.36	1.429	4.429	0.323
ES17	85	6.757	0.714	5.071	0.141

Table A5 - Table showing penetration depths corresponding to distances from the focus for 2mm mild steel samples welded at 120mm/min; 150mm f.l. ZnSe lens; samples ES

Appendix B

Sample	v (mm/min)	Power (W)	Current (A)	FD(mm)	PDC(mm)
AU1	360	0	120	0	0.929
AU2	360	1800	120	40	1.143
AU3	360	1800	120	50	1.143
AU4	360	1800	120	60	1.357
AU5	360	1800	120	70	1.357
AU6	360	500	120	0	2.357
AU8	360	650	120	0	3.000
AU7	360	800	120	0	3.000

Table A6 - Table showing penetration depths corresponding to TIG and laser–arc (TIG) welding of 3mm gauge AA5083; constant welding speed and arc current with different levels of laser power at various distances above focus

Sample	v (mm/min)	Power (W)	Current (A)	FD(mm)	PDC(mm)
BU1	360	0	120	0	0.929
BU4	360	340	120	0	2.500
BU3	360	540	120	0	3.000
BU2	360	800	120	0	3.000
BU6	420	0	120	0	0.714
BU5	420	540	120	0	1.857
BU7	420	640	120	0	2.214
BU8	420	820	120	0	3.000

Table A7 - Table showing penetration depths corresponding to TIG and laser–arc (TIG) welding of 3mm gauge AA5083; welding speeds of 360mm/min and 420mm/min with different levels of laser power at constant arc current

Appendix B

Sample	FD(mm)	SR(mm)	PD(mm)	WW(mm)	AR
GP22	10	0.68	0.410	1.385	0.296
GP23	20	1.06	0.923	2.308	0.400
GP24	30	1.49	2.000	3.590	0.557
GP25	40	1.94	2.000	4.564	0.438
GP26	60	2.86	2.000	3.730	0.536
GP27	80	3.79	1.744	3.949	0.442
GP28	100	4.72	0.667	3.487	0.191

Table A8 - Table showing penetration depths for CO_2 laser conduction welding of 2mm gauge AA5083 at a welding speed of 600mm/min; 254 mm f.l. ZnSe lens; samples GP

Sample	FD(mm)	SR(mm)	PDC(mm)	WW(mm)	AR
S1	5	0.74	0.621	2.069	0.300
S2	10	1.43	1.655	3.621	0.457
S3	15	2.12	2.379	4.448	0.535
S4	20	2.82	3.000	5.483	0.547
S5	25	3.52	2.938	5.586	0.526
S6	30	4.23	2.276	5.483	0.415
S7	35	4.93	1.034	4.759	0.217

Table A9 - Table showing penetration depths for Nd:YAG laser conduction welding of 3mm gauge AA5083 at welding speed of 600mm/min with a defocused laser beam; samples S

Appendix B

Sample	FD(mm)	SR(mm)	PD(mm)	WW (mm)	AR
SS6	5	0.74	0.931	2.069	0.450
SS5	10	1.43	1.345	3.517	0.382
SS4	15	2.12	2.069	4.345	0.476
SS1	20	2.82	2.483	5.276	0.471
SS2	25	3.52	1.759	4.862	0.362
SS3	30	4.23	1.034	4.034	0.256

Table A10 - Table showing penetration depths for Nd:YAG laser conduction welding of another set of samples of 3mm AA5083 at a welding speed of 720mm/min with a defocused laser beam; samples SS.

Surfaces	Specular included geometry (%)
As received	65.1
Sandblasted	52.28
Brushed	86.32
Sandblasted and brushed	81.61

Uncertainty ± 1.6 %

Table A11 - Table showing reflectance for various surfaces of AA5083 using laser irradiation of wavelength 1064nm (which corresponds to the Nd:YAG wavelength)